

NEUTRAL BEAM DRIVEN IMPURITY
FLOW REVERSAL IN TOKAMAKS

A THESIS
Presented to
the Faculty of the Division
of Graduate Studies

By

Richard Byron Bennett

In Partial Fulfillment
of the Requirements for the Degree
Doctor of Philosophy
in the School of Nuclear Engineering

Georgia Institute of Technology

March, 1984

NEUTRAL BEAM DRIVEN IMPURITY

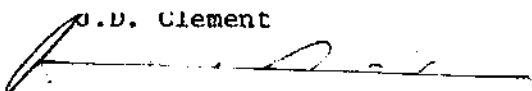
FLOW REVERSAL IN TOKAMAKS

Approved:

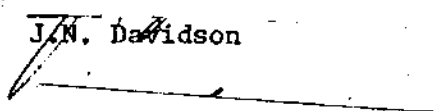


W.M. Stacey, Jr., Chairman *11/16*

R.G. Bateman



J.D. Clement



J.N. Davidson

A.V. Larson

Date Approved by Chairman 2/13/84

TABLE OF CONTENTS

	Page
ACKNOWLEDGEMENTS	iv
LIST OF TABLES	v
LIST OF ILLUSTRATIONS	vi
SUMMARY	x
Chapter	
I. INTRODUCTION	1
II. DERIVATION OF THE TRANSPORT EQUATIONS	13
2.1 Introduction	
2.2 Surface Flow Evaluation	
2.3 Parallel Flow Evaluation	
2.4 Transport Fluxes	
2.5 Approximations	
2.6 Reduction to the Collisional Regime	
2.7 Reduction to the Mixed Regime	
2.8 Reduction to the Collisionless Regime	
2.9 Investigation of the External Drag	
III. INTERPRETATION OF THE PLT EXPERIMENTS	88
3.1 Introduction	
3.2 PLT Experimental Data	
3.3 Analysis of the Experiment Before Injection	
3.4 Analysis of the Co-injected Experiment	
3.5 Analysis of the Counter-injected Experiment	
3.6 Calculation of Tungsten Accumulation in PLT	
3.7 Evaluation of Inertial Theory	
3.8 Review of Analyses of ISX-B	
3.9 Summary of the Model Developed in PLT	
IV. PREDICTIONS FOR FUTURE MACHINES	152
4.1 Introduction	
4.2 Predictions for the Tokamak Fusion Test Reactor	
4.3 Predictions for the Fusion Engineering Device	
4.4 Predictions for STARFIRE	
4.5 Summary	
V. CONCLUSIONS	222

Appendices

A. TWO SPECIES PARALLEL FLOW EVALUATION	225
B. TWO SPECIES ELECTROSTATIC POTENTIAL	233
C. BEAM DRIVEN FLUXES FOR MULTIPLE SPECIES	239
D. DEFINITIONS AND EVALUATION OF COEFFICIENTS	245
BIBLIOGRAPHY	255

ACKNOWLEDGEMENTS

I would like to thank my advisor, Weston M. Stacey, Jr., for suggesting this topic and his kind and patient guidance. Thanks are also given to the members of my reading committee, G. Bateman, J. D. Clement, J. N. Davidson, and A. V. Larson, for their suggestions for improving and clarifying this text. In particular, I deeply appreciate the contributions made by Drs. Davidson and Bateman to my understanding of the basic physical processes involved in this thesis.

The pursuit of the understanding of plasmas is as much an art as it is a science. In times of frustration, it has been very helpful and comforting to know that the art portion of this field is often treated in the same manner as the fifth classical element of the Pythagorans. This element is often considered now to be represented by a plasma. I sincerely hope that my contribution to the fifth suit of the Tarot will provide fertile ground for future images, and that a better understanding of plasmas will ensue.

LIST OF TABLES

Table	Page
2.6.1 Collisional Limit of Terms	60
2.7.1 Mixed Regime Limit of Terms	68
3.2.1 PLT Experimental Data	98
3.7.1 PLT Velocity Profiles	138
4.2.1 TFTR Study Parameters	169
4.3.1 FED Study Parameters	188
4.4.1 STARFIRE Study Parameters	210
D-1 Summary of Least Squares Fits for the Viscosity Coefficients	253

LIST OF ILLUSTRATIONS

Figure	Page
2.2.1 Generalized Axisymmetric Co-ordinate System	29
2.9.1 Central Toroidal Velocity in PLT with Neutral Beam Injection	87
3.2.1 Electron Density Profile in the Center of PLT During Flow Reversal Experiments	99
3.2.2 Electron Temperature Profiles in PLT During the Co-injected Flow Reversal Experiment	100
3.2.3 Electron Temperature Profiles in PLT During the Counter-injected Flow Reversal Experiment	101
3.2.4 Coronal Equilibrium Charge State Variance with Electron Temperature for Tungsten	102
3.2.5 Scaling of Ion Temperature Measurements vs. Line Average Electron Density	103
3.2.6 Radial Profiles of Ion Temperature Before and During Neutral Beam Injection from Doppler Broadening	104
3.2.7 PLT Momentum Input Profile at the Beginning of Injection	105
3.3.1 Analysis of PLT Impurity Flow Reversal Before Beam Injection, Co-injected Beam, $t=250$ msec	111
3.4.1 Analysis of PLT Co-injected Flow Reversal Experiment, $t=280$ msec	116
3.4.2 Analysis of PLT Co-injected Flow Reversal Experiment, $t=290$ msec	117
3.4.3 Tungsten Density Divided by Electron Density for $0 < r < 20$ cm During the PLT Co-injected Flow Reversal Experiment	118

3.5.1 Tungsten Density Divided by Electron Density for $0 < r < 20$ cm During the PLT Counter-injected Flow Reversal Experiment	122
3.5.2 Analysis of the PLT Counter-injection Experiment, $t=280$ msec	123
3.5.3 Analysis of the PLT Counter-injection Experiment, $t=290$ msec	124
3.5.4 Comparison of Experimental and Density Extrapolated Fluxes in the PLT Counter-injected Experiment, $t=290$ msec	125
3.6.1 Tungsten Density Profile Evolution in PLT During Co-injection from Model and Experiment	130
3.6.2 Tungsten Density Profile Evolution in PLT During Counter-injection from Model and Experiment	131
3.6.3 Tungsten Density Profile Evolution in PLT During Counter-injection from Model times Two and Experiment	132
3.7.1 PLT Central Rotation Velocity as a Function of Average Electron Density	139
3.7.2 Typical PLT Velocity Profile	140
3.7.3 Analysis of the PLT Before Injection Experiment Using Inertial Theory Only	141
3.7.4 Analysis of the PLT Co-injected Experiment Using Inertial Theory Only	142
3.7.5 Analysis of the PLT Counter-injected Experiment Using Inertial Theory Only	143
3.7.6 Analysis of the PLT Co-injected Experiment Using a Combination of Gradient, Momentum Driven, and Inertial Fluxes	144
3.7.7 Analysis of the PLT Counter-injected Experiment Using a Combination of Gradient, Momentum Driven, and Inertial Fluxes	145
4.1.1 Trends of Sputtering Yield for a Number of Materials for Deuterons	156

	viii
4.2.1 TFTR Neutral Beam Layout	170
4.2.2 Reference TFTR Density, Temperature, Safety Factor, and Momentum Deposition Profiles	171
4.2.3 Tungsten Density Profiles in TFTR for Base Case	172
4.2.4 Tungsten Density Profiles in TFTR for Centerline Temperatures T=2 keV and T=5 keV	175
4.2.5 Tungsten Density Profiles in TFTR for Centerline Temperatures T=22 keV and T=5 keV	176
4.2.6 Tungsten Density Profiles in TFTR with Edge Source Rates of 1×10^{16} /m sec and 0.5×10^{16} /m sec	177
4.2.7 Tungsten and Iron Concentrations in TFTR	178
4.3.1 Density and Temperature Profiles Used in FED	189
4.3.2 Neutral Beam Momentum Deposition Profiles in FED	190
4.3.3 Iron Density Profiles in FED for Base Case	191
4.3.4 Plasma Profiles Used to Calculate FED Profile Sensitivity	194
4.3.5 Iron Concentrations in FED with Low Edge Density and 90% of Centerline Edge Density Main Ion Profiles	195
4.3.6 Iron Concentrations in FED with Low Edge Density and 100% of Centerline Edge Density Main Ion Profiles	196
4.3.7 Iron Concentrations in FED with Centrally Peaked and Base Ion Temperature Profiles	198
4.3.8 Iron Concentration in FED with Parabolic and Base Ion Temperature Profiles	199
4.3.9 Iron Concentration in FED with Different Co-injected Powers	200
4.4.1 Density and Temperature Profiles Used in the Analysis of STARFIRE	211
4.4.2 Iron Profiles in STARFIRE for the Base Case	212

4.4.3	Iron Profiles in STARFIRE with Balanced Injection and 50 MWatts and 100 MWatts Co-injected Power	215
4.4.4	Relative Toroidal Momentum Deposition Profiles in STARFIRE at 30°, 60°, and 90° Injection Angles	215
4.4.5	Iron Profiles in STARFIRE with 30°, 60°, and 90° Injection Angles	215
4.4.6	Relative Momentum Deposition Profiles in STARFIRE with 100 keV, 200 keV, and 400 keV Injection Energies	216
4.4.7	Iron Concentrations in STARFIRE with Balanced Injection and Co-injection at 100 keV, 200 keV, and 400 keV Beam Energies	216
4.4.8	Relative Momentum Distribution Profiles Used for Regional Momentum Deposition Analysis in STARFIRE	217
4.4.9	Iron Concentrations in STARFIRE with Balanced Injection and Regional Deposition of Co-injected Momentum	217
D-1	Variance of Viscosity Ratio μ_2/μ_1 with Collisionality	254
D-2	Variance of Viscosity Ratio μ_3/μ_1 with Collisionality	254

SUMMARY

A theory for the effect of neutral beam injection on the transport of impurity ions in a tokamak plasma was extended to include the effect of temperature gradients. A theory for the effect of neutral beam momentum input on the radial heat conduction was also developed. Injection of neutral beam momentum in the direction of the toroidal magnetic field, called co-injection, was found to reverse the normally inward flow of impurities. The theory was found to provide a reasonable basis for interpretation of impurity flow reversal experiments performed in the Princeton Large Torus (PLT), when a multiplicative factor of two was applied to the predicted impurity fluxes.

The model that was adjusted to fit the experimental results in PLT was then applied to the Tokamak Fusion Test Reactor (TFTR) and to models based on designs of future tokamaks. Using the maximum available co-injected beam power (16 MW) in TFTR is predicted to lead to a substantial reduction (relative to balanced momentum injection) in the penetration of impurities to the center of the discharge and to substantially increase the impurity radiation from the plasma edge. This would possibly lead to a cold, radiating edge which would reduce sputtering erosion of the limiter. A modest amount (~ 30 MW) of co-injected beam power is

predicted to substantially reduce the penetration of impurities to the center of models of the Fusion Engineering Device (FED) and the STARFIRE commercial reactor. If these plasmas operate with a high edge density, as would be the case with a high rate of edge recycling, this amount of co-injected power is also sufficient to significantly increase the impurity radiation from the edge region, again possibly leading to a cold radiating edge and associated reduction in limiter erosion.

CHAPTER I

INTRODUCTION

The tokamak [1] is currently the most highly developed magnetic confinement concept. The tokamak confines a plasma in a toroidal confinement chamber. The magnetic configuration in a tokamak consists of a toroidal component produced by external coils and a poloidal component produced partially by external coils and partially by a toroidal current driven in the plasma. The resulting field is helical. Since ions drift upwards under the influence of the toroidal field component, the poloidal field component is necessary to average out any net radial displacement. In present day tokamaks, this current is driven by a transformer, limiting the tokamak to pulsed operations.

As tokamaks are developed from pulsed devices with operating times of fractions of a second to long-pulsed or quasi-steady state devices, it is very important to understand the radial movement of non-hydrogen "impurity" ions inside the plasma. These impurities cause enhanced radiation which, if controlled, could help to control the burn. If uncontrolled, the impurities could prevent

ignition of the plasma, possibly barring the tokamak from becoming a practical fusion power reactor. Also, the impurities with their associated electrons take up some of the plasma pressure, reducing the system efficiency.

The purpose of this thesis is to investigate the use of neutral beam injection to reduce or reverse the normal inward transport flux of impurity ions. The fluid model neoclassical transport theory, which had previously been developed to treat the effect of neutral beam momentum injection, is extended through the fourth moment equation to include temperature gradient effects and heat fluxes. The extended theory is first applied to analyze experiments in current generation machines, and then applied to predict the effects of neutral beam flow reversal in future machines.

The first goal of this thesis is to calculate the radially outward rate of particle transport across the magnetic field. In a magnetic field, ions move along the field lines to within a small excursion. This excursion is either the gyroradius (0.001 to 0.01 meter) if collisions are frequent in the plasma, or the banana shaped orbit width (0.03 to 0.1 meter) of particles trapped in magnetic wells if collisions are infrequent. As mentioned earlier, a magnetic field line follows a gentle helical path around the torus, which varies the field lines distance from the tokamak center and therefore the magnetic field strength. The varying magnetic field along the particle path forms a

magnetic well in which a particle can be trapped. The trapped particle executes "banana" shaped orbits since the magnetic gradient and curvature drift is in different directions for each leg of the orbit. Trapping is important when the time between collisions is long compared to the time required for the particle to complete a poloidal transit, since frequent collisions prevent completion of the banana orbits.

The field lines form nested, toroidal flux surfaces of constant pressure, temperature, and density in a tokamak. Excluding field irregularities, the only mechanism for driving particle transport across the flux surfaces is momentum exchange. Coulomb collisions among plasma particles of different species was the earliest form of momentum exchange that was recognized to drive particle transport across flux surfaces. Since the ion momentum exchange in collisions with impurities is greater than ion momentum exchange in collisions with electrons by a factor of $Z^2\sqrt{m_i/m_e}$, where Z is the charge state, m_i is the impurity mass, and m_e the electron mass, the ion-electron collisions can be ignored when $n_i Z^2/n_e > \sqrt{m_e/m_i}$, where n_i is the impurity concentration and n_e is the main ion concentration.

The most basic explanation of particle transport by momentum exchange is simple diffusion by Fick's Law. When a particle is displaced a root mean square distance of $\sqrt{\Delta x}$ in a

collision, and the mean time between collisions is Δt , the flux of particles crossing a plane perpendicular to the x direction is approximately $\Gamma_x \sim \Delta x^2 / \Delta t n$, where n is the particle density. This flux crosses the plane in both directions, leaving a net flux only if a density gradient exists. Only the gradient over the range of Δx is affected, leaving the net flux to be

$$\Gamma_{\text{net}} \approx \frac{\Delta x}{\Delta t} \left(n \Big|_{x-\frac{1}{2}\Delta x} - n \Big|_{x+\frac{1}{2}\Delta x} \right) \sim -\frac{\Delta x^2}{\Delta t} \frac{\partial n}{\partial x} \sim -D \frac{\partial n}{\partial x}$$

where D is the diffusion coefficient.

Three theoretical forms for particle transport are discussed here. The distinctions among these are mainly historical, as all can be included within the same framework, although the resulting transport effects differ greatly. The three, in order of historical development, are: classical, Pfirsch-Schluter, which introduced toroidal geometric effects, and banana plateau, which included trapped particle effects.

The first of these mechanisms, called classical transport, is dependent on random walk diffusion with the step size being the gyro-radius. This is the limit for cross field transport when the magnetic field is straight and uniform, as in a long circular cylinder with an axial magnetic field. Since the particles are tied closely to the

flux surfaces, the displacement in each collision is of the order of the gyroradius, and therefore the net particle flux is small. The first mention of collisionally driven impurity transport was given by Longmire and Rosenbluth in 1956 [2]. They found that classical transport theory predicted that impurities would be driven up main ion density gradients. The equilibrium impurity profile was predicted to be more sharply peaked than the main ion profile by a factor of the impurity charge state, $(n_z(r)/n_z(0)) \sim (n_i(r)/n_i(0))^z$. The gyroradius of any species is proportional to the species momentum perpendicular to the magnetic field divided by the species charge state. Since momentum is conserved in collisions, the diffusive step for each species in a collision is proportional to its inverse charge state. Hence, when the impurity gradient is its charge state times steeper than the main ion gradient, a diffusive balance exists since the diffusive step size times its gradient is equal for both species. A review by Braginskii [3] in 1965 summarizes classical transport. Since the effect of classical transport is usually small compared to the other transport mechanisms present in a tokamak, classical transport will not be treated further.

Classical transport does not take into account the magnetic field gradients and curvature, which give rise to particle drifts and thereby to transport across magnetic

surfaces. Pfirsch-Schlueter [4] transport is driven by collisions between particles on the same flux surface, and depends on poloidal particle and heat flows within the flux surface. In general, Pfirsch-Schlueter transport leads to an enhancement over classical transport by a factor $(1+2q^2)$, where q is the safety factor, or inverse rotational transform, and varies in value from ~ 1 in the center of the plasma to $\sim 3-6$ at the outer boundary.

Pfirsch-Schlueter theory was applied to impurity transport by Rutherford [5]. With the inclusion of first order corrections to the particle and heat friction coefficients, the possibility arose that the normally negative temperature gradients could inhibit or reverse the inward impurity flow. The case studied by Rutherford was for an impurity mass much larger than the main ion mass, for which this temperature screening effect is not predicted. Boley, Gelbard, and Stacey [6] extended this treatment for an arbitrary number of species.

The most recently developed theory in this line is banana-plateau, or "neoclassical", transport theory, which takes into account the magnetic trapping of particles. The diffusion displacement step for trapped particles is on the order of the banana orbit width, which is much larger than the gyroradius, so this mechanism can greatly enhance particle transport. Connor [7] and Hinton and Moore [8] applied this neoclassical transport formulation to impurity

transport theory and predicted, as before, that the main ion density gradient would drive impurities inward, but at the larger, collisionless rate. The collisionless diffusion rate is enhanced over the Pfirsch-Schluter rate by a factor of $(R/r)^{3/2}$, where R is the major radius and r is the minor radius.

To predict the impurity transport in the Pfirsch-Schluter regime, Rutherford had extended the fluid, or moment equation approach of Braginskii [3] to obtain his results for two species of disparate mass, since the geometry effects do not change the classical collisional friction or viscosity effects. Trapped particles, on the other hand, do substantially change the plasma viscosity. Therefore, until recently, the collisionless, or long mean free path regime, could not be treated as a fluid. The method of solution for long mean free path transport was then restricted to the solution of Fokker-Planck equations in velocity space with the choice of a tractable approximation of the collision operator. This limitation was overcome when Hirshman [9,10] derived an averaged parallel viscosity coefficient for a collisionless plasma, which placed the long mean free path effects calculated kinetically into the fluid framework.

A concept inherent in the calculation of the impurity transport fluxes is ambipolarity. This was introduced by Hazeltine and Ware [11], who proved that the radial particle

transport could not set up gross charge imbalance. This requirement dictates that a radial flux of one species must be offset by opposing radial fluxes of other species, so that the net charge flux is zero. Hirshman [9,10] later proved that one species being collisional would hold the magnitude of the differential transport of the two species to the magnitude of the transport with both species collisional, regardless of the collisionality of the other species. Samain [12] had earlier found this to be true when large concentrations of impurities were present.

Up to this point, the only effect considered in calculating ion-impurity transport was internal, collisional momentum exchange among the main plasma ions and impurity ions. Ohkawa [13] suggested that a source of external momentum, such as a neutral beam, could reverse the inward flow of impurities driven by gradients. El Derini and Emmert [14] produced a theory based on adding terms to account for the direct momentum effects of a beam. Stacey and Sigmar [15,16] included the effects of the momentum source and an external drag on the flows within the plasma and on the radial electric field, as well as the direct effects, to develop a consistent theory for transport in the presence of external momentum exchange. The drag could be from an external source, such as momentum loss by loss of charge exchanged ions, or by a viscous momentum loss to adjacent flux surfaces. The inclusion of these momentum

effects into the transport calculation subsequently led to an expression for radial impurity transport driven by a momentum source.

Ohkawa [17] also suggested that radial transport could be altered by the introduction of a poloidally asymmetric particle source. This theory was then developed by Burrell [18] and Wong [19] for collisional, two-species and multiple-species plasmas, respectively. Chu and Rawls [20] obtained similar results through a kinetic approach in the Pfirsch-Schlueter and plateau regimes. With a fluid model in the Pfirsch-Schlueter regime, Stacey [21] generalized the theory to include both momentum and particle sources simultaneously.

Further extensions to the fluid treatment of impurity transport theory including external sources were performed. Stacey and Sigmar [15,16] extended the multiple regime formalism to include both axisymmetric particle sources and momentum sources. They predicted that co-injection of the neutral beam power available in PLT would reverse the normally inward flow of impurities. Co-injection is defined as toroidal neutral beam injection in the direction of the magnetic field, and counter-injection is defined as toroidal neutral beam injection in the opposite direction. Stacey [22] further extended the theory to include heat sources and heat fluxes in any collisionality regime. Burrell [23] also did this calculation for a collisional plasma, and Parks,

Burrell, and Wong [24] included a momentum source for a collisional or collisionless plasma with the drag on the impurity species set to zero.

Burrell et al [25,26] included inertial effects on impurity transport, which is important when injected beams drive a toroidal plasma rotation. The rotation tends to induce poloidal variations of the concentrations of heavier impurities, and is important when the rotation velocity is near to or greater than the impurity thermal velocity. Stacey and Sigmar [27] recently included the effect of inertia, poloidal density variations, and momentum sources to formulate a self-consistent theory for the impurity fluxes.

Experiments to investigate neutral beam driven impurity flow reversal theory were performed in PLT [28,29], T-11 [30], and ISX-B [31]. All of these experiments indicated a greatly enhanced impurity accumulation at the plasma center with a counter-injected beam, and a reduced or slightly reversed impurity influx with a co-injected beam, qualitatively agreeing with the flow reversal theory. Part of this thesis is analysis of a well documented set of PLT experimental results.

The original Stacey and Sigmar theory [15,16] for impurity transport was based on the first two moment equations in the fluid formalism, and hence omitted temperature gradient effects. In Chapter 2 of this thesis,

the Stacey and Sigmar [15,16] theory is extended to include temperature gradients and heat sources in the calculation of particle transport across flux surfaces, and to calculate heat transport across flux surfaces. This calculation requires the use of four moment equations solved simultaneously, and includes all of the above referenced effects, except inertia, for any collisionality regime. The resulting theory is then reduced to a computationally tractable form.

In Chapter 3, the extended theory is applied to interpret one set of experimental data from PLT [29]. It is found that the theory agrees roughly with experiment to within a factor of two, which provides a basis for adjusting the theory to obtain a predictive model by scaling the predicted fluxes up by a factor of two.

The adjusted model is then used in Chapter 4 to predict the effect of neutral beam injection on impurity transport in larger experimental and reactor plasmas. In particular, beam injection is studied in three machines: the Tokamak Fusion Test Reactor (TFTR), currently in the initial stages of operation; a conceptual design of a larger engineering demonstration device (FED); and an even larger conceptual reactor (STARFIRE), thought to be typical of commercial tokamaks of the future. The goal in TFTR is to predict the magnitude of the effect of neutral beam driven flow reversal with the existing neutral beam system and to

estimate if flow reversal might be used for impurity control. For FED and STARFIRE, the objective is to estimate if neutral beam driven flow reversal might be a feasible means of impurity control in tokamak fusion reactors.

CHAPTER II

DERIVATION OF THE TRANSPORT EQUATIONS

2.1 Introduction

In this chapter, the radial transport properties of an impurity species and the heat conduction of ions in a tokamak are calculated. Since the transport is driven by momentum exchange, the momentum of each interacting species must first be determined. This is accomplished here by solving the moment equations for the particle and heat flows for each species. With these flows and a constitutive relation from kinetic theory, the momentum exchange rate and hence the particle and heat fluxes across flux surfaces can be calculated.

In Section 2.2, the equations obtained by taking the velocity moments of the Boltzmann equation are solved for the flows on a flux surface to within an arbitrary constant of integration. These constants are then determined from the flux surface average of the parallel momentum and heat flux equations, which in effect determine the average flows parallel to the magnetic field. Constitutive relations for the internal viscous and frictional properties are required in order to make an explicit determination. These relations are used in Section 2.3 to calculate the average flows

parallel to the field.

The toroidal momentum balance is employed in Section 2.4 to find the transport between two species. The constraint of ambipolarity is shown to be equivalent to toroidal momentum conservation. This ambipolarity condition provides the means of calculating the radial electric field, completing the general solution.

The general equations for the impurity fluxes are difficult to use and understand. If the collision rates are large enough for the plasma to be considered to be collisional, no long mean free path effects are seen, and the equations can be significantly simplified. Conversely, collisional effects are not significant in collisionless, or long mean free path, regimes. There is also a transition regime in which a heavy impurity may be collisional and the hydrogenic ions collisionless. In order to show important aspects of the transport equations, approximations are made to reduce the geometry to a large aspect ratio, low plasma pressure plasma limit in Section 2.5. The simplified transport equations are then given and discussed for three collisionality conditions: both species collisional in Section 2.6, one collisional and one collisionless in Section 2.7, referred to here as the mixed regime, and both species collisionless in Section 2.8.

2.2 Surface Flow Evaluation

The starting point in determining the particle and heat flows is the set of equations that are obtained by taking the velocity moments of the Boltzman equation. The derivation of these moment equations from kinetic theory is reviewed by Braginskii [3] and by Hinton and Hazeltine [32]. The first four moment equations, manipulated into forms which lend themselves to physical interpretation, are used in this study. Since each moment equation includes a higher moment, an assumption about the fifth velocity moment must be made to close the system.

The even moments for a species i ,

$$\frac{\partial n_i}{\partial t} + \nabla \cdot n_i \vec{V}_i = S_i^0 \quad 2.2.1)$$

and

$$\frac{3}{2} \frac{\partial p_i}{\partial t} + \vec{\Pi} \cdot \nabla \cdot \vec{V}_i + \frac{3}{2} \nabla \cdot (p_i \vec{V}_i) + p_i \nabla \cdot \vec{V}_i + \nabla \cdot q_i = \quad 2.2.2)$$

$$R_i^z + S_i^z - \vec{V}_i \cdot (\vec{R}_i^z + \vec{S}_i^z) + \frac{1}{2} m_i (\vec{V}_i \cdot \vec{V}_i) S_i^0$$

express the conservation of particles and energy respectively, while the odd moments,

$$m_i n_i \frac{\partial \vec{V}_i}{\partial t} + m_i n_i (\vec{V}_i \cdot \nabla) \vec{V}_i + \nabla p_i + \nabla \cdot \vec{\Pi} =$$

2.2.3)

$$n_i e_i (\vec{E} + \vec{V}_i \times \vec{B}) + \vec{R}_i + \vec{S}_i - m_i \vec{V}_i S_i^o$$

and

$$\frac{\partial}{\partial t} \left(\vec{Q}_i - \frac{\epsilon_i}{2} p_i T_i \vec{V}_i \right) + \frac{\epsilon_i}{2} n_i \vec{V}_i \frac{\partial T_i}{\partial t} + \nabla \cdot \vec{Q}_i - \frac{\epsilon_i}{2} \frac{T_i}{m_i} \nabla \cdot \vec{M}_i$$

$$- \frac{\epsilon_i}{m_i} \left(\vec{Q}_i - \frac{\epsilon_i}{2} p_i \vec{V}_i \right) \times \vec{B} - \frac{\epsilon_i}{m_i} \vec{E} \cdot \left(\vec{M}_i - \frac{1}{3} T_i [\vec{M}_i] \vec{I} \right) =$$

, 2.2.4)

$$\left(\vec{R}_i^3 - \frac{\epsilon_i}{2} \frac{T_i}{m_i} \vec{R}_i^1 \right) + \left(\vec{S}_i^3 - \frac{\epsilon_i}{2} \frac{T_i}{m_i} \vec{S}_i^1 \right)$$

describe the momentum and energy flux balances. The scalar terms involved are, for species i : m_i , e_i , n_i , T_i , and p_i ; the mass, charge, number density, temperature, and pressure, respectively. The vectors \vec{E} and \vec{B} are the electric and magnetic fields, and the vectors \vec{V}_i , \vec{Q}_i , and \vec{Q}_i represent the net average velocity, heat flux, and heat flow. The heat flow is the summation of the heat flux, which is heat conduction without net particle movement, and heat convection. Tensors describing the anisotropic shear

stress, energy flux, total pressure, and momentum stress are $\vec{\pi}$, \vec{Q}_i , \vec{P}_i , and \vec{M}_i . These quantities are the same as the quantities defined in the review by Hinton and Hazeltine [32], and the defining relations for these are given in Appendix D. Finally, \vec{R}_i^n and \vec{S}_i^n are the collisional friction and source moment of order n for species i . These equations, without the external source terms, have been studied extensively (see Reference 31 for a review). The study of these equations with external sources has begun only recently, as discussed in Chapter 1. Of particular relevance to this work is the development by Stacey and Sigmar [15,16], which was based on only the first two moment equations. One purpose of this thesis is to extend that work to four moment equations to develop a multispecies neoclassical transport theory including the effects of external sources and drag. The results given here are applicable in all collisionality regimes.

From plasma equilibrium considerations, the usual generalized axisymmetric co-ordinate system is defined [33], see Figure 2.2.1. By assuming that the distributions are Maxwellian plus a small correction, it is found that the plasma currents lie on surfaces of magnetic flux, often called flux surfaces, and that the plasma pressure is constant on these surfaces. The normal to these surfaces is the first co-ordinate direction, $\hat{\psi}$. In the cylindrical limit, $\hat{\psi}$ is equivalent to the radial direction. $\hat{\chi}$ is

the poloidal, subscript p direction, and $\hat{\phi}$ is the toroidal, subscript ϕ direction. The latter two co-ordinates lie on the flux surface.

By using the standard toroidal device notation of distance from the major axis, distance from the minor axis, and poloidal and toroidal magnetic fields (R , r , B_p , and B_ϕ , respectively), the following inter-relationships occur:

$$|\nabla\psi| = R B_p \quad , \quad 2.2.5a)$$

$$|\nabla\phi| = 1/R \quad , \quad 2.2.5b)$$

$$F \equiv R B_\phi = f(\psi) \quad , \quad 2.2.5c)$$

and

$$\vec{B} = B_\phi \hat{\phi} + B_p \hat{\chi} \quad . \quad 2.2.5d)$$

The gradients are in the form $\nabla\psi = dp/d\psi \nabla\psi = p'(\psi) \nabla\psi$, $p=p(\psi)$, where the prime denotes the derivative with respect to the flux surface normal, ψ . With this co-ordinate system, a unit vector along the magnetic field is defined

$$\hat{n} \equiv \vec{B}/|B| = (F \nabla\phi + \nabla\phi \times \nabla\psi)/|B| \quad . \quad 2.2.6)$$

Taking the vector product of this unit vector with the even moment equations, the perpendicular particle flows

$$\begin{aligned}
 n_i \vec{V}_{i\perp} = \frac{1}{e_i B} \hat{n} \times \left[m_i n_i \frac{\partial \vec{V}_i}{\partial t} + m_i n_i (\vec{V}_i \cdot \nabla) \vec{V}_i + \nabla p_i \right. \\
 \left. + \nabla \cdot \vec{\Pi}_i - n_i e_i \vec{E} - \vec{R}_i' - \left(\vec{S}_i' - m_i \vec{V}_i S_i^0 \right) \right]
 \end{aligned} \tag{2.2.7}$$

and heat flows

$$\begin{aligned}
 \left(\vec{Q}_i - \frac{5}{2} p_i \vec{V}_i \right) = \Omega_i^{-1} \hat{n} \times \left[\frac{\partial}{\partial t} \left(\vec{Q}_i - \frac{5}{2} p_i \vec{V}_i \right) + \frac{5}{2} n_i \vec{V}_i \frac{\partial T_i}{\partial t} \right. \\
 \left. + \nabla \cdot \vec{\Theta}_i - \frac{5}{2} \frac{T_i}{m_i} \nabla \cdot \vec{M}_i - \frac{e_i}{m_i} \vec{E} \cdot \left(M_i - \frac{1}{3} T_i (M_i) \vec{I} \right) \right. \\
 \left. - \left(\vec{R}_i' - \frac{5}{2} \frac{T_i}{m_i} \vec{R}_i' \right) - \left(\vec{S}_i' - \frac{5}{2} \frac{T_i}{m_i} \vec{S}_i' \right) \right]
 \end{aligned} \tag{2.2.8}$$

are found immediately.

In order to determine the important terms in these and following equations, an ordering system must be constructed. The usual scheme, as reviewed by Hinton and Hazeltine [32], is followed here. The definitions of scale length, $L \approx |d \ln p / dr| \approx |d \ln n / dr| \approx |d \ln T / dr|$, gyro-frequency $\Omega = eB/m$, and thermal velocity, $v_{th} = \sqrt{2T/m}$, lead to the ordering parameter

$$\delta_1 \equiv V_{th}/\Omega L = r_L/L \ll 1 \quad . \quad 2.2.9)$$

This ratio is equivalent to the ratio of the radius of the cyclotron orbit to the distance over which macroscopic parameters change. When this ratio is much less than unity, which is the case for strong magnetic fields, the change in pressure, temperature, et cetera is small over a cyclotron orbit and those properties are considered constant over the orbit.

From equilibrium, using the Maxwellian plus a small correction of order δ_1 , it is found that, in addition to the pressure, the density, temperature, and electrostatic potential are dependent on the order unity, or uncorrected, Maxwellian. These quantities are also constant on the flux surface. It is also found that the flow velocity and heat flux lie on the surface to lowest order and are dependent on the order δ_1 correction to the Maxwellian. For convenience, terms which are dependent solely on the uncorrected Maxwellian will be subsequently said to be of order unity or zeroeth order, δ^0 , quantities dependent of the first correction term to be first order, δ^1 , et cetera. The following relationships are found to hold from their respective definitions:

$$\vec{E} = -\nabla\Phi (1 + O(\delta, \delta_2)) \quad , \quad 2.2.10a)$$

where Φ is the electrostatic potential,

$$\vec{M}_i = n_i m_i \vec{V} \vec{V} + \vec{P}_i = n_i m_i \vec{V} \vec{V} + p_i \vec{I} + \vec{\pi}_i \quad , \quad 2.2.10b)$$

$$[\vec{M}_i - p_i \vec{I}] = O(\delta_i) \quad , \quad 2.2.10c)$$

$$\vec{V}_i = O(\delta_i) \quad , \quad 2.2.10d)$$

$$[\vec{Q}_i - \frac{\Sigma}{2} p_i \vec{V}_i] = O(\delta_i) \quad , \quad 2.2.10e)$$

and

$$\vec{q}_i = [\vec{Q}_i - \frac{\Sigma}{2} p_i \vec{V}_i] (1 + O(\delta_i)) \quad . \quad 2.2.10f)$$

Another parameter useful in ordering the equations is a time ordering parameter, defined by the ratio of the collision frequency to gyrofrequency,

$$\delta_2 \equiv \nu/\Omega \quad \ll 1 \quad , \quad 2.2.11)$$

where ν is the collision frequency. When this ratio is small, the particles will complete many cyclotron orbits between collisions and the orbit itself need not be directly considered. This leads to the friction being first order in δ_2 . Furthermore, the sources are considered to be first order in δ_1 , and the off diagonal tensor terms, which are

driven by order δ_1 effects, to be order δ^2 or smaller [2,32].

Since, in essence, Ω^{-1} is a multiplier of the equations for the perpendicular flows, Equations 2.2.7 and 2.2.8, only zero order terms need be evaluated to determine the flows, $n_i \vec{V}_{i\perp}$ and $\vec{q}_{i\perp}$. Utilizing the above ordering, the lowest order perpendicular to the magnetic field and on the flux surface are found,

$$n_i \vec{V}_{i\perp} = \frac{1}{e_i B} \hat{n} \times (\nabla p_i + n_i e_i \nabla \Phi) \quad (2.2.12)$$

$$= \frac{R B_p}{e_i B} \left(p_i' + n_i e_i \Phi' \right) \frac{\hat{n} \times \nabla \psi}{|\nabla \psi|} \equiv \frac{B_p}{B B_p} G(\psi) \hat{n}_\perp$$

and

$$\vec{q}_{i\perp} = \Omega^{-1} \hat{n} \times \left(\frac{\nabla \cdot \mathbf{P}_i T_i}{m_i} - \frac{\nabla T_i}{m_i} \cdot \nabla p_i \right) \quad (2.2.13)$$

$$= \frac{\nabla \cdot \mathbf{P}_i T_i}{e_i B} p_i T_i \hat{n}_\perp \equiv \frac{B_p}{B B_p} D(\psi) \hat{n}_\perp$$

Both of these flows lie in the flux surface, being functions of the radial variable ψ alone.

With the lowest order flows perpendicular to the magnetic field known, the odd moment equations are then

intergrated to evaluate the flows parallel to the field.

Before proceeding, the flux surface average is defined,

$$\langle A \rangle \equiv \frac{\oint dl_p / B_p A}{\oint dl_p / B_p} \quad , \quad 2.2.14a)$$

where dl_p indicates the differential length in the poloidal direction on the flux surface. It is useful to note that, for any differentiable quantity, A , that, because of axisymmetry,

$$\langle \vec{B} \cdot \nabla A \rangle = 0 \quad . \quad 2.2.14b)$$

The other device needed to continue with the odd moment equations is the scaling of the time derivatives to fit with the ordering scheme. Still following Stacey and Sigmar [15], changes taking place in the period of a cyclotron orbit $\partial / \partial t \sim \Omega$ can only be caused by changes in the electrostatic field and pressure, and are considered instantaneous for the purposes of transport. Changes that occur slowly such as magnetic field diffusion and plasma

collision rates that change with first order density, temperature, et cetera, are too slow to be considered and are treated as constants. The two time scales of interest are the time response of the electrostatic potential and flows due to a source input $\delta / \delta t_1$, and the slower buildup of particles and heat from the sources, $\delta / \delta t$, where the subscripts refer to the order of the changes made in that time scale.

The lowest order results from this time scale ordering are

$$\frac{\partial n_i}{\partial t_0} = 0 \quad 2.2.15)$$

for the first (V^0) moment and

$$\frac{3}{2} \frac{\partial P_i}{\partial t_0} = 0 \quad 2.2.16)$$

for the third (V^3) moment. By taking the flux surface average of these moments it is found that

$$\frac{\partial n_i}{\partial t_1} = \langle S_i^0 \rangle + O(\delta^2) \quad 2.2.17)$$

and

$$\frac{3}{2} \frac{\partial P_i}{\partial t_i} = \langle S_i^2 \rangle + O(\delta^2) \quad . \quad 2.2.18)$$

Note that the friction, R_i^2 , the energy transferred between species, is small since the ion-ion equilibration time is short.

By substituting the time derivatives in Equations 2.2.17 and 2.2.18 into the lowest order terms of the first and third moments, and by separating the flow divergence into perpendicular and parallel components, the following equations are obtained:

$$\nabla \cdot n_i \vec{V}_{i\parallel} + \nabla \cdot n_i \vec{V}_{i\perp} = S_i^0 - \langle S_i^0 \rangle \quad 2.2.19)$$

and

$$\nabla \cdot \vec{q}_{i\parallel} + \nabla \cdot \vec{q}_{i\perp} = S_i^2 - \langle S_i^2 \rangle \quad . \quad 2.2.20)$$

The divergences of the flux surface flows are therefore changed only by poloidally asymmetric sources. These last two equations are solvable, using the equations for the perpendicular flows, Equations 2.2.12 and 2.2.13, to obtain the flows parallel to the field,

$$n_i \vec{V}_{i\parallel} = \left[-\frac{G_i}{B} \left(1 - \frac{B^2}{\langle B^2 \rangle} \right) + B \left(I_i^0 - \langle B^2 I_i^0 \rangle / \langle B^2 \rangle \right) + \langle B n_i V_{i\parallel} \rangle B / \langle B^2 \rangle \right] \hat{n} \quad 2.2.21)$$

and

$$\vec{q}_{i\parallel} = \left[-\frac{D_i}{B} \left(1 - \frac{B^2}{\langle B^2 \rangle} \right) + B \left(I_i^2 - \langle B^2 I_i^2 \rangle / \langle B^2 \rangle \right) - \frac{\Sigma T_i}{2 m_i} B \left(I_i^0 - \langle B^2 I_i^0 \rangle / \langle B^2 \rangle \right) + B \langle B q_{i\parallel} \rangle / \langle B^2 \rangle \right] \hat{n} \quad 2.2.22)$$

The terms $\langle B n_i V_{i\parallel} \rangle$ and $\langle B q_{i\parallel} \rangle$ are constants of integration which will be determined subsequently. The terms I_i^{q2} arise from the asymmetric sources and are defined as

$$I_i^{o,2} \equiv \int_0^{l_p} \left(S_i^{o,2} - \langle S_i^{o,2} \rangle \right) / B_p \, dl_p \quad , \quad 2.2.23)$$

which vanish if the particle or heat source is uniform over the flux surface. It can be seen from Equation 2.2.22 that the heat flow is affected both by direct energy input to the species (I^2), such as radio frequency heating, and by heat input due to introduction of energetic particles (I^0).

This formulation leaves only the flux surface

averaged parallel flows, the constants $\langle B n_z V_{z\parallel} \rangle$ and $\langle B q_{z\parallel} \rangle$ undetermined in calculating the first order flows.

The parallel and perpendicular flows are combined to obtain

$$n_i \vec{V}_i = \left(\frac{\vec{B}_p \cdot n_i \vec{V}_i}{B_p^2} \right) \vec{B} - \frac{R}{e_i} \left(\rho_i' + n_i e_i \Phi' \right) R \nabla \phi \quad 2.2.24)$$

and

$$\vec{q}_i = \left(\frac{\vec{B}_p \cdot \vec{q}_i}{B_p^2} \right) \vec{B} - \frac{R}{e_i} \frac{1}{2} \rho_i T_i' R \nabla \phi \quad 2.2.25)$$

The last term in each equation represents the rigid body rotation in the toroidal direction. The poloidal flows which enter Equations 2.2.24 and 2.2.25 are expressed as

$$\Gamma_{i\phi} \equiv \left(\frac{\vec{B}_p \cdot n_i \vec{V}_i}{B_p^2} \right) = \frac{1}{e_i} \left[\frac{F}{\langle B^2 \rangle} \left(\rho_i' + n_i e_i \Phi' \right) + \langle B n_z V_{z\parallel} \rangle / \langle B^2 \rangle \right. \\ \left. + \left(I_z^0 - \langle B^2 I_z^0 \rangle / \langle B^2 \rangle \right) \right] \quad 2.2.26)$$

and

$$q_{i,p} \equiv \left(\frac{\vec{E}_p \cdot \vec{q}_i}{B_p^2} \right) = \frac{1}{e_i} \left[\frac{F}{\langle B^2 \rangle} \frac{\sigma}{2} p_i T_i' + \langle B q_{i,th} \rangle / \langle B^2 \rangle \right. \\ \left. + (I_i^2 - \langle B^2 I_i^2 \rangle / \langle B^2 \rangle) - \frac{\sigma}{2} T_i (I_i^0 - \langle B^2 I_i^0 \rangle / \langle B^2 \rangle) \right] \quad , \quad 2.2.27)$$

where $F = RB = f(\psi)$. Both of these flows lie strictly on the flux surface.

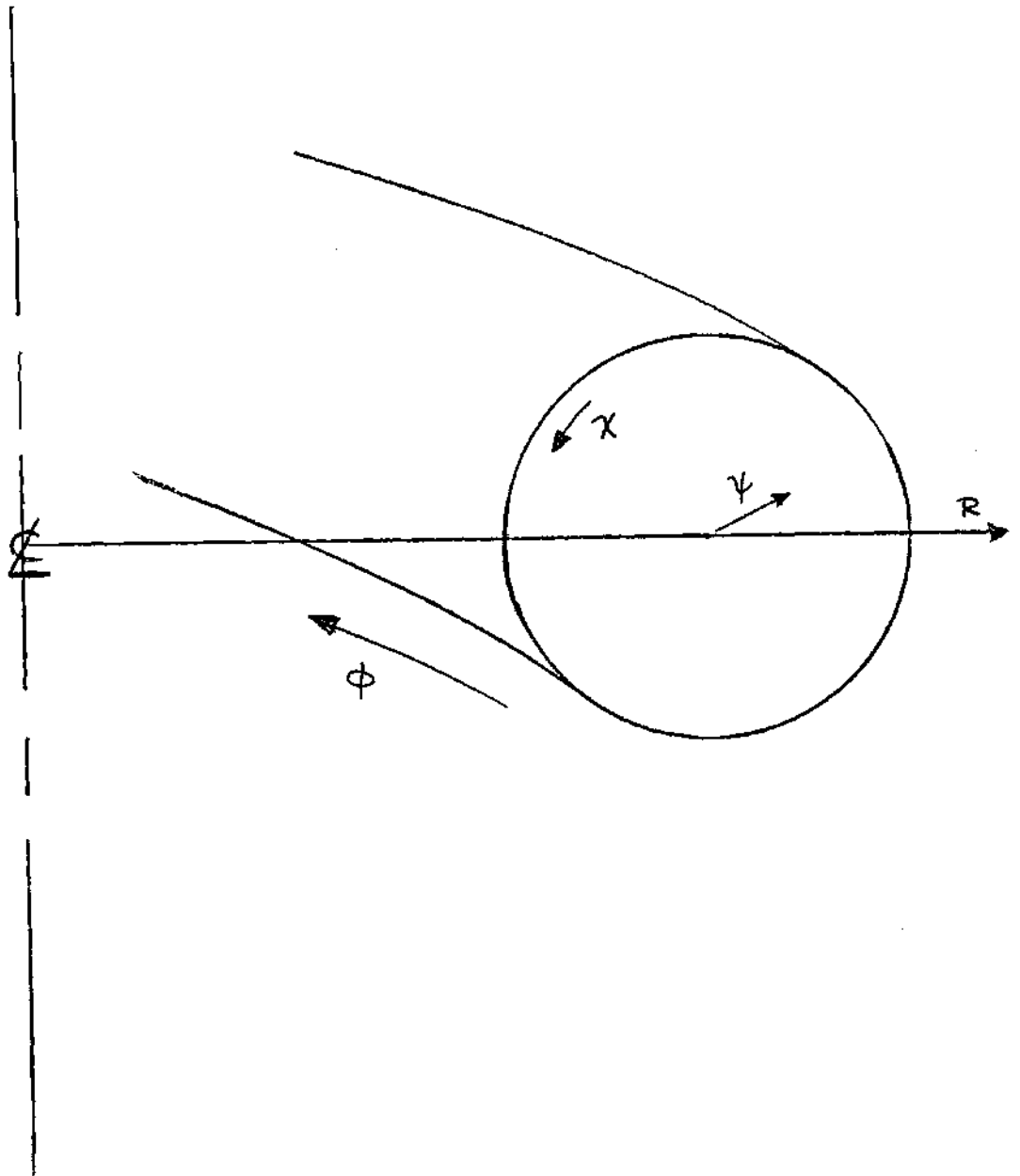


Figure 2.2.1 Generalised Axisymmetric Co-ordinate System

2.3 Parallel Flow Evaluation

In order to close the system of equations and explicitly determine the constants, it is necessary to introduce constitutive relations between the parallel viscous forces and the flows. Following Hirshman, it is assumed that if the lowest order particle and heat fluxes lie on the flux surface, then the viscous forces must also lie there and be linearly dependent on the flows. These flows were broken in the last section into a parallel component plus a rigid body rotation, the latter showing no viscous effect. Using this form, the viscous shear may be written [10]

$$\langle \vec{B} \cdot \nabla \cdot \vec{\Pi} \rangle = 3\mu_{zi} \langle (\hat{A} \cdot \nabla B)^2 \rangle \Gamma_{ip} \quad (2.3.1)$$

$$+ 3\mu_{zi} \langle (\hat{n} \cdot \nabla B)^2 \rangle q_{ip}$$

and

$$\langle \vec{B} \cdot \nabla \cdot \left(\vec{\Theta}_z - \frac{T_i}{m_i} \vec{P}_z \right) \rangle = \quad (2.3.2)$$

$$3 \langle (\hat{n} \cdot \nabla B)^2 \rangle \frac{T_i}{m_i} (\mu_{zi} \Gamma_{ip} + \mu_{zi} q_{ip})$$

where the $\mu_{\parallel n}$ are the parallel viscosity coefficients. The first term on the right hand side of Equation 2.3.1 was derived by Braginskii [3] for the collisional limit using the explicit collisional form of the pressure shear, $\overline{\tau}_{\parallel}$. The flux surface average of the parallel components of the even moment equations leads to

$$\langle \vec{B} \cdot \nabla \cdot \overline{\tau}_{\parallel} \rangle = \langle \vec{B} \cdot \vec{R}_{\parallel} \rangle + \langle \vec{B} \cdot \vec{S}_{\parallel} \rangle \quad 2.3.3)$$

and

$$\begin{aligned} \langle \vec{B} \cdot \nabla \cdot (\vec{\Theta}_{\parallel} - \frac{5}{2} \frac{T_{\parallel}}{m_i} \vec{P}_{\parallel}) \rangle &= \frac{T_{\parallel}}{m_i} \langle \vec{B} \cdot \vec{R}_{\parallel}^{\prime} \rangle + \langle \vec{B} \cdot \vec{S}_{\parallel}^{\prime} \rangle \\ &\quad - \frac{5}{2} \frac{T_{\parallel}}{m_i} \langle \vec{B} \cdot \vec{S}_{\parallel}^{\prime} \rangle \end{aligned} \quad 2.3.4)$$

This formulation extends Hirshman's multi-regime approach [10] to include asymmetric sources in the parallel viscosity terms as well as the heat input. Burrell [24] included the asymmetric sources and heat input, but his results were confined to the collisional regime, which, in effect, sets the right hand side of Equations 2.3.1 and 2.3.2 for the shear to zero.

The general constitutive relations for the friction forces in terms of the flows are given by Hirshman [34] as

$$\vec{R}_{ij} = -C_1^* m_i n_i v_{ij} (\vec{V}_i - \vec{V}_j^*) - 2/5 C_2^* m_i n_i v_{ij} \left(\frac{q_i}{p_i} - \left(\frac{q_i}{p_i} \right)^* \right)$$

2.3.5)

$$+ m_i n_i v_{ij} (\vec{V}_i - \vec{V}_j^*)$$

and

$$\vec{R}_{ij}^3 = (\vec{R}_{ij}^3 - 5/2 \frac{I_i}{m_i} \vec{R}_i^1) = C_2^* m_i n_i v_{ij} (\vec{V}_i - \vec{V}_j^*)$$

$$- 2/5 C_3 m_i n_i v_{ij} \left(\frac{q_i}{p_i} - \left(\frac{q_i}{p_i} \right)^* \right) , \quad 2.3.6)$$

where

$$V_i^* \equiv \frac{\sum_{j \neq i} v_{ij} \vec{V}_j}{\sum_{j \neq i} v_{ij}} , \quad 2.3.7)$$

and

$$\frac{g_i}{P_i}^* = \frac{\sum_{j \neq i} v_{ij} \left(\frac{g_i}{P_i} \right)}{\sum_{j \neq i} v_{ij}} \quad . \quad 2.3.8)$$

The terms C_n^* are the constants

$$C_1^* = 1 - \frac{.52 \alpha}{.59 + \alpha + 1.34 \sigma^2} \quad , \quad 2.3.9a)$$

$$C_2^* = 1.5 - \frac{.29 + 1.2 \alpha}{.59 + \alpha + 1.34 \sigma^2} \quad , \quad 2.3.9b)$$

and

$$C_3^* = 1.41 + 3.25 \alpha - \frac{(.41 + 1.66 \alpha)^2}{.59 + \alpha + 1.34 \sigma^2} \quad , \quad 2.3.9c)$$

where

$$\sigma = v_{th}/v_{ii} R_q = \epsilon^{-3/2} / v_{ii} \quad 2.3.9d)$$

is a collisionality parameter and

$$\alpha = n_e Z^2 / n_i \quad 2.3.9e)$$

is the effective charge for scattering. These last constants are classical corrections to the collision frequency which account for the faster particles seeing a smaller effective cross section, as was described by Braginskii [3] in terms of electrical conductivity. Hirshman [34] used the large mass ratio approximation, so that the lighter species do not affect the heavier species.

For the present purpose, all species are kept.

The source moments are also defined in terms of the velocity. The first four moments are:

$$S_i^0 = S_i \quad , \quad 2.3.10a)$$

$$\vec{S}_i^1 = \vec{K}_i^1 - m_i n_i v_{di} \vec{V}_i \quad , \quad 2.3.10b)$$

$$S_i^2 = K_i^2 - \frac{1}{2} m_i n_i v_{di} V_i^2 \quad , \quad 2.3.10c)$$

and

$$\vec{S}_i^3 = \vec{K}_i^3 - v_{di} \vec{Q}_i \quad , \quad 2.3.10d)$$

where the $K_i^{1(3)}$ are directed inputs of the momentum (heat) and S_i and K_i^2 are the sources of particles and heat, respectively. Note that larger velocity moments of each source in Equation 2.3.10 are included separately in the moment equations and not in the higher source term. The second portion of each term in Equation 2.3.10 is a net drag on the plasma from external sources, as used by Stacey and Sigmar [15,16]. The latter two drag terms are drag on the heat flow due to particle collisions, and drag on heat conductance. These two external drags can at least in part be a radial transfer of momentum or heat flux to an adjacent, "external", flux surface. The drags are more appropriately diffusive mechanisms, but they are modelled here as equivalent drags. A more detailed explanation of

this analogy is given in Section 2.9.

With these relations, the parallel momentum and heat flux balance equations are solvable for the constants $\langle Bq_{z\parallel} \rangle$ and $\langle Bn_z V_{z\parallel} \rangle$ in terms of gradients, sources, and the electrostatic potential. A complete algebraic solution for two species is found in Appendix A, producing solutions of the form

$$\langle \frac{Bq_{z\parallel}}{\rho_z} \rangle = \frac{1}{a_z} \left[\frac{Q_z}{m_e n_e v_{te}} + C_z (\langle BV_{z\parallel} \rangle - \langle BV_{z\parallel} \rangle) - \frac{n_e \hat{n}_z}{m_e n_e v_{te}} \frac{N_z}{\rho_z} \langle BV_{z\parallel} \rangle \right] \quad 2.3.11)$$

and

$$\langle BV_{z\parallel} \rangle = [(\xi_z + \lambda) N_z + \lambda N_z] / m_e n_e v_{te} \quad 2.3.12)$$

This solution procedure involves equating the two forms for the viscous shear equations, equating Equations 2.3.1 to 2.3.3 and equating Equation 2.3.2 to 2.3.4. By substituting a two species limit for the friction, ect., the parallel flows can be found directly by algebraic manipulation.

In the above terms, λ is a combination of friction coefficients. Both $\xi_{z,z}$ and $a_{z,z}$ are combinations of the

primary flow coefficients, including both internal parallel viscosity and external drag. The $Q_{i,z}$ and $N_{i,z}$ are the sum of the driving terms for that species. These terms are given in Appendix A.

In Appendix B, the electrostatic potential is found for a two species plasma (i and z),

$$\begin{aligned}
 & - \left[\left\langle 1 - \frac{B^2}{\langle B^2 \rangle} \right\rangle + \frac{1}{m_i n_i \nu_{iz} (\beta_i + \beta_e) d_{zi}} \left\{ \gamma_z \frac{[N_z]_{\phi}}{F_{\phi}} + \gamma_i \frac{[N_i]_{\phi}}{F_{\phi}} \right\} \right] \Phi' = \\
 & - \frac{\langle R^2 \nabla \phi \cdot (\vec{K}_i + \vec{K}_z) \rangle}{m_i n_i \nu_{iz} (\beta_i + \beta_e)} \frac{\langle B^2 \rangle}{F^2} + \left\langle 1 - \frac{B^2}{\langle B^2 \rangle} \right\rangle \left(\frac{\beta_i}{\beta_i + \beta_e} \frac{P_i'}{n_i e_i} + \frac{\beta_e}{\beta_i + \beta_e} \frac{P_e'}{n_e e_e} \right) \quad , \quad 2.3.13) \\
 & + \frac{1}{\beta_i + \beta_e} \left[\beta_i \frac{\langle \Delta_i^{\circ} \rangle}{n_i} + \beta_e \frac{\langle \Delta_e^{\circ} \rangle}{n_e} \right] + \frac{\gamma_i [N_i]_{\phi'} + \gamma_z [N_z]_{\phi'}}{m_i n_i \nu_{iz} (\beta_i + \beta_e) F d_{zi}}
 \end{aligned}$$

where the $[N_z]_{\phi}$ terms are the N_z terms of Appendix A which include only the electrostatic potential terms, and the $[N_z]_{\phi'}$ terms are those terms that do not include the electrostatic potential terms. The solution procedure followed in Appendix B for the electrostatic potential is again algebraic, and is directly a result of conservation of toroidal momentum and the radial Ampere's Law.

2.4 Transport Fluxes

The work of Stacey and Sigmar [16] is followed in deriving the particle flux across the flux surfaces. The flux surface average of the toroidal component of the momentum balance is taken,

$$\langle R^2 \nabla \phi \cdot n_x n_x \frac{\partial \vec{V}_x}{\partial t} \rangle = \langle R^2 \nabla \phi \cdot n_x e_x \vec{V}_x \times \vec{B} \rangle$$

$$+ \langle R^2 \nabla \phi \cdot (\vec{R}'_x + \vec{S}'_x) \rangle \quad 2.4.1)$$

to lowest order. By using the component form for the magnetic field given in Equation 2.2.5d), the $\vec{V}_x \times \vec{B}$ term becomes the flux normal to the magnetic surface,

$$\Gamma_x \equiv \langle \nabla \psi \cdot n_x \vec{V}_x \rangle = n_x \langle R^2 \nabla \phi \cdot \vec{V}_x \times \vec{B} \rangle \quad 2.4.2)$$

Hence, after equilibrium conditions are established, ($\partial / \partial t \rightarrow 0$), the flux is

$$\Gamma_x = \langle \nabla \psi \cdot n_x \vec{V}_x \rangle = -\frac{1}{e_x} \langle R^2 \nabla \phi \cdot (\vec{R}'_x + \vec{S}'_x) \rangle \quad 2.4.3)$$

As discussed in Appendix B, for steady state, the toroidal component of the sum of all the sources must vanish, $\sum_x \langle R^2 \nabla \phi \cdot \vec{S}'_x \rangle = 0$. This provides a unique determination of the radial electric field. From conservation of momentum, the same must be true of any component of the friction, and so

the asymptotic transport across flux surfaces must be ambipolar, or

$$\sum_{\text{all } i} e_i \Gamma_i = 0 \quad . \quad 2.4.4)$$

The fluxes can now be evaluated explicitly. For convenience, the fluxes are treated in two categories, type A for the fluxes arising from collisional friction, and type B for the fluxes driven by external sources. It is noted that the asymmetric particle and heat sources affect these fluxes only indirectly by modifying the surface flows.

The type A impurity flux driven by the frictional drag, Equation 2.3.5, is, for two species i and z ,

$$\begin{aligned} e_z \Gamma_z^A = - \langle R^t \nabla \phi \cdot \vec{R}_z^t \rangle = & - \frac{n_i n_z v_{iz}}{\langle B^t \rangle} \left\{ C_1 \langle R^t (B_\phi^t - \langle B^t \rangle) \rangle \left(\frac{P_i'}{n_i e_i} - \frac{P_z'}{n_z e_z} \right) \right. \\ & + C_1 F \left[\frac{\langle \Delta_i^0 \rangle}{n_i} - \frac{\langle \Delta_z^0 \rangle}{n_z} \right] + C_1 F \left[\langle B V_{iz} \rangle - \langle B V_{ze} \rangle \right] - C_2 \langle R^t (B_\phi^t - \langle B^t \rangle) \rangle \left(\frac{T_i'}{e_i} - \frac{T_z'}{e_z} \right), \quad 2.4.5) \\ & \left. - C_2 F^{z/s} \left[\frac{\langle \Delta_i^s \rangle}{P_i} - \frac{\langle \Delta_z^s \rangle}{P_z} \right] - C_2 F^{z/s} \left[\frac{\langle B q_{iz} \rangle}{P_i} - \frac{\langle B q_{ze} \rangle}{P_z} \right] \right\} \end{aligned}$$

where the constants $\langle B q_{iz} \rangle$ and $\langle B n_i V_{iz} \rangle$ are given by Equations 2.3.11 and 2.3.12, respectively. In order to fully express the impurity fluxes, it is instructive to present them in physically distinct components. The first

portion is the Pfirsch-Schlueter flux, which is an enhancement of the classical flux due to toroidal geometry effects, and signified by $\langle R^2 (B_\phi^2 - \langle B^2 \rangle) \rangle$ terms. The Pfirsch-Schlueter flux is then

$$\left[\Gamma_z^A \right]_{ps} = - \frac{m_i n_i v_{i\perp}}{e_i \langle B^2 \rangle} \left\{ C_1 \left(\frac{P_i'}{n_i e_i} - \frac{P_i'}{n_i e_i} \right) - C_2 \left(\frac{T_i'}{e_i} - \frac{T_i'}{e_i} \right) \right\} \langle R^2 (B_\phi^2 - \langle B^2 \rangle) \rangle \quad . \quad 2.4.6$$

The averaged flows do not contribute to Pfirsch-Schlueter effects, and hence do not enter at this point.

By substituting into the type A flux the constants $\langle B q_{z\parallel} \rangle$ and $\langle B n_i v_{i\parallel} \rangle$, the flux equation becomes

$$\begin{aligned} \Gamma_z^A = & \left[\Gamma_z^A \right]_{ps} - \frac{m_i n_i v_{i\perp}}{e_i \langle B^2 \rangle} F \left\{ C_1 \left(\frac{\langle \Delta_i^0 \rangle}{n_i} - \frac{\langle \Delta_i^0 \rangle}{n_i} \right) - \frac{1}{2} C_2 \left(\frac{\langle \Delta_i^2 \rangle}{P_i} - \frac{\langle \Delta_i^2 \rangle}{P_i} \right) \right\} \\ & - \frac{F}{e_i \langle B^2 \rangle} \left\{ (C_1 \zeta_i - \Theta_i) N_i / d_{zi} - (C_1 \zeta_i - \Theta_i) N_i / d_{zi} \right. \\ & \left. - C_2 \left(\frac{Q_i}{a_i} - \frac{Q_i}{a_i} \right) \right\} \quad , \quad 2.4.7 \end{aligned}$$

where

$$\begin{aligned} \Theta_i = & C_2^2 \left(\frac{1}{a_i} - \frac{1}{a_i} \right) \zeta_i - C_2 \frac{n_i \tilde{\mu}_i}{n_i m_i v_{i\perp}} \frac{\mu_{zi}}{\mu_{zi}} / a_i (\zeta_i + \lambda) \\ & + C_2 \frac{n_i \tilde{\mu}_i}{n_i m_i v_{i\perp}} \frac{\mu_{zi}}{\mu_{zi}} / a_i \lambda \quad . \quad 2.4.8 \end{aligned}$$

The expression Θ_z is obtained by exchanging subscripts.

Other physically significant distinct components, including the electrostatic potential gradient, or electric field, asymmetric sources, directed inputs, and gradients, separate out of this formulation by using the long form of the terms N_z , Q_z , found in Appendix A. It is seen that the asymmetric sources directly drive the flux, while these and other effects combine to drive it indirectly through modification of the averaged parallel flows. The sign and magnitude of all of these effects is dependent on the collisionality regime, and will be discussed in more detail in the next section.

Similarly, the type B flux, which is driven by external sources, is found by using the form for the source found in Equation 2.3.9. The type B flux for impurity transport is

$$\Gamma_z^B = -\frac{\langle R^2 \nabla \Phi \cdot \vec{S}_z' \rangle}{e_z} = -\frac{\langle R^2 \nabla \Phi \cdot \vec{K}_z' \rangle}{e_z} + \frac{m_i n_i v_{iz}}{e_z \langle B^2 \rangle} \beta_z \times$$

. 2.4.9)

$$\left[\langle R^2 (B_\phi^2 - \langle B^2 \rangle) \rangle \left(\frac{p_z'}{n_z e_z} + \Phi' \right) + F \frac{\langle \Delta \phi^2 \rangle}{n_z} + F \langle B V_{zH} \rangle \right]$$

The form of this equation is the same form found by Stacey and Sigmar [16]. Direct effects are the momentum input, an external drag operating on the Pfirsch-Schluter affected

pressure gradients and electrostatic potential, and an asymmetric input of impurities. The indirect effect is the external drag on the modified impurity flow parallel to the field. Non-impurity effects show up only through this and the electrostatic potential. Substituting the evaluated form of $\langle B n_z v_{z \parallel} \rangle$, the type B flux is obtained.

By inspection, the type A flux is seen to be directly ambipolar, as is necessary to conserve momentum in collisional friction. The type B flux is also seen to be ambipolar, as required by the equilibrium momentum balance equation and radial Ampere's law.

Combining the types A and B fluxes leads to the form

$$\begin{aligned} \Gamma_z &= \Gamma_z^A + \Gamma_z^B = -\frac{\langle R^2 \nabla \Phi \cdot \vec{K}_z^i \rangle}{e_z} - \langle R^2 (\Theta_z^i - \langle B^i \rangle) \rangle \times \\ & - \frac{m_i n_i v_{z \parallel}}{e_z \langle B^i \rangle} \left\{ C_1 \left(\frac{p_i'}{n_i e_z} - \frac{p_e'}{n_e e_z} \right) - C_2 \left(\frac{T_i}{e_z} - \frac{T_e'}{e_z} \right) - \beta_z \left(\frac{p_i'}{n_i e_z} + \Phi' \right) \right\} \\ & - \frac{m_i n_i v_{z \parallel}}{e_z \langle B^i \rangle} \left\{ C_1 \left(\frac{\langle \Delta_i^0 \rangle}{p_i} - \frac{\langle \Delta_i^0 \rangle}{p_e} \right) - \frac{1}{2} \left(\frac{\langle \Delta_i^1 \rangle}{p_i} - \frac{\langle \Delta_i^1 \rangle}{p_e} \right) - \beta_z \frac{\langle \Delta_i^0 \rangle}{p_e} \right\} \quad , \quad 2.4.10) \\ & - \frac{F}{\langle B^i \rangle} \left\{ -C_2 \left(\frac{Q_i}{a_i} - \frac{Q_e}{a_e} \right) + \left[(C_1 \zeta_z - \Theta_z - \beta_z \lambda) N_i \right. \right. \\ & \quad \left. \left. - (C_1 \zeta_z - \Theta_z + \beta_z (\zeta_z + \lambda)) N_e \right] / d_{z \perp i} \right\} \end{aligned}$$

which, with inclusion of the solution for the electrostatic potential found in Appendix B, is the total impurity flux in terms of gradients and sources only.

Comparing Equation 2.4.10 with the results of Stacey and Sigmar [16], this form differs in the first set of

brackets by the addition of the multiplier C_1 for the pressure gradients, and now includes the temperature gradients. For the asymmetric sources, the second set of brackets, the factor C_2 is again added and the difference of the heat sources is now included. The difference in the parallel averaged heat fluxes is added here. The solutions of the parallel averaged particle flows and electrostatic potential here are given in the same form as was used by Stacey and Sigmar, with the same general dependencies on the momentum input, particle source, and pressure gradient, but the C_n factors and higher moment terms are added here. The particulars of the effects are discussed below in the reduction to each collisionality regime.

The results of Burrell [24] are similar to the results above, but are restricted to the collisional regime. Additions to his results are then of course all non-collisional terms, i.e., those including $\tilde{\mu}_x$, $\tilde{\mu}_z$. Also, Burrell's result, given inclusive of his solution for the electrostatic potential and parallel averaged flows, does not include asymmetric heat sources to the impurities or the impurity temperature gradient, both of which are present here.

The pattern set in deriving the cross field particle fluxes is used here to find the heat fluxes. The flux surface average of the toroidal component of the heat flux equation, Equation 2.2.4, is taken, which leads to the

steady state heat flux,

$$q_{\psi i} = \langle \nabla \psi \cdot \vec{q}_i \rangle = \langle R^2 \nabla \phi \cdot \vec{q}_i \times \vec{B} \rangle = \frac{m_i}{e_i} \left(\langle R^2 \nabla \phi \cdot \vec{R}_i^3 \rangle + \langle R^2 \nabla \phi \cdot \left(\vec{S}_i^3 - \frac{1}{2} \frac{T_i}{m_i} \vec{S}_i^1 \right) \rangle \right) \quad (2.4.11)$$

As in the particle transport case, the heat transport is driven by friction and sources. Unlike the particle transport case, there is no conservation law for heat flux, and hence no ambipolarity-like constraint. This will be seen to allow long mean free path scaled heat conduction even when one of the interacting species is collisional.

All of the terms involved in the equation for the cross field heat flux are known, including the electrostatic potential. By substitution, the ion heat conduction flux is found to be

$$\begin{aligned} \frac{q_{\psi i}}{P_i} = & - \frac{m_i n_i v_{Li}}{e_i \langle B^2 \rangle} \langle R^2 (B_\theta^2 - \langle B^2 \rangle) \rangle \left\{ C_2 \left(\frac{P_i'}{n_i e_i} - \frac{P_i}{n_i e_i} \right) - \frac{1}{2} \frac{T_i}{e_i} \left(C_3 + \frac{\sqrt{2} v_{Li}}{v_{Li}} + \frac{1}{2} \beta_i \right) \right\} \\ & - \frac{m_i n_i v_{Li}}{e_i \langle B^2 \rangle} F \left\{ C_2 \left(\frac{\langle \Delta_i \rangle}{n_i} - \frac{\langle \Delta_i^2 \rangle}{n_i} \right) - \left(C_3 + \frac{\sqrt{2} v_{Li}}{v_{Li}} + \frac{1}{2} \beta_i \right) \frac{\langle \Delta_i^2 \rangle}{P_i} \right\} \\ & + \left(C_3 + \frac{\sqrt{2} v_{Li}}{v_{Li}} + \frac{1}{2} \beta_i \right) \frac{F}{e_i \langle B^2 \rangle} \frac{Q_i}{a_i} - \frac{1}{e_i} \langle R^2 \nabla \phi \cdot \vec{k}_i \rangle \\ & - \frac{F}{e_i \langle B^2 \rangle} \left[(C_2 \frac{1}{2} - A_i) N_i - (C_2 \frac{1}{2} + B_i) N_i \right] / d_{zi} \end{aligned} \quad (2.4.12a)$$

where

$$A_z = \frac{1}{a_z} \left[C_2 \frac{1}{2} - \frac{n_i \tilde{N}_i}{m_i n_i v_{iz}} \frac{V_{zi}}{\mu_i} \left(\frac{1}{2} + \lambda \right) \right] \left(C_3 + \frac{\sqrt{2} V_{zi}}{v_{iz}} + \frac{5}{2} \beta_i \right) \quad 2.4.12b)$$

and

$$B_z = \frac{1}{a_z} \left[C_2 \frac{1}{2} + \frac{n_i \tilde{N}_i}{m_i n_i v_{iz}} \frac{V_{zi}}{\mu_i} \lambda \right] \left(C_3 + \frac{\sqrt{2} V_{zi}}{v_{iz}} + \frac{5}{2} \beta_i \right) \quad 2.4.12c)$$

The heat flux will be discussed in some detail when this equation is reduced to specific collisionality regimes. Stacey [22] outlined the theory for heat transport including heat sources and an arbitrary collisionality plasma. Burrell [23] included the sources for a collisional plasma, and Parks, Burrell, and Wong [24] studied the heat transport effect of a momentum source for arbitrary plasma collisionality with no external impurity drag.

The results presented here extend the earlier results by the inclusion of all of the above mentioned effects, specifically external heat sources and drags, for any collisionality regime.

2.5 Approximations

The properties of the transport fluxes vary greatly

with the rate of inter-particle collisions. When the plasma has a relatively high density and low temperature, collisions are frequent, and the ions travel only a short distance between collisions. Banana orbits are not completed, and the effects associated with them are not observed. This is referred to as the collisional, or Pfirsch-Schlueter, regime. At lower densities and higher temperatures, collisions are infrequent and transport is greatly enhanced by the banana orbit sized diffusion steps. The region in which this occurs is classified here as the collisionless, or banana plateau regime. The main ions reach the collisionless regime while the heavier impurities are in the collisional regime. This mixed regime is an important regime for impurity transport, the transport exhibiting some properties of the other two regimes.

The relative frequency of inter-particle collisions is measured in terms of a collisionality parameter,

$$\nu_{*i} \equiv (\nu_{ii} / \omega_{ti}) \epsilon^{-3/2} \quad , \quad 2.5.1)$$

where

$$\omega_{ti} = V_{ti} B_{p0} / r B_0 \quad 2.5.2)$$

is the thermal particle transit frequency between banana

orbit turning points, distance qR , in a barely trapped orbit. The term ν_{ii} is the self collision frequency of species i , and ε is the geometric factor of inverse aspect ratio at radius r , $\varepsilon = r/R$. Hence, the collisionality parameter is basically the ratio of the time it takes to complete a banana orbit to the mean time between collisions. When the collisionality parameter is large, collisions dominate and the particles do not complete banana orbits; when the collisionality parameter is less than unity, magnetic trapping effects are important.

The direct effect of magnetic trapping on the previously described transport equations is taken into account through the parallel viscosity coefficients, μ_{nj} , and the collisional friction. In general, through any collisionality regime, they follow the fitted form

$$\mu_{nj} \sim \nu_{kj} / (1 + a \nu_{kj}) / (1 + b \nu_{kj} \varepsilon^{3/2}) \quad , \quad 2.5.3)$$

where a and b are numerically evaluated functions which are order unity. The actual coefficients and fitted forms are given by Hirshman [35,36] and reproduced, including a fit for μ_{3j} not given by Hirshman, in Appendix D. For a large collisionality parameter, i.e. highly collisional, each parallel viscosity coefficient becomes small, but the ratio of any two remains finite.

In order to study the transport fluxes defined in the previous section, it is useful to express these fluxes in a simpler geometry. This allows direct comparison of the sign and magnitude of each effect, which in turn directs more attention toward the more important effects as well as addressing the possible mechanisms for controlling impurity transport. A large aspect ratio, low beta approximation is used as is generally found in the literature [32], and follows the formalism used by Stacey and Sigmar [15,16].

When beta β , the ratio of the plasma pressure to the magnetic field pressure, is a small number, the particle pressure does little to change the magnetic field configuration. The vacuum magnetic field is then used to good approximation. A further approximation, based on a large aspect ratio, $A=1/\epsilon = R/a \gg 1$, coupled with the vacuum magnetic field approximation, allows the flux surface averages to be expressed in a simple, closed form.

The vacuum magnetic field varies inversely with the major radius, and, by using θ as the poloidal angle for a circular cross section, is written

$$B = B_0 / (1 + \epsilon \cos \theta) \quad , \quad 2.5.4)$$

since the major radius is

$$R = R_0 (1 + \varepsilon \cos \Theta) \quad . \quad 2.5.5)$$

The subscript 0 refers to the value on the toroidal axis, and the Θ angle is measured from the outer plasma midplane so that the maximum major radius occurs at $\Theta = 0$. The toroidal field dominates, so that the total field is used where it arises ($B_z = B_{\phi_0}$). In this limit, the flux surface average becomes

$$\langle A \rangle = \frac{1}{2\pi} \int_0^{2\pi} A (1 + \varepsilon \cos \Theta) d\Theta \quad . \quad 2.5.6)$$

By making use of the smallness of the inverse aspect ratio, the following flux surface averages and relations are found:

$$\langle B^2 \rangle \cong B_0^2 (1 + \frac{1}{2} \varepsilon^2) \quad , \quad 2.5.7a)$$

$$\langle R^2 (B_0^2 - \langle B^2 \rangle) \rangle \cong -2\varepsilon^2 R_0^2 B_0^2 \quad , \quad 2.5.7b)$$

$$\langle R^2 \nabla \phi \cdot \vec{K}_i' \rangle \cong R_0 K_{\phi i_0} (1 + \frac{1}{2} \varepsilon^2) \quad , \quad 2.5.7c)$$

$$\langle BK_{i||} \rangle \cong B_0 K_{\phi i} \quad , \quad 2.5.7d)$$

$$\Gamma_z \cong R_0 E_{p0} \langle n_z V_{zr} \rangle \quad , \quad 2.5.7e)$$

$$F \equiv R B_\phi = R_0 B_{\phi 0} \quad , \quad 2.5.7f)$$

and, for any quantity A,

$$A' = \frac{1}{R B_\phi} \frac{\partial A}{\partial r} \quad . \quad 2.5.7g)$$

The asymmetric particle sources on a flux surface are assumed to be dependent only on the poloidal angle. Defining a term consistent with this poloidal dependency,

$$S_i^{o,z} \equiv \frac{1}{\pi} \int_0^{2\pi} d\theta \cos \theta \int_{\pi/2}^{\theta} (S_i^{o,z} - \langle S_i^{o,z} \rangle) (1 + \epsilon \cos \theta') d\theta' \quad , \quad 2.5.8)$$

leads to a low beta approximation form for the asymmetric sources,

$$\langle \Delta_i^0 \rangle \approx \epsilon^2 \frac{R_0 B_0^2}{B_{p0}} \delta_i^2 \quad (2.5.9)$$

and

$$\langle \Delta_i^2 \rangle \approx \epsilon^2 \frac{R_0 B_0^2}{B_{p0}} \left(\delta_i^2 - \frac{5}{2} \frac{T_i}{m_i} \delta_i^0 \right) \quad (2.5.10)$$

2.6 Reduction to the Collisional Regime

The first plasma collisionality regime studied here is the collisional regime, where the particle transport effects are dominated by the high rate of inter-particle collisions. This regime is the first reached experimentally, and is the lowest regime for which this multiple ion species approach is applicable.

In this limit, the collisionality parameters, $\nu_{\kappa i}$ and $\nu_{\kappa 2}$ are very high, causing the parallel viscosity coefficients to be set to zero. The ratio of two viscosity coefficients, $\mu_{n i} / \mu_{m i}$, is found to be finite. Since there is always a viscosity coefficient multiplying this ratio, no viscosity coefficients appear. The effect of this limit is then to set the right hand side of both Equations 2.3.1 and

2.3.2 for the viscous shears to zero. This is the limit to which Burrell's results [23] are confined, although he has separated the effects of inter-species equilibration. As before, Stacey and Sigmar [16] also reduced their solution to this limit, but did not include the higher moment, temperature gradient effects.

By first applying the highly collisional limit but not the low beta limit to the particle transport, the origins of the effects are seen. The low beta limit is then imposed to approximate the flux surface integrals and to show the magnitude and direction of the flux components. The limit of the terms used is given in Table 2.6.1.

By imposing the collisional limit on the coefficients of the combinations of terms N_i and N_z in the equation for the total radial impurity flux, Equation 2.4.10, it can be shown that the coefficients multiplying N_i cancel completely, $C_i \xi_z - \Theta_z - \beta_z \lambda = 0$, and that the coefficients multiplying N_z reduce to its denominator, $d_{z,i}$, $C_i \xi_z - \Theta_z + \beta_z (\xi_i + \lambda) = d_{z,i}$. Due to the subsequent cancellation of the $Q_{i,z}$ terms, only the averaged parallel momentum source, $\langle BK_{z//} \rangle$, is left in the last set of brackets in Equation 2.4.10.

With the inclusion of the collisional limit of the two species electrostatic potential found in Appendix B, the radial impurity flux becomes

$$\begin{aligned}
\Gamma_z = & -\frac{m_i n_i v_{iz}}{e_z \langle B^2 \rangle} \left\{ \left(C_1 + \frac{\beta_i \beta_e}{\beta_i + \beta_e} \right) \left(\frac{p_i'}{n_i e_i} - \frac{p_e'}{n_e e_e} \right) - \left(\frac{T_i'}{e_i} - \frac{T_e'}{e_e} \right) \right\} \langle R^2 (B_z^2 - \langle B^2 \rangle) \rangle \\
& + \frac{1}{e_z} \frac{\beta_e}{\beta_i + \beta_e} \left\{ \langle R^2 \nabla \phi \cdot (\hat{R}_i + \hat{R}_e) \rangle - \frac{F}{\langle B^2 \rangle} \langle B (k_{in} + k_{en}) \rangle \right\} + \frac{\langle R^2 \nabla \phi \cdot \hat{R}_i' \rangle}{e_z} - \frac{F}{e_z \langle B^2 \rangle} \langle B k_{en}' \rangle. \quad 2.6.1) \\
& - \frac{m_i n_i v_{iz}}{e_z \langle B^2 \rangle} F \left\{ \left(C_1 + \frac{\beta_i \beta_e}{\beta_i + \beta_e} \right) \left(\frac{\langle \Delta_i^2 \rangle}{n_i} - \frac{\langle \Delta_e^2 \rangle}{n_e} \right) - C_2 \frac{2}{5} \left(\frac{\langle \Delta_i^2 \rangle}{P_i} - \frac{\langle \Delta_e^2 \rangle}{P_e} \right) \right\}
\end{aligned}$$

It is seen that this flux is independent of directed heat flux input and is driven by differences in gradients, momentum inputs, and asymmetric sources, each set being obviously ambipolar.

The low beta, large aspect ratio limit of the particle flux can now be expressed as the sum of these components, each of which is associated with a specific driving force:

$$\left. \langle n_z v_z \rangle \right|_{\text{grad}} = \frac{z e^2 m_i n_i v_{iz}}{e_z B_p^2} \left\{ \left(C_1 + \frac{\beta_i \beta_e}{\beta_i + \beta_e} \right) \left(\frac{1}{n_i e_i} \frac{\partial p_i}{\partial r} - \frac{1}{n_e e_e} \frac{\partial p_e}{\partial r} \right) - C_2 \left(\frac{1}{e_i} \frac{\partial T_i}{\partial r} - \frac{1}{e_e} \frac{\partial T_e}{\partial r} \right) \right\} \quad 2.6.2)$$

is the particle flux driven by pressure and temperature gradients;

$$\left. \langle n_z v_z \rangle \right|_{\text{Source}} = \frac{z e^2 B_0}{e_z B_{p0}} m_i n_i v_{iz} \left\{ \left(C_1 + C_2 + \frac{\beta_i \beta_e}{\beta_i + \beta_e} \right) \left(\frac{\delta_i^0}{n_e} - \frac{\delta_e^0}{n_i} \right) - \frac{2}{5} C_2 \left(\frac{\delta_i^0}{P_e} - \frac{\delta_e^0}{P_i} \right) \right\} \quad 2.6.3)$$

is the particle flux driven by poloidally asymmetric particle and heat sources; and

$$\left. \langle n_2 V_z \rangle \right|_{\text{momentum}} = -E^2 \frac{\beta_i K_{\theta z} - \beta_e K_{\theta i}}{e_2 B_p (\beta_i + \beta_e)} \quad 2.6.4)$$

is the particle flux due to the neutral beam momentum input.

These results extend the results of Stacey and Sigmar [16] by inclusion of temperature gradient effects, the last term in Equation 2.6.2, and by inclusion of poloidally asymmetric heat sources, the last term in Equation 2.6.3. Since more general forms of the parallel viscosity and friction are used, Equations 2.3.1 and 2.3.3, the previous results of Stacey and Sigmar [16] are assured. These results reduce to the results of Stacey and Sigmar when the temperature gradient and poloidally asymmetric heat sources are omitted, and in the limit $C_1 \rightarrow 1$ and $C_2 \rightarrow 0$. If the external drag terms are omitted, the flux due to the pressure and temperature gradients is identical to the results obtained by Rutherford [5].

The results of Burrell [23] are equivalent to the results given in this limit, except for the impurity temperature gradient and heat source, which he did not include, and a different approximate form that he used for the directed inputs.

In order to compare the effects of gradients, sources, and momentum inputs, it is necessary to use typical numerical values of the transport coefficients and to use models for the sources. Fits to the values of the transport coefficients C_n are found in Equation 2.3.9. For an effective impurity density of one, $\alpha = n_2 Z^2 / n_i \sim 1$, the constant C_1 is .67 and C_2 is .56. These differ by less than $\sim 20\%$, giving the density gradient the most important role in the gradient driven flux when the density and temperature scale lengths are approximately equal,

$$\langle n_2 v_z \rangle_r \Big|_{\text{grad}} \approx \frac{Ze^2 m_i n_i v_{Tz}}{e_2 B_T^2} \left\{ .67 \left(\frac{1}{n_i e_i} \frac{\partial n_i}{\partial r} - \frac{1}{n_2 e_2} \frac{\partial n_2}{\partial r} \right) + .11 \left(\frac{1}{e_i} \frac{\partial T_i}{\partial r} - \frac{1}{e_2} \frac{\partial T_2}{\partial r} \right) \right\} \quad . \quad 2.6.5$$

Since the main ion and impurity temperatures equilibrate rapidly, the temperature gradient difference becomes $(Z-1)/Ze \, dT/dr$. In the usual case of negative temperature and main ion gradients, the impurities will be driven inward by both gradients.

Similarly, the impurity flux due to asymmetric particle and heat sources for a typical plasma becomes

$$\langle n_2 v_z \rangle_r \Big|_{\text{source}} = \frac{e^2 B}{e_2 B_T} m_i n_i v_{Tz} \left\{ 1.23 \left(\frac{\delta_2^0}{n_2} - \frac{\delta_i^0}{n_i} \right) - .22 \left(\frac{\delta_2^Z}{P_2} - \frac{\delta_i^Z}{P_i} \right) \right\} \quad . \quad 2.6.6$$

Approximating the density gradient by $|d \ln n/dr| \approx 1/a$, where a is the plasma minor radius, leads to the requirement that the source is approximately

$$\delta_i^0 \sim 3.4 \frac{n_i T_i}{B_0 a} \quad (2.6.7)$$

in order for its effect to be comparable to the main ion gradient. The source needed to significantly affect the impurity transport is large, but may be an important effect at the plasma edge and is needed in properly calculating the effect of reflux from the walls on edge impurity transport.

The neutral beam current needed in order for the momentum driven flux $\Gamma_{z, \text{beam}}$ to be comparable to the ion density gradient driven flux, $\Gamma_{z, \text{grad}}$, is

$$I_b = \frac{2m_i n_i v_{b2} \left| \frac{1}{n_i} \frac{dn_i}{dr} \right|}{m_b v_b Z_i e r_0} K_0^{-4} H V \quad (2.6.8)$$

found by using the momentum input form given in Appendix D. The term V is the volume fraction injected into, and the term

$$H \equiv C_i (1 + \beta_i / \beta_e) + \beta_e \quad 2.6.9)$$

is defined.

Stacey and Sigmar [16], using an average pressure gradient, found that the currents available would have a first order effect on various present-day experimental devices. Impurity flow modification was subsequently observed experimentally [28-31]. They required that H be approximately unity. In the present case, their approximations would not be greatly modified, so these approximations are not repeated. Their results showed that in a first generation reactor with $R = 5$ m., $a = 1.5$ m., $I = 5$ MAmp, $T_o = 15$ keV., $\bar{T} = 5$ keV., $\bar{n}_i = 10^{20} / m^3$, and $E_{beam} = 160$ keV., flow reversal could be achieved with less than 10 MWatts of power injected into one fifth of the plasma volume.

First principle mechanisms capable of explaining the experimentally observed drag, and therefore the drag factors β_i and β_e , are not known [37]. These drag factors are discussed in more detail in Section 2.9. If the ratio β_e / β_i is small, H is large and neutral beam driven transport effects comparable to gradient driven effects would not be seen. Burrell [23] assumed the drag ratio

β_z/β_i to be small, concentrating on the second term in Equation 2.6.4. His results showed counter-injection driving impurities outward. Experimental results, showing co-injection driving impurities outward and counter-injection driving impurities inward [28-31], indicate that the ratio β_z/β_i must be $> K'_{\phi z}/K'_{\phi i}$.

From the large aspect ratio, low beta, collisional limit of the ion heat flux,

$$\begin{aligned} \frac{q_{ir}}{P_i} &= \frac{2\varepsilon^2 m_i n_i v_{iz}}{e_i B_p^2} \left[C_2 \left(\frac{1}{n_i e_i} \frac{\partial p_i}{\partial r} - \frac{1}{n_i e_i} \frac{\partial p_e}{\partial r} \right) - \frac{1}{2} \frac{1}{e_i} \frac{\partial T_i}{\partial r} \left(C_3 + \frac{\sqrt{2} v_{iz}}{v_{iz}} + \frac{1}{2} \beta_i \right) \right] \\ &\quad - \frac{\varepsilon^2 m_i n_i v_{iz}}{e_i B_p^2} \left[\left(C_2 + C_3 + \frac{\sqrt{2} v_{iz}}{v_{iz}} + \frac{1}{2} \beta_i \right) \frac{\delta_i^0}{n_i} - C_2 \frac{\varepsilon_z^0}{n_z} \right. \\ &\quad \left. - \left(C_3 + \frac{\sqrt{2} v_{iz}}{v_{iz}} + \frac{1}{2} \beta_i \right) \frac{\delta_i^z}{P_i} \right] - \frac{\varepsilon^2}{e_i B_p} k_{\phi i} \end{aligned} \quad , \quad 2.6.11a)$$

where

$$K_{\phi i} = \frac{m_i}{T_i} K_{\phi i}^2 - \frac{1}{2} K_{\phi i}^1 \quad . \quad 2.6.11b)$$

The heat flux is found to be of order ε^2 , as expected. The results given above extend Burrell's results [23] to include the impurity temperature gradients, asymmetric impurity heat sources, and directed heat fluxes. As Burrell found, a co-injected beam increases the outward heat flux, and driving a toroidal heat flux in the co-direction opposes the outward directed heat flux. The work of Stacey [22] was not

carried to an actual solution for the fluxes, and Rutherford [5] did not calculate the effect of impurities on the gradient driven main ion heat fluxes.

When the effects on the heat flux of density gradients are compared to neutral beam injection, the beam current needed to produce a beam driven heat flux equal in magnitude to the flux driven by gradients is estimated to be

$$I_b = \frac{2\sqrt{2} m_i n_i v_{i,z} T/a}{m_b v_b B_p} \sqrt{K_b^{-1}} f(\alpha) \quad , \quad 2.6.12)$$

where

$$f(\alpha) = (1 + \alpha (C_3 - \frac{7}{3} C_2)) \quad . \quad 2.6.13)$$

Stacey and Sigmar [16] compared the gradient driven and beam driven impurity fluxes in PLT using the following data: a 40 keV deuteron beam into a hydrogen plasma with major radius $R = 1.3\text{m}$, plasma radius $a = 0.4\text{m}$, average density $\bar{n}_e = 2 \times 10^{19} / \text{m}^3$, plasma current $I = 600 \text{ kA}$, and average temperature $\bar{T}_i = 1 \text{ keV}$. This data is used to compare the gradient and beam driven heat fluxes. The beam current needed to provide a level of flux equal to the gradient driven flux is found to be

$$I_b \approx 50 V f(\alpha) K_b^{-1} \quad [\text{amp}], \quad 2.6.14)$$

where K_b^{-1} is a beam coupling factor, $\alpha = n_e Z^2/n_i$ and V is the volume fraction injected into. In a clean plasma, $\alpha \sim 0$, $f(\alpha) \sim 1$, the beam current needed to drive a heat flux comparable to the gradient driven flux is 500 to 1000 kWatt, which is available in PLT. When the plasma contains more impurities, a much larger beam power is required. For example, $f(\alpha=1) = 2.7$, nearly tripling the gradient driven flux while not changing the beam driven heat flux.

Table 2.6.1 Collisional Limit of Terms

$$a_i = \frac{5}{2} \beta_i + \frac{v_{ii}}{v_{iz}} \sqrt{2} - C_3$$

$$a_z = \frac{5}{2} \beta_z + \frac{v_{zz}}{v_{zi}} \sqrt{2}$$

$$\xi_i = \beta_i \quad ; \quad \xi_z = \beta_z$$

$$\lambda = C_1 - C_2 \left(\frac{1}{a_i} + \frac{1}{a_z} \right)$$

$$d_{zi} = (\beta_i + \beta_z) \lambda + \beta_i \beta_z$$

$$C_1 \xi_z - \Theta_i - \lambda \xi_z = 0$$

$$C_1 \xi_i - \Theta_z + \beta_z (\xi_i + \lambda) = d_{zi}$$

$$C_2 \xi_z - A_i = C_2 \xi_i - B_z = 0$$

$$N_i = \langle BK'_{i\parallel} \rangle + \frac{5}{2} C_2 \left(\frac{Q_i}{a_i} - \frac{Q_z}{a_z} \right)$$

$$N_z = \langle BK'_{z\parallel} \rangle + \frac{5}{2} C_2 \left(\frac{Q_z}{a_z} - \frac{Q_i}{a_i} \right)$$

2.7 Reduction to the Mixed Regime

As the temperature of the plasma increases, the interactions among the plasma ions decrease, the ions thus entering the banana-plateau regime. Heavier impurity ions will not reach this transition until higher temperatures or lower densities are achieved. To study this transition phase, referred to as the mixed regime, the impurities are treated using the highly collisional limit, $\tilde{\nu}_z \rightarrow 0$, while the main ions are not, $\tilde{\nu}_i \neq 0$.

Since only the impurity viscosity is set to zero, the terms are not in general found by simply exchanging i and z subscripts. The mixed regime limits of several important terms are listed in Table 2.7.1. The electrostatic potential for this regime is found in Appendix B. A large aspect ratio, low beta approximation of Equation B-7, dropping the ϵ^2 term in the denominator, leads to

$$F\Phi' = -\frac{\langle BK_{iR} \rangle + \langle BK_{zR} \rangle}{m_i n_i \nu_{iz} (\beta_i + \beta_z)} - \frac{1}{m_i n_i \nu_{iz}} \frac{\mu_{zi}}{\mu_{ic}} \frac{\langle BK_{iR} \rangle}{a_z} \quad . \quad 2.7.1)$$

$$- F \left(\frac{p_i'}{n_i e_i} + \frac{\mu_{zi}}{\mu_{ic}} \frac{T_i}{e_i} \right)$$

As in the collisional regime, the coefficients of N_i and N_z in the equation for the total radial impurity flux, Equation 2.4.10, can be reduced. The coefficient of N_i

reduces to zero and the coefficient of N_2 reduces to its denominator, d_{z_i} . With this simplification, the electrostatic potential enters only in the Pfirsch-Schlueter coefficients. The Pfirsch-Schlueter term is already of order ε^2 , so the potential is required only to zeroth order in ε .

The mixed regime limit thus gives, without the low beta limit, the following form for the impurity transport flux:

$$\begin{aligned} \Gamma_z = & -\frac{\langle R^2 \nabla \Phi \cdot \vec{K}_z' \rangle}{e_z} + \frac{F \langle B K_{z11}' \rangle}{e_z \langle B^2 \rangle} - \frac{m_i n_i v_{iz}}{e_z \langle B^2 \rangle} \langle R^2 (B_\phi^2 - \langle B^2 \rangle) \rangle \times \\ & \left\{ C_1 \left(\frac{R'}{n_i e_i} - \frac{P_z'}{n_z e_z} \right) - C_2 \left(\frac{T_1'}{e_i} - \frac{T_2'}{e_z} \right) - \beta_z \left(\frac{P_z'}{n_z e_z} + \Phi' \right) \right\} \quad . \quad 2.7.2) \\ & - \frac{m_i n_i v_{iz}}{e_z \langle B^2 \rangle} F \left\{ C_1 \left(\frac{\langle \Delta_i^2 \rangle}{n_i} - \frac{\langle \Delta_z^2 \rangle}{n_z} \right) - \frac{1}{2} C_2 \left(\frac{\langle \Delta_i^2 \rangle}{P_i} - \frac{\langle \Delta_z^2 \rangle}{P_z} \right) - \beta_z \frac{\langle \Delta_z^2 \rangle}{n_z} \right\} \end{aligned}$$

It is seen that, with the main ions collisionless, the dependence of the flux on external drag is dominated by the impurity drag, β_z . Recall that an effective drag, $\beta_i \beta_z / (\beta_i + \beta_z)$, was the dominant effect in the collisional regime.

In the low beta, large aspect ratio limit, the entire flux reduces to order ε^2 . Again, the flux can be written as the sum of three separate effects:

$$\left. \langle n_z V_z \rangle_r \right|_{\text{grad}} = \frac{z \varepsilon^2 m_i n_i v_{iz}}{e_z B_p^2} \left\{ (C_1 + \beta_2) \left(\frac{1}{n_i e_i} \frac{\partial p_i}{\partial r} - \frac{1}{n_z e_z} \frac{\partial p_z}{\partial r} \right) - C_2 \left(\frac{1}{e_i} \frac{\partial T_i}{\partial r} - \frac{1}{e_z} \frac{\partial T_z}{\partial r} \right) + \beta_2 \frac{\mu_{zi}}{\mu_{ie}} \frac{1}{e_i} \frac{\partial T_i}{\partial r} \right\} \quad (2.7.3)$$

is the flux component driven by temperature and pressure gradients;

$$\left. \langle n_z V_z \rangle_r \right|_{\text{source}} = \frac{\varepsilon^2 m_i n_i v_{iz}}{e_z B_p^2} B \left\{ (C_1 + C_2 + \beta_2) \frac{\xi_z^0}{n_z} - (C_1 + C_2) \frac{\xi_i^0}{n_i} - \frac{2}{5} C_3 \left(\frac{\xi_z^0}{P_z} - \frac{\xi_i^0}{P_i} \right) \right\} \quad (2.7.4)$$

is the flux component driven by asymmetric sources; and

$$\left. \langle n_z V_z \rangle_r \right|_{\text{momentum}} = \frac{\varepsilon^2}{e_z B_p (\beta_i + \beta_z)} (2\beta_z K_{0i} + (\beta_z - \beta_i) K_{0z}) + \frac{z \varepsilon^2}{e_z B_p} \frac{\mu_{zi}}{\mu_{ie}} \frac{k_{pi}}{a_i} \quad (2.7.5)$$

is the flux component driven by directed sources.

These results extend Stacey and Sigmar's work [16] by including the more general friction relationships of

Equations 2.3.1 and 2.3.2, and by including temperature gradient, asymmetric heat source, and externally driven heat flux effects. The present results reduce to the Stacey and Sigmar results when the above mentioned effects are omitted.

Comparing Equations 2.6.2 and 2.7.3, the gradient driven flux is seen to be modified little in the transition from collisional to mixed regimes. In addition to the external impurity drag being important instead of the mean drag as mentioned above, the external drag portion of the temperature gradient term has been changed to include the ratio μ_{2i}/μ_{1i} . Numerical ranges for the ratios of viscosity coefficients are found in Appendix D to be order unity, and hence this gradient effect will be of no greater importance than other gradient effects.

When the mixed regime momentum driven flux, Equation 2.7.5, is compared to the collisional regime momentum driven flux, Equation 2.6.4, the mixed regime term is seen to be always larger in the injection direction by the addition of $\beta_2/(\beta_1 + \beta_2)K_{\phi_{total}}$. This mixed regime formulation produces a constraint of $\beta_2(2K_{\phi_1} + K_{\phi_2}) > \beta_1 K_{\phi_2}$ for flow reversal by using co-injection.

Unlike the main ion particle flux in the mixed regime, the heat transport flux is not held to collisional magnitudes by ambipolarity. By substituting the mixed regime limits found in Table 2.7.1 into the equation for the heat flux, Equation 2.4.11, the main ion heat flux in the

mixed regime is found,

$$\begin{aligned} \frac{q_r}{F_c} = & \frac{n_i \tilde{\mu}_i}{e_i^2 B_{p0}} \left[\frac{N_{zi}}{N_{ii}} - \left(\frac{N_{zi}}{N_{ii}} \right)^2 \right] \frac{\partial T_i}{\partial r} (1-X) - \frac{a_i}{e_i B_{p0}} X \left(\frac{K_{\phi i}}{a_i} - \frac{K_{\phi z}}{a_z} \right) \\ & + \frac{1}{e_i B_{p0}} \left(\frac{n_i \tilde{\mu}_i}{m_i n_i v_{iz}} \frac{N_{zi}}{N_{ii}} \right) \frac{K_{\phi i} + K_{\phi z}}{\beta_i + \beta_z} (1-X) - \frac{a_i}{C_2} X \frac{1}{e_i B_{p0}} K_{\phi z} \end{aligned} \quad , \quad 2.7.6)$$

where

$$X = \frac{\lambda}{d_{zi}} \frac{C_2}{a_z} \frac{n_i \tilde{\mu}_i}{m_i n_i v_{iz}} \frac{N_{zi}}{N_{ii}} < 1 \quad . \quad 2.7.7)$$

The term X is dimensionless and is found to be always less than unity, which determines the sign of the $(1-X)$ term.

When the radial heat transport in this regime is examined, it can be seen that the pressure gradient has no effect in this ordering, which agrees with subject reviews [32,38]. A negative temperature gradient drives an outward heat flux, as expected. When the ratio of neutral beam injection driven heat flux to the gradient driven heat flux is studied,

$$\frac{q_{\text{beam}}}{q_{\text{grad}}} \sim \frac{\frac{\mu_{zi}}{\mu_{zi}} \frac{K_{\text{oc}} + K_{\text{op}}}{m_i n_i v_{iz} (\beta_i + \beta_e)}}{\frac{\mu_{zi}}{\mu_{zi}} \frac{1}{e_i B_p} T/a} \sim \frac{\mu_{zi}}{\mu_{zi}} \frac{V_{\text{rotation}}}{e_i B_p T/a} \quad , \quad 2.7.8)$$

it is seen that co-injection of momentum will enhance the normally outward heat conduction. In a typical PLT plasma, with $\bar{T}_e = 1$ keV, $a = 0.4$ m, and $B_p = 0.3$ T, it is predicted that 1 MWatt of co-injected beam, which rotates the plasma toroidally at $\sim 10^5$ m/sec, will cause an order unity increase in the outward heat conduction. An order unity decrease in energy confinement is observed with beam injection into PLT [37], but it is observed for both co- and counter-injection, whereas this theory would predict an increase in energy confinement with counter-injection. In PLT, the energy confinement is thought to be dominated by electron losses, so no conclusions can be drawn. Extrapolating to TFTR, with 16 MWatts of co-injected beam, and $\bar{T}_e = 5$ keV., and $B_p = .3$ T., the gradient and beam driven terms are again found to be comparable in magnitude. Previous studies have not calculated the effects of sources on heat transport in this regime, so no comparisons with these results can be made. The dominant directed heat flux term is

$$\left. \frac{q_{r1}}{P_c} \right|_{\text{heat flux}} = - \frac{a_1}{c_1 B_p} \times \left(\frac{R_{\phi 1}}{a_1} - \frac{R_{\phi 2}}{a_2} \right) \quad , \quad 2.7.9)$$

which reduces the outward conduction of heat if $k_{\phi 1}/a_1 > k_{\phi 2}/a_2$. Although a directed heat flux can be driven by radio frequency heating, little is known about the plasma coupling and penetration of this effect, so no estimates can be made here of the effects of driving a co-directed toroidal heat flux.

Table 2.7.1 Collisionless Limit of Terms

$$\xi_i = \beta_i + \frac{n_i \tilde{\nu}_i}{n_i m_i \nu_{iz}} - \left(\frac{n_i \tilde{\nu}_i}{n_i m_i \nu_{iz}} \frac{\mu_{zi}}{\mu_{ci}} \right)^2 / a_i + C_2 \frac{n_i \tilde{\nu}_i}{n_i m_i \nu_{iz}} \frac{\mu_{zi}}{\mu_{ci}} / a_i$$

$$\xi_z = \beta_z - C_2 \frac{n_i \tilde{\nu}_i}{n_i m_i \nu_{iz}} \frac{\mu_{zi}}{\mu_{ci}} / a_i$$

$$\lambda = C_1 - C_2^2 \left(\frac{1}{a_i} + \frac{1}{a_z} \right) + \frac{C_2}{a_i} \left(\frac{n_i \tilde{\nu}_i}{n_i m_i \nu_{iz}} \frac{\mu_{zi}}{\mu_{ci}} \right)$$

$$N_i = \langle BK_{i||} \rangle - n_i \tilde{\nu}_i \left\{ F \left(\frac{p_i'}{n_i e_i} + \Phi' \right) + \frac{\langle \Delta_i \rangle}{n_i} + \frac{\mu_{zi}}{\mu_{ci}} \left(F \frac{T_i'}{e_i} + \frac{\langle \Delta_i \rangle}{p_i} \right) \right\} \\ + C_2 \left(\frac{Q_i}{a_i} - \frac{Q_z}{a_z} \right) - \frac{n_i \tilde{\nu}_i}{n_i m_i \nu_{iz}} \frac{\mu_{zi}}{\mu_{ci}} Q_i / a_i$$

$$N_z = \langle BK_{z||} \rangle - C_2 \left(\frac{Q_i}{a_i} - \frac{Q_z}{a_z} \right)$$

$$Q_i = \langle BK_{i||} \rangle - n_i \tilde{\nu}_i \frac{\mu_{zi}}{\mu_{ci}} \left\{ F \left(\frac{p_i'}{n_i e_i} + \Phi' \right) + \frac{\langle \Delta_i \rangle}{n_i} \right\} - n_i \tilde{\nu}_i \frac{\mu_{zi}}{\mu_{ci}} \left\{ F \frac{T_i'}{e_i} + \frac{\langle \Delta_i \rangle}{p_i} \right\}$$

$$C_1 \xi_z - \Theta_i - \beta_z \lambda = 0$$

$$C_1 \xi_i - \Theta_z + \beta_z (\xi_i + \lambda) = d_{zi}$$

$$C_2 \xi_z - A_i \cong \frac{n_i \tilde{\nu}_i}{n_i m_i \nu_{iz}} \frac{\mu_{zi}}{\mu_{ci}} \lambda$$

$$C_2 \xi_i - B_z \cong 0$$

2.8 Reduction to the Collisionless Regime

In a high temperature plasma, the lighter impurities may also go into the collisionless regime. The coefficients of the N terms do not reduce to the same values as that of the previous regimes, $C_1 \xi_z - \Theta_i - \beta_z \lambda \neq 0$, and $C_1 \xi_z - \Theta_z + \beta_z (\xi_z + \lambda) \neq d_{zc}$. Without this cancelation, the plasma goes to a totally collisionless type of transport which does not reduce to the ξ^2 ordering of the collisional regimes, but rather is order $\sqrt{\xi}$, as will be seen. The Pfirsch-Schlueter terms and asymmetric sources are therefore of minor effect and are dropped, leaving to lowest order

$$\Gamma_z = -\frac{R_0 k_{\theta i}}{e_z} - \frac{R_0}{e_z B_0} \left\{ -C_2 \left(\frac{Q_i}{a_i} - \frac{Q_z}{a_z} \right) + \left[(C_1 \xi_z - \Theta_i - \beta_z \lambda) N_i - (C_1 \xi_z - \Theta_z + \beta_z (\xi_z + \lambda)) N_z \right] / d_{zc} \right\} \quad 2.8.1)$$

where the terms Q_i and N_i are

$$Q_i = B_0 k_{\theta i} - n_i \tilde{\mu}_i F \left[\frac{N_{zi}}{\mu_i} \left(\frac{P_i'}{n_i e_i} + \Phi' \right) + \frac{N_{zi}}{\mu_i} \frac{T_i'}{e_i} \right] \quad 2.8.2a)$$

$$N_i = B_0 K_{0i} - n_i \tilde{\rho}_i F \left[\frac{\rho_i'}{n_i \epsilon_i} + \Phi' + \frac{N_{zi}}{\mu_{iz}} \frac{T_i'}{\epsilon_i} \right] + C_z \left(\frac{Q_i}{a_i} - \frac{Q_z}{a_z} \right) \quad . \quad 2.8.2b)$$

The terms Q_z and N_z are obtained from Equation 2.8.2a and 2.8.2b by interchanging i and z subscripts. The electrostatic potential to lowest order is

$$F\Phi' = - \frac{\langle B(K_{0i} + K_{0z}) \rangle}{m_i n_i v_{iz} (\beta_i + \beta_z)} - \frac{B}{n_i \tilde{\rho}_i + n_z \tilde{\rho}_z} \times \left[\frac{n_i \tilde{\rho}_i}{m_i n_i v_{iz}} \frac{\mu_{zi}}{N_{zi}} \frac{K_{0i}}{a_i} + \frac{n_z \tilde{\rho}_z}{m_i n_i v_{iz}} \frac{\mu_{zz}}{\mu_{iz}} \frac{K_{0z}}{a_z} \right] - \frac{F}{n_i \tilde{\rho}_i + n_z \tilde{\rho}_z} \left\{ n_i \tilde{\rho}_i \left(\frac{\rho_i'}{n_i \epsilon_i} + \frac{\mu_{zi}}{\mu_{iz}} \frac{T_i'}{\epsilon_i} \right) + n_z \tilde{\rho}_z \left(\frac{\rho_z'}{n_z \epsilon_z} + \frac{N_{zz}}{\mu_{iz}} \frac{T_z'}{\epsilon_z} \right) \right\} \quad . \quad 2.8.3)$$

In order to sort out the major effects, the numerical values of the coefficients are estimated. The viscosity terms are approximated by

$$\frac{n_i \tilde{\rho}_i}{m_i n_i v_{iz}} \sim \sqrt{\epsilon} / \alpha \quad 2.8.4)$$

and

$$\frac{n_z \tilde{\nu}_z}{m_i n_i \nu_{iz}} \sim \sqrt{\epsilon} \propto \left(\frac{m_z}{m_i}\right)^{1/2} \quad , \quad 2.8.5)$$

When it is assumed that the external drag is of the same order as the parallel viscosity, the fluxes can be found to lowest order in $\sqrt{\epsilon}$. The effective external drag was found to be the same magnitude as the parallel viscosity in experiments in PLT [37].

The impurity flux component driven by pressure and temperature gradients becomes

$$\begin{aligned} \langle n_z V_z \rangle_r = & \frac{n_z \tilde{\nu}_z n_i \tilde{\nu}_i}{(n_i \tilde{\nu}_z + n_z \tilde{\nu}_z) e_z B_p^2} \left\{ \left(\frac{1}{n_i e_i} \frac{\partial p_i}{\partial r} - \frac{1}{n_z e_z} \frac{\partial p_z}{\partial r} \right) \right. \\ & \left. + \left(\frac{\mu_{zi}}{\nu_{iz}} \frac{1}{e_i} \frac{\partial T_i}{\partial r} - \frac{\mu_{zz}}{\nu_{iz}} \frac{1}{e_z} \frac{\partial T_z}{\partial r} \right) \right\} \quad , \quad 2.8.6) \end{aligned}$$

This equation is the usual neoclassical result [32].

The flux driven by the directed momentum sources is

$$\langle n_z V_z \rangle_{\text{momentum}} = \frac{1}{e_z B_p} \frac{n_i \tilde{\rho}_i n_z \tilde{\rho}_z}{n_i \tilde{\rho}_i + n_z \tilde{\rho}_z} \left[1 + \frac{C_2}{a_i} \frac{\mu_{zi}}{\mu_{ii}} + \frac{C_2}{a_z} \frac{\mu_{zz}}{\mu_{zz}} \right] \times \quad . \quad 2.8.7)$$

$$\left\{ \frac{\beta_z k_{zi} - \beta_i k_{iz}}{\lambda (\beta_i + \beta_z)} + C_2 (\xi_i + \xi_z) \left(\frac{n_i \tilde{\rho}_i}{a_i} \frac{\mu_{zi}}{\mu_{ii}} - \frac{n_z \tilde{\rho}_z}{a_z} \frac{\mu_{zz}}{\mu_{zz}} \right) \frac{k_{zi} + k_{iz}}{d_{zi} (\beta_i + \beta_z)} \right\}$$

This reduces to the results of Stacey and Sigmar when the higher viscosity coefficients vanish, $\mu_3 = \mu_2 = 0$, and when $C_1 = 1$ and $C_2 = 0$, as would be expected. The first term indicates that co-injection of momentum drives impurities outward if $\beta_z k_{zi} > \beta_i k_{iz}$ as in the collisional regime.

The additional effect of a directed heat flux source is first found here for the collisionless regime,

$$\langle n_z V_z \rangle_{\text{heat flux}} = \frac{1}{e_z B_p} \frac{n_i \tilde{\rho}_i n_i \tilde{\rho}_i}{n_z \tilde{\rho}_z + n_i \tilde{\rho}_i} \left\{ \left[1 + \frac{C_2}{a_i} \frac{\mu_{zi}}{\mu_{ii}} + \frac{C_2}{a_z} \frac{\mu_{zz}}{\mu_{zz}} \right] \frac{C_2 (\xi_i + \xi_z)}{d_{zi}} \left[\frac{k_{zi}}{a_i} - \frac{k_{iz}}{a_z} \right] \right.$$

$$\left. + \left[\frac{\mu_{zi}}{\mu_{ii}} \frac{k_{zi}}{a_i} - \frac{\mu_{zz}}{\mu_{zz}} \frac{k_{iz}}{a_z} \right] + \frac{1}{n_i \tilde{\rho}_i + n_z \tilde{\rho}_z} \right\} \quad . \quad 2.8.8)$$

$$\left[\frac{\beta_z \xi_i}{d_{zi}} - \frac{\beta_i \xi_z}{d_{zi}} + \frac{n_i \tilde{\rho}_i}{m_i n_i d_{iz}} \left(\frac{\mu_{zi}}{\mu_{ii}} \right)^2 / a_i = \frac{n_z \tilde{\rho}_z}{m_z n_z d_{iz}} \left(\frac{\mu_{zz}}{\mu_{zz}} \right)^2 / a_z \right] \left[\frac{n_i \tilde{\rho}_i}{m_i n_i d_{iz}} \frac{\mu_{zi}}{\mu_{ii}} \frac{k_{zi}}{a_i} + \frac{n_z \tilde{\rho}_z}{m_z n_z d_{iz}} \frac{\mu_{zz}}{\mu_{zz}} \frac{k_{iz}}{a_z} \right]$$

Although evaluation of the major terms would be needed to give an accurate indication of the direction of the impurity flow driven by this source, the sign of most of the terms indicates that an ion heat flux driven in the co-direction will drive impurities outward.

The main ion heat conduction had reached collisionless scaling in the mixed regime. In the collisionless regime, the main ion heat conduction is

$$\frac{q_{ir}}{P_i} \approx -\frac{n_i \tilde{\mu}_i}{e_i^2 B_p^2} \left[\frac{\mu_{zi}}{\mu_{ii}} \frac{1}{n_i} \frac{\partial p_i}{\partial r} + \frac{\mu_{zi}}{\mu_{ii}} \frac{\partial T_i}{\partial r} \right] \quad (2.8.9)$$

$$-\frac{\lambda}{e_i B_p B \partial z_i} \left[\frac{n_i \tilde{\mu}_i}{m_i n_i \nu_{iz}} \frac{\mu_{zi}}{\mu_{ii}} N_i + \frac{n_z \tilde{\mu}_z}{m_i n_i \nu_{iz}} \frac{\mu_{zr}}{\mu_{iz}} N_z \right]$$

The N terms in this regime are complicated functions of the directed sources, pressure and temperature gradients, and the solution for the electrostatic potential for this regime found in Appendix B. No simplifications are evident.

When the impurities are fully collisionless, the ratio of the impurity viscosity to ion viscosity is

$$\frac{n_z \tilde{\mu}_z}{n_i \tilde{\mu}_i} \sim \alpha^2 \sqrt{\frac{m_z}{m_i}} \quad (2.8.10)$$

which can easily be comparable to or larger than unity. To evaluate and compare the magnitude of the different heat conduction driving terms, three limits of the viscosity terms will be discussed: the limit $n_i \tilde{\mu}_i \gg n_z \tilde{\mu}_z$, which is the mixed regime limit studied in the last section, Equation 2.7.6; the limit $n_i \tilde{\mu}_i \mu_{zi}/\mu_{ii} = n_z \tilde{\mu}_z \mu_{zr}/\mu_{iz}$; and the limit

$$n_z \tilde{\mu}_z \gg n_i \tilde{\mu}_i.$$

By setting the coefficients of N_i and N_z in Equation 2.8.9 equal, $n_i \tilde{\mu}_i \mu_{zi} / \mu_{ii} = n_z \tilde{\mu}_z \mu_{iz} / \mu_{iz}$, the ion heat conduction for this limit is found to be

$$\frac{q_{ir}}{P_i} = -\frac{n_i \tilde{\mu}_i}{e_i^2 B_{\theta}^2} \left[\frac{\mu_{zi}}{\mu_{ii}} \frac{1}{n_i} \frac{\partial P_i}{\partial r} + \frac{\mu_{zi}}{\mu_{ii}} \frac{\partial T_i}{\partial r} \right] - \frac{1}{e_i B_{\theta}} \frac{K_{\theta i} + K_{\theta z}}{\beta_i + \beta_z} \quad . \quad 2.8.11)$$

Thus, the sign of the effect of co-injection has changed in the transition from the mixed regime, Equation 2.7.6, to the collisionless regime. A co-injected beam increases the outward heat conduction in the mixed regime, or in the collisionless regime when the impurity viscosity is collisionless but small relative to the ion viscosity. A co-injected beam decreases the outward heat conduction when the impurity viscosity is comparable to the main ion viscosity. The effect of the pressure gradient, which was absent when the impurity viscosity was small, now combines with the temperature gradient in driving heat outward. In this limit, the toroidally driven heat flux is seen not to have an effect on the radial heat conduction.

The final case for the main ion heat conduction in the collisionless regime studied here is when the impurity viscosity dominates, $n_z \tilde{\mu}_z \gg n_i \tilde{\mu}_i$. In a tokamak, only light impurities can reach significantly into the collisionless

regime, so a concentration of $\alpha \sim 1$ is needed for this limit to be valid. Terms of $n_i \tilde{\mu}_i / n_z \tilde{\mu}_z = 1 / (\alpha^2 \sqrt{m_z / m_i}) \sim 1 / \sqrt{Z}$ will be ignored, as well as impurity terms involving the inverse charge state, $1/Z$. Using this limit, the ion heat conduction is approximately

$$\frac{q_{ir}}{P_i} \approx - \frac{n_i \tilde{\mu}_i}{e_i^2 B_p} \left[\frac{N_{zi}}{\mu_i} \frac{1}{n_i} \frac{\partial P_i}{\partial r} + \frac{N_{zi}}{\mu_i} \frac{\partial T_i}{\partial r} \right] - \frac{1}{e_i B_p} \frac{n_z \tilde{\mu}_z}{m_i n_i v_{iz}} \frac{N_{zz}}{\mu_{iz}} \times$$

$$\left[K_{\phi z} + \frac{n_z \tilde{\mu}_z}{m_i n_i v_{iz}} \frac{K_{\phi i} + K_{\phi z}}{\beta_i + \beta_z} - \frac{C_z}{a_i} k_{\phi i} \right] \quad . \quad 2.8.12)$$

The effect of the temperature and pressure gradients is unchanged from the comparable ion and impurity case, again both gradients driving heat conduction outward. As in the comparable ion and impurity case, co-injected momentum reduces the outward heat conduction. In this impurity dominated case, driving a co-directed, toroidal heat flux increases the outflow of heat. The opposite was true when the impurity viscosity was insignificant. The transition at which the externally driven heat flux has no effect occurs when $n_i \tilde{\mu}_i \mu_{iz} / \mu_i = n_z \tilde{\mu}_z \mu_{zz} / \mu_z$.

The total heat flux is the sum of heat conduction and heat convection. For an impurity-ion plasma, this total heat flux is

$$Q_r = q_{ir} + q_{rz} - T_i (Z-1) n_z v_{zr} \quad . \quad 2.8.13)$$

The impurity heat conduction has not been calculated since it is generally small, being proportional to $1/Z$. It is seen that ion temperature and pressure gradients from both conduction and convection add to drive heat radially outward. If a co-injected beam drives impurities outward, Z times that number of ions is driven inward, helping to contain the particle heat. When the impurity viscosity is comparable to or greater than the ion viscosity, $n_z \tilde{\rho}_z > n_i \tilde{\rho}_i$, a co-injected beam also aids in heat retention by reducing the heat conduction.

Summarizing the effect of a co-injected beam, in an impurity laden plasma with $n_z \tilde{\rho}_z \gg n_i \tilde{\rho}_i$, the beam drives impurities outward, as well as opposing the outflow of heat through both the heat conduction and convection. When the impurity viscosity is lower than the main ion viscosity, $n_z \tilde{\rho}_i > n_i \tilde{\rho}_z$, the beam still drives impurities outward. The effect on heat retention requires a detailed analysis of the plasma conditions, since it is possible to drive heat in either radial direction depending on the plasma condition.

2.9 Investigation of External Drag

Attention is now turned to the nature of the drags which were introduced into the previous formalism. First, it is noted that some portion of these drags may represent a radial transfer of momentum. The purposes of this section are: to present a general review of rotation experiments, as they apply to the total drag magnitude in particular; to review possible mechanisms for this drag; and, using these possible drag mechanisms, to estimate the ratio of impurity to main ion drag. As will be seen, none of the theories adequately explain the total drag magnitude observed. Flow reversal during co-injection of neutral beams has been observed, and, as was discussed in the preceding sections, the drag ratio $\beta_z / \beta_i = n_z m_z v_{dz} / n_i m_i v_{di}$ must be order unity for the theory to produce significant flow reversal. Given this, it is particularly important to discuss drag mechanisms which will lead to an order unity drag ratio ($\beta_z / \beta_i \sim 1$).

Toroidal rotation during neutral beam injection has been observed in many devices [31,37,39-42]. The overall confinement time of the momentum was found to be in the same range as the energy confinement time of electrons, due to anomalous transport, and ions, due to neoclassical, banana regime heat transport. The most detailed analysis of rotation was performed on data from PLT [37], and the

relevance of the PLT data will be discussed here as it relates to the plasma drag. Similar data from ISX-B has recently been published [41]. In general, the rotation data produced in other experimental devices is similar to the data produced in PLT.

There are three methods used to measure the toroidal flow velocity [39]: the measurement of the propagation velocity of sawtooth oscillations, the measurement of the charge-exchange neutral spectra, and the measurement of the Doppler shift of impurity spectral lines. The latter method was used in the PLT experiments [37], since it allowed measurements of the velocity at different radial locations, and is generally less ambiguous than the other measurements. Maximum rotation in PLT was measured at $\sim 10^5$ m/sec, and the accuracy of the method is $\sim \pm 1.5 \times 10^4$ m/sec.

An example of the time evolution of the central rotation is shown in Figure 2.9.1. As the injection begins, the plasma velocity increases on a time scale of 10 to 30 msec, only slightly slower than the ~ 15 msec rise time of the beam power. The plasma then reaches an asymptotic rotation which is maintained until the injector is turned off. The rotation velocity then decays to the before injection value. The drag can be calculated both from a force balance at the steady state rotation plateau and from the decay time of the rotation. The values calculated for the drag by both methods are similar, indicating that the

injection itself does not significantly enhance the drag mechanism.

In PLT, the increase in rotation velocity with momentum input is linear, indicating that the drag is not dependent on plasma velocity. The magnitude of the velocity, and therefore the drag, is also not direction dependent.

The radial velocity profile in PLT is parabolic, rather than following the profile of the momentum deposition, which is centrally peaked. This led researchers to conclude that momentum was lost from the plasma center by radial momentum diffusion. Modeling of the data led to an effective momentum diffusion coefficient of $(1-5) \times 10^4 \text{ cm}^2/\text{sec}$, and, for typical cases, this value was roughly constant over the plasma radius. This is one to two orders of magnitude larger than predicted by neoclassical theory for the perpendicular viscosity [43]. As mentioned above, the momentum diffusion rate is roughly the same order as the particle and heat diffusion rates, the overall momentum confinement time being ~ 25 msec, corresponding to a drag frequency of $\sim 40/\text{sec}$. Lack of sufficient operational variance made it impossible for the researchers to produce any momentum confinement time scaling laws [37]. Momentum which has diffused to the edge must finally be removed from the plasma by some other mechanism.

In current experiments, the final momentum removal

mechanism is generally thought to be charge exchange. Neutral particles from near the plasma wall diffuse into the plasma, and undergo a charge exchange reaction, the neutral particle becoming an ion and the ion becoming a neutral. Since the neutral particles from the edge have no net momentum, this exchanges a plasma particle with net momentum for one without, the newly created neutral often escaping the plasma to the wall. Another possible edge drag source field ripple, which is discussed below.

In the previous sections, the external drag on each particle species was used. It is necessary here to show that the effect of external drag is equivalent to the effect of momentum diffusion in the calculations that were presented. At the simplest level, momentum diffusion is a drag on particles on a flux surface by particles on a nearby, "external", flux surfaces. In the large aspect ratio limit, the toroidal momentum balance is

$$m_i n_i \langle R^2 \nabla \phi \cdot \frac{\partial \vec{V}_i}{\partial t} \rangle = \langle R^2 \nabla \phi \cdot \vec{K}_i \rangle - \langle R^2 \nabla \phi \cdot m_i n_i v_{di} \vec{V}_i \rangle$$

, 2.9.1)

$$- m_i n_i \langle R^2 \nabla \phi \cdot \frac{1}{r} \frac{\partial}{\partial r} r \eta_L \frac{\partial V_\phi}{\partial r} \rangle + \langle R^2 \nabla \phi \cdot \vec{R}_i \rangle$$

where η_L is the momentum diffusion coefficient in units of m^2/sec . This momentum diffusion term is simply the toroidal component of the divergence of the stress tensor, $\langle R^2 \nabla \phi \cdot \nabla \cdot \vec{\Pi}_i \rangle$. The stress tensor itself is the friction

between neighboring surfaces, expressed here as the viscosity times the velocity gradient. This differential equation can evidently be solved with boundary constraints. The velocity profile can then be treated in the same manner as the density or temperature profiles. The equivalent external drag can be defined,

$$\gamma_{q_i}^{\text{equivalent}} = \frac{-\langle R^2 \nabla \phi \cdot \frac{1}{r} \frac{\partial}{\partial r} r n_{\perp} \frac{\partial V_{\phi}}{\partial r} \rangle}{\langle R^2 \nabla \phi \cdot \vec{V}_i \rangle} \sim n_{\perp} / a^2 \quad . \quad 2.9.2)$$

This definition allows the equations derived in the previous sections to be used to represent both momentum diffusion and true external drag mechanisms such as charge exchange. Seen in this light, the momentum diffusion and true external drag mechanisms are additive.

Three conceptual mechanisms for external drag and momentum diffusion are discussed here. The first of these, true external drag, must transfer momentum directly out of the plasma. The other two are diffusive mechanisms. As the terms are used in the literature, convective mechanisms refer to a property carried on a net flux of particles, and conductive mechanisms refer to the transport of a property without a net movement of particles.

The most obvious drag mechanism is collisions with the wall, limiter, or background neutral gas [42]. The wall

and limiter drag is evidently localized at the edge of the plasma. From observations in PLT, the neutral density at the center of the plasma is insufficient to explain the observed drag [37]. At the edge of the plasma, where the neutral density is much higher, charge exchange is a significant mechanism. In PLT, charge exchange is sufficient to maintain a near zero plasma rotation at the limiter. Near the plasma edge, the neutral density is $\sim 10^{10}/\text{m}^3$, leading to a charge-exchange drag frequency of $\sim 300/\text{sec}$ for a 10 eV edge temperature. This is sufficient to remove the diffused momentum from the plasma.

The only other true drag mechanism, known to this author, is due to the field asymmetries, usually magnetic ripple [44]. The plasma is alternately compressed and expanded as it moves through the ripple wells, transferring the directed energy to heat and the momentum to torque on the field coils. With a velocity of $\sim 10^5 \text{ m/sec}$ in PLT, a compression-expansion phase lasts in the range of 10^{-5} sec . The ion collision rate is approximately $10^3/\text{sec}$, so few collisions occur during compression, and little momentum is lost. In general, the collision rate is so low that ripple makes an insignificant contribution to the total drag. This direct ripple drag is separate from convective momentum losses through ripple diffusion.

Before continuing with the momentum diffusion mechanisms, it is necessary to eliminate momentum loss

through the electron channel as a factor. Since a current is always present in a tokamak, the electron velocity is always counter directed and large. If the ion momentum were transmitted through this channel, the total drag would be direction dependent. This direction dependence is not observed in experiment, and the electron drag channel can be ignored.

Outward convection alone cannot slow central rotation. Convection only reduces momentum at the center by reducing the number of particles at the center, not changing the momentum per particle. Possible particle transport mechanisms which can transport momentum are plentiful. Neoclassical [45], ripple induced [44,45], drift wave [46-48], and turbulent [49] mechanisms can all convect momentum, and data from PLT indicates that the momentum diffusion is about the same magnitude as particle and heat diffusion. In ISX-B shots, the particle diffusion is generally inward, which obviously does not convect momentum outward. Experiments on ISX-B with half of the TF coils turned off do indicate that ripple induced convection is responsible for the enhanced momentum diffusion seen in that experiment [50]. With this large magnetic ripple, particle confinement time as well as momentum and heat confinement time are greatly reduced. Ripple convection of momentum is too small to account for the momentum confinement times in both PLT and ISX-B when all coils are operational.

Since net particle transport does not seem to be totally responsible for the drag, conduction would seem to be a prime contributor. As with heat conduction, it was suspected that long mean free path effects would cause banana regime momentum transport. Neoclassical theory has indicated that momentum conduction remains in the Pfirsch-Schlueter regime regardless of the collisionality [43]. Experience in PLT showed that Pfirsch-Schlueter scaled conduction was too small to account for the observed drag by at least an order of magnitude. No other conductive mechanisms have been proposed to the knowledge of this author.

Now that the physical mechanisms for drag have been examined, this information is used to investigate the drag ratio β_z/β_c which is important in the theory. For viscous drag, it is assumed that the drag ratio scales as the known neoclassical drag although the magnitude is clearly larger than neoclassical,

$$\frac{\beta_z}{\beta_c} = \frac{\nu_{dz}}{\nu_{dc}} \frac{\nu_{iz}}{\nu_{ic}} \sim \frac{\nu_{dz}}{\nu_{di} + \nu_{iz}} \frac{\nu_{iz}}{\nu_{ic}} \sim \frac{\kappa^2}{1+\kappa} \sqrt{\frac{m_z}{m_i}} \quad , \quad 2.9.3)$$

which is of order unity for the small concentrations of tungsten found in the PLT flow reversal experiments.

In charge exchange, a hydrogen ion with an average

toroidal momentum is replaced by a newly ionized hydrogen ion with no average toroidal momentum. This ion can not be considered part of the bulk ion distribution until it has been accelerated to the average speed of the plasma. Both hydrogen and impurity species will collide with this new ion, distributing the drag among the species present.

A problem analogous to the charge exchange neutral drag problem presented above is found in Krall and Trivelpiece [52]. A cold test particle with a velocity relative to a two component plasma is brought to the velocity of the bulk plasma. When the rotation velocity is slower than the thermal velocities of both the impurity and main ion, the ratio of the drags becomes

$$\frac{\beta_z}{\beta_i} = \frac{\kappa}{2} \left(\frac{m_z}{m_i} \right)^{3/2} \quad 2.9.4)$$

Even though this is extreme, it is evident that the ratio β_z/β_i can be large for small concentrations of impurities. When the rotation velocity is three times the thermal velocity, the ratio can still be of order unity for heavy impurities ions,

$$\frac{\beta_z}{\beta_i} \sim \frac{3\sqrt{\pi}}{8} \frac{\left(\frac{m}{2kT}\right)^{3/2}}{V_{ii}^3} \sim \frac{\kappa}{2} \left(\frac{m_z}{m_i}\right)^{3/2} \quad (2.9.5)$$

Although a fluid limit is taken in this thesis, momentum transported by convection or conduction may be carried by a portion of the distribution that is colder or hotter than the mean. Since the relative net velocity is small, cool particles will preferentially transfer momentum to the impurities, and particles hotter than the mean will transfer the momentum preferentially to the main ions. When the transporting particles are approximately the same temperature as the temperature of the local particles, the ratio of β_z/β_i is

$$\frac{\beta_z}{\beta_i} = \frac{m_z n_z v_{zx}}{m_i n_i v_{ix}} \sim \alpha \sqrt{\frac{m_x}{m_i}} \quad (2.9.6)$$

This is $\propto \alpha$ for momentum transported by ions and $\propto \sqrt{m_x/m_i}$ for momentum transported by the heavier impurities.

CHAPTER III

INTERPRETATION OF PLT EXPERIMENTS

3.1 Introduction

The theory of the previous chapter is now applied to interpret experimental observations. Detailed experimental data of impurity flow during co- and counter- beam injection is available for the Princeton Large Torus (PLT) [29]. The first objective is to determine if the observed effects of neutral beam injection can be accounted for by the theory. The second objective is then to adjust the numerical coefficients in the theory to agree quantitatively with the experiment, thus obtaining a predictive model which will subsequently be applied to future experiments and reactors.

The first step in approaching this problem is to collect the pertinent plasma parameters for the experiment. Not all information can be recorded for each shot, and some relevant parameters must be extrapolated or assumed from other information. Experimental error and shot reproducibility must also be taken into account. Section 3.2 covers the development of the background data used to model the experiment from the available information on this series of experiments.

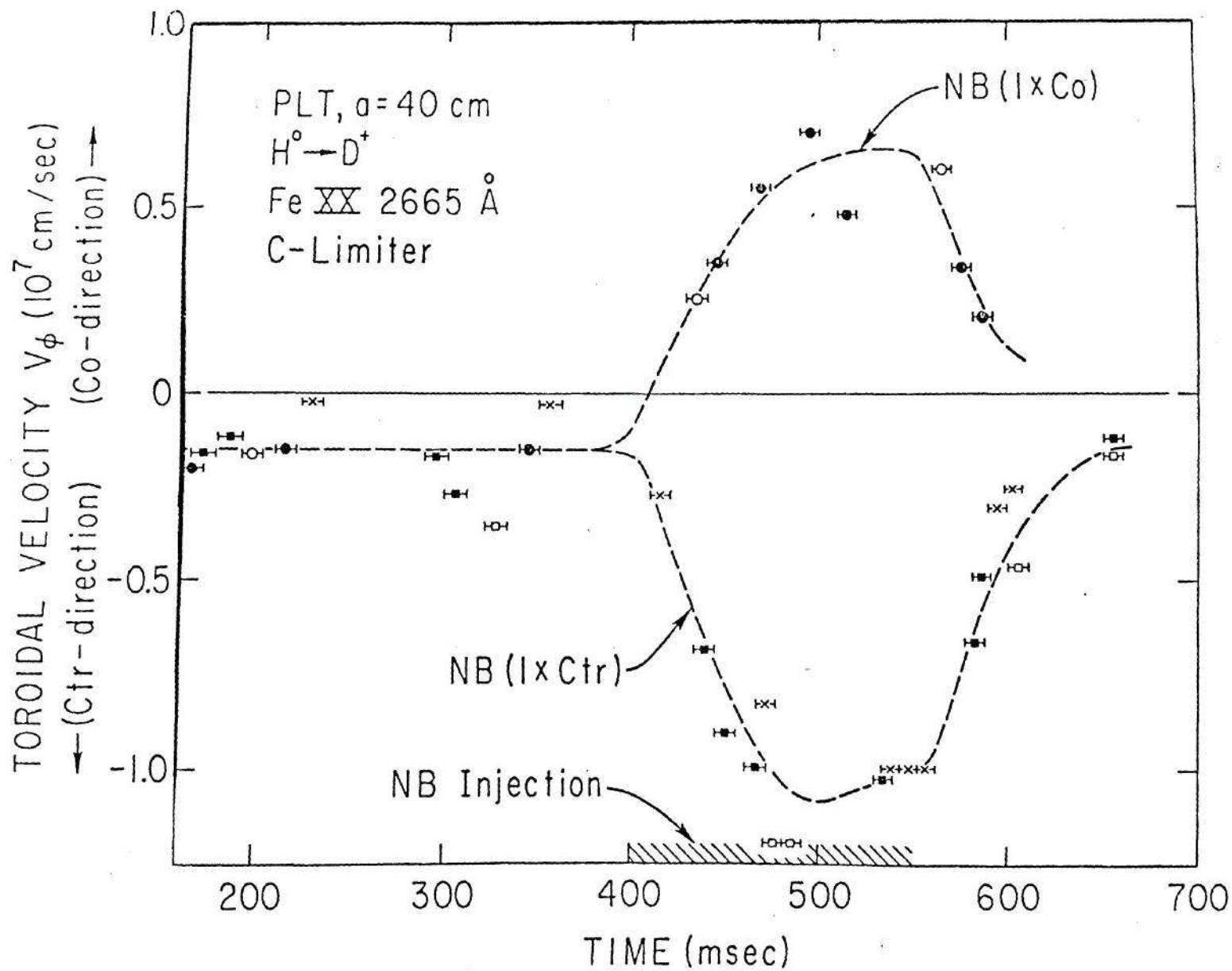


Figure 2.9.1 Central Toroidal Rotation Velocity in PLT with Neutral Beam Injection
 Co-injected Beam 400 kWatt; Counter-injected Beam 500 kWatt;
 Injection from 400 to 550 msec, from Reference 36

The part of the radial impurity transport theory developed in Chapter 2 which is pertinent to the PLT experiments consists of two separate effects, transport driven by gradients and transport driven by external momentum sources. Asymmetric particle and heat sources are not important away from the plasma edge region, and will not be treated here. By analyzing the experimental data before injection begins, the gradient driven portion of the theory can be compared with experiment without the added effect of the beam. The analysis before-injection is presented in Section 3.3. The portion of the model dependent on the co-injected beam is developed in Section 3.4. When the beam is injected, the effect of the gradients is still important, and the validity of the gradient driven portion of the model when the beam is injected is addressed in this and subsequent sections. The model is checked against the counter-injected beam impurity profile data in Section 3.5. Using an impurity transport code, the model is evaluated by comparing the calculated impurity profiles to the measured values in Section 3.6. Burrell et al [25] produced an impurity transport theory based on inertial effects, the $n_e m_e (\vec{V}_e \cdot \nabla) \vec{V}_e$ term in Equation 2.2.3. This inertial theory is compared with the experiment in Section 3.7. A brief discussion of analyses of the impurity flow during beam injection in ISX-B performed by Sigmar and Howe [53,54] and later by Crume [31] is given in Section 3.8. A summary of

the "benchmarked" model, which has been adjusted to quantitatively reproduce the PLT results, is given in Section 3.9.

3.2 PLT Experimental Data

Eames [29] carried out measurements of tungsten impurity fluxes in PLT deuterium discharges in which neutral beams injection took place from 250-350 msec. He measured chordal distributions of ultra-soft X-rays. This X-ray data was Abel inverted to obtain radial tungsten density profiles as a function of time. He then calculated the tungsten fluxes from the rate of change of the tungsten density. The radiation is proportional to both the tungsten density and the electron density, so that any error in the electron density produces the opposite error in the tungsten density and fluxes. Eames used the radiation coefficient from Reference 54, which is insensitive to the electron temperature in this temperature range. The data was taken over the inner 20 cm. of plasma, which is 40 cm. in total radius. Two experiments were analyzed in detail, a co-injected experiment with 585 kW of beam power, and a counter-injected experiment with 430 kW of beam power.

Since the purpose of this analysis is to determine if the theoretical prediction of the effect of the neutral beam injection on the impurity fluxes is consistent with the experiment, the experimentally determined density and

temperature profiles are used in the analysis in order to minimize extraneous effects.

The electron density profile, reproduced in Figure 3.2.1, was taken from previous work [55], and was assumed to be constant in time and identical in both the co- and counter- injection cases. Since the impurity concentration was low, the deuterium density distribution was assumed to be the same as that of the electron density. The deuterium and tungsten density data used in this analysis is given in Table 3.2.1. It was necessary to extrapolate from the deuterium densities at 15 and 20 cm. in order to estimate the deuterium density at 25 cm.

The electron temperature profiles during the appropriate time range were measured for both the co- and counter- injection cases, and are reproduced here as Figures 3.2.2 and 3.2.3 [29]. Eames showed that the tungsten was in coronal equilibrium. Coronal equilibrium is a collisional equilibrium state, in which the electron ionization rate balances the recombination rate. This approximation is valid when the radial mean free path of the impurity ion is short enough that the ion cannot move out of the local electron temperature region faster than the ionization and recombination rates can adjust its average charge state. The average charge state for an impurity species in coronal equilibrium is dependent only on the local electron temperature. The variation of the average tungsten charge

state with electron temperature is shown in Figure 3.2.4. Thus, the coronal equilibrium model and the measured electron temperature distributions are used to determine effective values of the tungsten charge state, Z , to use in the transport calculation of the tungsten fluxes at different locations and at different times during the discharge.

The ion temperature was not measured for this series of experiments. Hence, it was necessary to extrapolate the ion temperature profile from limited data. Figure 3.2.5 [56] gives the total increase in central ion temperature per unit beam power in PLT. Using this data, the ion temperature is calculated to rise 900 eV in the 585 kWatt, co-injected case and 650 eV in the 430 kWatt, counter-injected case.

With a starting temperature, the above estimate gives a value for the peak, steady state ion temperature. However, the beam has just been turned on. The temperature rise time is reported to be the same as the combined beam power rise and fast particle thermalization times [56],

$$\frac{1}{\tau_{\text{rise}}} = \frac{1}{\tau_{\text{beam rise}}} + \frac{1}{\tau_{\text{fast ion slowing}}} \approx \frac{1}{30 \text{ msec}} \quad . \quad 3.2.1)$$

The temperature is assumed to approach the peak temperature

by a decaying exponential with this rise time. The peak temperature at any time is interpolated,

$$T_i(t) = [T_i(t=\infty) - T_i(t=250)] (1 - e^{-t/\tau_{rise}}) + T_i(t=250) \quad . \quad 3.2.2)$$

Typical before and during injection ion temperature profiles are given in Figure 3.2.6 [56]. These profiles were based on calculation and correlated well with the two measured points for each curve. The final ion temperature presented in Table 3.2.1 is based on extrapolation between those two curves and the projected peak temperature at each time.

In addition to the profiles mentioned above, typical profiles [57] of the safety factor were used in evaluating the local impurity transport flux. The safety factor is given in Table 3.2.1.

The beam momentum deposition was calculated using the beam section of the PROCTR [58] code, which was based on earlier Fokker-Planck theory [59]. This code calculates the momentum deposition in two steps. First, the actual deposition profile is calculated, and then the momentum is split between the species present and losses.

First, in calculating the momentum deposition profile, the neutral beam attenuation, N_B , along the path, s , is

calculated by

$$N_B(s) = N_E(0) \exp \left\{ - \int_{-\infty}^s \langle \sigma v \rangle_{\text{total}}(s') n_e(s') ds' \right\} \quad . \quad 3.2.3)$$

This total cross section includes electron and ion impact ionization and charge exchange,

$$\langle \sigma v \rangle_{\text{total}} = \frac{n_i}{n_e} \left(\langle \sigma v \rangle_{\text{ex}} + Z_{\text{eff}} \langle \sigma v \rangle_{\text{ii}} \right) + \langle \sigma v \rangle_{\text{ie}} \quad , \quad 3.2.4)$$

where Z_{eff} is a correction to include the impact ionization on impurities as well as ions. Once the fast ions are born, the ions go into tokamak orbits which are determined by the injection geometry. This process is treated in detail in Reference [59] for tangential injection. The particle deposition profile is then calculated by taking the flux surface average over these fast ion orbits.

Next, the code calculates the split in momentum deposition among the particles present. In this calculation, it is assumed that the fast ion which is slowing down remains very near to a given flux surface, the usual "small banana width" approximation. For example, the momentum to all ions, including impurities, is

$$X_i \equiv \frac{1}{v_0} \int_0^{v_0} dv \frac{v_c^3}{v^3 + v_c^3} \left[1 - \frac{m_i \langle z \rangle}{m_e [Z]} \right] P_{cx}(v) b(v) \quad , \quad 3.2.5)$$

where v_0 is the initial velocity of the fast ion, m_i is the ion mass, m_e is the beam ion mass, and v_c is called the critical velocity,

$$v_c = \left(\frac{3\sqrt{\pi}}{4} \right)^{1/3} \left(\frac{m_f}{m_p} \right)^{1/6} \left(\frac{m_f}{m_i} \right)^{1/3} [Z]^{1/3} \sqrt{\frac{2kT}{m_f}} \quad . \quad 3.2.6)$$

Above this critical velocity, the fast ion slows down predominantly on the electrons, and below this velocity the fast ion slows down predominantly on the plasma ions. $P_{cx}(v)$ is a fractional loss of momentum due to loss of fast particles through charge exchange, and $b(v)$ is

$$b(v) = \left[\frac{v_0^3 + v_c^3}{v^3 + v_c^3} \frac{v^3}{v_0^3} \right] \frac{m_i \langle z \rangle}{3 m_f [Z]} \quad . \quad 3.2.7)$$

The other terms are the effective charge state for scattering,

$$Z_{eff} = \langle Z \rangle = \frac{\sum_R n_R Z_R^2}{\sum_R n_R Z_R} \quad , \quad 3.2.8)$$

and the effective charge for momentum coupling,

$$[Z] = \frac{\sum_R \frac{m_{proton}}{m_R} n_R Z_R^2}{\sum_R n_R Z_R} \quad . \quad 3.2.9)$$

The momentum to any ion species is calculated in a similar manner. When $m_z \gg m_i$ and the impurity concentration, α , is low, the corresponding critical velocity between the main ion and impurity is low. Thus, the momentum to the impurity species is

$$K_z \approx K_{i\ total} \frac{\alpha}{\frac{m_p}{m_i} + 1 + \alpha} \quad . \quad 3.2.10)$$

The total momentum deposition profile in PLT is shown in Figure 3.2.7 for the time $t = 250$ msec., when injection had just begun.

Some of the beam injected momentum is initially transmitted to the electrons. this momentum is very rapidly transferred to the main ion and impurity species, since the

electron-ion collision frequency is very large.

TABLE 3.2.1 PLT Experimental Data

Machine						
Major Radius	1.3 m					
Minor Radius	.4 m					
Toroidal Field	3.2 T					
Radially Varying Data						
Radius (cm)	0	5	10	15	20	25
Density ($1/m^3$) ($\times 10^{19}$)	5.2	5.0	4.7	4.3	4.0	3.6
Safety Factor	1.0	1.2	1.4	1.8	2.2	-
Electron Temp (keV)						
CO-240	-	0.88	0.85	0.77	0.68	-
CO-280	-	1.10	1.05	0.96	0.84	-
CO-300	-	1.18	1.13	1.03	0.90	-
CN-280	-	0.73	0.85	0.85	0.70	-
CN-300	-	0.73	0.80	0.80	0.65	-
Tungsten Charge State						
CO-240	-	25.0	24.5	23.0	22.0	-
CO-260	-	27.5	26.0	25.5	24.5	-
CO-300	-	28.5	27.5	26.0	25.0	-
CN-280	-	22.5	24.5	24.5	22.0	-
CN-300	-	22.5	23.5	23.5	21.0	-
Ion Temp (keV)						
CO-240	1.10	1.07	0.90	0.75	0.60	0.45
CO-280	1.65	1.60	1.35	1.03	0.70	0.50
CO-300	1.80	1.73	1.41	1.11	0.73	0.50
CN-280	1.41	1.36	1.15	0.91	0.67	0.47
CN-300	1.63	1.59	1.34	1.01	0.70	0.50
Impurity Density ($1/m^3$) ($\times 10^{16}$)						
CO-240	-	1.10	1.03	1.00	1.13	-
CO-260	-	1.40	1.17	1.00	1.13	-
CO-280	-	1.35	1.22	1.10	1.12	-
CO-300	-	1.20	1.20	1.18	1.24	-
CN-240	-	1.10	0.95	0.70	0.65	-
CN-260	-	1.10	0.95	0.80	0.84	-
CN-280	-	3.10	2.10	1.20	1.04	-
CN-300	-	6.20	4.30	2.20	1.50	-

Key

CO - Co-injected experiment
 CN - Counter-injected experiment
 CO-XXX Co-experiment at time t=XXXmsec.

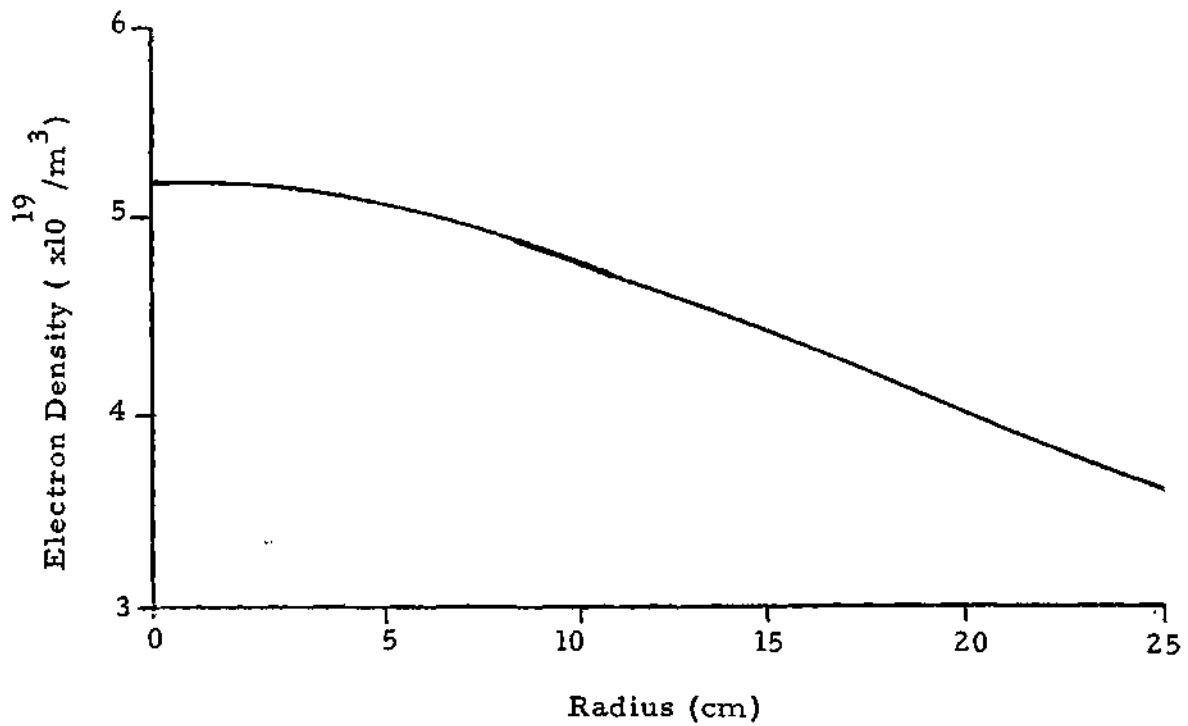


Figure 3.2.1 Electron Density Profile in the Center of PLT During Flow Reversal Experiments

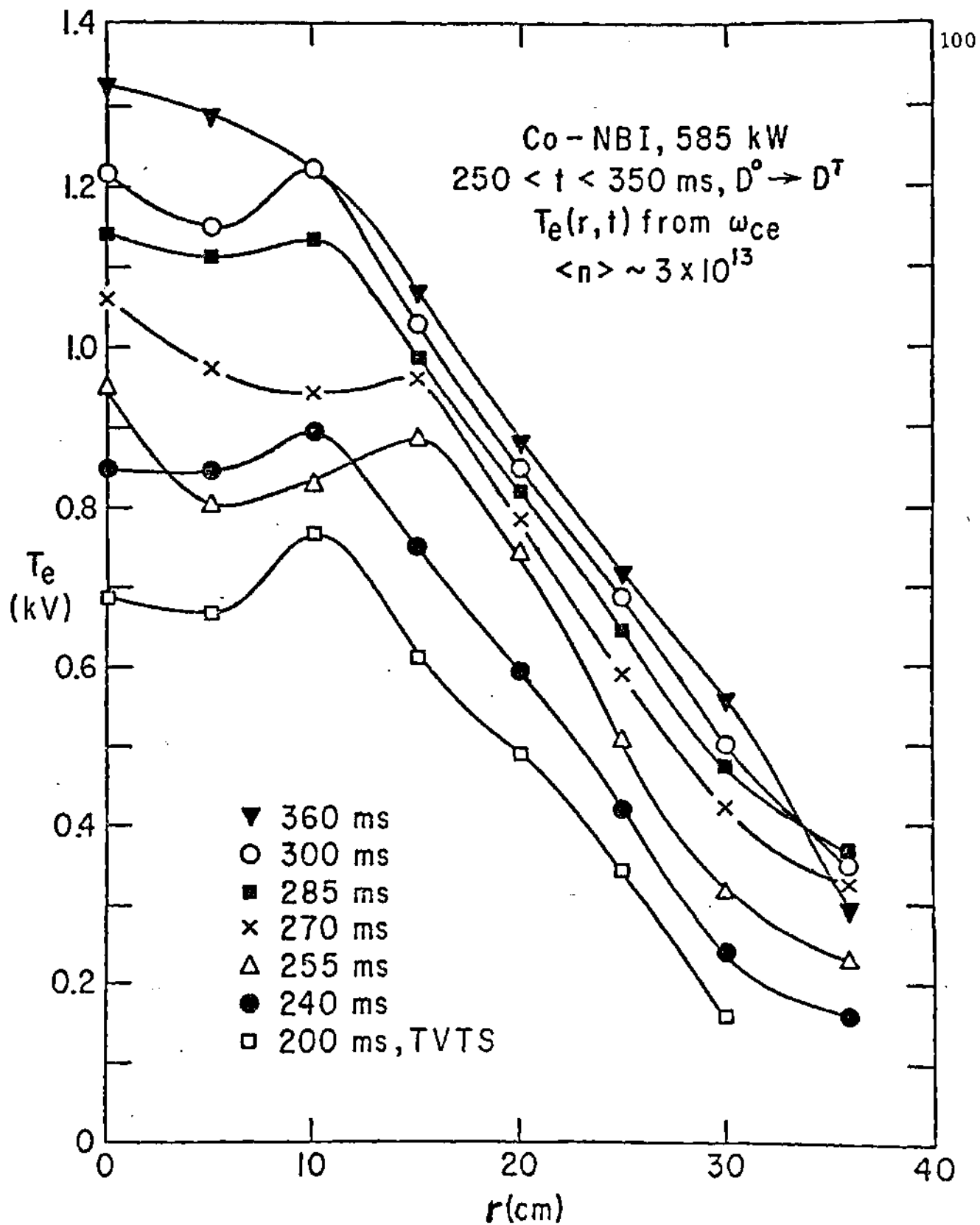


Figure 3.2.2 Electron Temperature Profiles in PLT During the Co-injected Flow Reversal Experiment, from Reference 34
 585 kWatt of Co-injected Beam from $t=250$ to $t=350$ msec

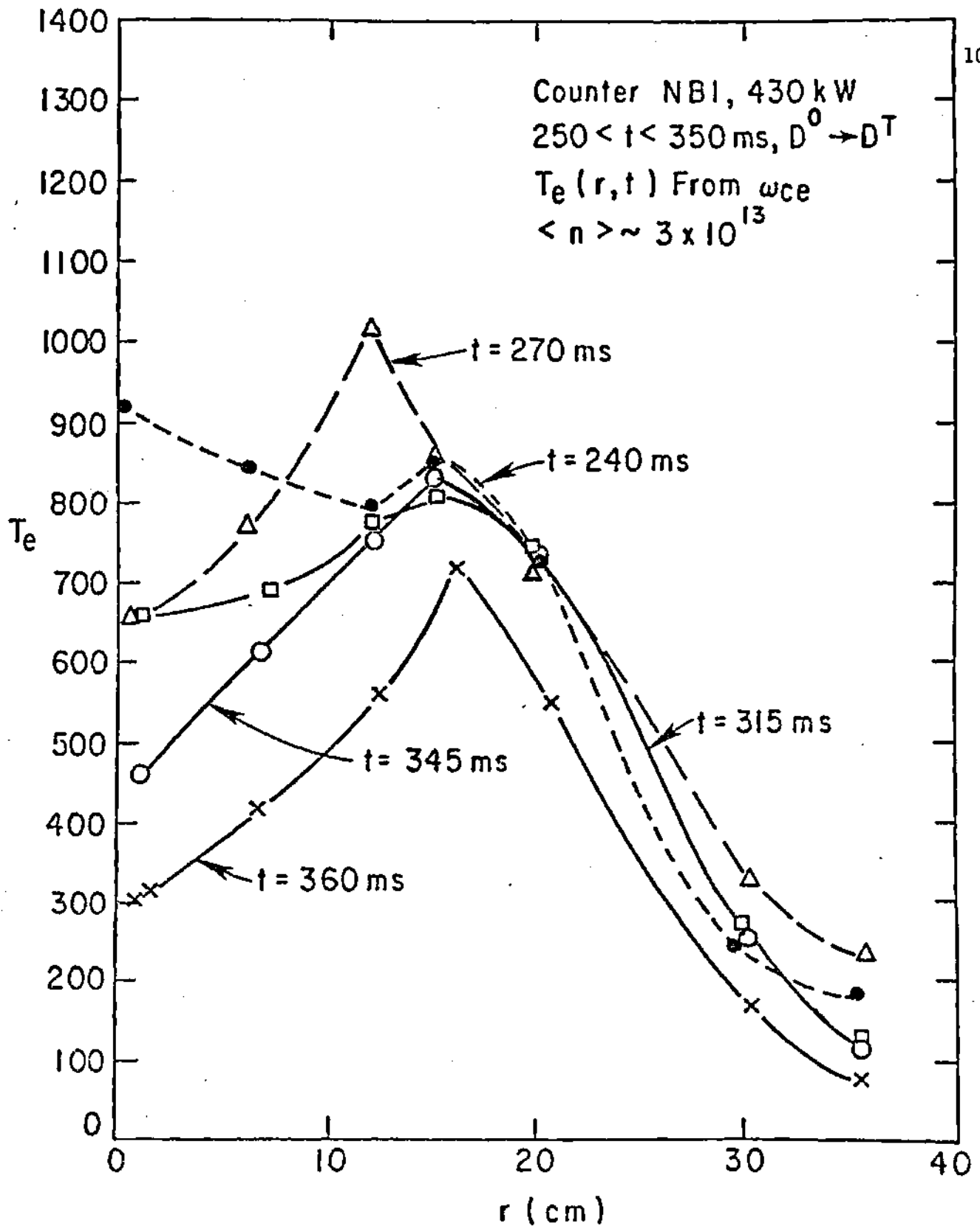


Figure 3.2.3 Electron Temperature Profiles in PLT During the Counter-injected Flow Reversal Experiment, from Reference 34
 430 kWatt of Counter-injected Beam from $t=250$ to $t=350$ msec.

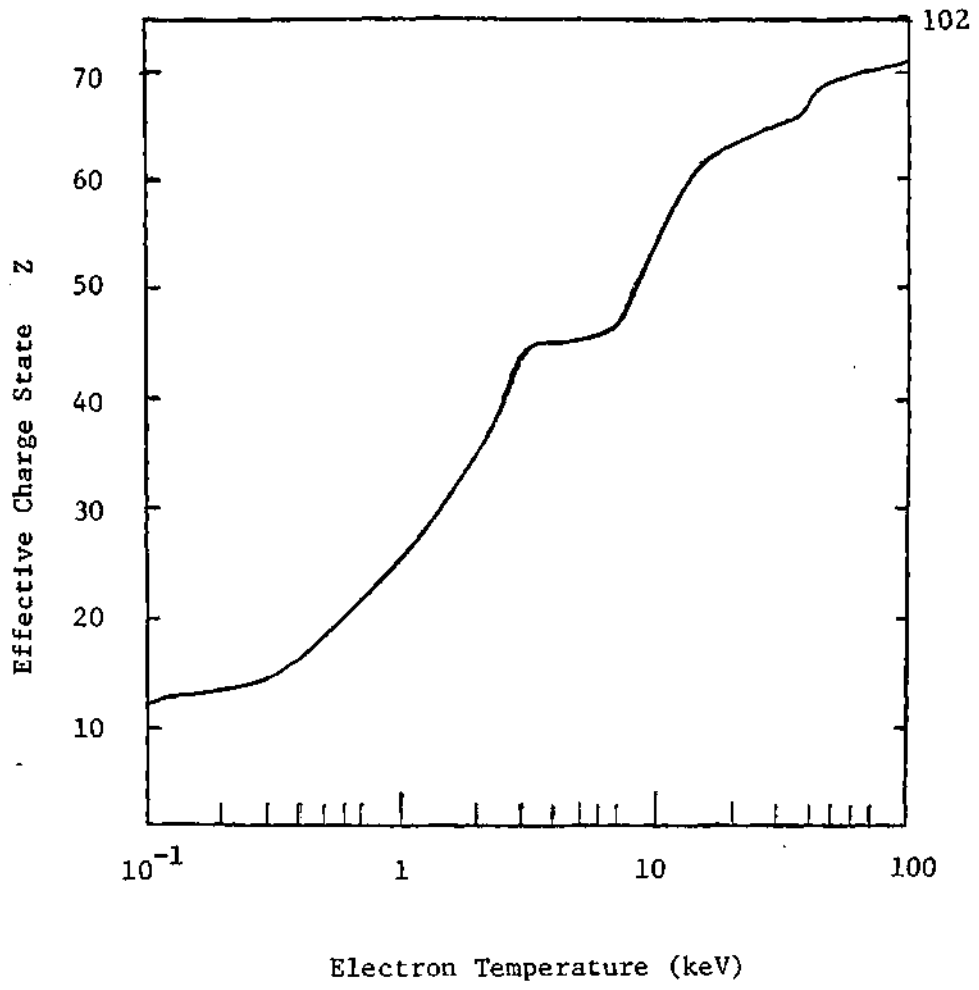


Figure 3.2.4: Coronal Equilibrium Charge State Variance
with Electron Temperature for Tungsten, Z=74, A=184
From Reference 56

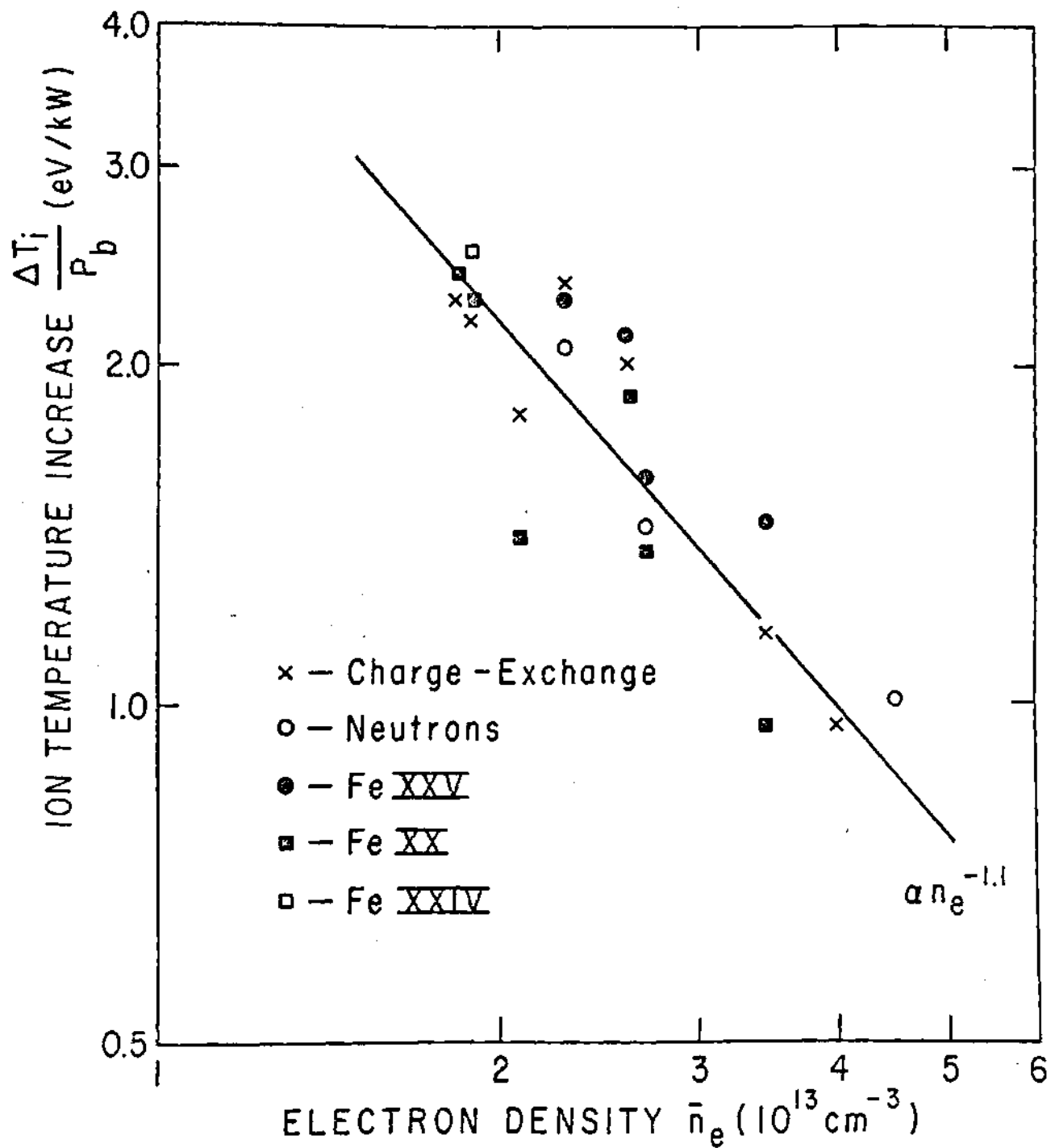


Figure 3.2.5
 Scaling of ion temperature measurements vs. line average electron density. from Reference 57

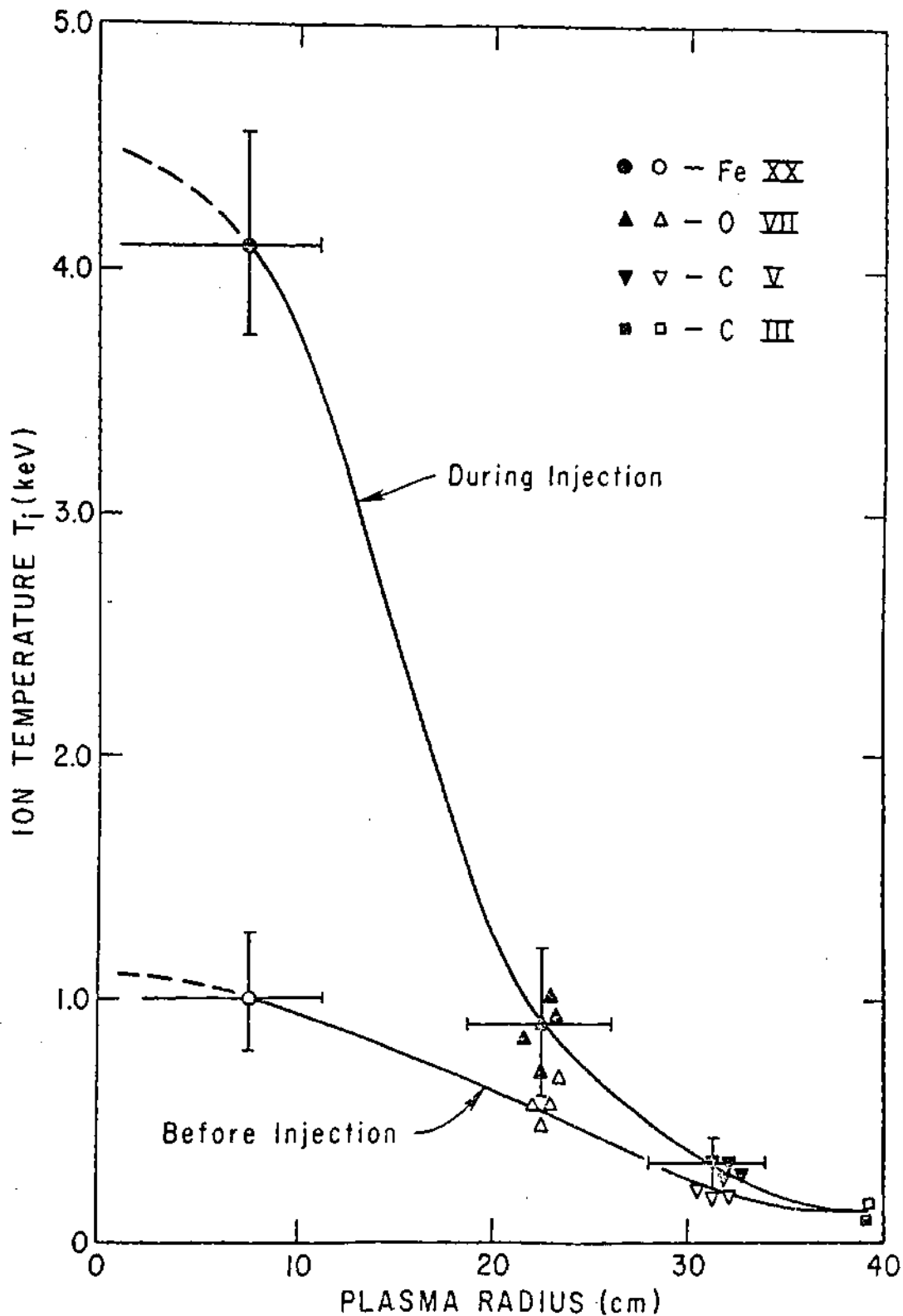


Figure 3.2.6

Radial profile of ion temperature before and during neutral beam injection ($H^0 \rightarrow D^+$; $P \approx 1.6$ MW) from Doppler broadening of Fe XX 2665 Å, OVII 1623 Å, CV 2271 Å and CIII 2237 Å lines. From Reference 57

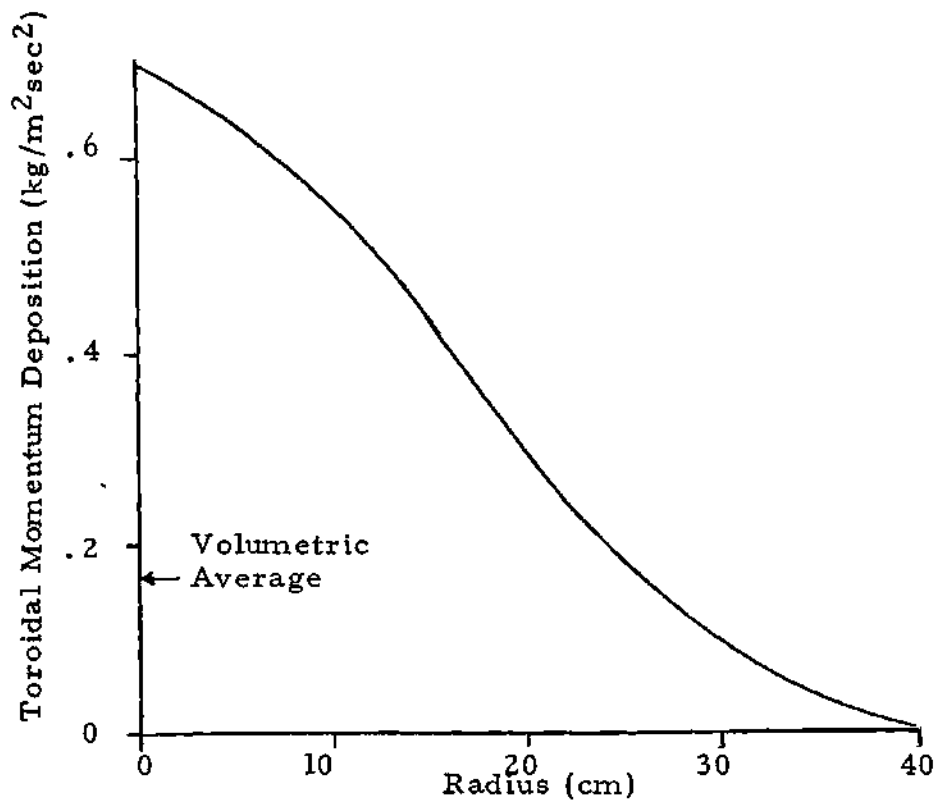


Figure 3.2.7 PLT Momentum Input Profile at the Beginning of Injection, $t=250$ msec.

Beam Current 10.5 amp @ 40 keV
 5.2 Amp @ 20 keV
 5.2 Amp @ 13.3 keV

Beam Power = 585 kWatt

3.3 Analysis of the Experiment Before Beam Injection

The gradient driven flux component of Equation 2.7.3 is used in this section to interpret the experimental data taken prior to beam injection. The co-injection case is studied here, although the counter-injection case is virtually the same before injection. Figure 3.3.1 shows the experimental fluxes (dashed lines), and the theoretical fluxes (solid lines). Fractional values of the experimental fluxes are also shown. The theoretical expression for the impurity flux in the absence of beam injection is, from Equation 2.7.3,

$$\langle n_z V_z \rangle_r = \frac{2g^2 m_i n_i v_{Te}}{e^2 E_0^2 Z} \left[C_1 \left(\frac{1}{n_i} \frac{\partial n_i}{\partial r} - \frac{1}{n_z} \frac{\partial n_z}{\partial r} \right) + (C_1 - C_2) \frac{Z-1}{Z} \frac{\partial T_e}{\partial r} \right] \quad , \quad 3.3.1$$

where the drag ratio, β , is neglected since it is small relative to unity. The constants C_1 , C_2 are calculated from the fits [38] of Equations 2.3.9a-e. The collisionality factor, σ , is large ($\sigma \gg 1$) when the main ions are collisionless, and very small ($\sigma \ll 1$) when the main ions are collisional. The collisional limits for these values were calculated earlier by Rutherford [5]. Since the ions are collisionless, the limit for C_1 and C_2 in which dominates can be used, producing $C_1 = 1.0$ and $C_2 = 1.5$. The factor ($C_1 - C_2$) is negative, so that a typically negative

temperature gradient drives the impurities outward, opposing the inward driving effect of a typically negative main ion density gradient. This is known as temperature screening. These mixed regime values of the coefficients C_1 and C_2 produce the curve labeled mixed, which shows that the temperature screening effect is dominant in the calculation, causing the impurities to flow outward, which clearly does not match the experimentally observed inward impurity fluxes. It is noted that Howe and Sigmar [53] using the same model also predicted large temperature screening effects in ISX-B, which also were contrary to the experimental evidence. These results indicate that the collisional ion expressions of Rutherford [5] should be tried. The Rutherford expressions are obtained by setting $\sigma=0$ in the equations for C_1 and C_2 , Equations 2.3.9a and b.

The fluxes calculated using the Rutherford values of C_1 and C_2 predict inward impurity fluxes that are in reasonable agreement with the experimental results. The magnitude of the observed fluxes are underpredicted by about a factor of two. The predicted fluxes using the Rutherford values of C_1 and C_2 are shown by the curve labeled collisional.

Several variations of the model parameters were investigated to see if the mixed regime values of C_1 and C_2 could lead to a prediction of the inward impurity fluxes observed. In all of the cases studied, the predicted fluxes

based upon a mixed regime calculation of C_1 and C_2 never showed a significant correlation to the experiment. The calculation of the C_n are based on idealized deviations of the particle distributions from thermal equilibrium. Since the mixed regime calculations are based on a greater deviation from Maxwellian distributions than the collisional, Rutherford values, it is suggested here that perhaps a less anisotropic view of the distributions or their effects on the impurity species is appropriate. The Rutherford values ($\sigma=0$) will be used hereafter in this work.

Not all quantities used in the above analysis were measured in this experiment. The ion temperature and safety factor profiles were taken from other data, and hence are more likely to introduce error into the analysis. Since the sensitivity analysis of theory and experiment represent different problems, they will be addressed separately. Further justification for the choice of collisionally calculated friction coefficients C_1 and C_2 will be made after the beam driven portions of the experiment are analyzed.

The electron temperature, electron density and impurity density were measured throughout the 60 msec. period (240-300msec.) of interest in the experiment. The electron temperature affects the impurity fluxes only through the impurity charge state, $\Gamma_{z_{\text{rad}}} \propto Z$. Figure 3.2.3

shows that in the range of 1 keV, a 10 % electron temperature change results in less than a 10 % change in the average charge state and therefore less than a 10 % change in the impurity flux.

The measurement of the electron and impurity densities is related since the observed impurity radiation is proportional to the electron density and impurity density, $P_{\text{rad}} \propto n_e n_z$. The impurity flux is proportional to both the ion density and the impurity density, $\Gamma_{zq\text{rad}} \propto n_i n_z$. Since the electron density is approximately equal to the deuterium density, the error in the calculated gradient driven flux is approximately the same as the error in the measured radiation power, probably in the range of 10 to 20 %.

Two important parameters were taken from data from other PLT experiments, the safety factor and ion temperature profiles. The safety factor, $q = rB_\phi / R_0 B_p$, will not change rapidly during this phase of the experiment, so any differences associated with these values will be consistent at all times in the analysis. If the safety factor is greatly in error, the numerical factor difference between the theory and experiment will change somewhat, but the trends seen and the conclusions drawn from the analysis will not change. The ion temperature is not accurately known, but the magnitude of the flux scales as $\Gamma_{zq\text{rad}} \propto 1/\sqrt{T}$; a 50 % inaccuracy in the ion temperature would make only a 20 %

difference in the resulting flux.

The gradients of both the ion density and the ion temperature also contribute linearly to the fluxes, the fluxes scaling both as $\Gamma_{z,rad} \propto 1/n \, dn/dr = d \ln n/dr$ and $\Gamma_{z,rad} \propto 1/T \, dT/dr = d \ln T/dr$. These gradients are dependant mainly on the slope of the quantity, and not the magnitude of the quantity. Therefore, errors which consistently overestimate or underestimate the quantity will not change the conclusions.

Calculating [29] the impurity fluxes from the measured X-ray radiation involved: Abel inversion of the line integrated radiation profiles; relating the absolute radiation intensity and the electron density to the impurity concentration; and calculating the fluxes from the rate of change of impurity concentration. Both the first and last steps require taking numerical differences, which greatly enhances the possible error. The best evaluation of the accuracy of the measured fluxes is the consistency of the values. The impurity fluxes were calculated at four radial locations at three steps in time for both the co- and counter-injection experiments. This gives a total of 24 calculated values. As can be seen, the impurity flux profiles do not vary erratically either radially or through time. This consistency in measurement and calculation indicated that the experimental fluxes reported do represent the experiment.

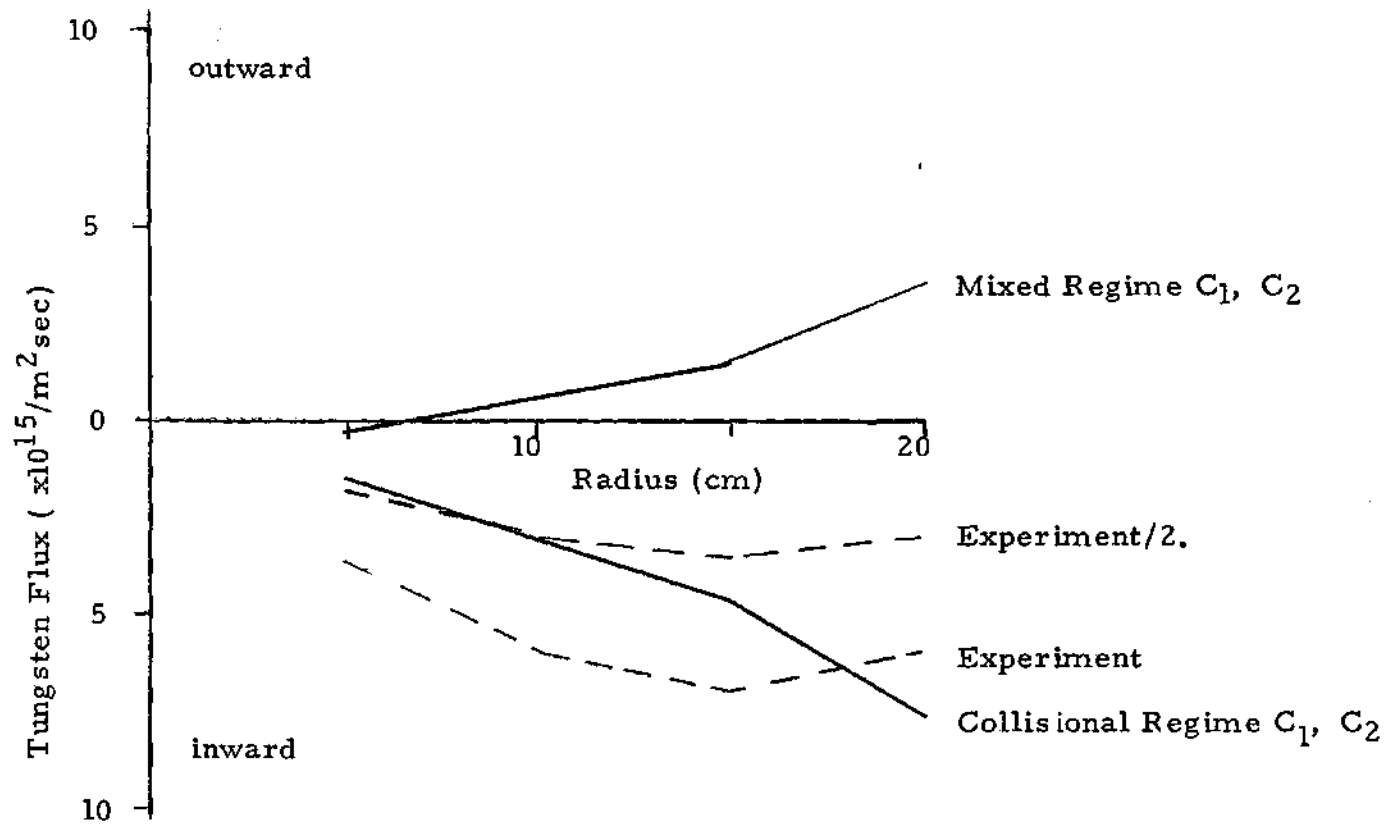


Figure 3.3.1 Analysis of PLT Impurity Flow Reversal Before Beam Injection, Co-directed Beam, $t=250$ msec

3.4 Analysis of the Co-injected Experiment

Neutral beam injection of 535 kWatts of co-injected power took place over the period 250-350 msec in the PLT flow reversal experiment. The tungsten fluxes were reported for the times $t = 280$ and $t = 290$ msec. Beam injection had begun 30 msec. earlier (at 250 msec.), so that the beam is thermalized and providing approximately 0.6 N of toroidally directed force at a steady rate. About 20 % of the total momentum is estimated to be lost due to charge exchange and trapped particle losses. The initial ($t=250$ msec) momentum deposition profile calculated by the Fokker-Planck code is shown in Figure 3.2.6.

The experimental data is interpreted by using the gradient driven flux component of Equation 3.3.3, with the Rutherford values of C_1 and C_2 , and the beam driven flux component for the mixed collisionality regime of Equation 2.7.5, which may be written

$$\langle n_z v_z \rangle_{\text{beam}} = \frac{\epsilon^2}{e \tilde{z} B_p} \frac{2 \beta_z / \beta_i K_{\omega i} + (\beta_z / \beta_i - 1) K_{\omega z}}{(1 + \beta_z / \beta_i)} \quad , \quad 3.4.1)$$

where $K_{\omega j}$ is the toroidally directed momentum input to species j . The drag ratio β_z / β_i is not known from first principles, as discussed in Section 2.9. Therefore, the drag ratio is treated as an adjustable parameter. This

model scales linearly with momentum input, and the coefficient involving the drag ratio asymptotically approaches unity; i.e.

$$\frac{\beta_z/\beta_i}{1 + \beta_z/\beta_i} \longrightarrow 1 \quad (3.4.2)$$

for large β_z/β_i .

The tungsten flux measured in the experiment at $t = 280$ msec. is shown in Figure 3.4.1 (dashed lines). At this time, the tungsten flux has clearly been reversed by the neutral beam injection and is outward. From Equation 3.4.1, the condition,

$$\beta_z/\beta_i (2K_{\phi i} + K_{\phi z}) > K_{\phi z} \quad (3.4.3)$$

must be met for the beam driven component of the tungsten flux to be outward. Since most of the beam momentum goes to the main ions, $K_{\phi i} \gg K_{\phi z}$, the beam driven flux component is outward except for $\beta_z/\beta_i \ll 1$.

A value for the drag ratio of two ($\beta_z/\beta_i = 2$) is chosen. Thus, the combined momentum and gradient driven fluxes, Equation 3.3.1 plus Equation 3.4.1, lead to an outward impurity flux which underpredicts the experimental

flux by about a factor of two. The fluxes drawn with solid lines on Figure 3.4.1 were calculated using the gradient driven flux with collisional values of C_1 and C_2 , and the beam driven flux component of Equation 3.4.1, the fluxes drawn with solid lines were calculated; see Figure 3.4.1. Calculations with two values of the drag ratio, $\beta_z / \beta_i = 1$ and 2, were made. The fluxes calculated using $\beta_z / \beta_i = 2$ are seen to provide a reasonable interpretation of the experimentally observed reversal of impurity fluxes with co-injected beams. It is noted that the results are relatively insensitive to β_z / β_i for $\beta_z / \beta_i > 2$.

In Figure 3.4.2, the experimentally measured fluxes at the time $t=290$ msec. are shown (dashed lines). The calculated fluxes are also shown (solid lines). The experimental fluxes at this time are smaller than at the previous time, but still outward except that the flux at a radius of 20 cm. has changed directions to inward. This reduction in the magnitude of the outward flux is predicted by the theory. The electron temperature has increased, which leads to an increase in the average tungsten charge state. This reduces the outward beam driven flux component ($\Gamma_{z, beam} \propto 1/Z$), while increasing the inward gradient driven flux component, ($\Gamma_{z, grad} \propto Z$). The gradient driven flux component is also reduced, but to a smaller extent, by the increasing ion temperature ($\Gamma_{z, grad} \propto 1/\sqrt{T}$).

In addition to the temperature effects, the tungsten

density has changed. The tungsten densities for the co-injected experiment are shown in Figure 3.4.3. The increased tungsten concentrations at 15 and 20 cm. have increased the inward gradient driven flux component, $(\Gamma_{z_{grad}} \propto n_z)$, while the outward beam driven flux component is relatively unchanged. The beam driven flux component is dependent on the impurity concentration only through the momentum transferred to the impurity, K_{ϕ_2} , which is a small term for small impurity concentrations ($\alpha < 1$).

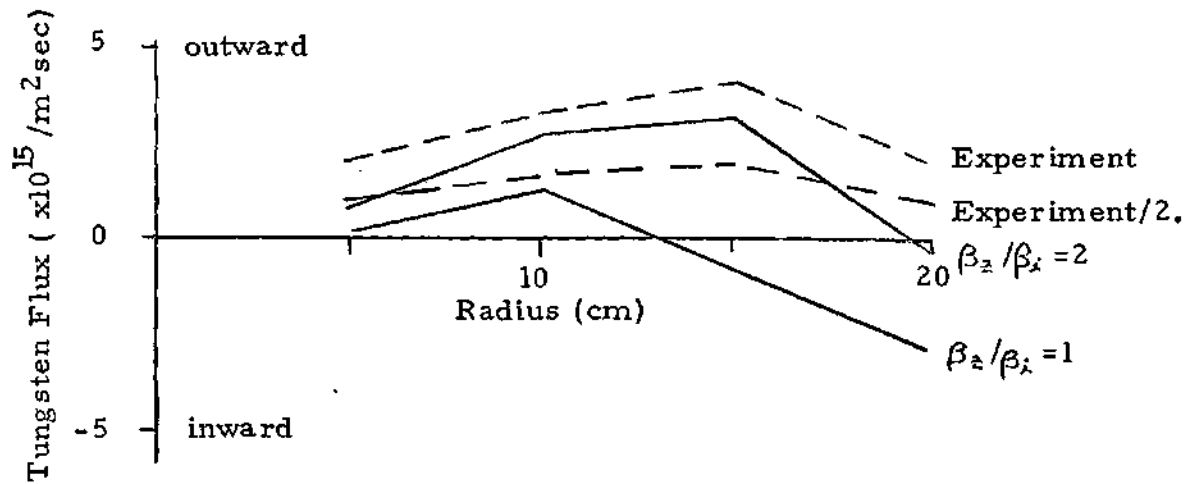


Figure 3.4.1 Analysis of PLT Co-injected Flow Reversal Experiment, $t = 280$ msec, $P_b = 585$ kWatt

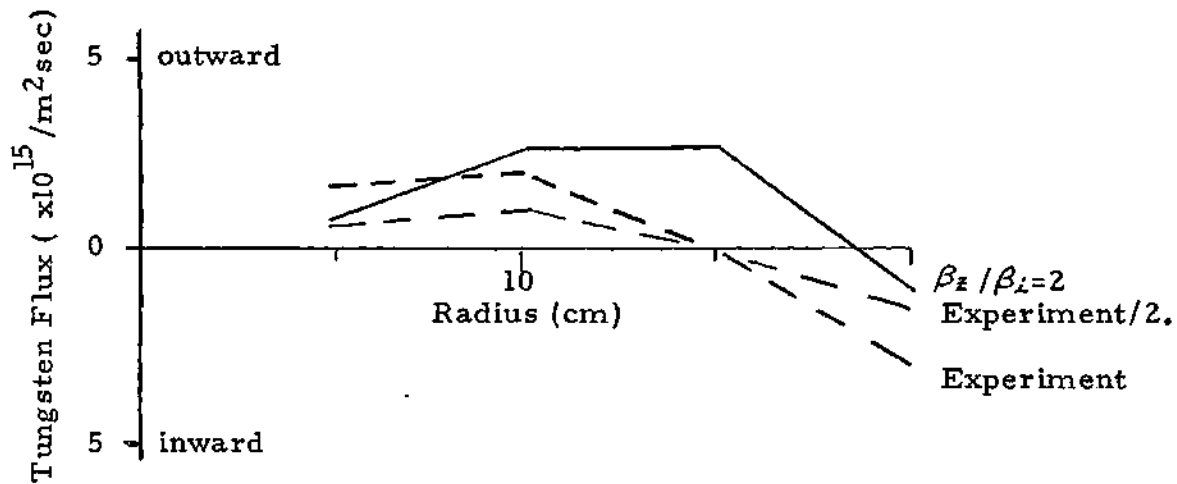


Figure 3.4.2 Analysis of PLT Co-injected Flow Reversal Experiment, $t = 290 \text{ msec}$, $P_b = 585 \text{ kWatt}$

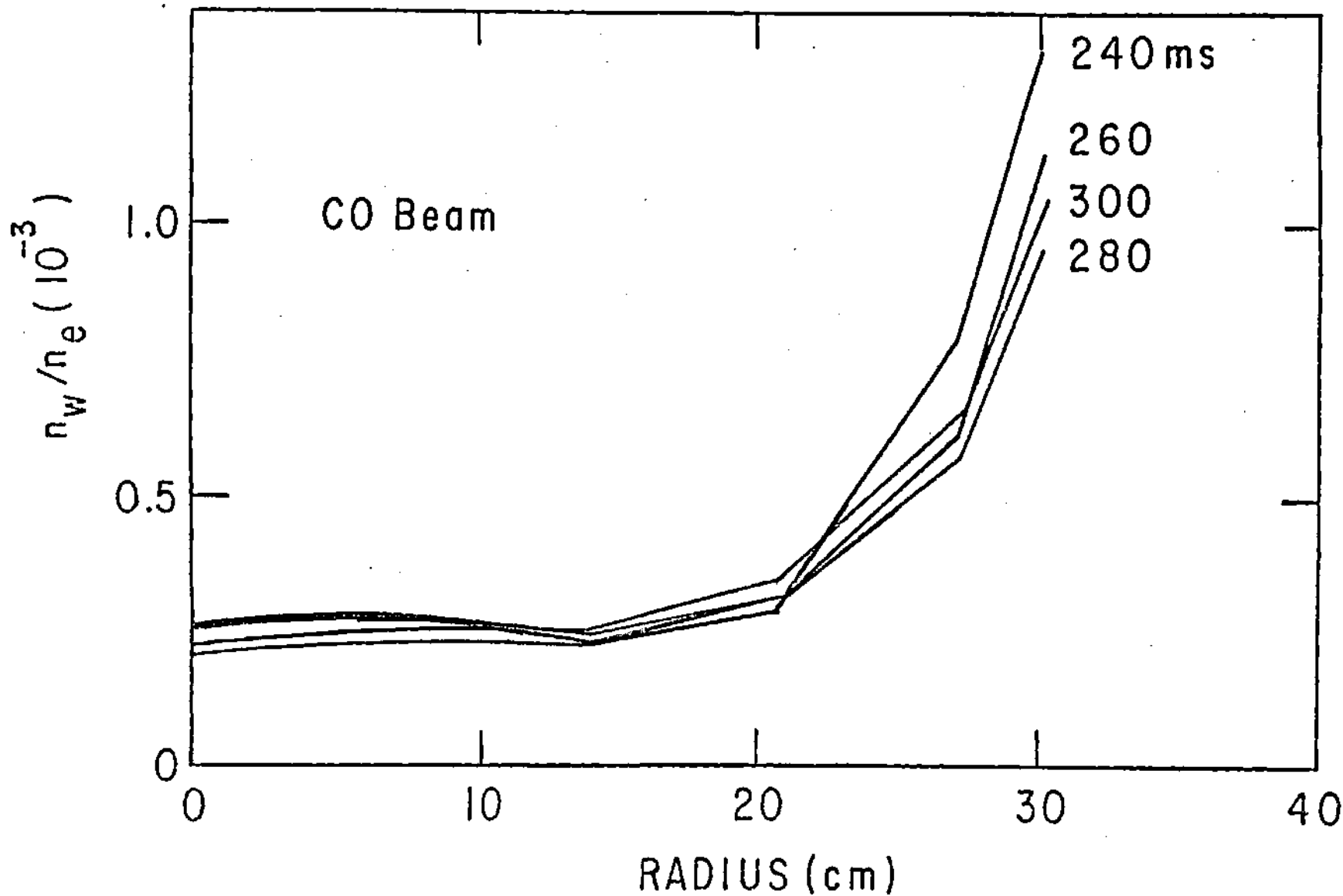


Figure 3.4.3 Tungsten Density Divided by Electron Density for $0 < r < 20$ cm During the PLT Co-injected Flow Reversal Experiment, from Reference 34 585 kWatt of Co-injected Power from $t=250$ to $t=350$ msec.

3.5 Analysis of the Counter-injected Experiment

In the PLT experiment, the plasma conditions of the counter-injected experiment were matched as closely as possible to the co-injected experiment discussed in the previous section.. The similarity of the two experimental runs is attested to by the similarity of the tungsten densities at $t = 240$ msec., before neutral beam injection. Plasma disruptions are a problem in counter-injected experiments, so the beam power was kept lower, to 430 kWatts. As in the co-injected experiment, injection was begun at 250 msec., and tungsten flux data was given for $t = 280$ and 290 msec. The evolving tungsten density is shown in Figure 3.5.1. During co-injection of the beam, the electron temperature has dropped due to the radiation from the tungsten accumulation at the plasma center; see Figure 3.2.3. Because of the electron temperature drop, the average charge state of the tungsten has also dropped, although only by about 10 % from $t=250-300$ msec.

The impurity fluxes at $t = 280$ msec. were calculated using Equations 3.3.1 and 3.4.1, and are plotted on Figure 3.5.2 (solid line). Various fractional values of the experimental fluxes are also plotted (solid lines) for comparison. The experimental fluxes are inward and much larger than before injection (compare Figures 3.5.2 and 3.3.1). The calculated fluxes exhibit the same trend, but now the calculations underpredict the experiment by a factor

of about four to five.

The calculated and experimental fluxes for $t = 290$ msec. are shown in Figure 3.5.2. The calculations again underpredict the experiment by a factor of about four to six.

It is interesting that the counter-injected fluxes scale with the tungsten density. By calculating fluxes at $t = 290$ msec. from the fluxes at $t = 280$ msec. by a simple tungsten density ratio,

$$\langle n_z V_z \rangle_{r, \text{exp}, t=290} = \langle n_z V_z \rangle_{r, t=280} \frac{n_z t=290}{n_z t=280}, \quad 3.5.1)$$

Figure 3.5.4 is produced, showing that the tungsten fluxes scale as the tungsten density during counter-injection. The theory predicts that the gradient driven flux but not the beam driven flux should scale as the impurity density. This scaling of the theory fits with the experimental observations, since the beam driven flux, which was equal in magnitude to the gradient driven flux when the impurity density was small at the beginning of injection, is at the later time small compared with the larger gradient driven flux, which dominates the scaling at high impurity concentrations. This scaling is not observed during co-injection. Other parameters which may be important in

scaling the flux do not change significantly during this time. The ion temperature is projected to change less than 10 % between $t = 280$ and $t = 290$ msec., and the electron temperature and tungsten charge state also change little.

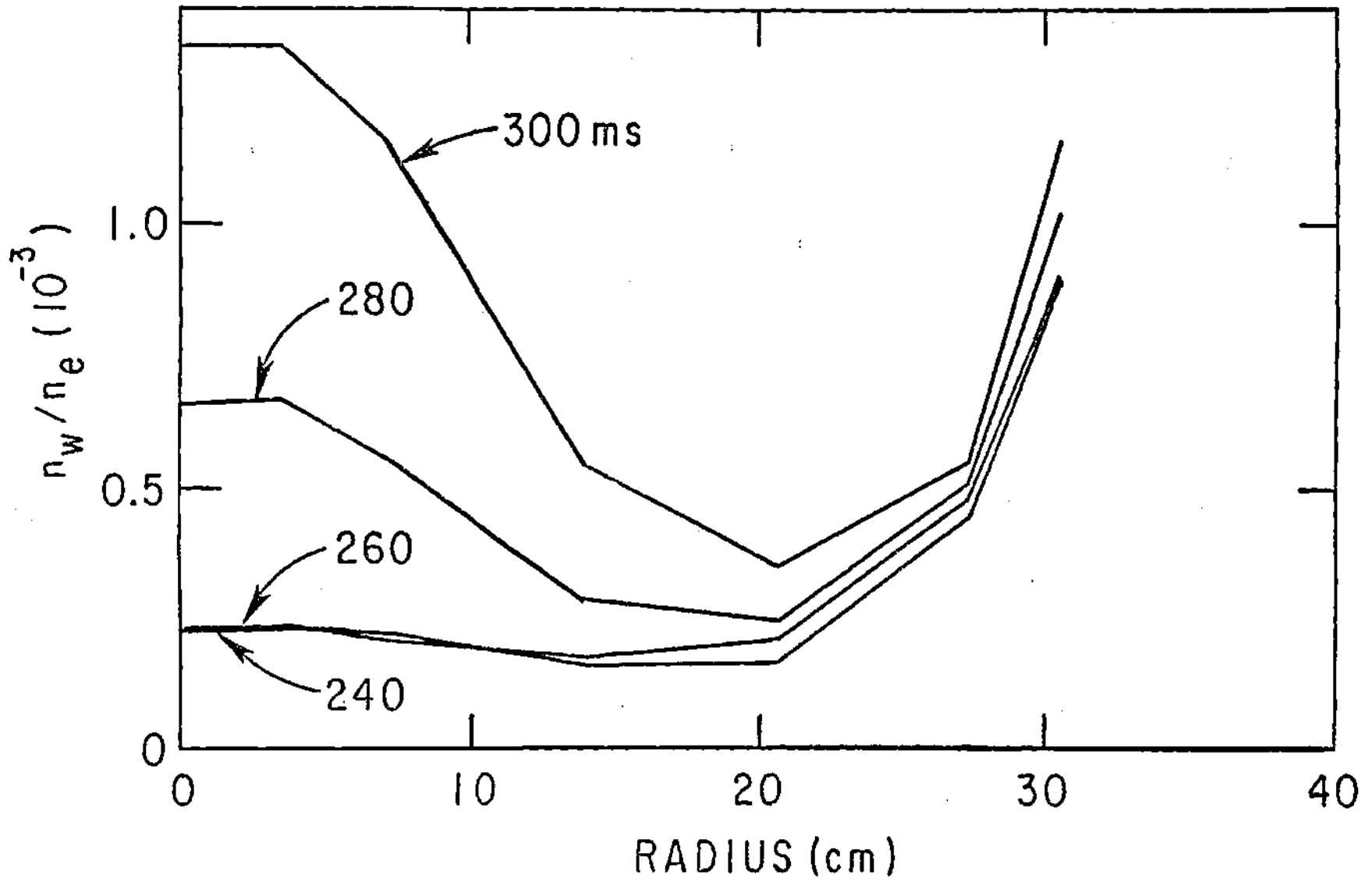


Figure 3.5.1 Tungsten Density Divided by Electron Density for $0 < r < 20$ cm During the PLT Counter-injection Flow Reversal Experiment, from Reference 34 430 kWatt of Counter-injected Power from $t=250$ to $t=350$ msec.

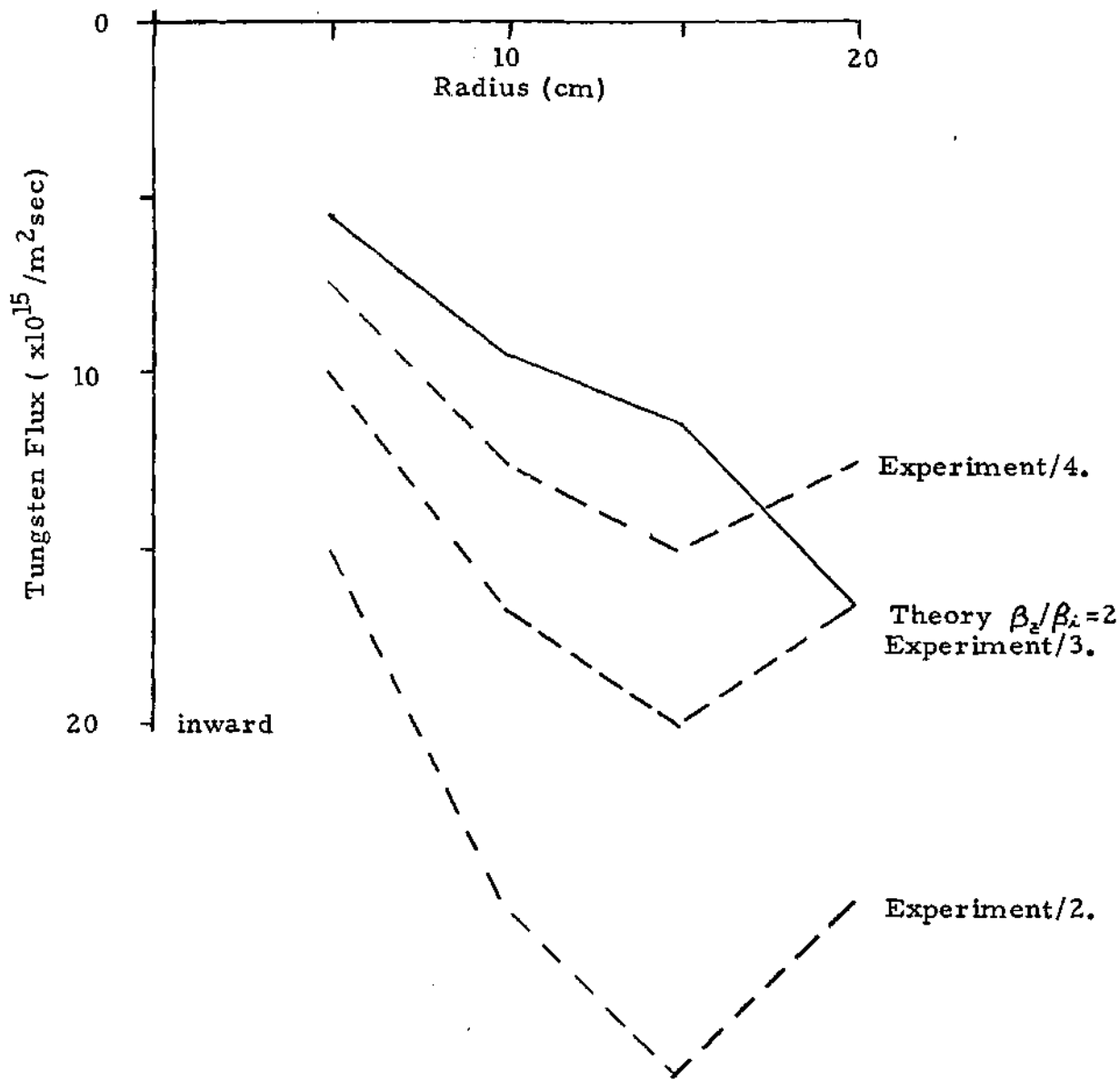


Figure 3.5.2 Analysis of the PLT Counter-injection Experiment
 $t=280 \text{ msec}$ $P_b=430 \text{ kWatt}$

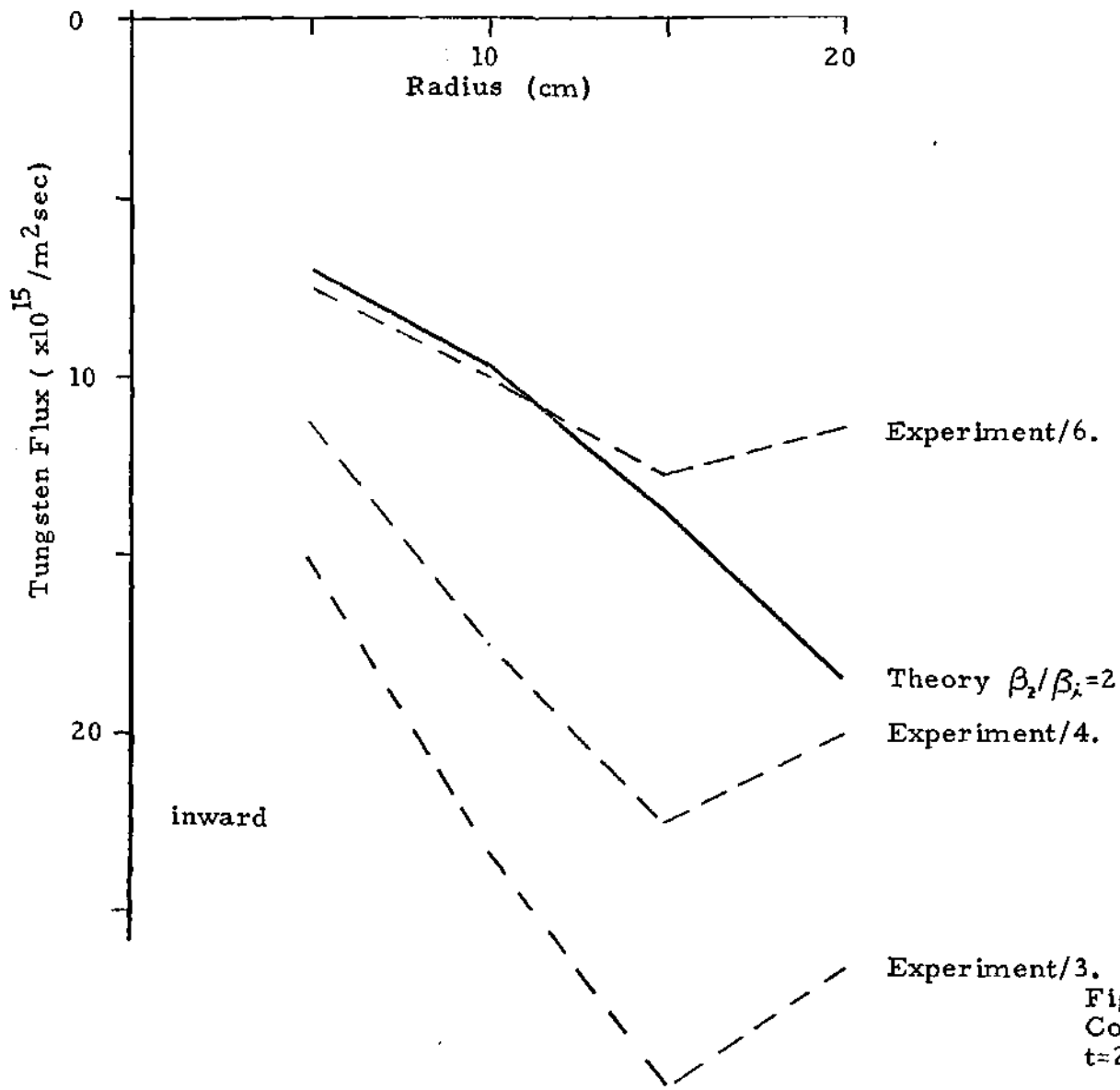


Figure 3.5.3 Analysis of the PLT Counter-injection Experiment
 $t=290$ msec, $P_b=430$ kWatt

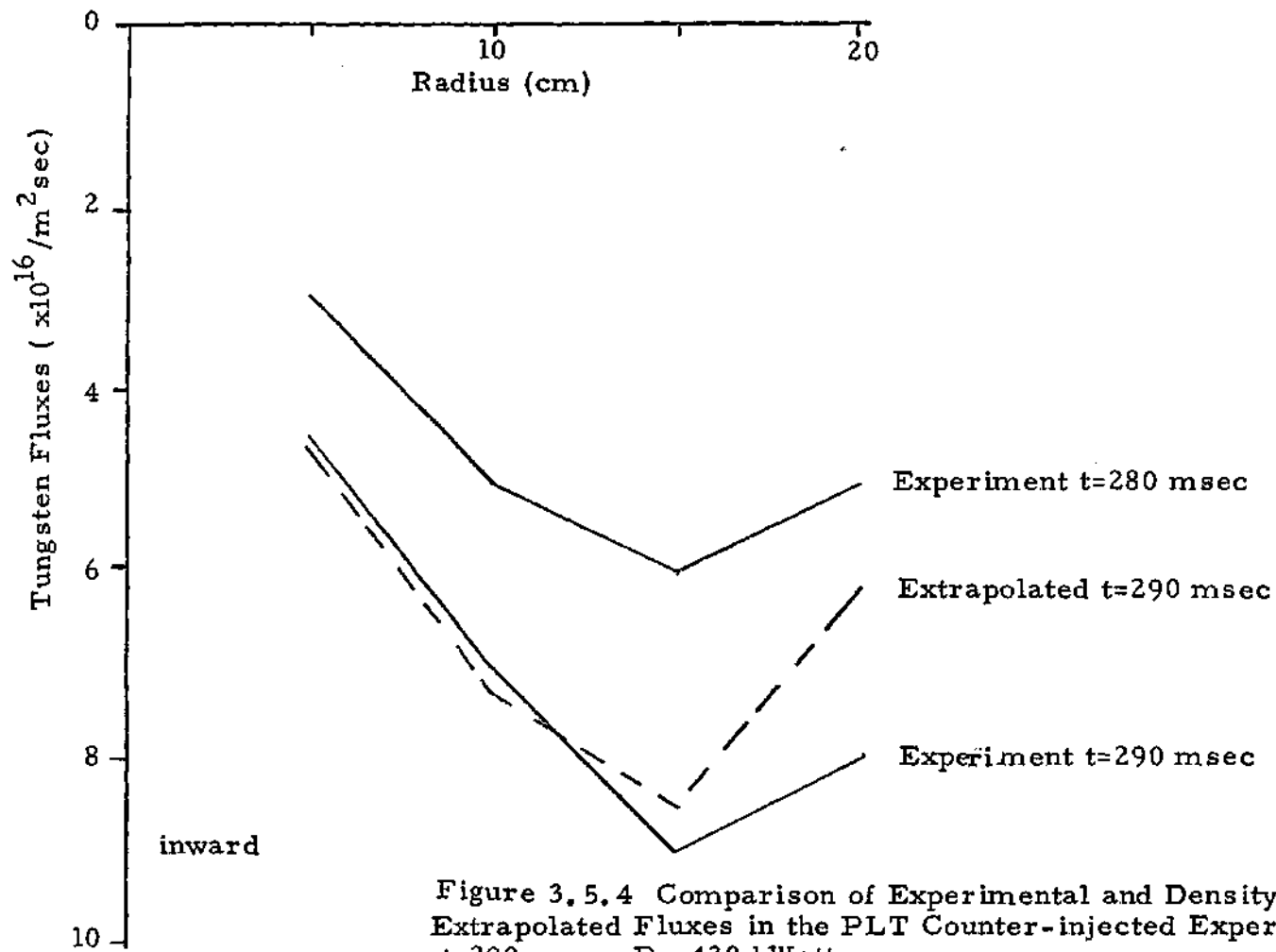


Figure 3.5.4 Comparison of Experimental and Density Extrapolated Fluxes in the PLT Counter-injected Experiment t=290 msec, $P_b=430$ kWatt

3.6 Calculation of Tungsten Accumulation in PLT

In this section, the model for impurity fluxes that is suggested by the results of the previous sections is used in an impurity transport code to compare the tungsten profiles calculated by the code to the experimental values. The impurity flux model is Equations 3.3.1 plus 3.4.1, multiplied by a factor of two, and $\beta_e / \beta_i = 2$.

The PROCTR transport code was modified to analyze the experiment. First, the model developed here was added to the code. To match the experiment more exactly, the calculation of the electron and ion temperatures and densities was suppressed, and the plasma temperature data values were input as a function of time. The temperature data given in Table 3.2 was used for 240, 260, 280, and 300 msec., and the temperature at any time was found by linear interpolation. The ion density and safety factor was also set to the values in Table 3.2.

Starting with the calculation at $t = 240$ msec., and using a tungsten profile similar to the experimental data at that time, the tungsten profile alone was allowed to evolve until $t = 300$ msec. The code printed the tungsten profiles at 260, 280, and 300 msec., so that these profiles could be compared directly to the experimental data.

The results of this analysis for the co-injected, $P = 585$ kWatt experiment are presented in Figure 3.6.1. For clarity, the tungsten profile evolution is shown as a series

of transitions, from 240 to 260 msec., 260 to 280 msec., and 280 to 300 msec., for both the calculated and experimental values. Beam injection is begun at 250 msec., with a 30 msec. rise time on the momentum.

Before the tungsten transport driven by the neutral beam becomes significant, the model matches the experiment well. At the end of the time period of 240 to 260 msec., the beam has been on only 10 msec., rising to only $\sim 30\%$ of its maximum momentum deposition rate at the end of this time interval. By comparing the calculated tungsten density rise on the left hand side to the observed rise on the right, the average tungsten density rise over the 20 cm. of radius recorded is approximately the same. The experiment indicates a greater tungsten accumulation at the center, and a lesser accumulation at the outside (15 to 20 cm.) of this region than the calculation.

As the beam momentum increases, the model again provides good agreement with the experiment. From 260 to 280 msec., the calculation using the model developed here indicates a density increase at the center and density decrease in the 15 to 20 cm. range, a small net change over the entire region. The density in the experiment during this time interval only increased slightly at a radius of 15 cm., again a small net change in tungsten concentration.

In the final time period, from 280 to 300 msec., the correlation between the calculated and experimental values

is lower but still qualitatively accurate. The model shows a tungsten density decrease over the entire 20 cm. region, during which time the experimental tungsten density increases at the outer edge of the region (15 to 20 cm.) and decreases at the center. Both the experiment and model show an increased outward tungsten flow over the previous time state.

Overall, the adjusted model has predicted reasonably well the tungsten densities observed in the co-injected experiment. The total change in tungsten concentration in the inner 20 cm. of PLT is modeled better than the details of the profiles in that region. Considering the difficulty of measuring the actual impurity densities, this agreement must be considered to be good.

The model developed for the co-injected fluxes is next applied to the counter-injected experiment. Only 430 kWatts of beam power was injected, lowering the beam driven fluxes as well as the ion temperature increase. The ion and electron temperatures are input from the data in Table 3.2.1. As discussed earlier, the electron temperatures in the counter-injected experiment are significantly lower than those in the co-injected experiment due to radiation from the large concentration of tungsten.

The model significantly underpredicts the counter-injected experiment's tungsten profiles. The evolution of the tungsten profile for the counter-injected

experiment is shown in Figure 3.6.2. The right hand plot shows the experimentally measured tungsten profiles, and the calculated profiles are shown on the left.

The model predictions do not diverge from the experimental values until the beam power becomes important. The calculated rise in tungsten density between 240 and 260 msec. is small, comparable to the rise observed in the experiment. The beam has only been on for half of this time interval, and the beam has risen only to $\sim 30\%$ of the full momentum deposition rate at the end of this time interval. In the later time intervals, the divergence between the model and experimental values is much greater.

The inability of the model to match the counter-injected experiment is expected from the analysis of the counter-injected experiment in Section 3.5, where the theory was found to underpredict the experiment by a factor of four instead of the factor of two found in the co-injected experiment. An analysis of the counter-injected experiment was made using an additional factor of two multiplying both the gradient and momentum driven fluxes. The results are presented in Figure 3.6.3. The corrected model overpredicts the tungsten rise between 240 and 260 msec. since the beam is not yet a significant effect. After this point in time, the model with the additional factor of two does correctly follow the tungsten profile evolution.

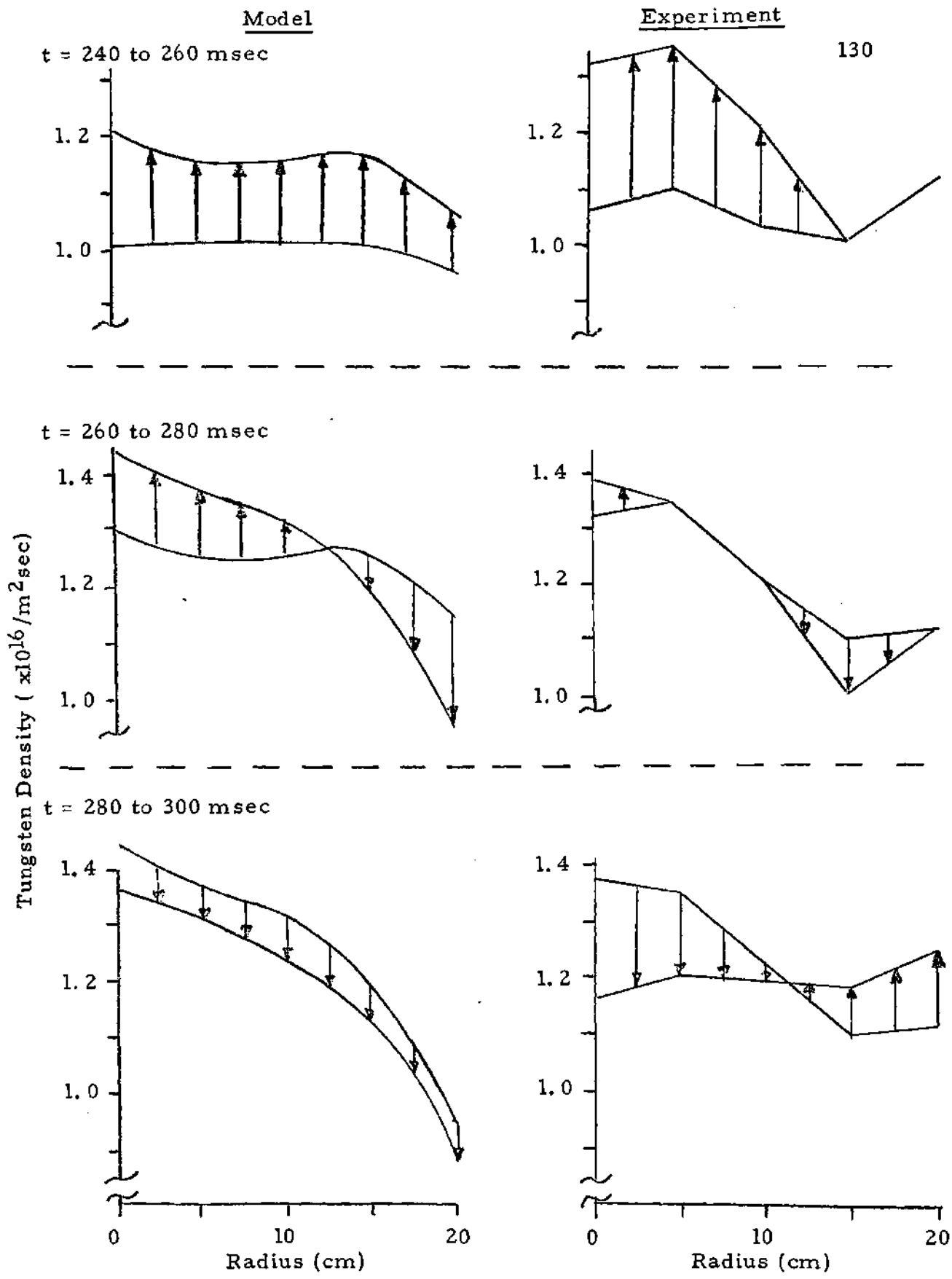


Figure 3.6.1 Tungsten Density Profile Evolution in PLT during Co-injection from Model and Experiment, $P_b = 585$ kWatt

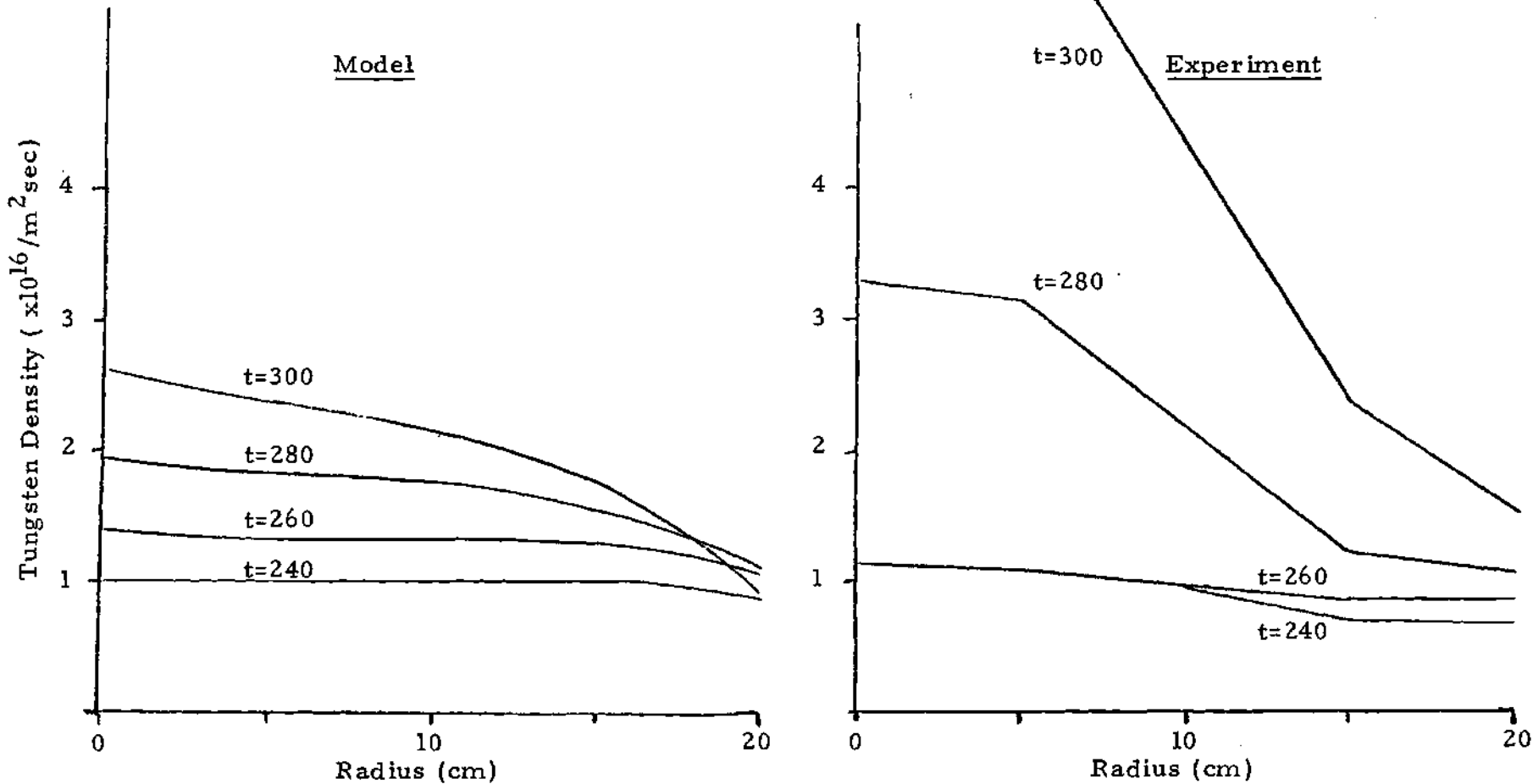


Figure 3.6.2 Tungsten Density Profile Evolution in PLT during Counter-injection from Model and Experiment, $P_D=430$ kWatt, time in msec.

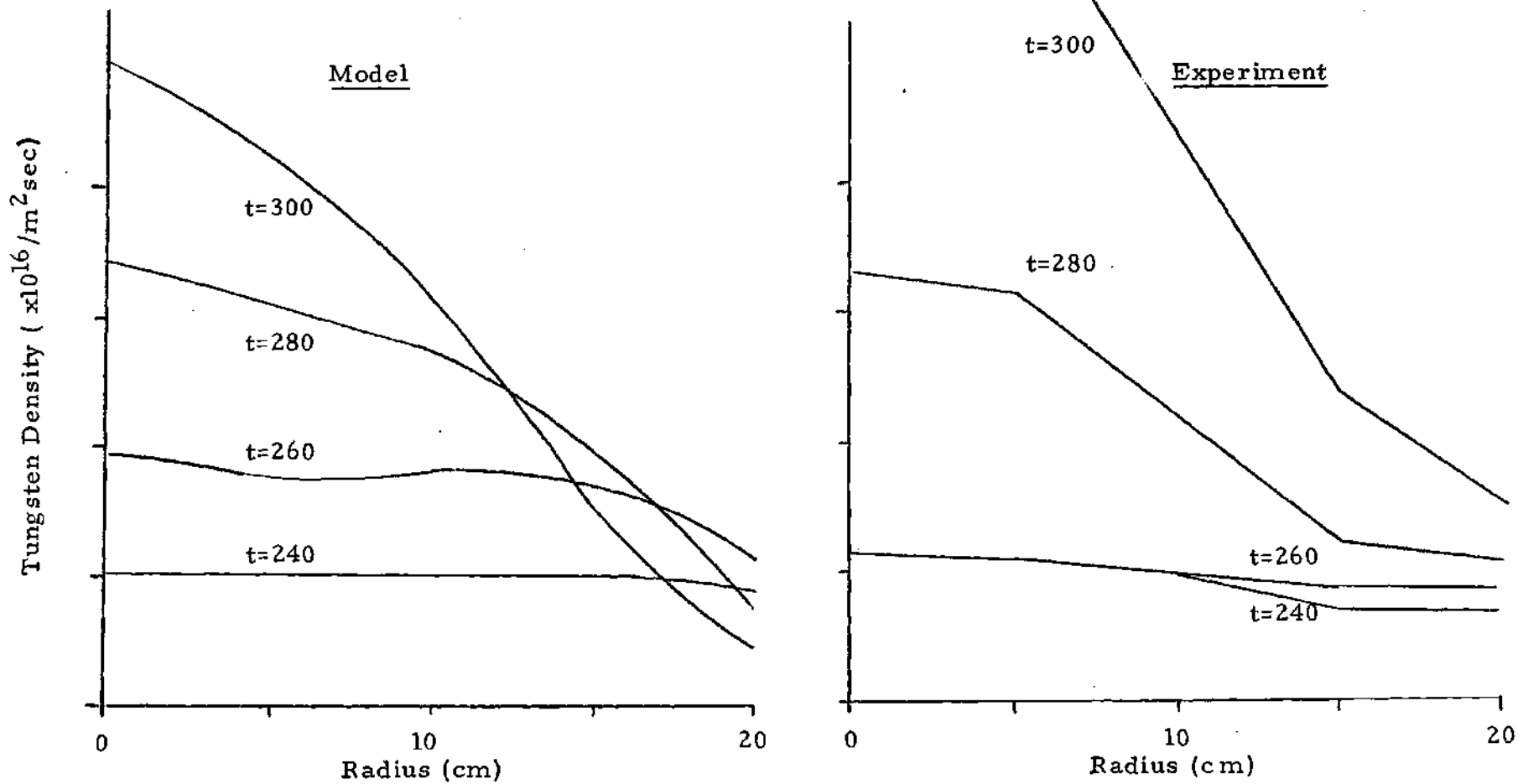


Figure 3.6.3 Tungsten Density Evolution in PLT during Counter-injection from Model times two and Experiment, $P_b=430$ kWatt, time in msec.

3.7 Evaluation of Inertial Theory

There is a possible explanation for the discrepancy between the theory of Chapter 2 and the counter-injected experiment offered by Burrell et al [25]. In solving the momentum balance equations of Chapter 2, the inertial, $m_i n_i (V_i \cdot \nabla V_i)$, term was neglected, which is valid when $V_\phi \ll V_{thz}$. The thermal velocity of tungsten in the PLT experiments was $V_{th} \sim 3 \times 10^5$ m/sec, which is comparable to the observed toroidal rotation velocity, $V_\phi \sim 10^5$ m/sec. Burrell et al [25] have shown that the inertial term produces a poloidal variation in the impurity density, which is predicted to enhance gradient driven impurity fluxes. In this theory, the impurity flux is

$$\langle n_z V_z \rangle_{inertial} = \frac{2 q^2 m_i n_i v_{iz} T_i}{e^2 B_0^2 Z} \frac{(1 - \frac{1}{2}(\gamma - z))}{\delta^2 + (1 - \gamma^2)} \times \quad , \quad 3.7.1)$$

$$\left\{ \left[1 - \frac{1}{2}(\gamma - z) \right] \frac{1}{n_i} \frac{\partial n_i}{\partial r} - \left[1 - \xi + \frac{1}{2} \gamma (\xi + \gamma - 1) + \frac{1}{2} z (1 + g) \right] \frac{1}{T} \frac{\partial T}{\partial r} \right\}$$

where

$$\xi = m_i v_{iz} Z^2 q R V_{ii} / T \quad , \quad 3.7.2a)$$

$$V_{ii} = - \frac{T_i}{e_i B_{\theta 0}} \left[\frac{1}{n_i} \frac{\partial n_i}{\partial r} + (1 + g) \frac{1}{T_i} \frac{\partial T_i}{\partial r} \right] \quad , \quad 3.7.2b)$$

$$V_{E_0} = U - V_{11} \quad , \quad 3.7.2c)$$

$$y = m_z V_{11}^2 / T \quad , \quad 3.7.2d)$$

and

$$z = m_z V_{E_0}^2 / T \quad . \quad 3.7.2e)$$

The constants are $\xi = 1.5$ and $g = .5$ in PLT, and U is the observable toroidal rotation velocity.

This theory is now applied to interpret the experimental tungsten fluxes, using the data presented in Section 3.2 to model the experiment. In addition to this data, the toroidal rotation velocity is needed. This velocity is interpolated from the experimental data in a manner similar to the calculation of the ion temperature found in Section 3.2. Figure 3.7.1 [37] shows the variance of the PLT maximum central rotation velocity with the line averaged electron density. Since the rotation velocity was calculated from the shift in the velocity distribution of charge exchanged particles escaping the plasma center, it was necessary for the beam and main plasma isotopes to differ so that they could be distinguished. Two lines were

added here to extrapolate this data to cases where the beam and plasma isotopes are the same. This was accomplished by scaling the beam momentum at a constant power to a new beam particle mass,

$$V_{\phi_0}(0)_{x^0 \rightarrow x^+} = V_{\phi}(0)_{y^0 \rightarrow x^+} \left(\frac{m_{x^0} V_{x^0}}{m_{y^0} V_{y^0}} \right) = V_{\phi_0}(0)_{y^0 \rightarrow x^+} \sqrt{\frac{m_{x^0}}{m_{y^0}}} \quad . \quad 3.7.3)$$

For deuterium injection into a deuterium plasma with $\bar{n}_e = 3 \times 10^{13} / \text{cm}^3$, the experimental condition, this shows a final central velocity of $1.25 \times 10^5 \text{ m/sec}$ for one MWatt of injected power, or $7 \times 10^4 \text{ m/sec}$ for the 585 kWatts of power co-injected and $5.5 \times 10^4 \text{ m/sec}$ for the 430 kWatts of power counter-injected. A rotational velocity rise time of 30 msec was used (Equation 3.2.1), and the velocity profile was found by scaling the central velocity to the velocity profile shown in Figure 3.7.2. This data is summarized in Table 3.7.1. A toroidal rotation velocity of $-1.5 \times 10^4 \text{ m/sec}$ was observed without injection in most cases. The cause and effect on impurity transport of this offset rotation is not known, and is ignored here. Calculations made by including the rotational offset into the total rotational velocity in the inertial theory ($U = U_{\text{rot}} + U_{\text{off}}$) do not produce calculated fluxes which explain the experiment better than the fluxes calculated without the offset.

Figure 3.7.3 shows the experimental fluxes and fluxes calculated using the inertial theory at 240 msec, before beam injection. The inertial theory does not predict well the tungsten fluxes before beam injection. Agreement is good only at the 5 cm. radial point. The theory and experiment diverge with increasing radius until the theory overpredicts the experiment by a factor of 20 at 20 cm.

Agreement between the inertial theory and experiment is somewhat better in the co-injected case, Figure 3.7.4. The inertial theory corresponds with the experiment qualitatively by predicting flow reversal, and matches the experiment in magnitude between 5 and 10 cm. in radius. The theory diverges from the experiment with increasing radius to a factor of four at 20 cm.

The inertial theory most closely matches the experiment in the counter-injected case. As seen in Figure 3.7.5, the inertial theory overpredicts the experiment by a factor of two or less for the radial range of 5 to 15 cm. for both $t = 280$ and $t = 290$ msec. The theory and experiment again diverge with increasing radius up to a factor of four at 20 cm.

Since the inertial theory alone does not match the experiment, the inertial theory is combined here with the gradient and beam driven theory developed in this thesis to see if some combination of the theories can better match the experiment. The total flux is calculated as

$$\Gamma_{z_{total}} = a(\Gamma_{ps} + \Gamma_{beam}) + b(\Gamma_{inertia} - \Gamma_{inertia}(U=0)) \quad , \quad 3.7.4)$$

where the coefficients a and b are adjusted to match the theory to experiment. In the previous sections, the coefficient a was found to be two when the inertial term was not present. Therefore, it is assumed here that a should be in the range of one to two. Since the inertial flux is based on and includes the gradient driven flux, the inertial flux calculated when the toroidal rotation is zero (U=0) is subtracted from the inertial flux, so that only the added effect of inertia is used.

The calculated fluxes best match the counter-injected experiment when the coefficients a=2 and b=.5 are chosen (Figure 3.7.6). In this case, the inertial theory corrected the deficiency of the gradient and beam theory developed in Chapter 2 during counter-injection. Unfortunately, during co-injection, Figure 3.7.7, the agreement between theory and experiment is lost. No choice of coefficients was found which could provide agreement between theory and experiment better than that found without the inertial term (b=0). Even so, development of the inertial theory, including the direct moment effects, may well be very important in ultimately explaining the experiment.

TABLE 3.7.1 PLT Velocity Profiles

Radius (cm)	0	5	10	15	20	25
Toroidal Velocity ($\times 10^4$ m/sec)						
CO-240	-	0.0	0.0	0.0	0.0	-
CO-280	-	4.0	3.5	2.5	2.0	-
CO-290	-	5.0	4.2	3.0	2.2	-
CN-280	-	3.0	2.6	1.9	1.5	-
CN-290	-	3.8	3.1	2.2	1.7	-

****Key****

CO - Co-injected experiment

CN - Counter-injected experiment

CO-XXX Co-experiment at time $t=XXX$ msec.

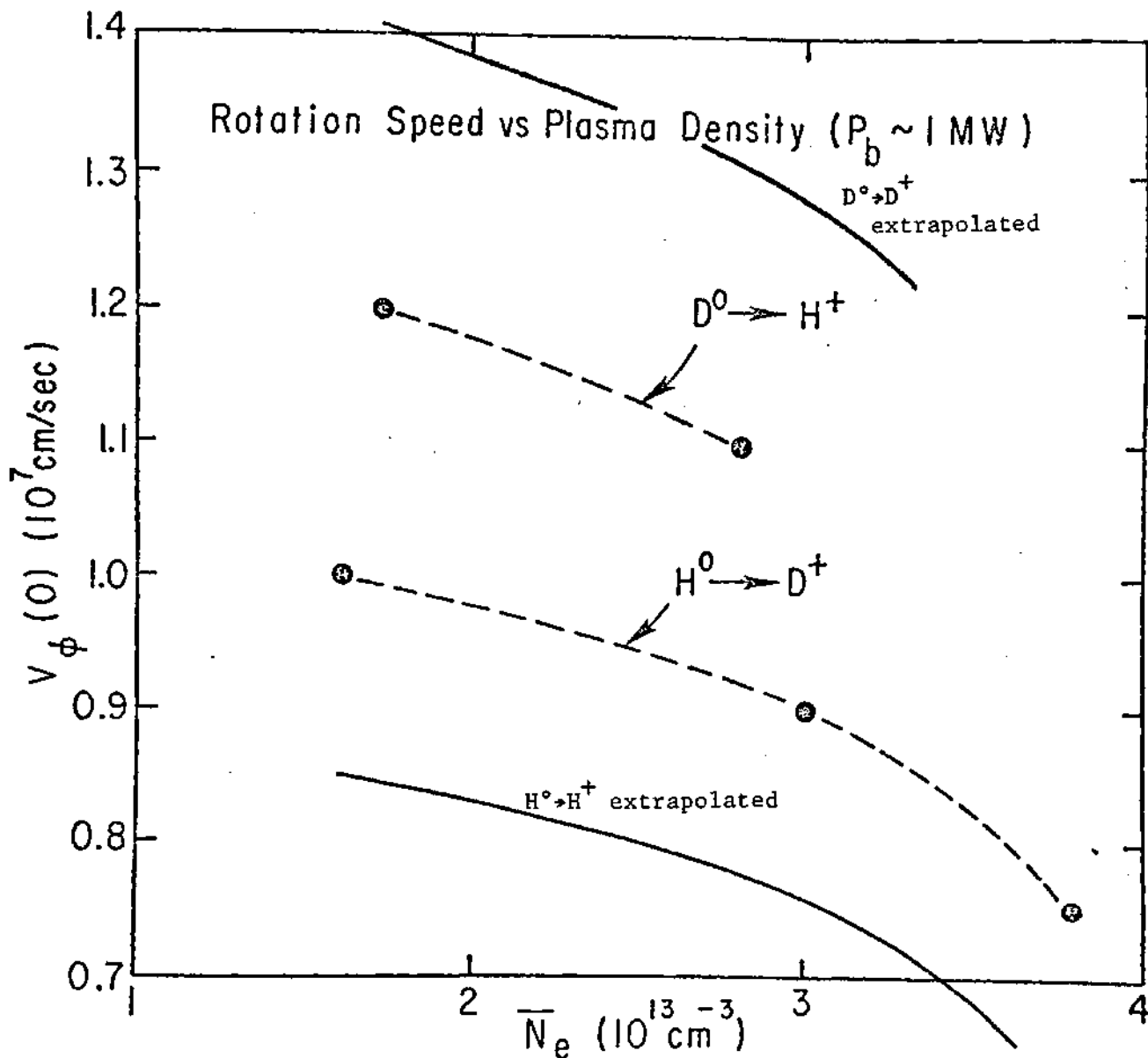


Figure 3.7.1 PLT Central Rotation Velocity as a Function of Average Electron Density, from Reference 36
Solid lines here by extrapolation

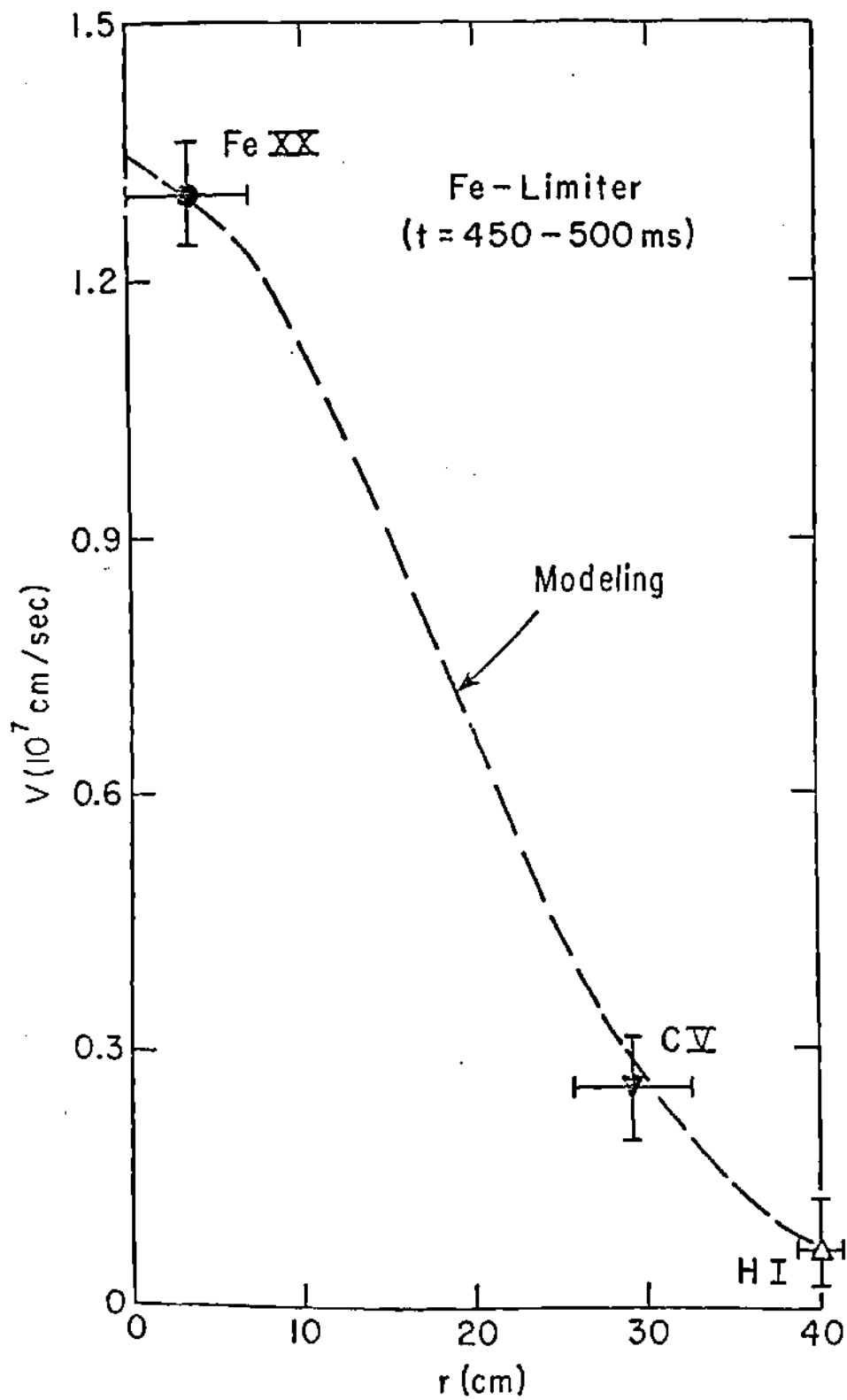


Figure 3.7.2 Typical PLT Velocity Profile
From Reference 36

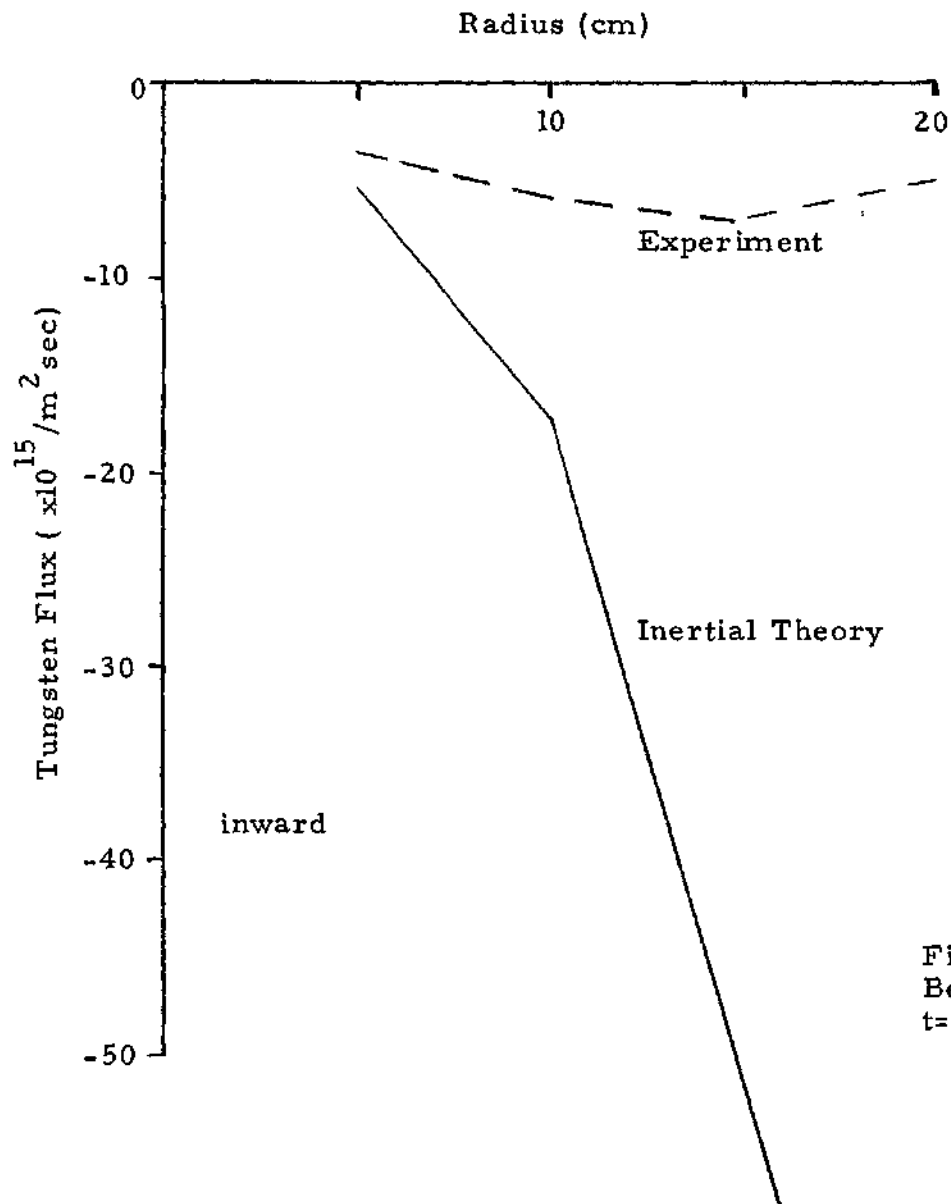


Figure 3.7.3 Analysis of PLT Experiment Before Injection Using Inertial Theory Only $t=250$ msec, Co-injected Beam Case

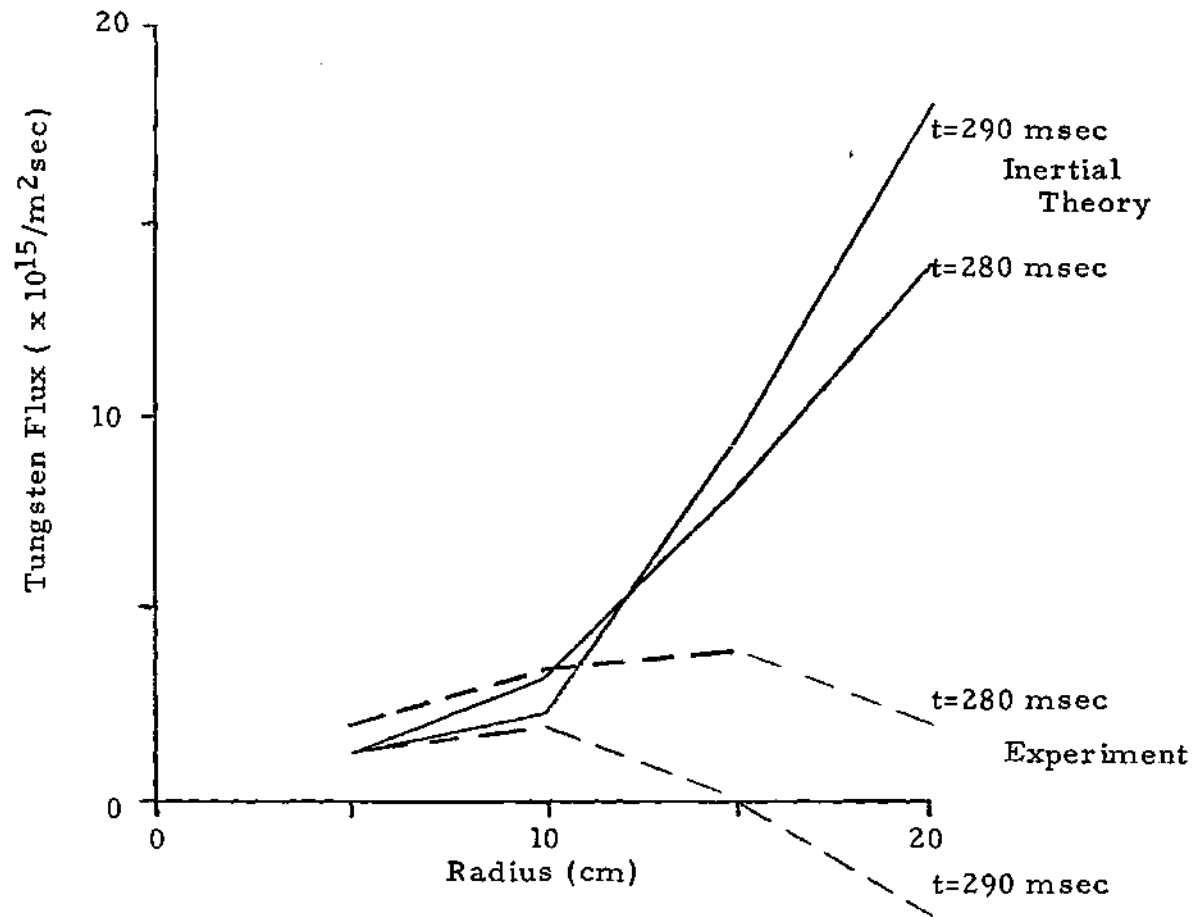


Figure 3.7.4 Analysis of PLT Co-injected Experiment Using Inertial Theory Only $P_b=585$ kWatt

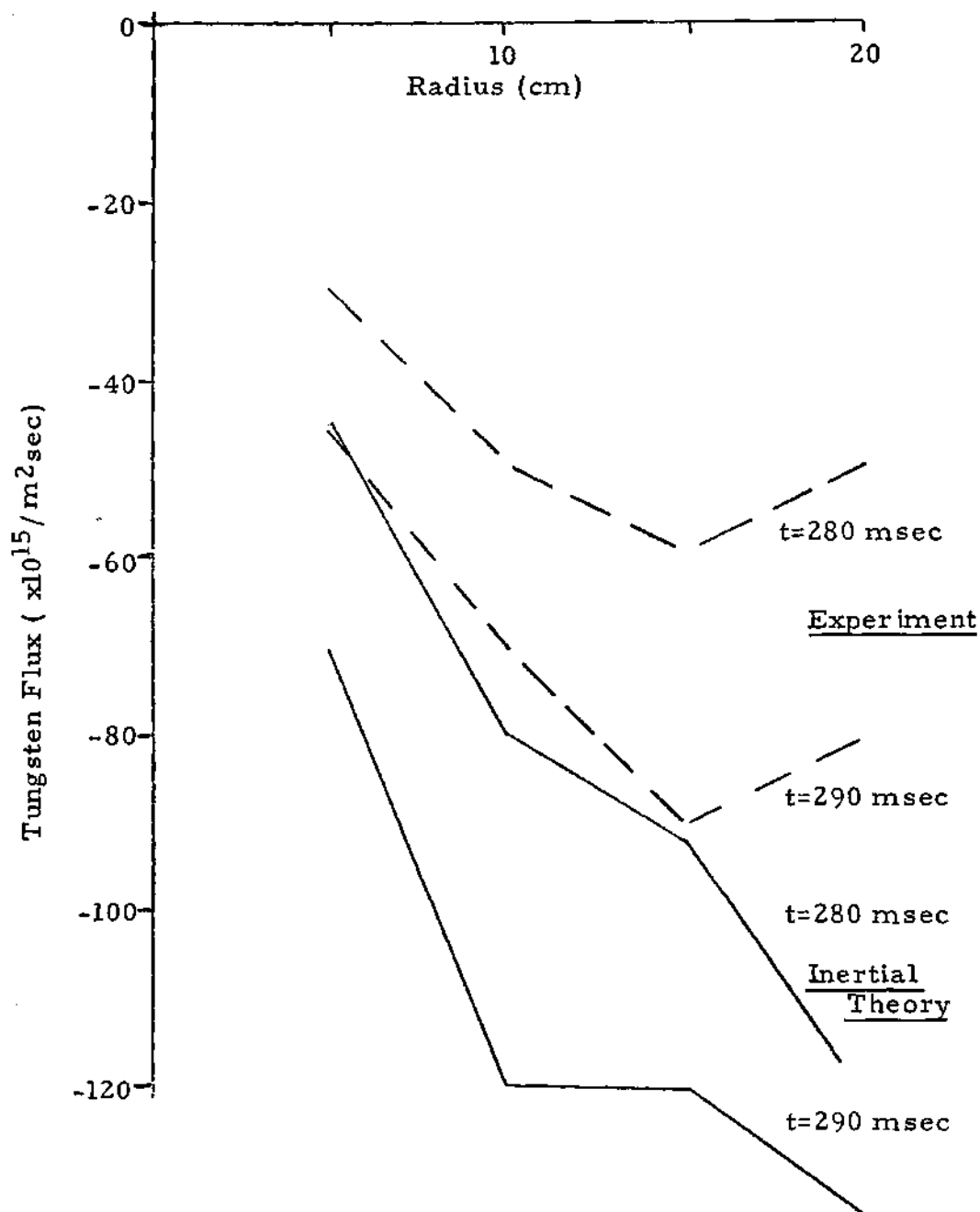


Figure 3.7.5 Analysis of the PLT Counter-injected Experiment using Inertial Theory Only $P_b=430$ kWatt

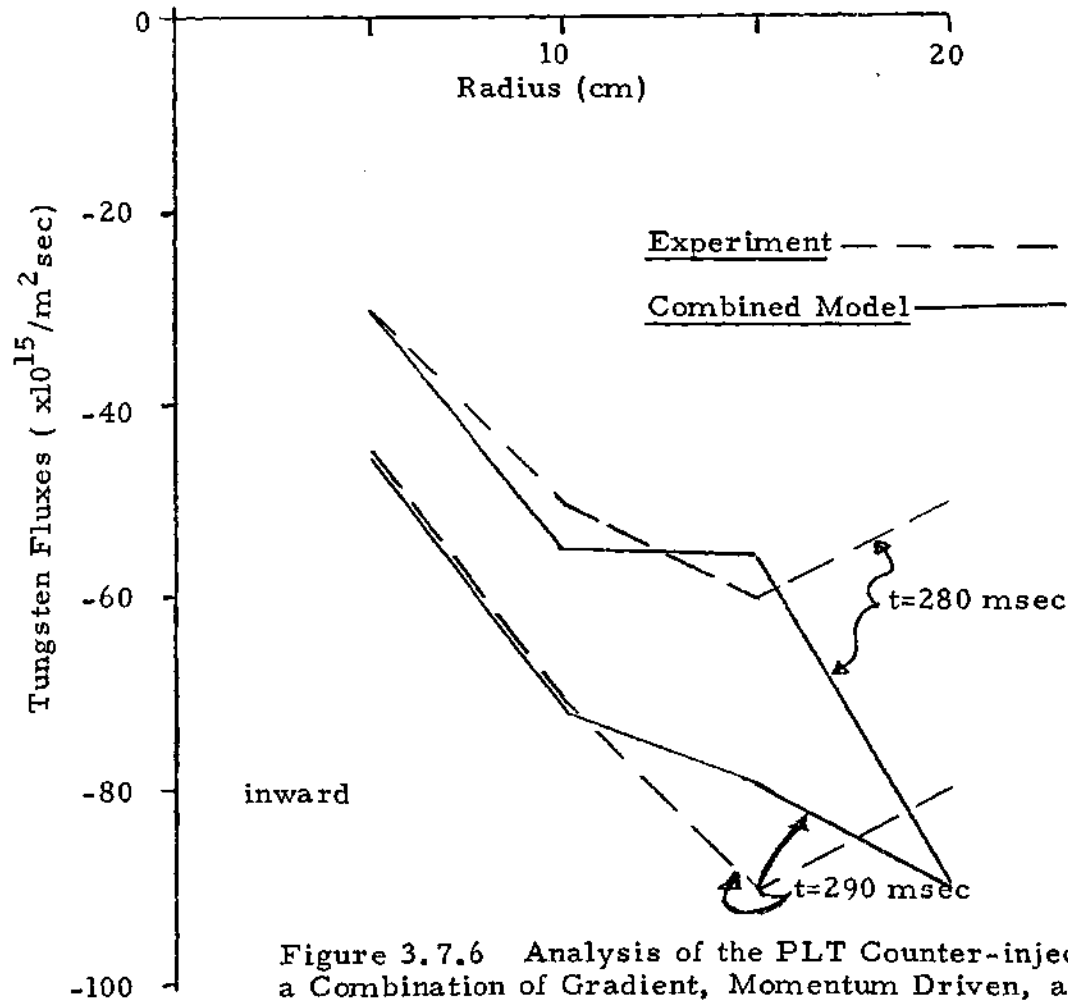


Figure 3.7.6 Analysis of the PLT Counter-injected Fluxes using a Combination of Gradient, Momentum Driven, and Inertial Fluxes $P_b=430 \text{ kWatt}$

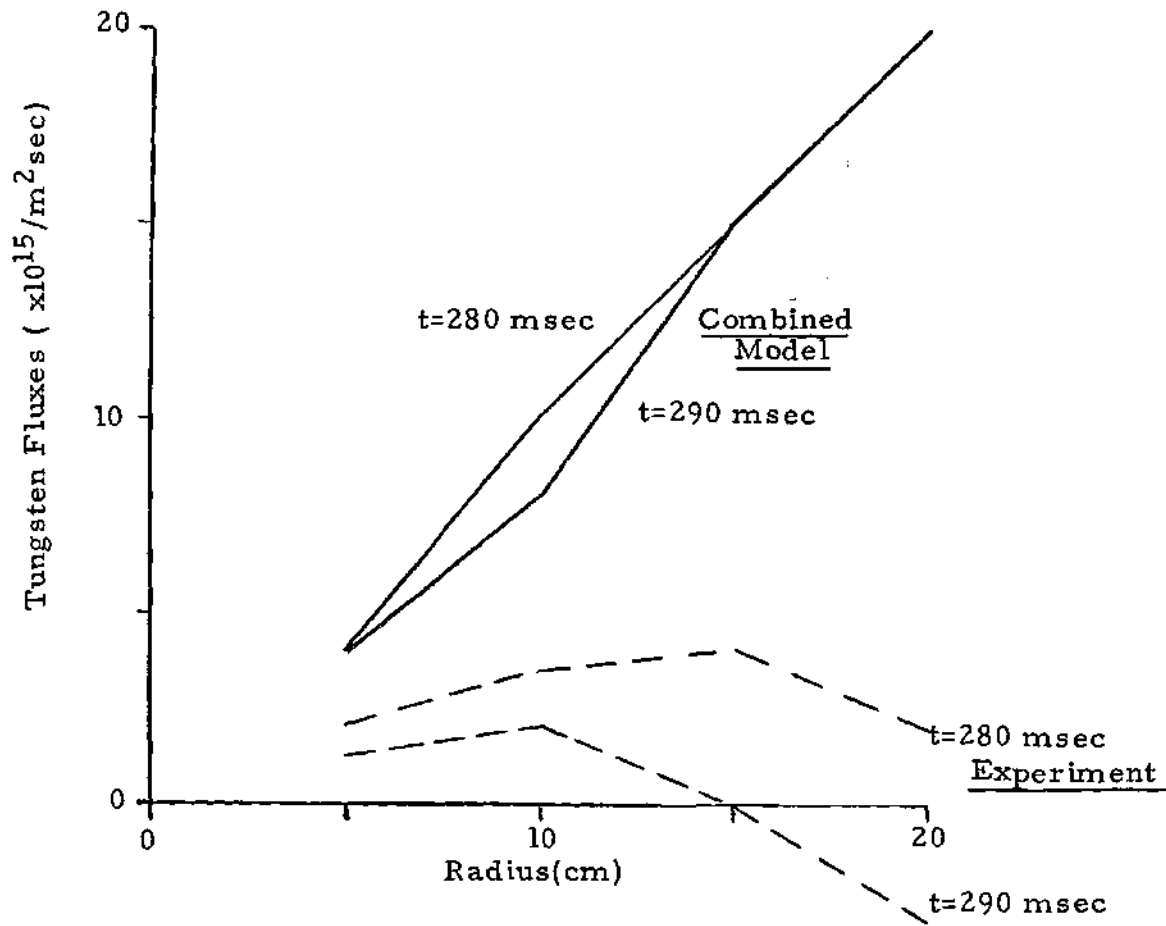


Figure 3.7.7 Analysis of PLT Co-injected Experiment using a Combination of Gradient, Momentum Driven, and Inertial Fluxes $P_D=585$ kWatt

3.8 Review of Analyses of ISX-B

Two separate studies of ISX-B neutral beam driven flow reversal experiments are reviewed in this section. The first study, performed by Sigmar and Howe [53], analyzes the co-injected experiment utilizing the Stacey and Sigmar direct momentum driven flow reversal theory [16]. The second study, performed by Crume [31], evaluates both co- and counter-injected experiments and utilizes both the Stacey and Sigmar theory [16] and the inertial driven theory of Burrell et al [25]. Only the relative change in impurity concentration though time is measured in ISX-B, so the experimental data is semi-quantitative, and the conclusions of these studies are therefore only semi-quantitative. The conclusions of both of these studies agree in general with the conclusions drawn in the analysis of PLT that was presented in the preceding sections.

Between February 1979 and October 1981, experiments were run in ISX-B to measure both the impurity flow and toroidal plasma rotation during beam injection. The experiment used a deuterium plasma, since neoclassical transport of impurities had not been observed in ISX-B using a hydrogen plasma. Measurements of the central accumulation of impurities was performed with both test sources of argon and titanium and with intrinsic impurities, in particular iron and oxygen.

In all the ISX-B experiments, central accumulation of

impurities observed with ohmic heating alone is stopped or reversed with co-injection of a neutral beam. With counter-injection, the accumulation rate is greatly enhanced. Although the impurity densities are not known quantitatively, a comparison of two similar discharges showed that 18-50 times more iron collected at the center of ISX-B during counter-injection than during co-injection. In addition, in an experiment in which 1.2 MWatts of beam power was co-injected at 80 msec and an additional 1.2 MWatt was co-injected at 160 msec, the radiation from both the iron and oxygen central concentrations was seen to be reduced by 50 to 75% when the second beam was activated.

In the study by Sigmar and Howe, the evolution of an argon density profile though time was calculated using a 1-1/2 D transport code. The effects of impurity radiation, thermal particle transport, and wall recycling of argon was included. Different cases were compared in which the ratio β_z / β_c and the average argon concentration were varied. As in the analysis in this thesis, the choice of $\beta_z / \beta_c = 2$ was found to best match the experiment. In the Sigmar and Howe study, a preliminary inertial theory by Burrell was also analyzed. Since this preliminary theory was subsequently extensively modified, that portion of the analysis is ignored here.

The later study by Crume [31] analyzed both co- and counter-injected experiments by comparing the sum of the

impurity transport terms, including gradient driven, direct momentum driven, and inertial driven effects. In this analysis, the ratio β_z / β_i was chosen to be unity ($\beta_z / \beta_i = 1$). To determine the direction of the impurity transport, the radial convective velocities of titanium was calculated over the plasma radius. The net convection was found to be outward and of comparable magnitude to the gradient driven fluxes during co-injection, and the net convection was found to be inward and of much greater magnitude than the gradient driven fluxes during counter-injection. These results are qualitatively the same as those presented in Section 3.7 when the inertial term was included in the analysis, but the quantitative accuracy of the results was found to be poor.

3.9 Summary of the Model Developed in PLT

The impurity transport model based on the extended neoclassical theory of Chapter 2 and analysis of beam driven flow reversal in the Princeton Large Torus tokamak (PLT) consists of two separate driving mechanisms. The first driving mechanism is the ion density and temperature gradients, which has been known for some time [29],

$$\langle n_z V_z \rangle_{\text{quad}} = 2 \cdot \frac{Z q^2 m_i n_i v_{zT_i}}{e^2 B_0^2 Z} \left\{ C_1 \left(\frac{1}{n_i} \frac{\partial n_i}{\partial r} - \frac{1}{n_z Z} \frac{\partial n_z}{\partial r} \right) \right. \\ \left. + (C_1 - C_2) \frac{Z-1}{Z} \frac{1}{T_i} \frac{\partial T_i}{\partial r} \right\} \quad 3.9.1)$$

The analysis of PLT has added a factor of two to the original theory, and has required calculation of the factors C_1 and C_2 by a collisional rather than collisionless ion model,

$$C_1 = 1 - \frac{.52 \alpha}{.59 + \alpha} \quad 3.9.2a)$$

and

$$C_2 = 1.5 - \frac{.29 + 1.2 \alpha}{.59 + \alpha} \quad 3.9.2b)$$

The second driving mechanism is neutral beam injected momentum. This theory was recently presented [15,16], and was extended here to include heat flux effects,

$$\langle n_z V_z \rangle_{\text{beam}} = \frac{2 \xi^2}{e Z \bar{B}_{p0}} \frac{2 \beta_z / \beta_c K_{\phi c} + (\beta_z / \beta_c - 1) K_{d z}}{(1 + \beta_z / \beta_c)} \quad . \quad 3.9.3)$$

To model the experiment, the drag ratio was chosen to be two ($\beta_z / \beta_c = 2$), and again a factor of two was added to the original theory.

Calculations of the tungsten density profile evolution using this model correlates well with the profiles seen in the PLT experiments before and during co-injection for the inner 20 cm of radius.

An additional factor of two multiplying both terms in the model is required to match the counter-injected experiment.

Page missing from thesis

CHAPTER IV

PREDICTIONS FOR FUTURE MACHINES

4.1 Introduction

In this chapter, the feasibility of using neutral beam driven impurity flow reversal as an impurity control method for future tokamaks is investigated. In particular, the possibility that co-injected neutral beams could be used to prevent impurities from penetrating to the center of the plasma, thereby causing an accumulation of impurities in the plasma edge region which would radiatively cool the plasma edge, is examined. For a sufficiently cool plasma edge, the particles striking the first wall would produce only a small sputtering erosion compared with more energetic particles. A graph of energy dependent sputtering yields for various materials, Figure 4.1.1, is shown here as examples of the high sensitivity of sputtering rates to edge temperature. Control of the impurity concentrations is also a possible mechanism for control of the plasma power balance.

Three representative machines are considered. The first machine discussed is the Tokamak Fusion Test Reactor, referred to as TFTR, which has recently begun operation at the Princeton Plasma Physics Laboratory [59]. The purposes

of this machine are to achieve fusion reactor conditions and to demonstrate plasma energy breakeven. The second machine to be treated is a tokamak with parameters similar to those specified for the Fusion Engineering Device, FED [60]. FED is similar in size to the International Tokamak Reactor, INTOR [61], and the predictions made for FED will apply to INTOR as well. These machines are being designed as engineering test reactors to follow the TFTR generation of experiments. They would demonstrate the engineering technology needed in making tokamak reactors into a reliable power source. Both FED and INTOR are in the conceptual design stage. The final tokamak to be studied here is a conceptual design of a commercial reactor based on the STARFIRE [62] design parameters.

In order to isolate the effect of the beam, fixed, "typical" profiles of main ion density, temperature, and safety factor are taken from the literature. The transport of the impurity species is calculated for a constant edge source of impurities.

Based on the analysis of the PLT experiments discussed in the previous chapter, the predictive model summarized in Section 3.9 is adopted, which consists of impurity fluxes driven by neutral beams and by pressure and temperature gradients, and includes the Rutherford values of C_1 and C_2 , a multiplicative factor of two on the theoretically calculated fluxes, and a value $\beta_e / \beta_i = 2$.

TFTR has 24 MWatt of co- and 8 MWatt of counter-directed beam injectors, which are very powerful for the size of the machine. The momentum driven transport would be expected a priori to be comparable to other transport mechanisms. The effect of the beam momentum on impurity transport is found to be substantial, and is discussed in Section 4.2.

The projected FED and INTOR plasmas are much larger than the TFTR plasma. At present, there are no plans to install neutral beams injectors. Thus, the purpose here is to investigate what magnitude of impurity flow reversal could potentially be accomplished if a modest amount of co-injected neutral beam power were installed. The momentum driven impurity transport effects predicted in the study of FED, Section 4.3, are less dramatic than those in TFTR, but are sufficiently large to indicate that neutral beam driven impurity flow reversal is a promising method for impurity control in a next generation tokamak engineering test reactor. Since the design is not fixed, the operating parameters were varied in order to provide insight into the variability and possible optimization of this impurity control mechanism. In this case, the effect of various density and temperature profiles was studied.

The STARFIRE sized commercial reactor, which is a relatively small size increase over the FED reactor, exhibits a similar level of neutral beam driven impurity

control effect. In keeping with the optimization and variability strategy of Section 4.3, the effect of different beam parameters is studied in Section 4.4. The injection angle is varied, with steeper angles both increasing penetration and decreasing the parallel component of the momentum. Different injection energies are also studied, again offering a tradeoff in momentum vs. penetration.

A summary of the predictions made for these three machines is presented in Section 4.5.

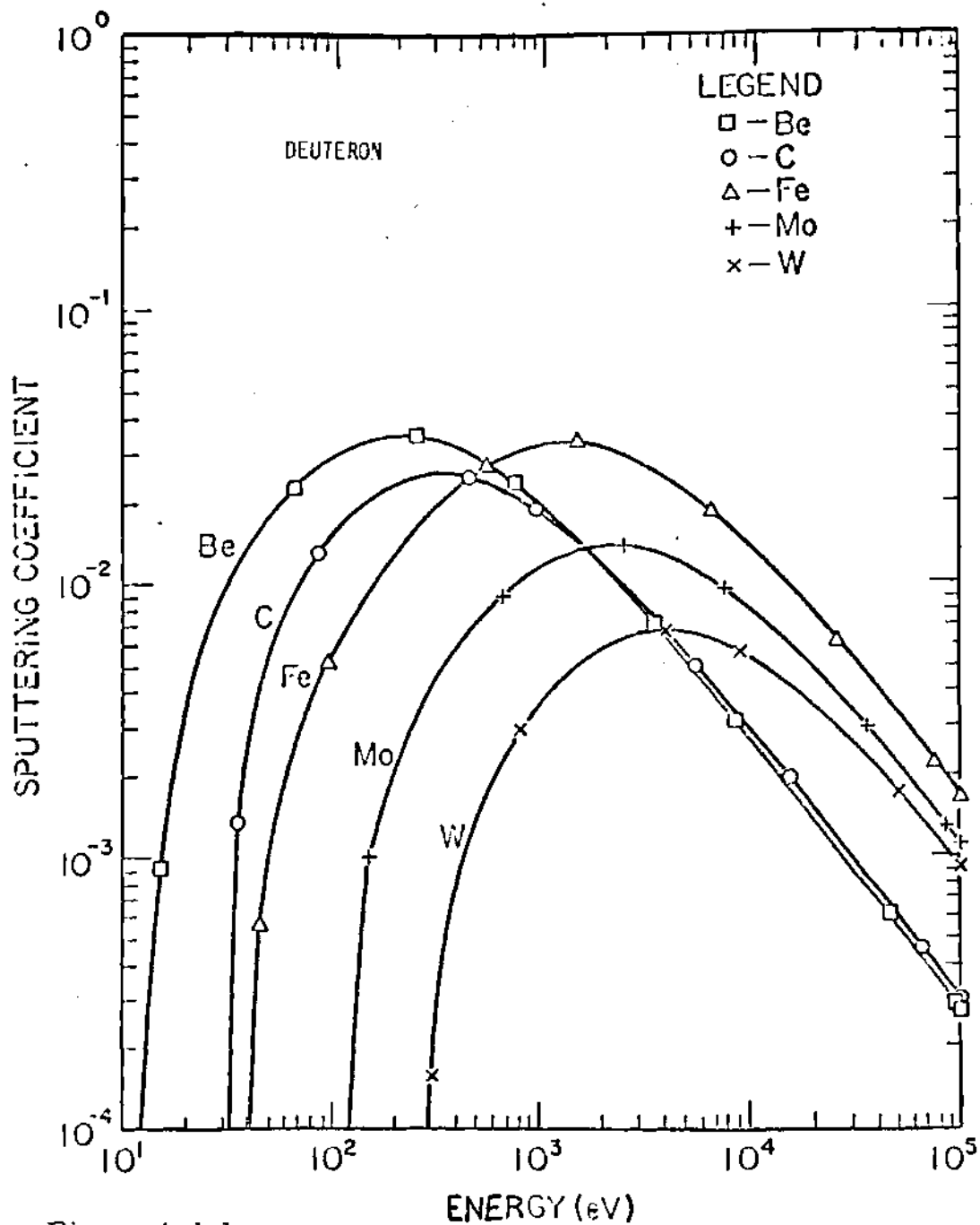


Figure 4. 1.1

Trends of sputtering yield for a number of materials for deuterons.

From Reference 64

4.2 Predictions for TFTR

In this section, the effect of beam injection on impurity transport in the Tokamak Fusion Test Reactor (TFTR) is predicted. A description of this machine is first given to provide a background for this portion of the study. The impurity transport is then studied for different plasma conditions, impurity source rates, and types of impurity.

TFTR is currently in the initial stages of operation, the first plasma having been achieved in December, 1982. The major and minor radii are both double those of the Princeton Large Torus (PLT), providing about eight times the plasma volume. The plasma pulse time is designed to be 1 to 1 1/2 seconds, and, with anticipated peak ion temperatures in the range of 20 keV, TFTR is expected to achieve plasma energy breakeven when operated with a plasma of deuterium and tritium. Plasma energy breakeven is defined as when the power produced by fusion equals the power input to maintain the plasma temperature. Machine parameters for TFTR are given in Table 4.2.1 [63-65].

TFTR is heated ohmically, by neutral beams, and by toroidal compression. The tokamak neutral beam layout is shown in Figure 4.2.1. The neutral beam system consists of four injectors [59,65], three in the co-direction and one in the counter-direction. The total available power is 32.5 MWatts. The deuteron energy in the beam is 120 keV. As in many beam systems, particles of one-half and one-third

the primary energy are produced. Combined beam currents at both the lower energies are approximately half of the beam current at the highest energy.

Since the momentum diffusion coefficient in PLT was not sensitive to the radial position [37], and therefore to the density and temperature, the total drag can be assumed to scale to different sized machines as a diffusive mechanism. The drag then simply scales as the cross sectional area, $\gamma_d = \gamma_{d_0} (a/a_0)^2$. Given this scaling, full power injection with a net co-directed power of 16 MWatts will rotate the plasma at approximately 5×10^5 m/sec, somewhat less than the thermal velocity of deuterium ($V_{thD} \sim 7 \times 10^5$ m/sec), but greater than the thermal velocity of iron ($V_{thFe} \sim 1.3 \times 10^5$ m/sec) or tungsten ($V_{thW} \sim 0.7 \times 10^5$ m/sec).

Both tungsten and iron impurities are examined below. The initial limiter material in TFTR is tungsten carbide. Tungsten will not become completely stripped of its electrons in TFTR ($T_0 \sim 5$ keV, $T_{edge} \sim 35$ eV), so a large amount of power will be radiated from only a small amount of this impurity. Iron is a portion of the first wall material, and will be a significant radiator at the plasma edge where it is only partially ionized. The iron wall offers the opportunity to compare the impurity transport for impurities with different mass and charge. Since only incompletely stripped ions can be observed spectroscopically, the lighter ions are of less interest experimentally. These low charge

ions radiate much less than the higher charge ions, so that their degradation of the plasma is also less severe.

The temperature and density profiles used for the TFTR calculations are shown in Figure 4.2.2.a and b, respectively. These profiles were suggested for use as a standard base for comparative studies of TFTR [64]. The main ion density profile shown in Figure 4.2.2a is used in all TFTR cases. The case shown is used here as the baseline case, with the central ion and electron temperatures both being 5 keV at the plasma centerline. The safety factor is calculated from the current and plasma resistivity, although it is not allowed to fall below unity. This calculated safety factor is shown in Figure 4.2.2c.

To calculate the beam momentum distribution, a Fokker-Planck slowing down code is used [58]. This code first calculates the radial deposition of ions from the neutral beam. Charge exchange is the primary mechanism for conversion of fast beam neutrals to fast ions. These fast beam ions are assumed to be confined on the flux surface, and a Fokker-Planck slowing down model is then used to calculate the momentum deposition to each species. Figure 4.2.2d shows a momentum deposition profile calculated for the base case plasma parameters given in Table 4.2.1.

Using the impurity transport model benchmarked in the last chapter in a 1-D transport code, and holding $n_e(r)$ and $T_e(r)$ fixed, the impurity density profile is allowed to

evolve in time. This model is summarized in Section 3.9. The impurity temperature at each location is assumed to be the same as the main ion temperature. A constant tungsten source strength at the plasma edge of $1 \times 10^{16} / \text{m}^2 \text{sec}$ is used here for the base case. This source strength was chosen to produce a significant, but not overwhelming tungsten concentration in the plasma. The actual tungsten source will depend upon the interaction of many complex edge region phenomena, treatment of which is beyond the scope of this work. By using a constant source the transport effects can be examined without the complications of the edge region effects. In order to directly examine the effect of the beam, calculations of the impurity profile evolution are made both by using two co-directed beams to inject 16 MWatt of power and substantial net momentum and by using one co-injected and one counter-injected beam to inject 16 MWatt of power but no net momentum.

Figures 4.2.3a and b show the time evolution of the tungsten profile up to one second in the balanced momentum and co-injected momentum cases, respectively. Note that the incoming flux fills the outer regions of the plasma to an equilibrium level. The outermost portion of the plasma reaches this equilibrium first, and the progression of plasma radii reaching equilibrium moves inward. In these areas of equilibrium, the total number of impurity particles passing a radial surface per unit time is the same as the

total wall source.

Since there is a fixed source of impurities and the net impurity flow is always inward at the edge of the plasma because of the steep main ion gradient, the total impurity concentration in the plasma is the same regardless of the beam orientation. However, the effect of the co-injected beam is to inhibit the inward flow driven by the main ion gradients, so that the impurity density distribution is shifted outward when the co-injected beam is used. Figure 4.2.3c shows the difference between the radial tungsten density distributions for the co-injected and balanced injection cases after one second. As can be seen relative to balanced injection, the co-directed beam has significantly reduced the tungsten density inside of $r=35$ cm and significantly increased the tungsten density outside of this radius. For example, the impurity concentration at a radius of ~ 35 cm has been reduced from $\alpha \sim 2.2$ to $\alpha \sim 1.1$, while the impurity concentration has been increased from $\alpha \sim 3$ to $\alpha \sim 4$ ($\alpha = n_i Z^2 / n_e$) at a radius of 42 cm.

The power radiated due to the impurities is also calculated. The power is calculated from data given in Reference [66], which is based on the coronal equilibrium model discussed in the previous chapter. In this model, electron collisions with the impurity ions determine both the charge state of the impurity and the radiation level. The radiation is due to three dominant mechanisms:

electron-ion recombination radiation, line radiation, and bremsstrahlung radiation. All of the radiation mechanisms directly cool the electrons. The ions are subsequently cooled through collisions with the electrons. The power radiated is dependent only on the electron temperature, the electron density, and the impurity density.

The profile of the power radiated from the electrons due to the impurity for the base case is shown in Figure 4.2.3d. The total radiated power is approximately 50% of the total power input from the beams. This power is approximately the total power input at this time since ohmic heating is ineffective at this temperature. The secondary peak in both profiles is due to enhanced radiation from tungsten at that electron temperature. Figure 4.2.3e shows the redistribution of radiated power due to the beam effect, which is directly related to the impurity density redistribution shown in Figure 4.2.3c. Although the total amount of tungsten is the same in both cases, the total radiated power differs. The total radiation from the plasma in the balanced momentum case is lower than in the co-directed beam case by seven percent, from 8 MWatts in the co-directed case to 7.4 MWatts in the balanced momentum case. The power radiated from the outer 25 cm increases from 1.6 MWatt to 2.5 MWatt for co-injection relative to balanced injection. This result suggest that co-injection of 16 MWatt of beam power would increase the central plasma

temperature and decrease the plasma edge temperature relative to balanced injection of the same amount of power. The reduced plasma edge temperature would lead to reduced sputtering of tungsten from the limiter.

The plasma temperature will change during the TFTR burn. Figure 4.2.4a shows the final tungsten concentration profiles of a case calculated using temperatures typical of earlier times in the plasma startup. The centerline electron and ion temperatures are both 2 keV, and the profiles used are the same as those used in the base case. The final low temperature tungsten profiles in the balanced momentum and co-directed momentum cases are shown with solid lines, and the base case ($T=5\text{keV}$) profiles are shown for comparison with dashed lines.

For both the balanced momentum and co-directed momentum, the tungsten penetrated less deeply into the plasma in the reduced temperature case than in the base case. The gradient flux scales as $\Gamma_{\text{grad}} \propto Z(T)/\sqrt{T}$. The charge state in the low temperature case is much smaller than in the base case, outweighing the enhancement due to the inverse square root of the lowered temperature, $1/\sqrt{T}$. The beam driven flux, which scales as $1/Z$, is larger at lower temperatures.

Plotted in Figure 4.2.4b is the difference between the low temperature balanced and co-directed momentum predictions. The effect of the co-injected beam relative to

the balanced injection was to reduce the tungsten concentrations significantly inside $r=40$ cm and increase it outside this radius, as before. For example, α was reduced from $\alpha \sim 2.2$ to zero at a radius of ~ 40 cm, and increased from $\alpha \sim 2.1$ to $\alpha \sim 3$. at a radius of ~ 50 cm.

At the end of burn ($t=1.5s$), the centerline temperatures are predicted [63] to be 22 keV for the ions and 14 keV for the electrons when the full 32 MWatts of power is injected. Although these temperatures should not be reached with 16 MWatts of injected power, these temperatures represent the highest extreme important in TFTR, and therefore their effect on the impurity transport is examined here. Using these values for the transport calculation, and assuming the same parabolic profiles as before, Figure 4.2.5a is produced. As in the previous cases, this figure shows final tungsten profiles for the balanced momentum and co-directed momentum cases, with the base case profiles plotted using dashed lines for comparison. Since the impurity penetration into the plasma in the low temperature case is less than in the base case, it might be expected that the impurity penetration would be even deeper in the high temperature case. Contrary to this, for the higher temperature plasma impurity penetration, the tungsten penetration in the high temperature plasmas is also less than in the base case. Referring to Equation 3.9.1, the higher temperatures here reduced the gradient driven

fluxes by the inverse of the square root of the temperature, which was greater than the increase due to the increased charge state,

$$\frac{\Gamma_{z_{base}}}{\Gamma_{z_{highT}}} \approx \frac{z_{base}}{z_{highT}} \sqrt{\frac{T_{highT}}{T_{base}}} > 1 \quad . \quad 4.2.1)$$

Looking now at Figure 4.2.5b, the difference between the balanced momentum and co-injected momentum cases for the high temperature case, the co-injected beam effect is seen to be less than the effect in the base and low temperature cases. The co-directed beam here reduces the tungsten concentration at ~ 40 cm by $\approx .7$, and increases the concentration by a similar amount at ~ 50 cm. The continually decreasing beam effectiveness with increasing temperature is due to the increasing impurity charge state, since $\Gamma_{z_{beam}} \propto 1/z$. The gradient driven fluxes with which the beam driven flux competes are less effected by temperature, having both an increasing and decreasing component with temperature, $\Gamma_{z_{grad}} \propto z(T)/\sqrt{T}$.

The tungsten source rate that has been used up to this point is $1 \times 10^{16} / m^2 \text{sec}$. The actual source rate will be a complex function of many plasma and wall parameters. If the plasma actually is exposed to the tungsten source rate used here, concentrations of incompletely stripped tungsten

at a radius of 40 to 50 cm will be in the range of $\alpha = n_z z^2 / n_i \sim 4$. This would significantly degrade the plasma performance. In the base case, the tungsten at this point radiates at $\sim 700 \text{ kWatt/m}^3$, more than double the local power input to the electrons due to beam injection, and even 25% greater than the power injected to both the electrons and ions at this location. To examine the beam effectiveness at different impurity source strengths, a source rate of $0.5 \times 10^{16} / \text{m}^2 \text{sec}$, one-half the standard source rate, was used to calculate the results shown in Figure 4.2.6a. This is compared to the full source strength tungsten profiles, shown with dashed lines. The peak in the tungsten profile occurs at approximately the same radial location, $\sim 40 \text{ cm}$, for both source strengths when no net momentum is injected. This indicates that the penetration depth with balanced injection is not dependent on the source rate. This is due to the radial penetration velocity driven by gradients being independent of the impurity concentration, $V_{zr \text{ grad}} \neq f(n_z)$; see Equation 3.9.1. The radial transport velocity due to the beam, Equation 3.9.3, is inversely dependent on the impurity concentration, $V_{zr \text{ beam}} \propto 1 / n_z$. When the co-injected beams are used, the peak concentrations with the half source strength is pushed $\sim 5 \text{ cm}$ radially outward relative to the location of the peak with the full source strength, from ~ 43 to $\sim 48 \text{ cm}$.

Figure 4.2.6b shows the redistribution of the

tungsten due to the effect of beam co-injection. The effect of the co-directed beam on the half source rate case is less than the effect in the full source strength case, but the effect is not linear in density. The effect of the co-injected beam on the impurity flux is relatively independent of the impurity concentration when the drag ratio β_z / β_i is held constant. At the lower source rate, the beam is more effective on a per particle basis. This increased effectiveness is self limiting, since the impurities are kept to an outer region region of the plasma where the beam momentum input density is low.

Lighter impurities will be more affected by the beam than heavier impurities due to their smaller charge state, $\Gamma_{z, \text{beam}} \propto 1 / Z$. Tungsten will not be the only impurity present in TFTR. The wall is constructed of stainless steel, represented here by iron for calculational purposes. Iron is a factor of four less than tungsten in mass and three in atomic number, so the transport properties will differ substantially. Figure 4.2.7a shows the results of a transport calculation with an iron source at the plasma edge of $1 \times 10^{16} / \text{m}^2 \text{sec}$, the same numerical source as the tungsten base case. The iron penetrates into the plasma much less than the tungsten, the iron concentration peaking at ~ 60 cm instead of peaking at ~ 40 cm as in the tungsten case. The scaling of $\Gamma_{z, \text{grad}} \propto m_i Z$ of the gradient driven fluxes, Equation 3.9.1, accounts for the lowered penetration, since both the

mass and charge of the iron is less than those of tungsten. The beam driven flux, Equation 3.9.3, which scales as $1 / Z$, is larger for the lower charged iron. The net result is larger concentrations of impurities displaced outward, as seen in Figure 4.2.7b.

TABLE 4.2.1 TFTR Study Parameters

Machine

Major Radius	2.48 m
Minor Radius	.85 m
Toroidal Field	5.2 T
Plasma Current	2.5 MAmp
Loop Voltage	1.5 Volt
Volume	35 m ³

Performance

Average Density	8.x10 ¹⁹ /m ³
Electron Temperature	5. keV
Ion Temperature	5. keV
Edge Temperature	35. eV
Burn Time	1. to 1.5 sec

Beam

Injectors	4 (3 Co, 1 Counter)
Energy	120 keV
Beam Mass	2 amu
Power	32.5 MWatt total
Current Fractions	E .42
	E/2 .33
	E/3 .25
Injection Angle	68° from perpendicular

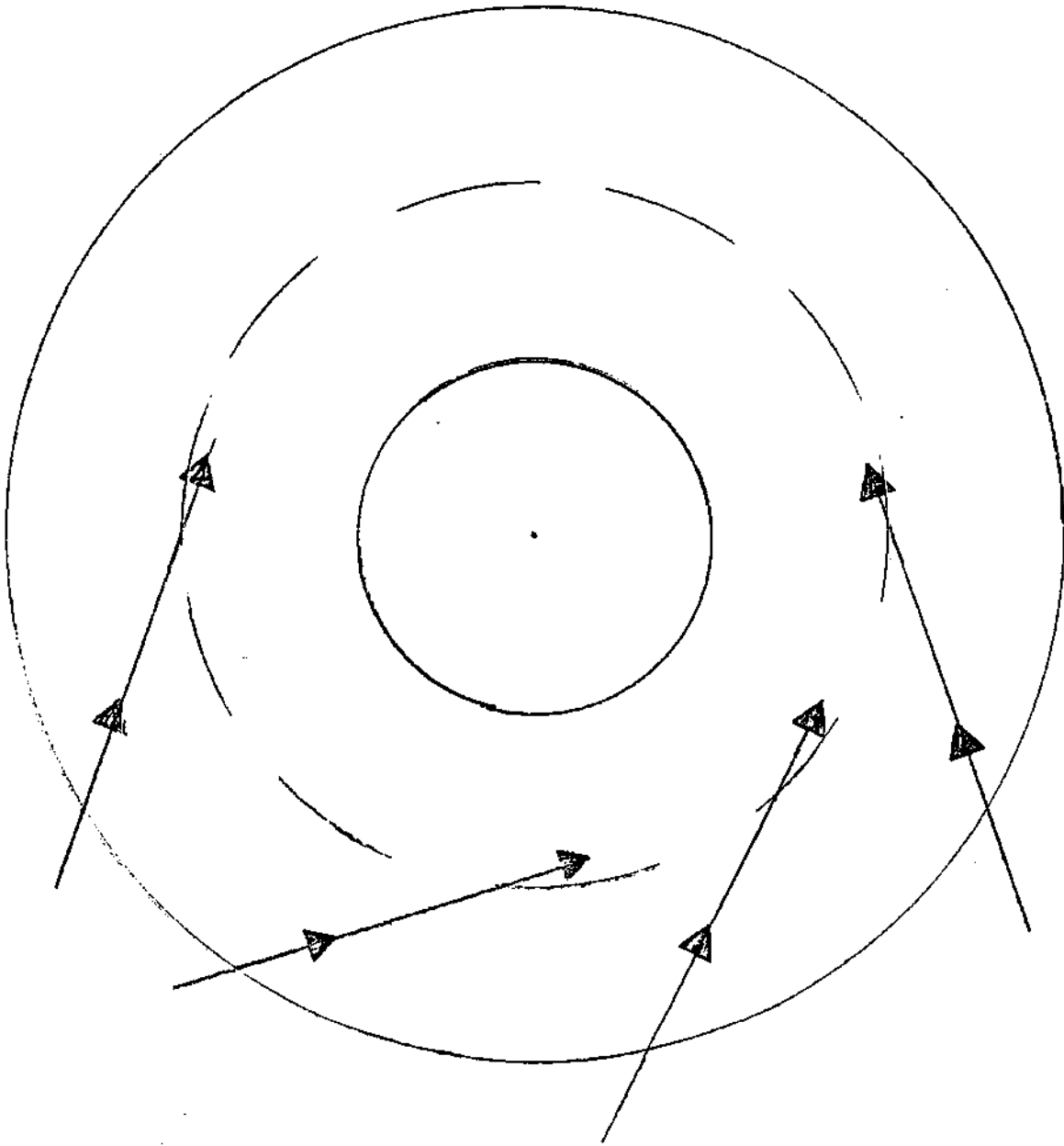
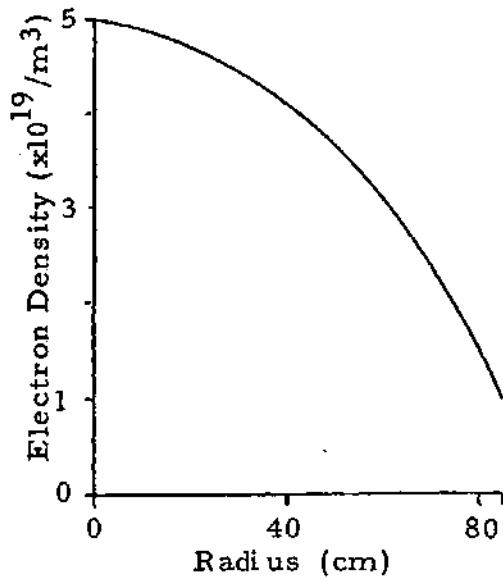
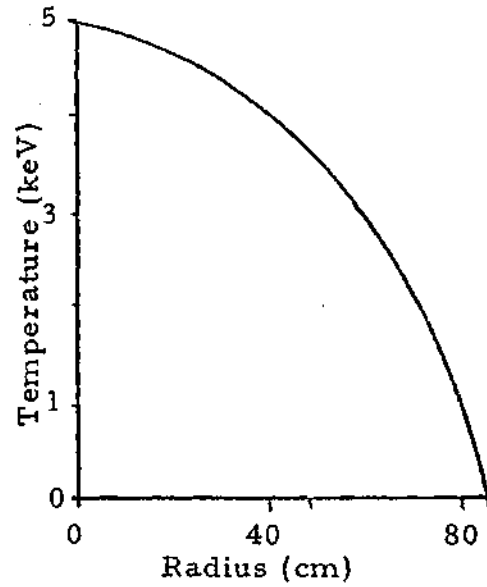


Figure 4.2.1 TFTR Neutral Beam Layout



(a) Electron Density



(b) Ion and Electron Temperature

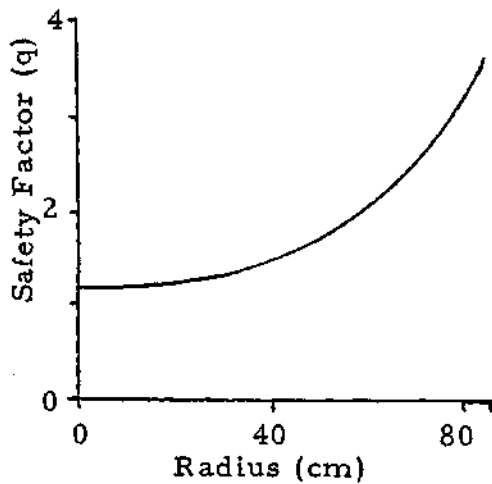
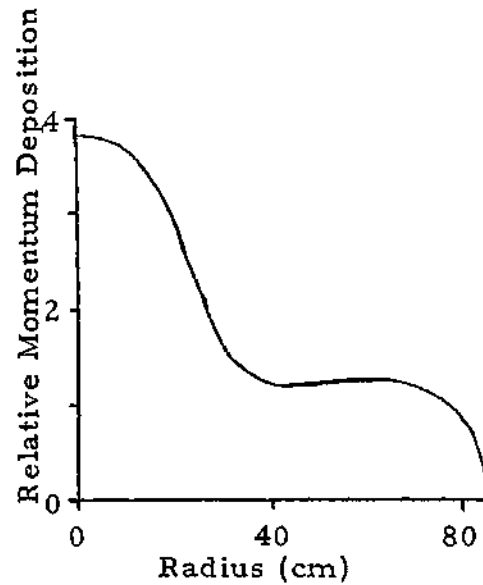
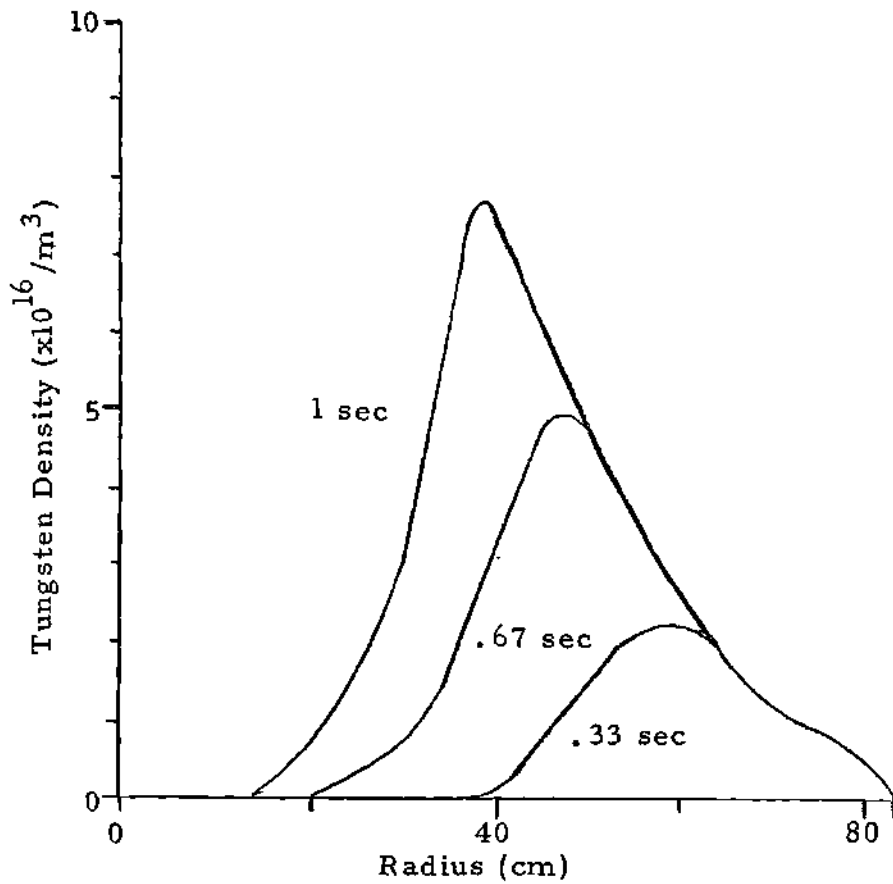
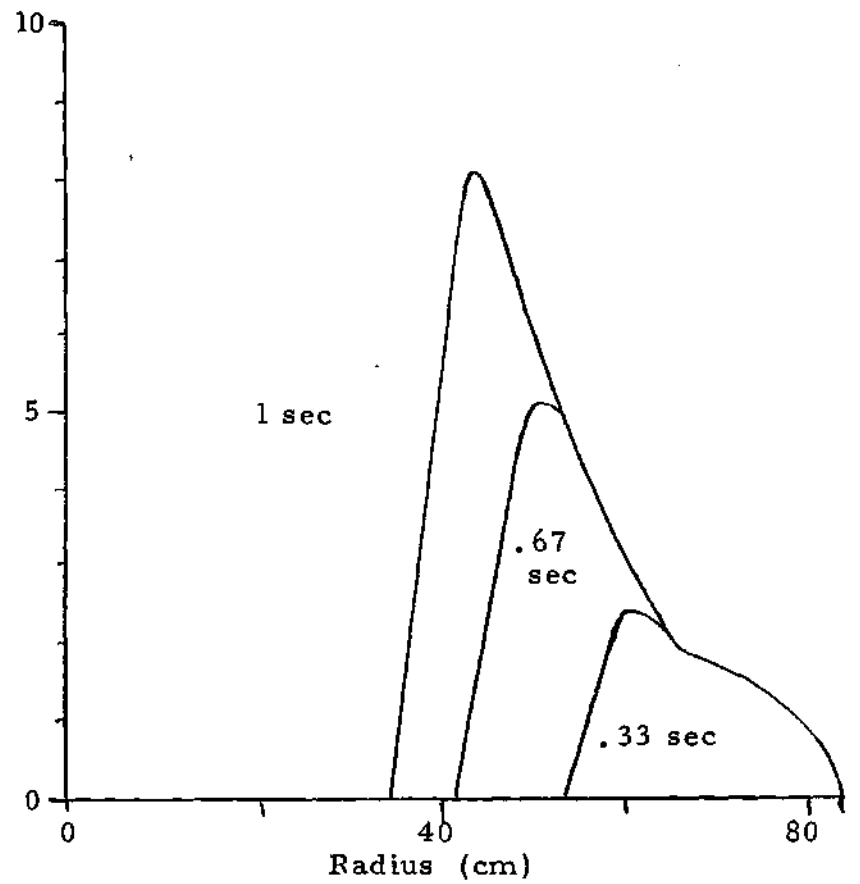
(c) Calculated Safety Factor
for above profiles(d) Calculated Momentum
Deposition for above
profiles, $E_b=120$ keV

Figure 4.2.2 Reference TFTR Density, Temperature, Safety Factor, and Momentum Deposition Profiles
(a) and (b) from Reference 62

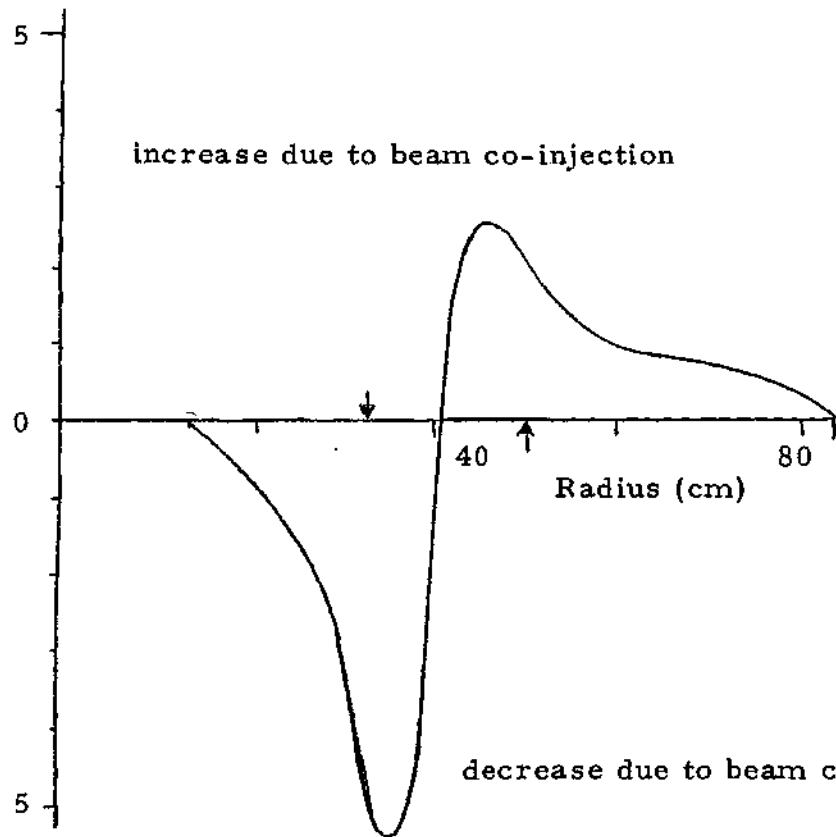


(a) Balanced Momentum



(b) 16 MWatts Co-injected

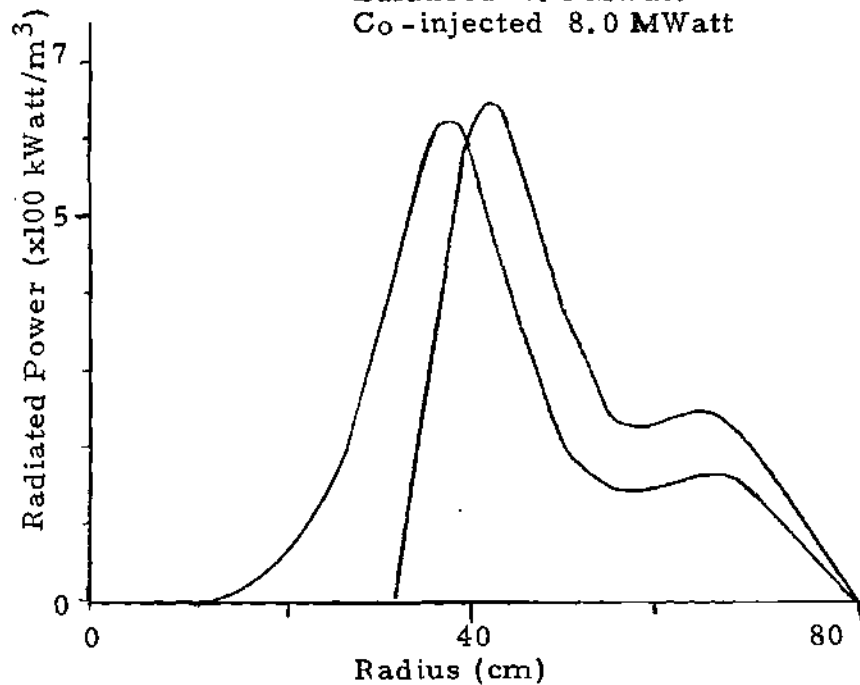
Figure 4.2.3 Tungsten Density Profiles in TFTR for Base Case



(c) Change in Tungsten Concentration Due to Neutral Beam Driven Impurity Flow Reversal in TFTR, $P_b=16$ MWatt

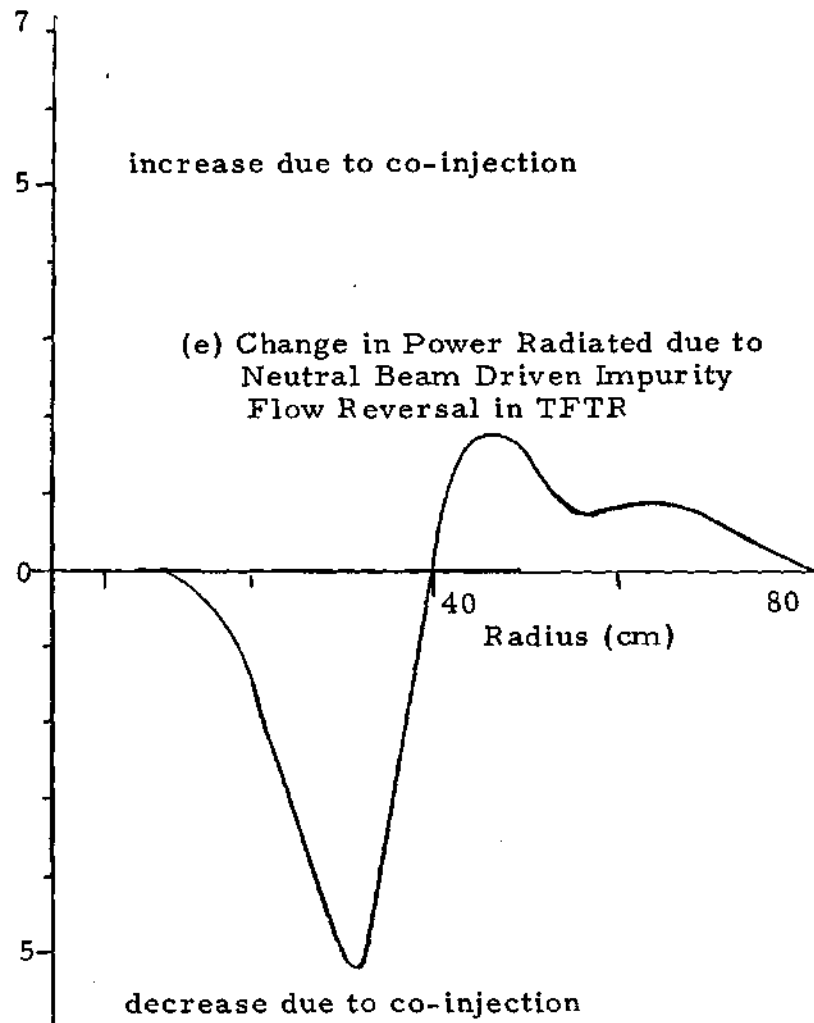
Figure 4.2.3 (continued) Tungsten Density Profiles in TFTR for Base Case

Total Power Radiated
 Balanced 7.4 MWatt
 Co-injected 8.0 MWatt

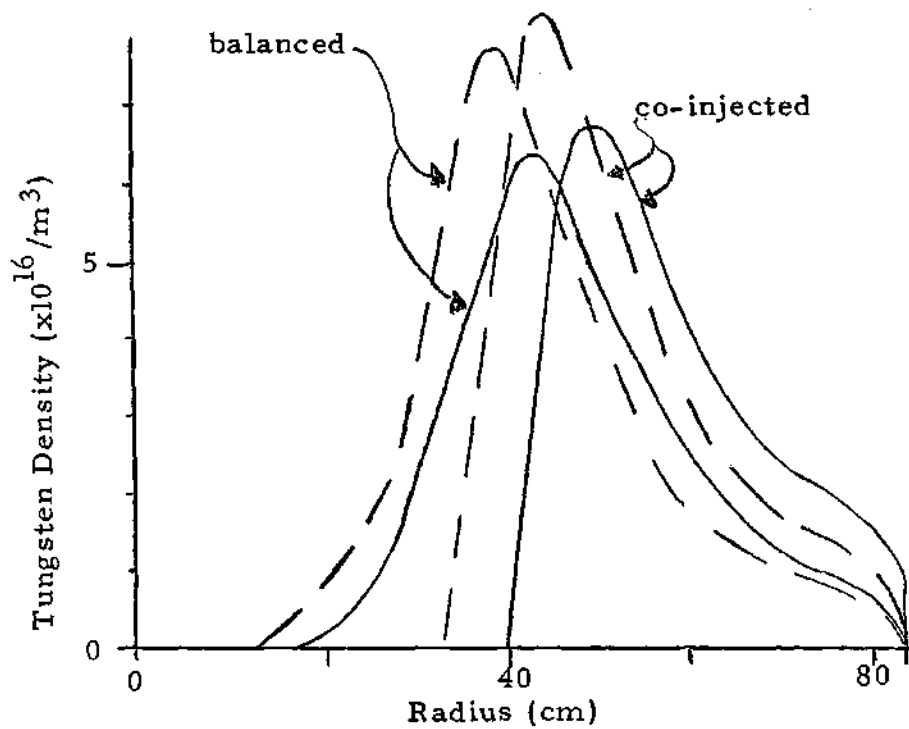


(d) Power Radiated from TFTR due to Tungsten Concentrations

Figure 4.2.3 (continued) Tungsten Density Profiles in TFTR for Base Case, $P_b=16$ MWatt

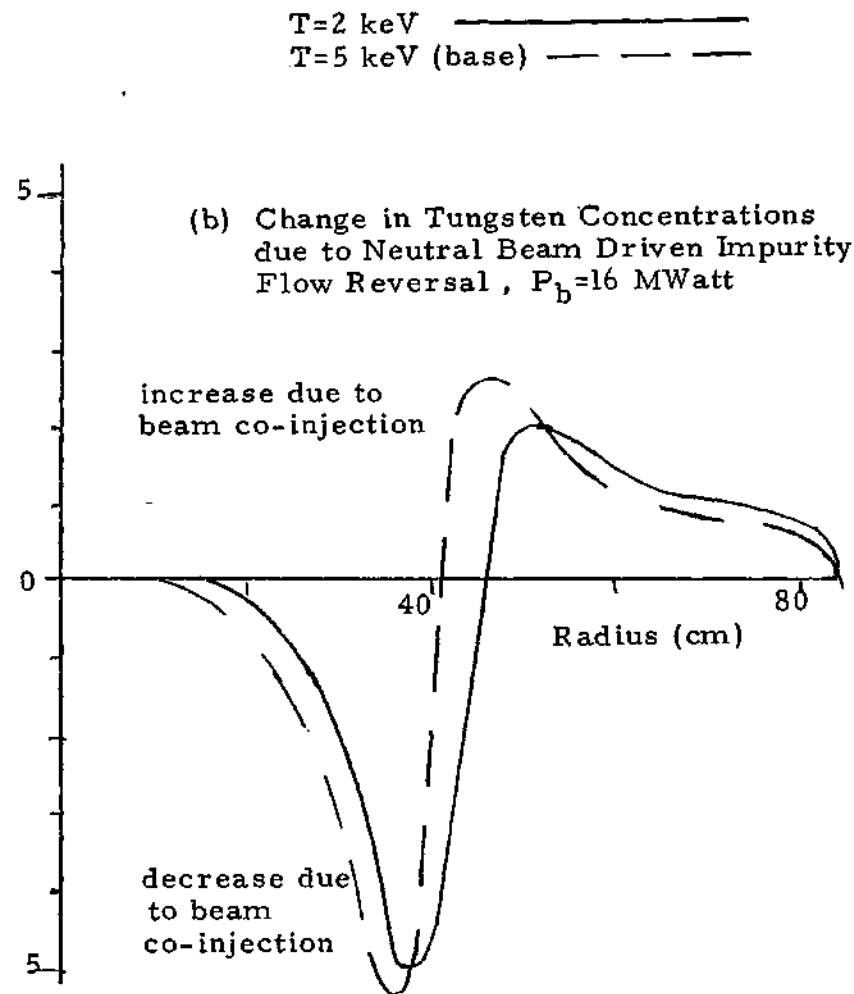


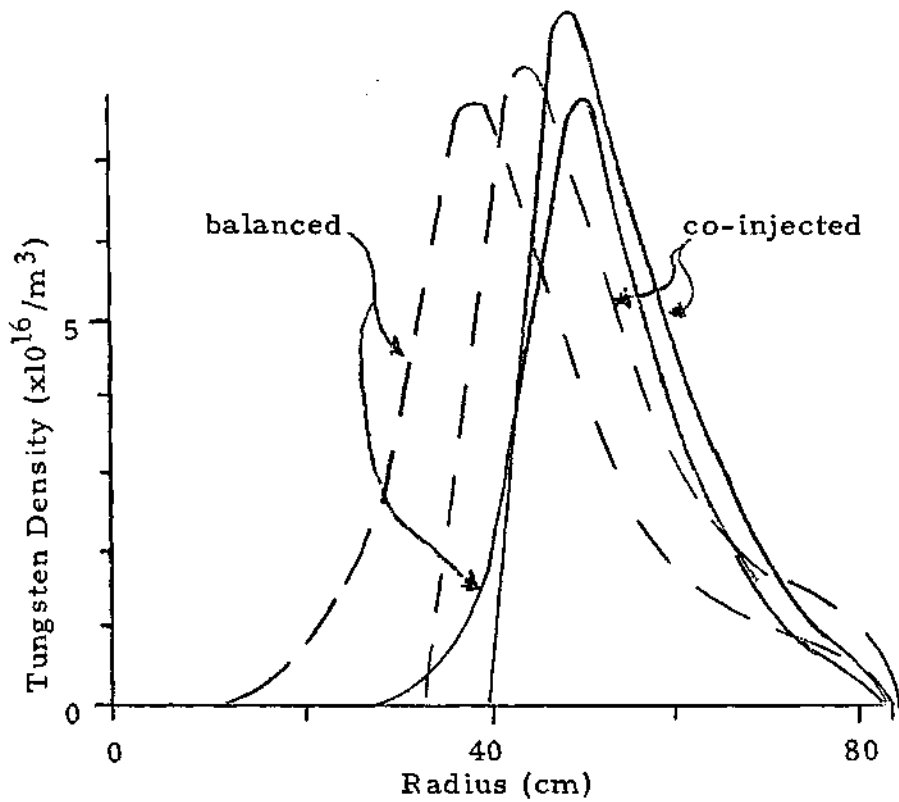
(e) Change in Power Radiated due to Neutral Beam Driven Impurity Flow Reversal in TFTR



(a) Tungsten Profiles

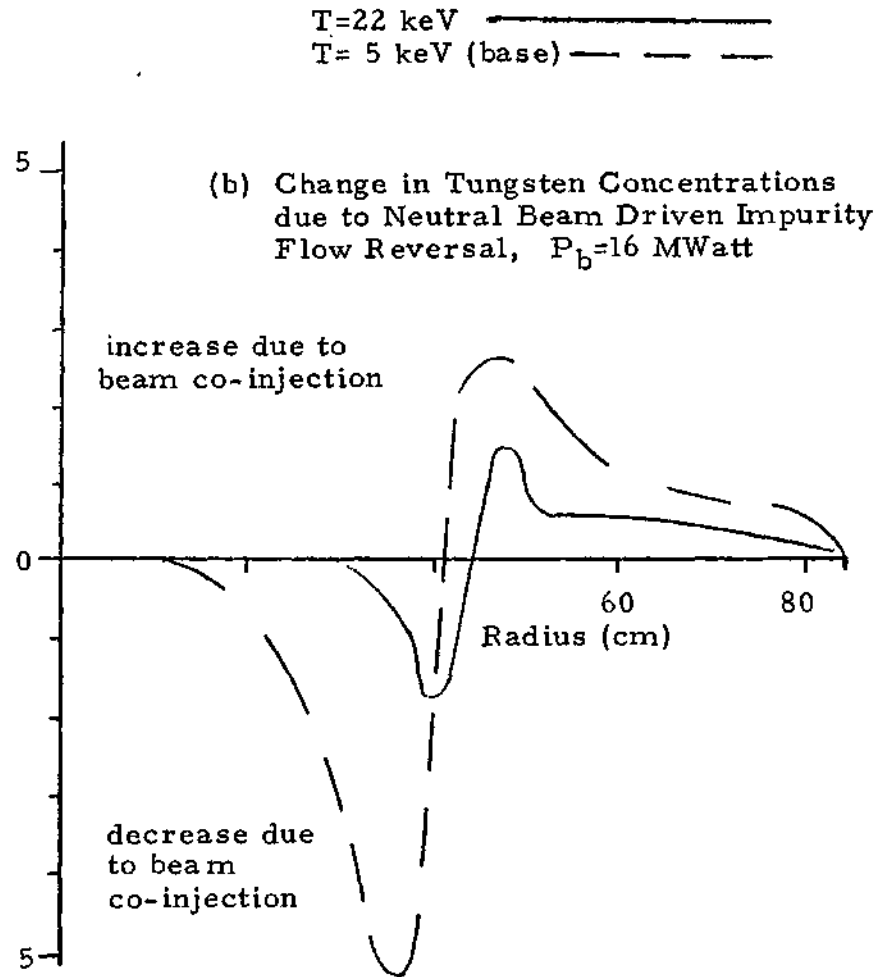
Figure 4.2.4 Tungsten Density Profiles in TFTR for Centerline Temperatures $T=2$ keV and $T=5$ keV

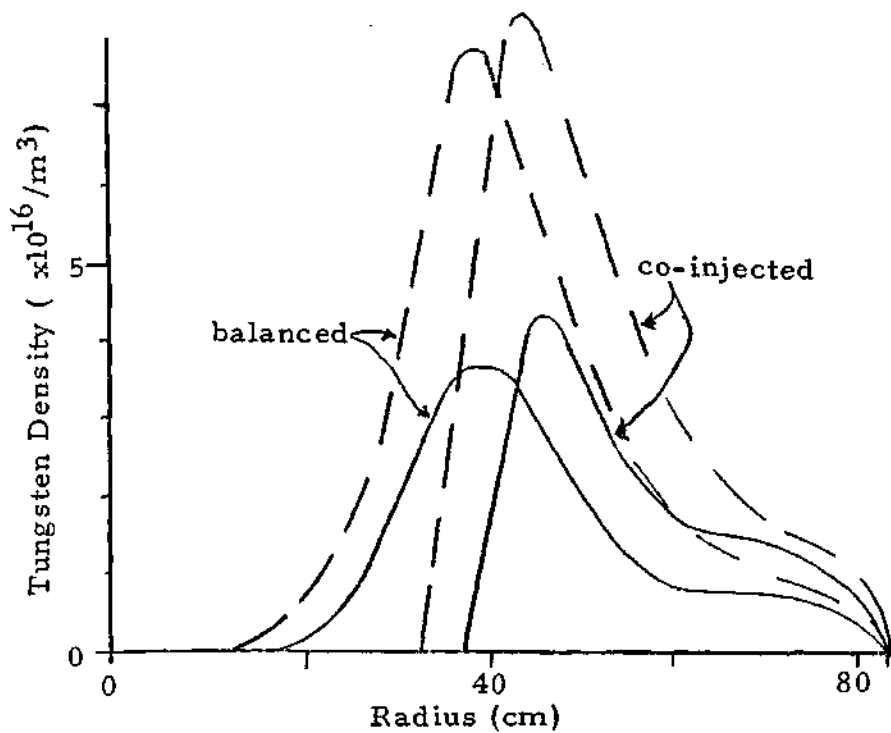




(a) Tungsten Profiles

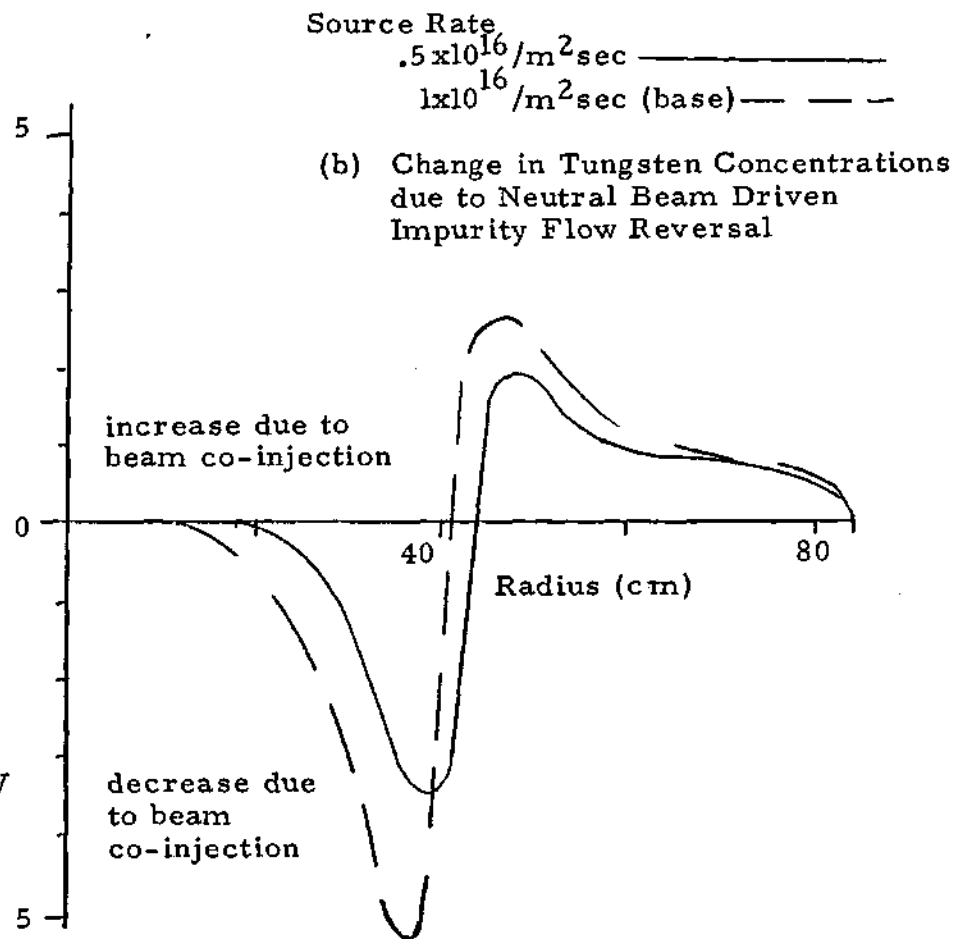
Figure 4.2.5 Tungsten Density Profiles in TFTR for Centerline Temperatures $T=22 \text{ keV}$ and $T=5 \text{ keV}$





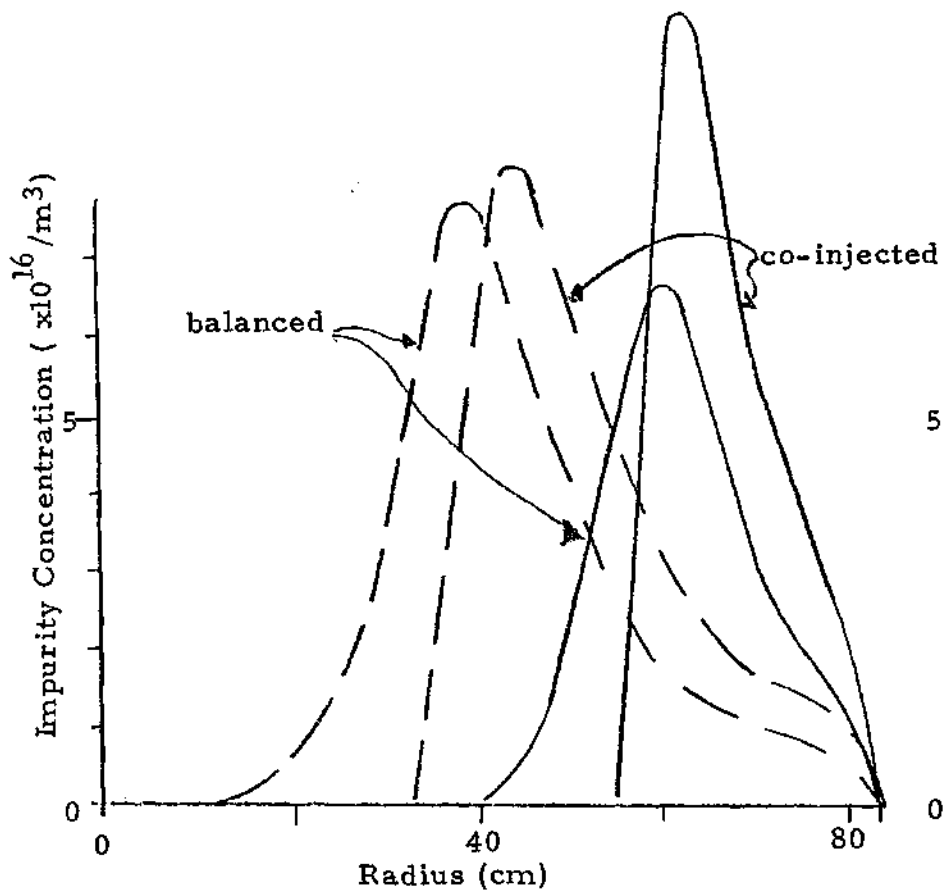
(a) Tungsten Profiles

Figure 4.2.6 Tungsten Density Profiles in TFTR with Edge Source Rates of $1 \times 10^{16}/\text{m}^2\text{sec}$ and $0.5 \times 10^{16}/\text{m}^2\text{sec}$ $P_b = 16$ MWatt, $T_i = T_e(\underline{Q}) = 5$ keV



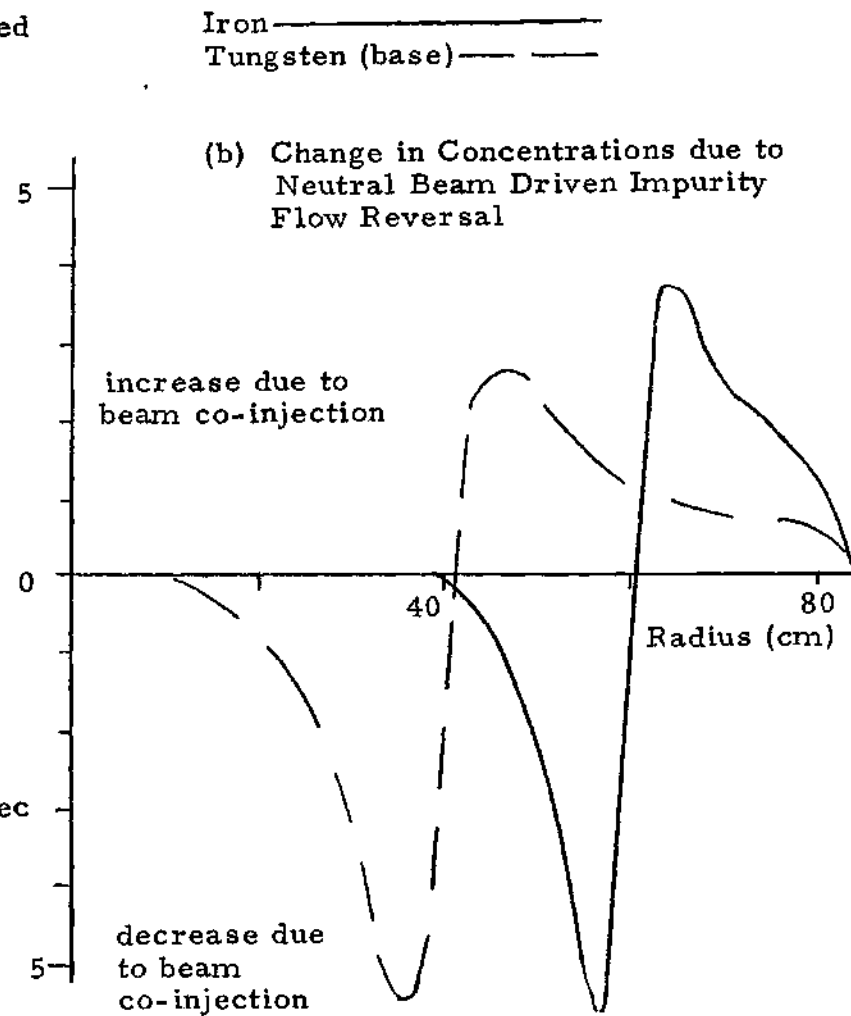
Source Rate
 $0.5 \times 10^{16}/\text{m}^2\text{sec}$ ———
 $1 \times 10^{16}/\text{m}^2\text{sec}$ (base) — — —

(b) Change in Tungsten Concentrations due to Neutral Beam Driven Impurity Flow Reversal



(a) Tungsten and Iron Profiles

Figure 4.2.7 Iron and Tungsten Profiles in TFTR
 $T_i = T_e(\text{core}) = 5 \text{ keV}$, $P_b = 16 \text{ MWatt}$, $\text{Source} = 1 \times 10^{16}/\text{m}^2\text{sec}$



4.3 Predictions for FED

The effect of co-injected neutral beams upon radial transport of impurities in the future Fusion Engineering Device (FED) [60] is studied in this section. FED is similar in size and design goals to the International Tokamak Reactor (INTOR) [61], so predictions made for FED will be valid for INTOR and other designs of tokamak engineering test reactors as well. Machines of this size class, planned for the 1990's, are in the conceptual design stages. Their general objective is to demonstrate the engineering feasibility of many reactor components and component interactions. Recent studies [61] indicate that the sputtering erosion of limiter or divertor collector plate material may be a serious problem unless a cold, radiating edge can be achieved which would reduce the energy of particles striking these components below the sputtering threshold. The purpose of this work is to examine the possibility that the co-injection of a moderate amount of neutral beam power can be used to accumulate impurities in the plasma edge region to produce a cold radiating edge, while preventing the penetration of the impurities to the center of the plasma.

FED will require external heating in addition to ohmic heating. The two leading candidates are neutral beam injection and radio frequency heating. Net toroidal momentum can be supplied both by beam injection and by some

types of radio frequency heating. Momentum deposition by radio frequency heating, as well as the practicality of heating with radio frequency methods that also induce toroidal momentum, are outside the scope of this investigation, and will not be addressed here.

The injection scenario is also not set in this machine. It is possible to run the tokamak in a sub-ignition mode, where auxiliary heating is needed at all times to maintain the plasma temperature. If the reactor is ignited, heating is only needed to bring the reactor to ignition, although additional injection can be used for plasma temperature or impurity control.

The FED design parameters used for this study are listed in Table 4.3.1 [60]. The plasma volume is a factor of approximately ten larger than TFTR, and the pulse length approximately a factor of fifty longer. Since the ratio of surface area to volume of FED is only a factor of two smaller than TFTR, and the pulse length a factor of fifty longer, FED can tolerate a much smaller edge source strength of impurities. For FED, a source rate of $1 \times 10^{15} / \text{m}^2 \text{sec}$ of iron was chosen. With this source strength, the average impurity concentration in terms of $\bar{\alpha} = \overline{n_i Z^2} / \bar{n}_e$ is $\bar{\alpha} \sim 0.5$ at the end of the 50 sec plasma burn.

The total beam power used here for a reference base is 30 MWatt, about half the power that will be needed for startup. The auxiliary power needed to maintain the plasma

in $Q = 5$ operation is 36 MWatts total. The beam system parameters used here are taken from the FED design [60]. This neutral beam system is an alternate to the R-F heating system. The injection angle is limited to 53° from the perpendicular to the magnetic axis by access limitations between the toroidal field coils. The low efficiency of neutralization of D^+ limits the practical beam energy to about 150 keV since the neutralization efficiency drops from 53% to 19% as the energy rises from 100 keV to 200 keV. Good beam penetration to the plasma center was found at both the primary (150 keV) and the secondary (75 keV) beam energies.

The temperature and density profiles projected for an FED like machine are taken from the design document [60], and held fixed during the calculation. The density profile used for this study is shown in Figure 4.3.1a. This profile is very flat out to the plasma edge, where it drops sharply. The temperature profile shown in Figure 4.3.1b is more centrally peaked than those of TFTR, the large fusion power at the center accounting for most of this peaking.

As in the previous section, the model developed in Chapter 3 is used for the calculations. The Fokker-Planck code is used to calculate the beam momentum deposition, a sample of which is shown for the base case in Figure 4.3.2. The sharp central peak in the momentum deposition profile is simply due to geometric factors, since the beam passes

through a much greater portion of the small center flux surfaces than it does the larger, outer flux surfaces.

Figures 4.3.3a and b show the time evolution of the iron profile for 50 seconds in the balanced momentum and co-directed momentum cases, respectively. As in TFTR, the incoming flux fills the outermost regions of the plasma to an equilibrium level. The radii at which this equilibrium is reached then progresses inward. Figure 4.3.3c shows the difference in the iron concentrations due to the effect of the co-injected beam. The density differential driven by the co-injected beam relative to the balanced input involves approximately 17% of the total amount of iron. The increase in iron concentrations due to the effect of the co-injected beam is volumetrically centered 55% closer to the plasma edge ($r=1.4\text{m}$) than the decrease in iron concentrations. Since much of the tungsten did not penetrate to the center of TFTR, the radial displacement on a percentage basis is lower than in FED. Fewer of the impurities are deterred in FED, mainly due to the lower beam momentum density, since approximately double the TFTR beam power is injected into ten times the plasma volume. The iron concentration near the plasma edge is very small, since the steep ion gradients drive the iron through this region very quickly.

The impurity radiation profiles due to the iron concentrations presented in Figures 4.3.3a and b are shown in Figure 4.3.3d. The peak power radiated from the

electrons occurs where the peak iron concentration occurs. This peak is $\sim 55 \text{ kW/m}^3$ for the balanced momentum case and $\sim 65 \text{ kW/m}^3$ for the co-injection of momentum case, in both cases constituting about 50 % of the power injected to the electrons at that radius. The total power radiated from the plasma is about 10 MWatt, which can be compared to 200 MWatt of projected fusion power. The radiated power is 2% higher when the beams are co-injected relative to balanced injection. This is due to more iron being kept to radial regions where some of the iron is incompletely stripped of its electrons, enhancing the ionization and recombination radiation. The difference between the balanced momentum and co-injected momentum radiation profiles are shown in Figure 4.3.3e. The radiation is decreased at the plasma center by 10 to 20 kW/m^3 , and increased by a maximum of 10 kW/m^3 at a radius of 85 cm, which would help to maintain a cooler edge.

Now that a substantial effect of the co-injected beam on the impurity accumulation in FED has been predicted, it is appropriate to investigate the effect of different plasma operating conditions. First, the plasma main ion density and temperature profiles are varied. The profiles used for this study are shown in Figure 4.3.4a and b, with the dashed lines representing the base case profiles. For the ion density profile, the plasma edge was filled with cool ions to 90% and 100% of the centerline ion density, significantly reducing and eliminating the density gradients,

respectively. These are plausible situations in which the high plasma edge density would serve to protect the first wall from fast ion bombardment by maintaining a cool edge temperature [61]. The impurity transport effect of two additional temperature profiles is also examined. As seen in Figure 4.3.4b, one of these profiles is more centrally peaked than the base profile, and the other is less centrally peaked. The same centerline temperature is used with all three ion temperature profiles. These represent plausible variations in the possible operational characteristics of the tokamak.

Figure 4.3.5a shows the final iron profile for FED when the edge is increased to 90% of the centerline density value. Both with and without net momentum injection, the iron density at the plasma edge is increased due to the lowered ion density gradient driven inward transport. This enhances the edge radiation somewhat. With more of the iron kept to the plasma edge, less is in the plasma interior, as can be seen by comparing the base iron profiles to the profiles calculated with a 90% main ion edge density. The edge density change has affected transport in the outer 30 cm of the plasma radius only, since both the balanced momentum and co-injected momentum cases exhibit similar profiles throughout the rest of the plasma. The profile peaks for both injection situations are the same for both edge densities.

Comparing now the effect of the 90% edge density on the deterrence of iron penetration driven by co-injection of momentum, it is directly observed that overall, the impurity is less effected by the beam in the 90% edge density case. This is due primarily to the fact that the momentum source has less to effect. For both density profiles, the first 20 cm of the plasma radius has been kept impurity free by the co-injected momentum source.

In the next case, the ion density at the plasma edge was increased to the central ion density value, so that no density gradient exists. Using this, the iron profiles in Figure 4.3.6a were calculated. The iron concentrations in the outer 30 cm of the plasma are significantly higher than even the 90% edge density case, which greatly enhances the radiation at the plasma edge, see Figure 4.3.6c. The plasma edge radiation for this case is $\sim 350 \text{ kW/m}^3$, about three times the volume averaged injected power ($\sim 100 \text{ kWatts/m}^3$) at 30 MWatts. Without the co-injected beam, the radiation power at the plasma edge is $\sim 200 \text{ kW/m}^3$, about 60% of the radiation relative to when the beam is co-injected. As in the 90% edge density case, the amount of iron which penetrates to the rest of the plasma is significantly reduced.

The inhibition of iron penetration due to the effect of co-injection of a beam when there is no density gradient is plotted in Figure 4.3.6b. Comparing this to the beam

driven iron concentration difference of the base case, shown with dashed lines, it can be seen that the total beam effect is again less than in the base case. Although there is less central accumulation to displace, the increase in edge iron density due to co-injection is much higher than even the 90% edge density case. This increase is caused by the removal of the ion gradient driven flux, which dominated the previous cases.

A more peaked ion temperature profile allows greater penetration of iron into FED. This is due to the gradient driven flux being larger over most of the plasma, the gradient driven flux scaling as $\Gamma_{Egrad} \propto 1/\sqrt{T}$. Figure 4.3.7a shows the final iron profiles after 50 seconds calculated using the peaked ion temperature profile of Figure 4.3.3b. The iron penetration is greater than in the base case for both the balanced momentum and co-injected momentum cases. The larger gradient driven flux also reduces the relative effectiveness of the co-injected momentum source on reducing the iron influx, as can be seen in Figure 4.3.7b, which shows the inhibition of iron penetration by co-injection.

If the main ion temperature profile is less peaked than the base case, as plotted in Figure 4.3.4b, iron penetrates less deeply into the plasma than it penetrates in the base case. It was noted above that a lower overall temperature enhanced the penetration of iron into FED. Figure 4.3.8a shows that the reverse is also true. Less

penetration of iron is allowed when the main ion temperature profile is less peaked since the temperature is higher in most of the plasma. The amount of iron displaced by the co-injected beam, shown in Figure 4.3.8b, is also larger for the less peaked ion temperature profile, the momentum driven flux having a smaller gradient driven flux with which to compete.

The inhibition of iron penetration is dependent on the co-injected power. The $t = 50$ sec iron profiles using none, 10 MWatts, 30 MWatts, and 50 MWatts of co-injected power are shown in Figure 4.3.9a. As expected, the profile difference driven by the beam effect relative to the balanced beam input, Figure 4.3.9b, increases with co-injected beam power.

TABLE 4.3.1 FED Study Parameters

Machine

Major Radius	4.8 m
Minor Radius	1.4 m
Plasma Elongation	1.6
Toroidal Field	3.6 T
Plasma Current	2.5 MAmp
Volume	300 m

Performance

Average Density	$1 \times 10^{20} / \text{m}^3$
Electron Temperature	22. keV
Ion Temperature	26. keV
Edge Temperature	35. eV
Burn Time	50 sec

Beam Used

Energy	150 keV
Beam Mass	2 amu
Power	30. MWatt Co-injected
Current Fractions	E .5
	E/2 .25
	E/3 .25
Injection Angle	53° from perpendicular

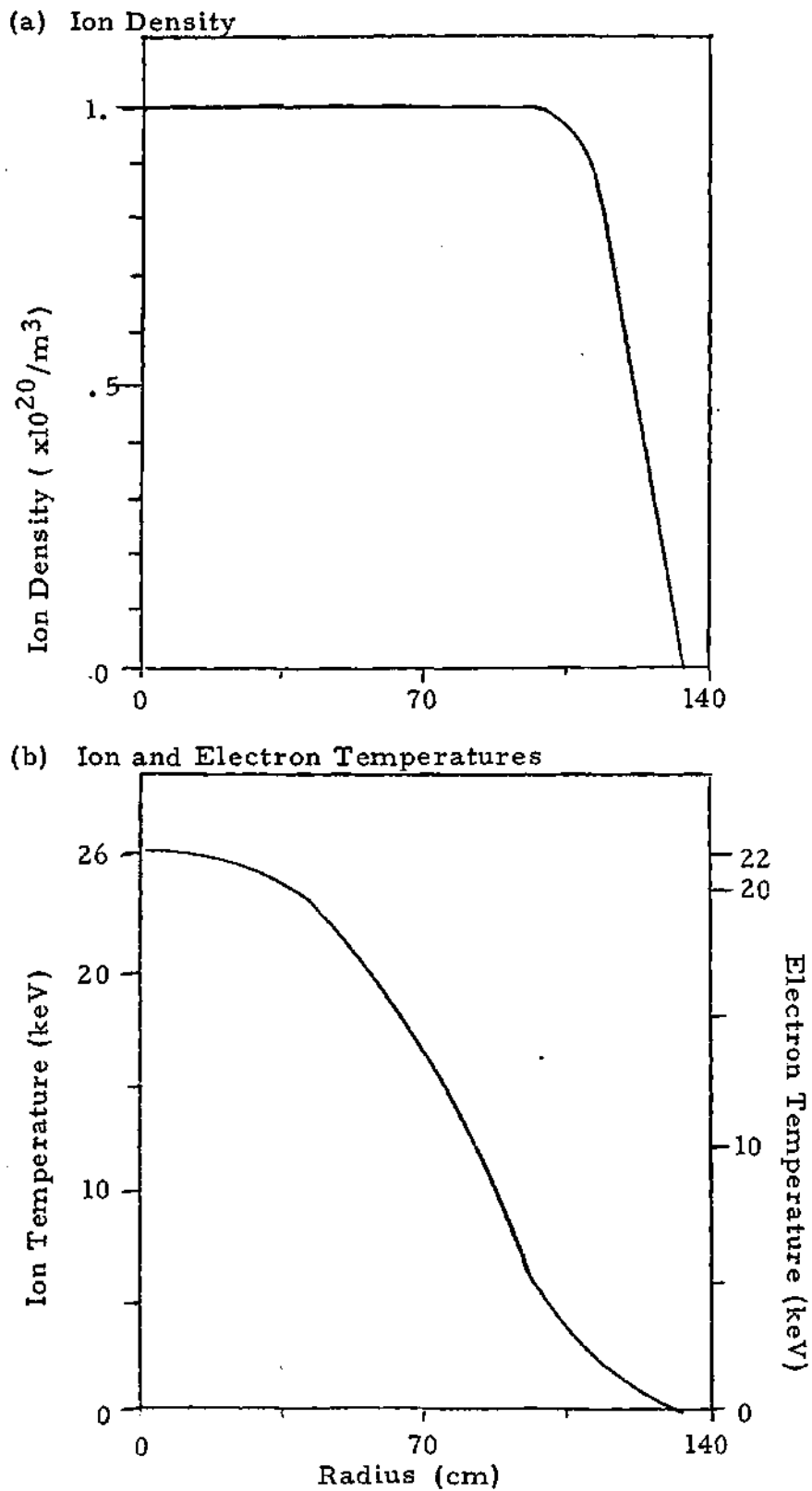


Figure 4.3.1 Density and Temperature Profiles Used in FED

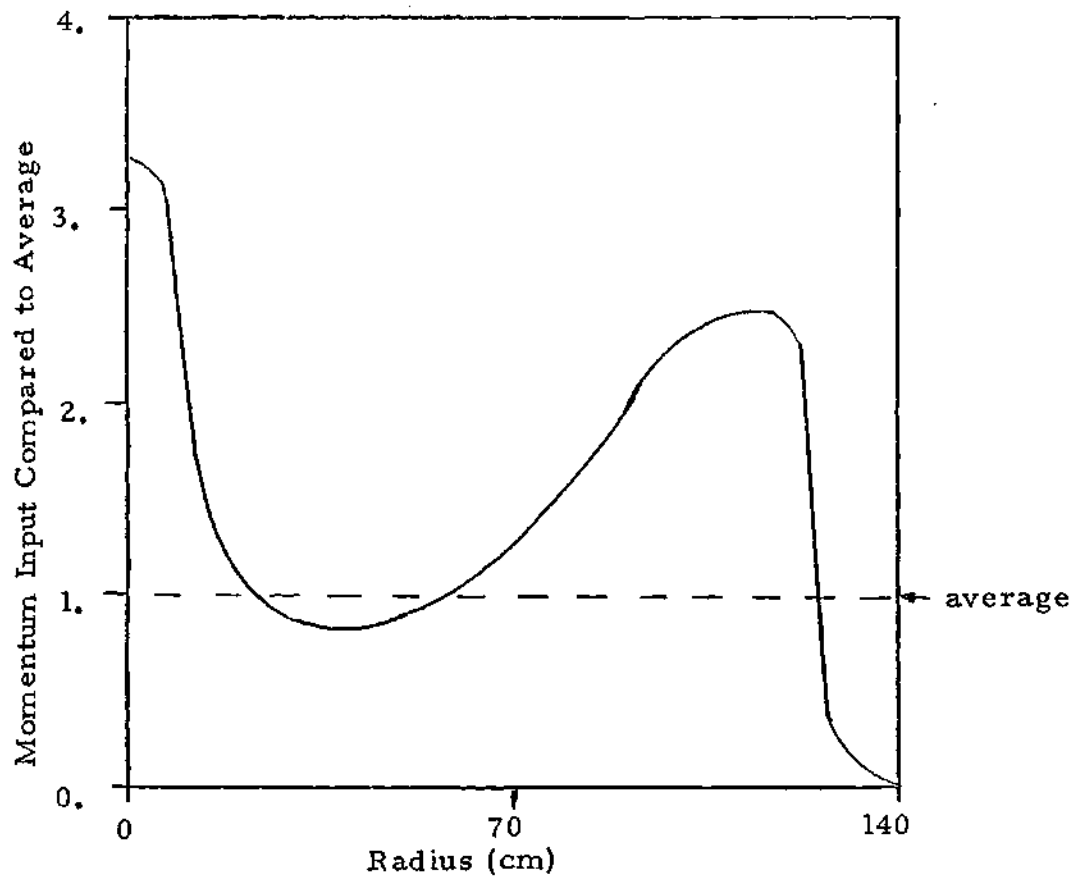
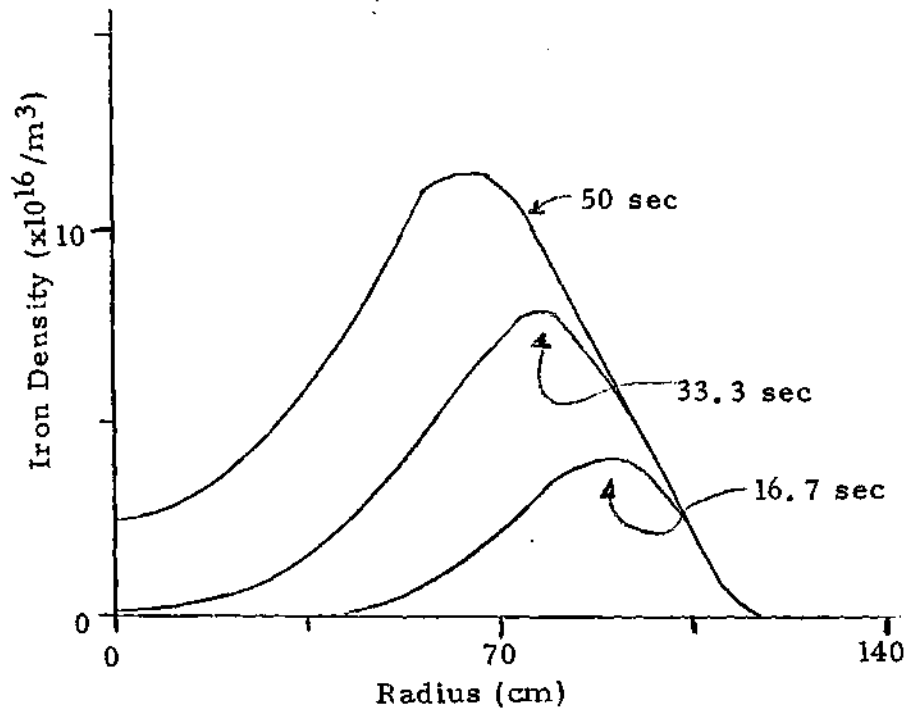
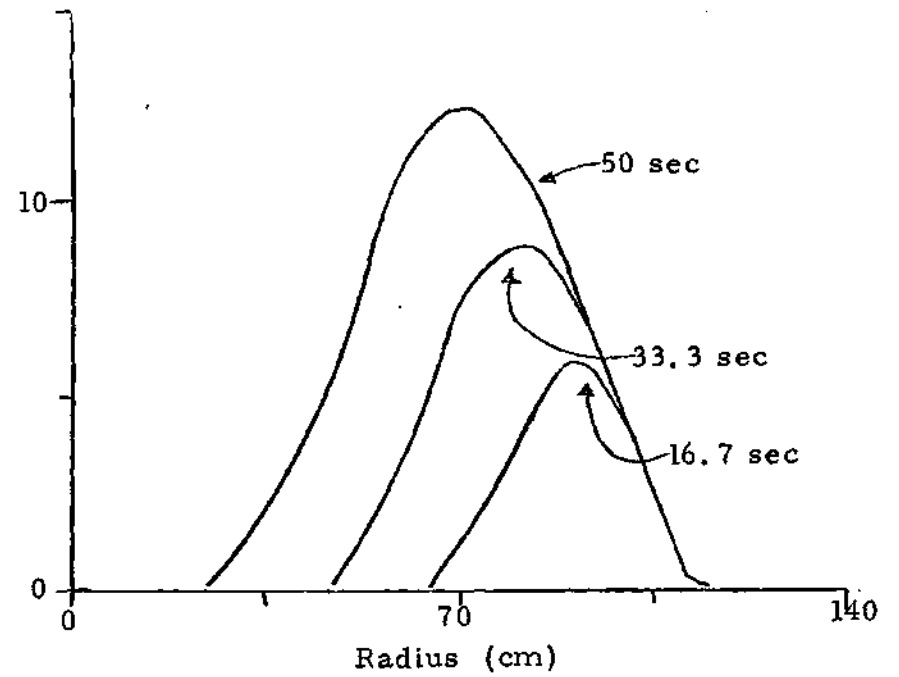


Figure 4.3.2 Neutral Beam Momentum Deposition Profile in FED

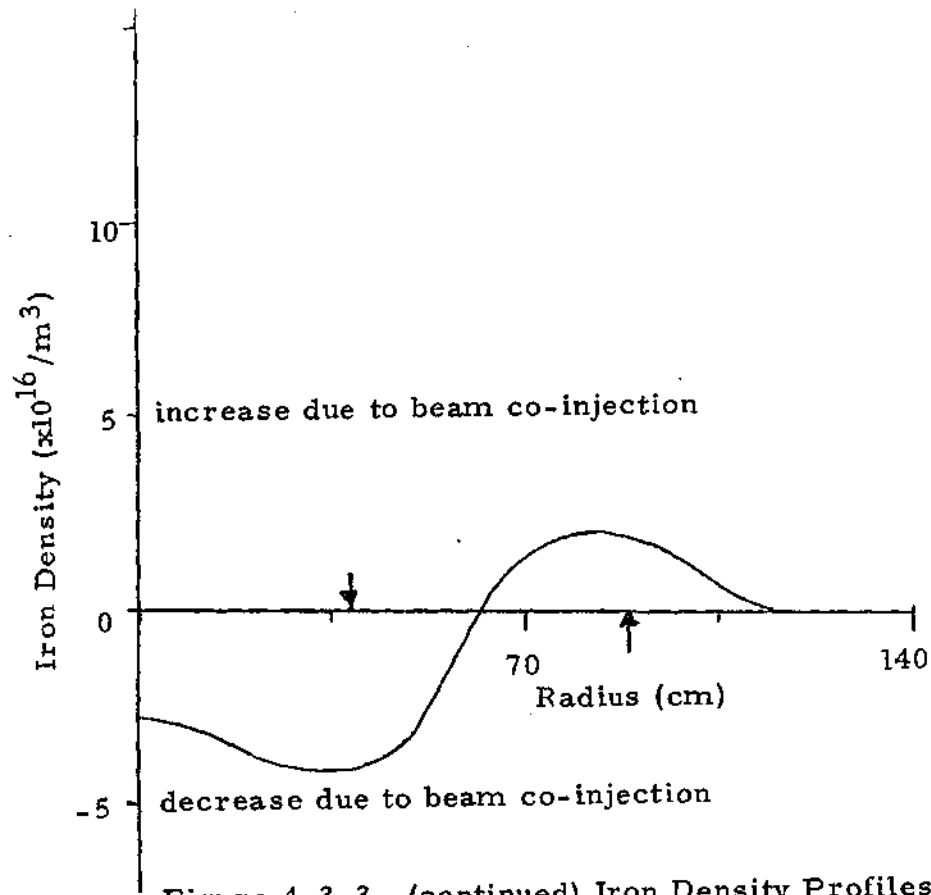


(a) Balanced Momentum



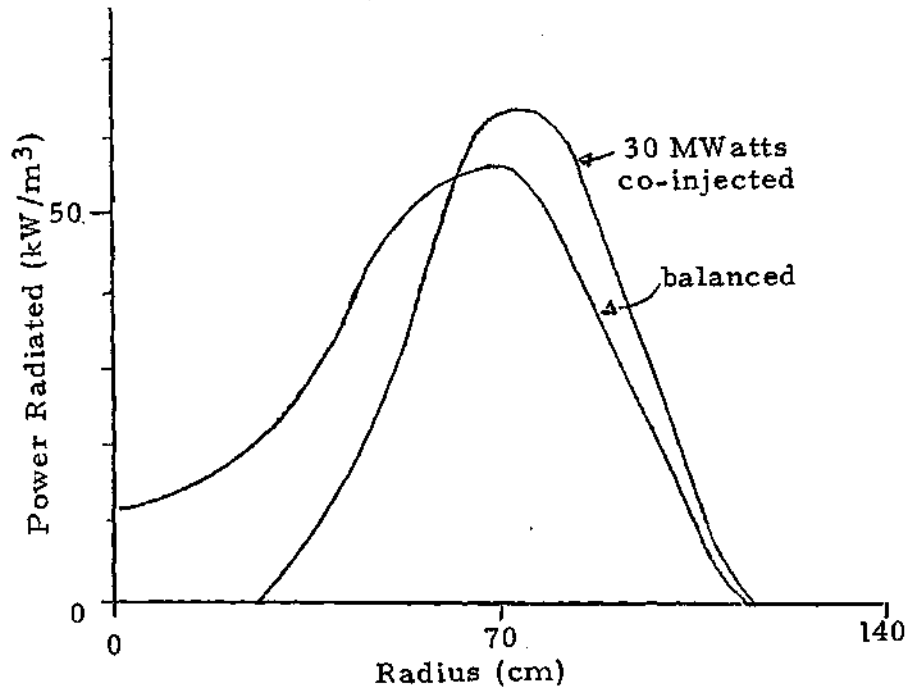
(b) 30 MWatts Co-injected

Figure 4.3.3 Iron Density Profiles in FED for Base Case



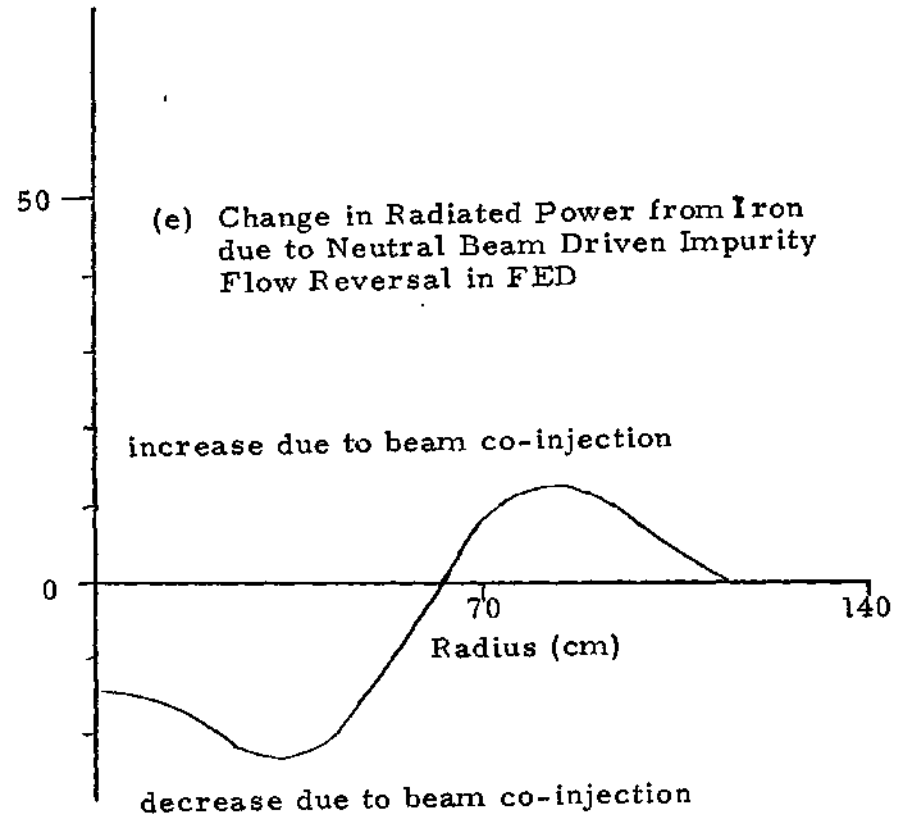
(c) Change in Iron Concentrations due to Neutral Beam Driven Impurity Flow Reversal
 $P_b = 30$ MWatt

Figure 4.3.3 (continued) Iron Density Profiles in FED for Base Case

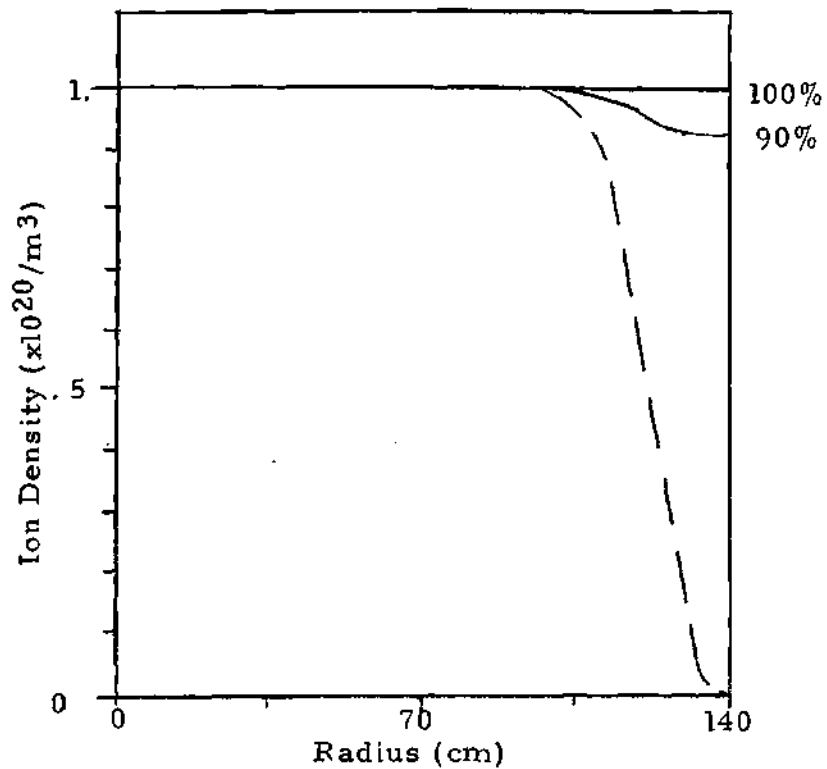


(d) Power Radiated from Iron

Figure 4.3.3 (continued) Iron Density Profiles in FED for Base Case



(a) Ion Density



(b) Ion Temperature

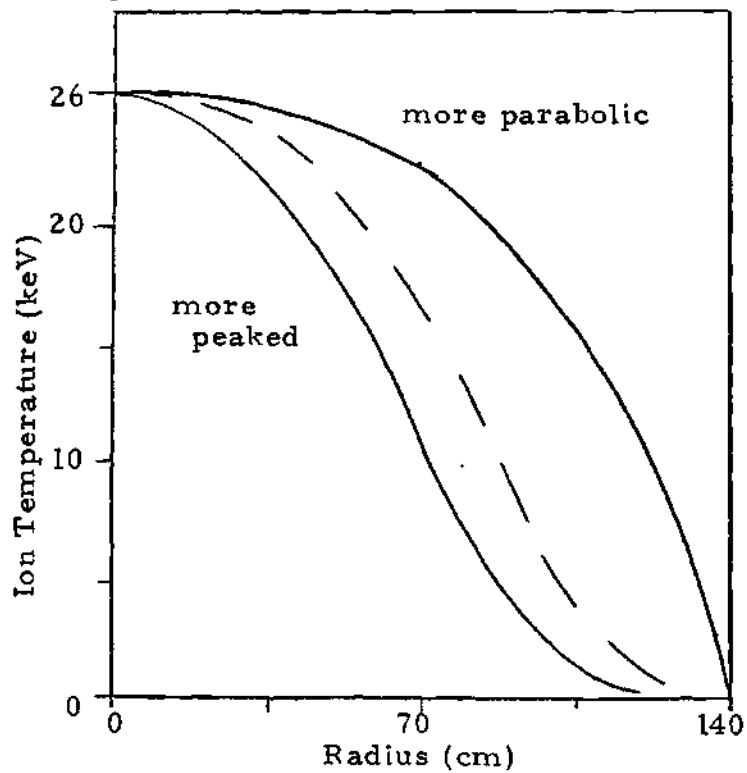


Figure 4.3.4 Plasma Profiles Used to Calculate FED Profile Sensitivity

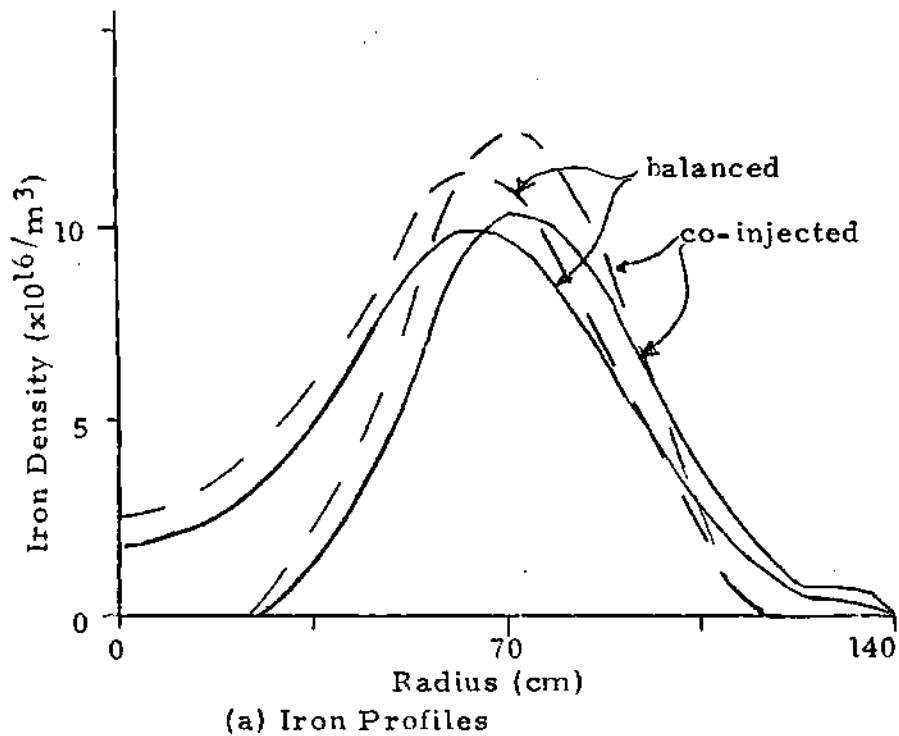
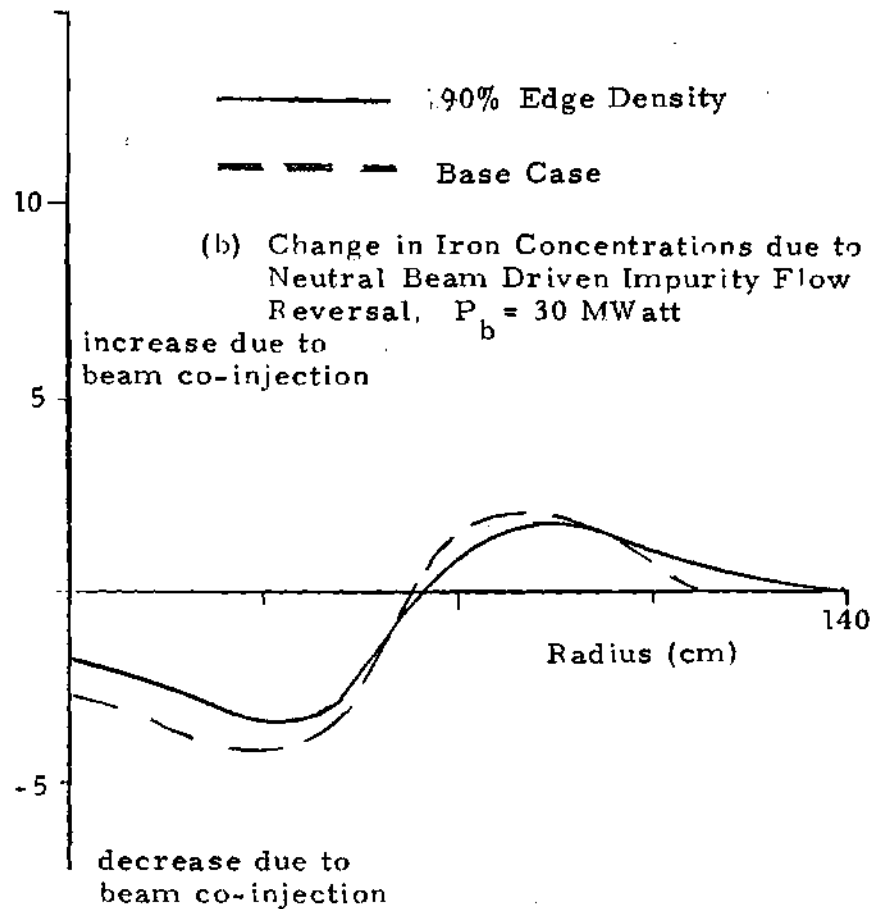


Figure 4.3.5 Iron Concentrations in FED with Low Edge Density and 90% of Centerline Edge Density Main Ion Profiles



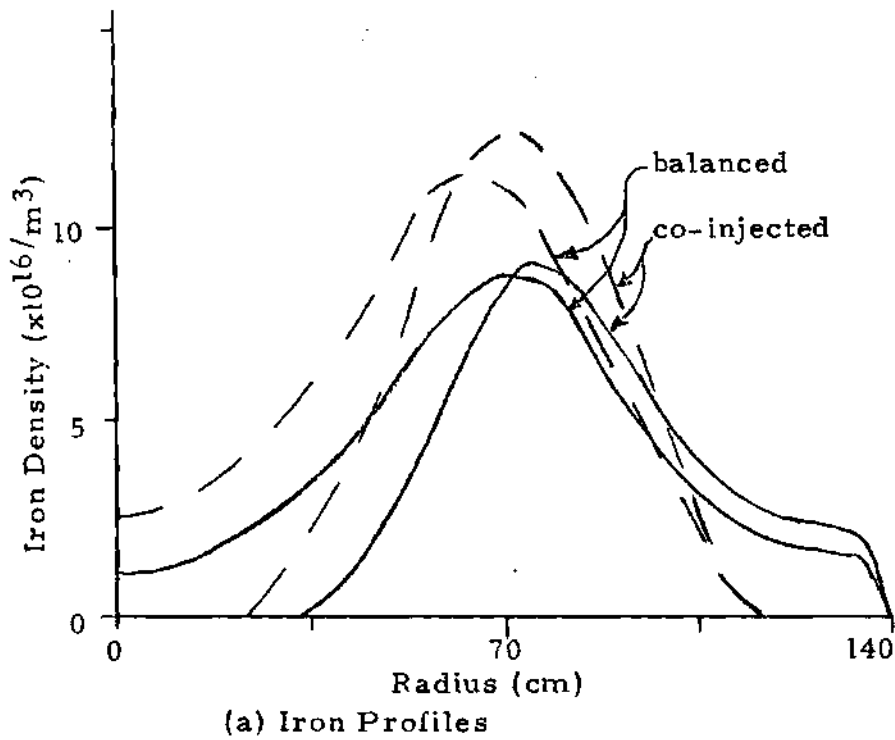
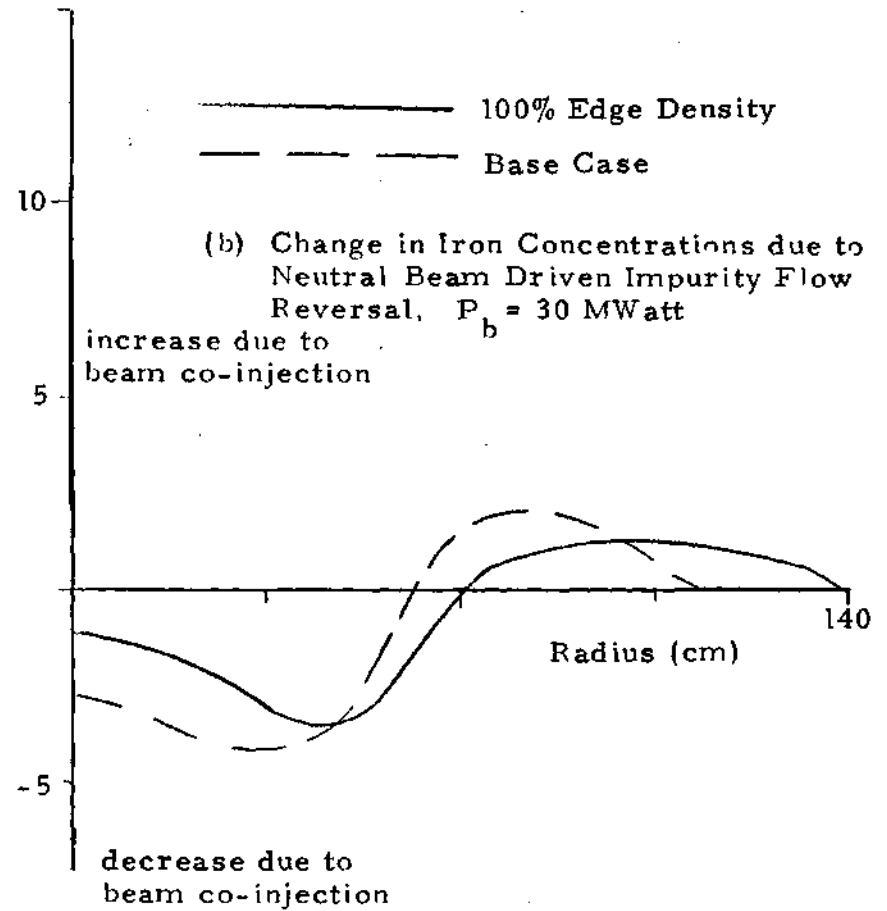
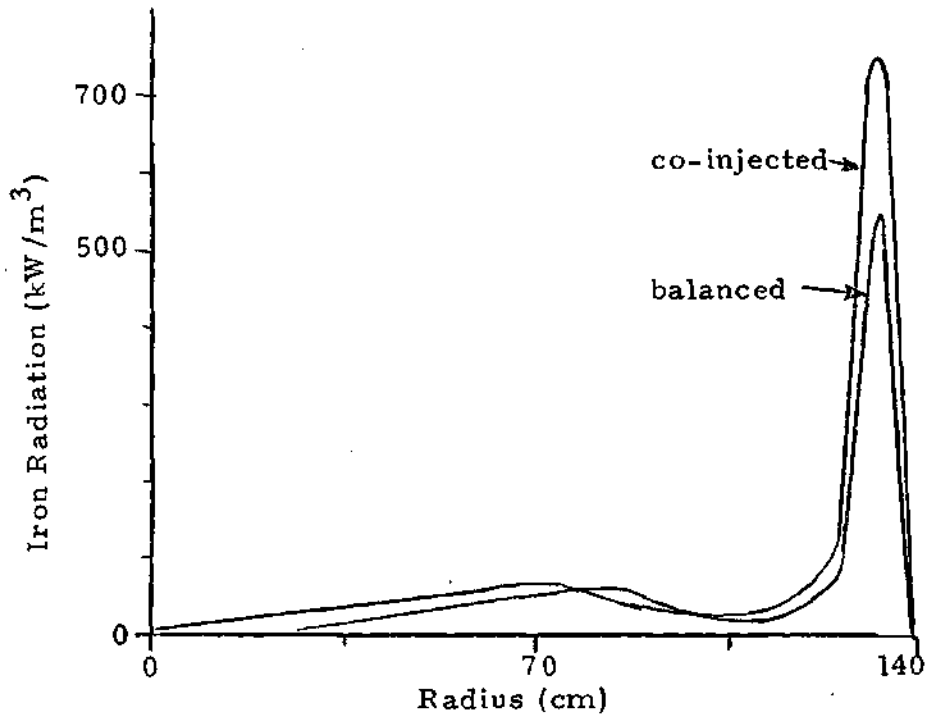


Figure 4.3.6 Iron Concentrations in FED with Low Edge Density and 100% of Centerline Edge Density Main Ion Profiles





(c) Iron Radiation Profiles
for 100% Edge Density Case

Figure 4.3.6 Iron Concentrations in FED with Low Edge Density and 100% of Centerline Edge Density Main Ion Profiles, $P_b = 30$ MWatts (continued)

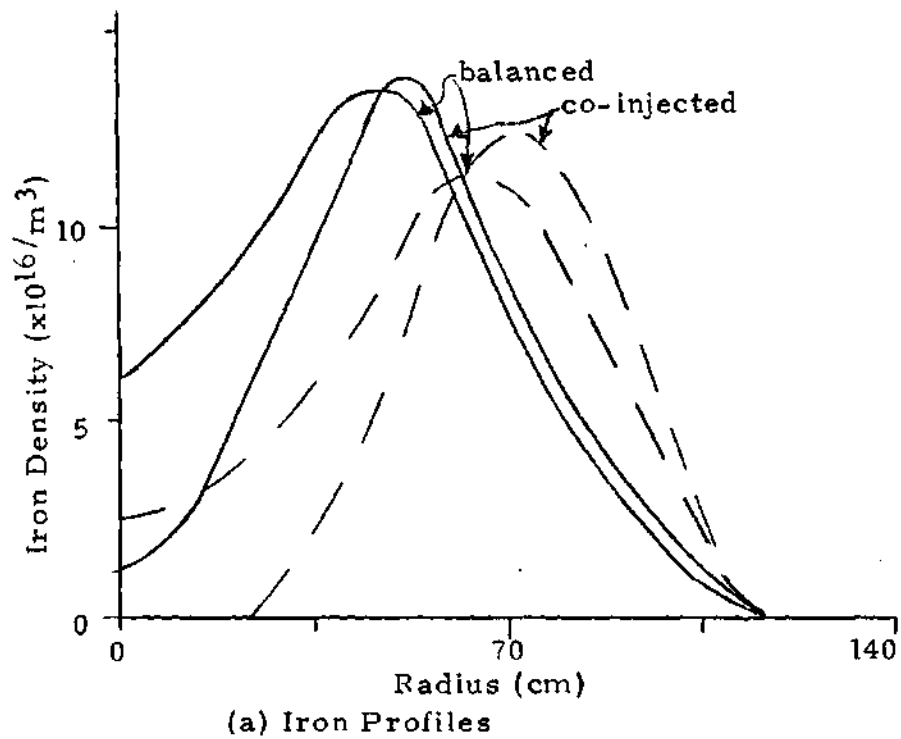
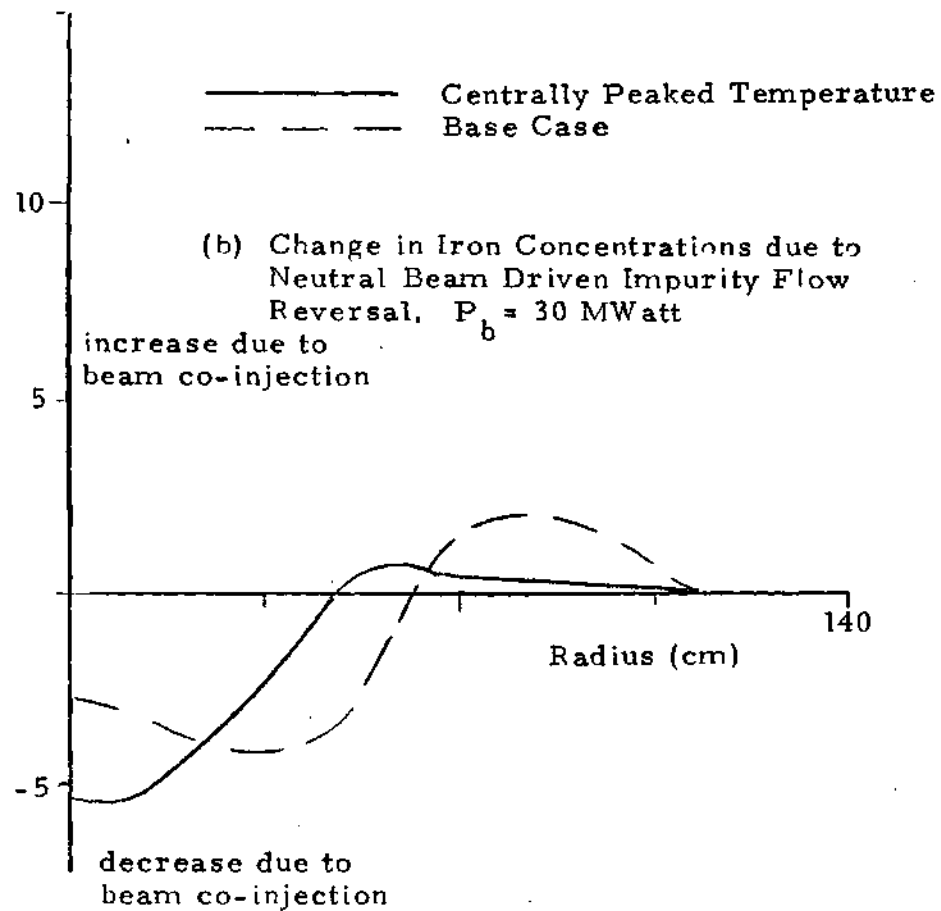
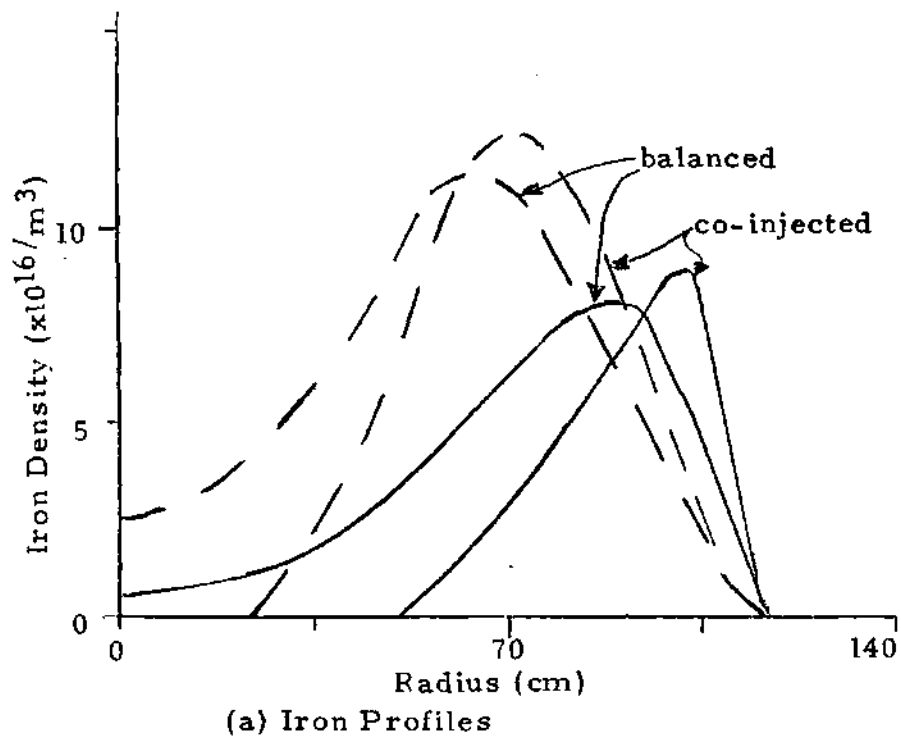


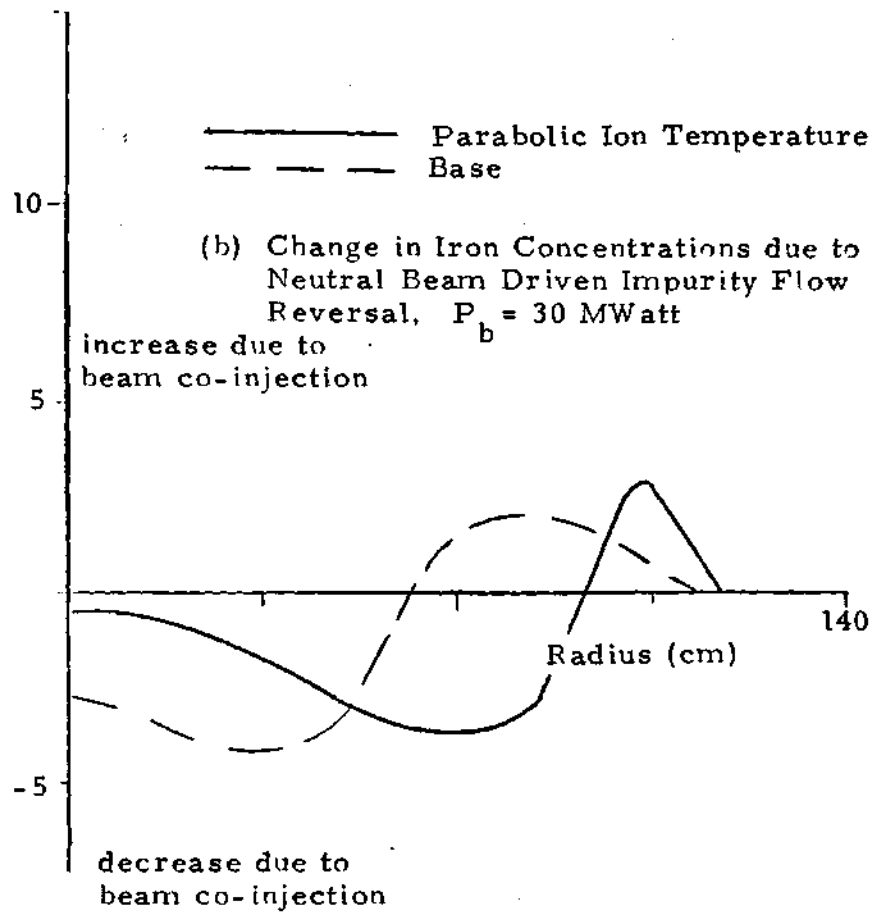
Figure 4.3.7 Iron Concentrations in FED with Centrally Peaked and Base Ion Temperature Profiles

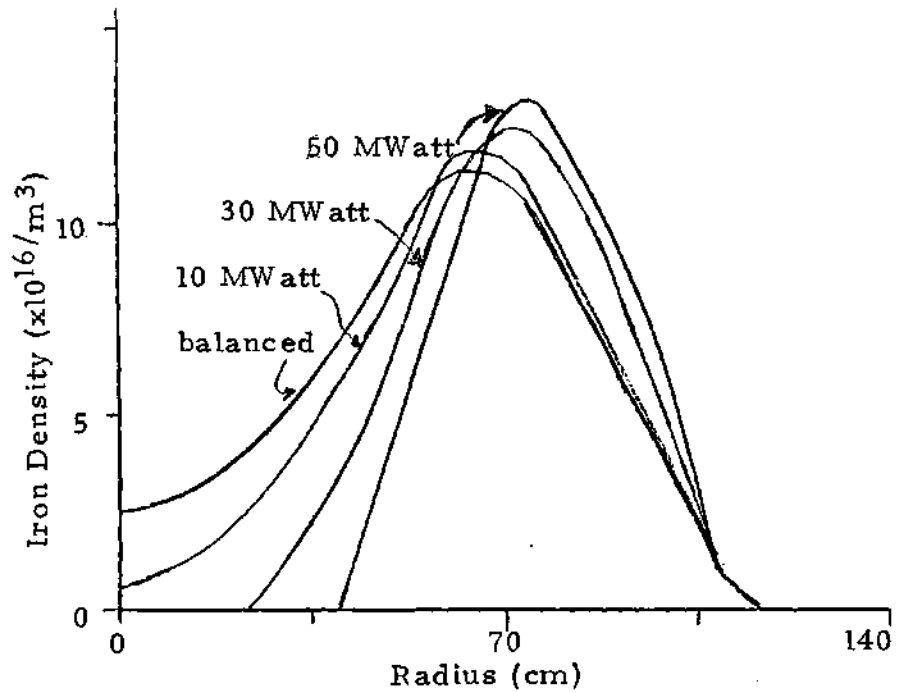




(a) Iron Profiles

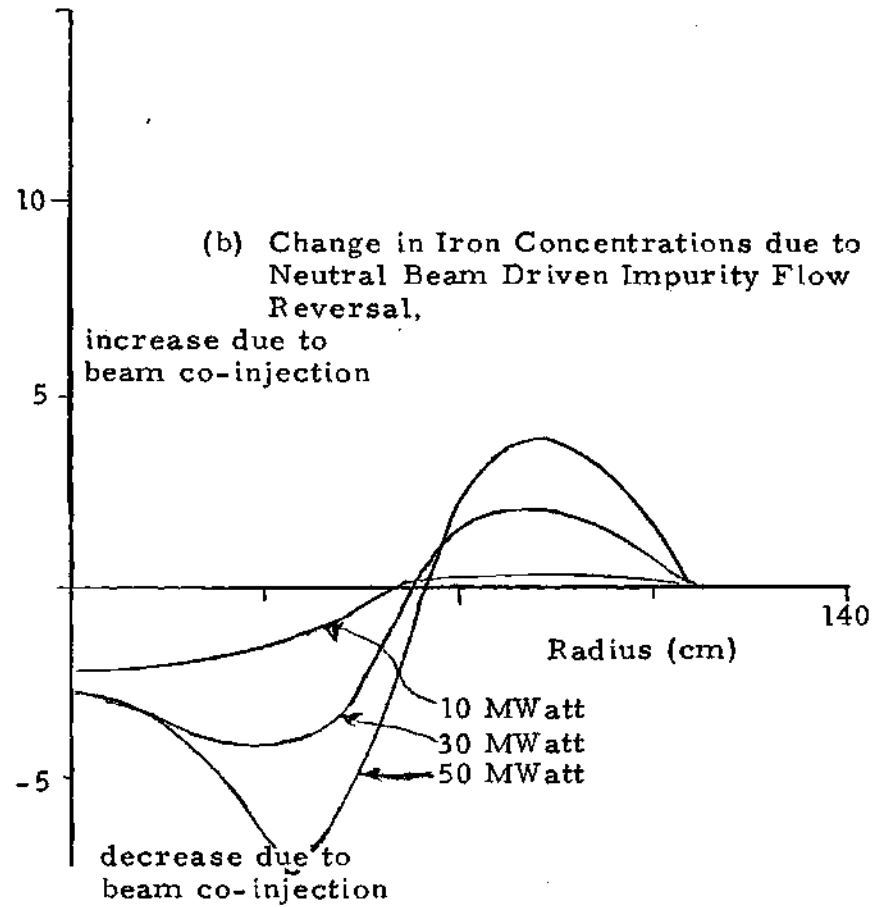
Figure 4.3.8 Iron Concentrations in FED with Parabolic and Base Ion Temperature Profiles





(a) Iron Profiles

Figure 4.3.9 Iron Concentrations in FED with Different Co-injected Powers $P_b = 10, 30, \& 50$ MWatt



4.4 Predictions for STARFIRE

The final tokamak to be studied for the effect of co-injected neutral beams upon the radial impurity transport is a machine with the general specifications of STARFIRE. The STARFIRE study [62] produced a conceptual design of a commercial reactor with 1200 MWatts of net electrical power. This reactor was chosen for use here as a representative commercial reactor, although predictions for this machine should be equally valid for other reactors in this size range.

As originally envisioned, STARFIRE would run in steady state. Radio-frequency heating would be used near the plasma edge both to drive the plasma current and to fill in the outer edge of the temperature profile in order to hold a flatter temperature profile through the plasma center. This flat temperature profile would distribute the fusion power production throughout more of the plasma. The high edge temperature, flat temperature profile is in conflict with the lower edge temperature needed to protect the first wall and reduce the sputtered impurity source, as was discussed in the previous section. In this work, the possibility that an acceptable co-injected beam power level can drive impurity accumulation at the plasma edge to produce a cold radiating edge, while preventing impurity penetration to the tokamak center, is examined. In addition, this reactor design will be used to study the

effect of different beam injection scenarios on the effectiveness of impurity control with a co-injected beam.

To be consistent with the STARFIRE design, a beam power level of 50 MWatts is chosen. This is half the supplemental radio-frequency power of the design, of which 66 MWatt is current drive and 24 MWatt is pure heating. A beam energy of 200 keV was chosen, which is sufficient to provide significant penetration to the plasma center. The angle of injection is chosen here to be tangent to the magnetic axis, or 90° from the perpendicular. This angle may not be obtainable due to access limitations between the toroidal field coils. Since the injection angle is one of the parameters varied in this analysis, the angle choice is not a limitation of the study. The STARFIRE plasma shape was simplified here from the triangular shape originally planned to a simple ellipse.

The STARFIRE design parameters used in this study are listed in Table 4.4.1 [62]. STARFIRE was designed to operate in steady state, so the time interval for the analysis of the impurity profile evolution was chosen to be 50 sec. The pulse length in FED was also 50 sec, so the final profiles in the two machines can be directly compared. A source rate of $1 \times 10^{15} / \text{m}^2 \text{sec}$ of iron was chosen. Again, this is the same source species and rate used in the analysis of FED. The volume of STARFIRE is only 2.8 times larger than FED, the surface area only two times larger, and

the average main ion density .8 times lower, so the final average concentration of iron will be approximately the same as in FED, $\bar{\alpha} = \overline{n_z Z^2} / \bar{n}_i \sim 0.5$.

The temperature and density profiles used here are taken from the STARFIRE design document [62] and are shown in Figure 4.4.1a and b. Both the ion and electron temperature profiles are relatively flat, being much less centrally peaked than those of FED. The density profile is approximately parabolic, so the density gradient is roughly constant throughout the outer 1.5 m of the plasma. All of these profiles are held fixed during the calculation. As in the preceding sections, the beam momentum deposition is calculated using the Fokker-Planck code.

Figures 4.4.2a and b show the time evolution of the iron profiles for 50 seconds in the balanced and co-directed momentum cases, respectively. As in the previous two machines analysed, the incoming flux fills the outermost regions of the plasma to an equilibrium level, this equilibrium progressing radially inward. The difference driven by the co-injected beam relative to the balanced beam is shown in Figure 4.4.2c. The concentration change due to the effect of the co-injected beam involves 4% of the iron ions present. By calculating the mean radial locations of the changes in the iron distribution, which are at 40 cm for the reduction in iron concentration and at 135 cm for the increase in iron concentration due to the effect of the

co-injected beam, the beam is found to have kept 4% of the iron distribution 40% closer to the outer plasma boundary.

Comparing the iron density profiles with those of FED, the iron is seen to penetrate deeper into STARFIRE and to be affected less by beam co-injection. The increased iron penetration in STARFIRE is due to the density being larger in STARFIRE relative to FED over much of the plasma radius, the density gradient in FED being large only in the outer 30 cm of that plasma. The effect of beam co-injection is lower in STARFIRE relative to FED both because the gradient driven terms are larger in STARFIRE and because the momentum per unit volume is lower,

$$\frac{K_{STAR}}{K_{FED}} \propto \sqrt{\frac{E_{bFED}}{E_{bSTAR}}} \cdot \frac{P_{bSTAR}}{P_{bFED}} \cdot \frac{Vol_{FED}}{Vol_{STAR}} < 1 \quad . \quad 4.4.1)$$

Approximately 50 MWatts of power is radiated from the electrons in STARFIRE due to the iron concentrations shown in Figures 4.4.2a and b. These radiation profiles are shown in Figure 4.4.2d. Four percent (2 MWatts) more power is radiated when balanced momentum is injected relative to when the beams are co-injected. By analysing the radiation profiles, a 10% drop (from 30.9 to 27.6 MWatts; a 3.3 MWatt drop) in radiation in the inner 80 cm of the plasma is found, along with a 1.3 MWatt increase over the rest of the

plasma. The large increase in radiated power seen at the outer edge of the FED plasma is not observed here since the electron temperature is very high in STARFIRE out to the plasma edge, so that the iron in the plasma is always completely stripped, and therefore radiating much less.

Having predicted the effect of co-injected neutral beams on the iron accumulation in STARFIRE, the effect of different beam energies, powers, and injection angles is investigated. First, the effect of different beam powers is studied. Figure 4.4.3a shows the iron profiles after 50 sec for none, 50 MWatt, and 100 MWatt of net co-injected power at a beam energy of 200 keV and injection angle of 90° from the perpendicular. The balanced momentum and 50 MWatt co-injected profiles are the same as in Figures 4.4.2a and b. The density differences with co-injection relative to the balanced injection is shown in Figure 4.4.3b, the larger power driving the larger density change. As can be seen directly, the change driven by 100 MWatts is twice the change driven by 50 MWatts. This need not always be true, i.e., if the impurities are kept at the outer edge of the plasma, the larger power may keep impurities out of regions where the relative momentum deposition is greater, reducing the advantage gained by the larger beam power.

The next beam parameter to be analysed here is the injection angle. Figure 4.4.4 shows the relative toroidal momentum deposition profiles found using injection angles of

90° (the base case), 60° , and 30° , as measured from the perpendicular. The beam injected parallel to the magnetic axis (90°) must traverse the most plasma, and this beam deposits most of its momentum at the outside of the plasma. Injection at 60° and 30° reduces the total toroidal momentum. Since these beams traverse less plasma than the 90° beam, penetration to the plasma center is better, and the toroidal momentum at the plasma center is also larger. The beam injected at 30° deposits the least total toroidal momentum, the least toroidal momentum in the outer radii of the plasma, and the most toroidal momentum at the plasma center.

Figure 4.4.5 shows the iron profiles calculated using the three injection angles and balanced momentum injection. Although the beam injected at 30° deposits the most toroidal momentum at the plasma center, the effect of this beam on the central iron profiles is the least. The important factor in reducing the central accumulation of the impurity in this case is the amount of toroidal momentum deposited in the outer radii of the plasma. Toroidal momentum near the plasma edge allows impurity accumulation at the edge, reducing the amount which reaches the center. The beam injected parallel to the magnetic axis (90°) provides for the greatest edge accumulation, and therefore the least central accumulation. The effect of the beam injected at 60° is intermediate to the effects of the beams injected at

90° and 30°.

The effect of different beam energies on iron accumulation is analysed next. Both the total momentum and the momentum deposition profile changes with beam energy when the same power is injected. This is shown in Figure 4.4.6, where the momentum deposition profiles are shown for injection energies of 100 keV and 400 keV, in addition to the reference injection energy, 200 keV. It can be seen that the most toroidal momentum reaches the plasma center at the 400 keV injection energy due to the greater penetration, and the most momentum is deposited near the plasma edge (120 to 190 cm) at the 100 keV beam energy. When the injection power is constant, the total momentum is greater at lower beam energies, since the momentum is proportional to the inverse of the square root of the energy,

$$K \propto 1 / \sqrt{E_{beam}} \quad . \quad 4.4.2)$$

The iron accumulation profiles calculated using the three beam injection energies are shown in Figure 4.4.7. All three energies have approximately the same effect on central accumulation, the change in central accumulation due to co-injection increasing somewhat with lower beam energy. The two lower energy beams increase the iron concentration

in the radial regions where their momentum deposition is the greatest, from 120 to 194 cm for the 100 keV beam and from 80 to 160 cm for the 200 keV beam. The effect of the 400 keV beam is also an increase of iron concentration in the 80 to 160 cm radial region, but to a lesser extent than the 200 keV beam due to the lower momentum input to the region. This lower outer accumulation relative to the effect of the 200 keV beam is the reason for the larger central accumulation when the 400 keV beam is injected.

In the above analyses of the effect of the injection angle and beam energy on the iron profiles in STARFIRE, the radial location at which the momentum was deposited was found to be very important in determining the amount of central accumulation. To study this further, the final iron profiles are calculated with injection of the full beam momentum into three radial regions of STARFIRE: the inner third, the middle third, and the outer third, all by volume. The momentum deposition profiles relative to the average deposition are shown in Figure 4.4.8. The volumes and peak deposition rate differ slightly to fit the numerical deposition mesh of the computer code, but the total momentum to each region is equal to the total momentum input by the beam.

Figure 4.4.9 shows the final iron profiles calculated using the beam momentum deposition profiles of Figure 4.4.8. The iron profiles calculated using the outer and middle

deposition profiles have increased iron concentrations relative to when balanced momentum is input in the radial region into which their respective momentum is deposited. The same effect was seen in the above analyses of the effect of injection energy and angle. The change in iron concentration is greater when the momentum is deposited in the middle region than it is when the momentum is deposited to the outer region, as can be seen directly by comparing the profiles labeled outer and middle at the center of the plasma. When the momentum is injected to the inner region, a large drop in the accumulation at the magnetic axis is seen. Only the iron distribution in the region of injection is modified in this case, more iron being held to the outside of the region. In summary, with an edge impurity source, momentum injection at a radial location does not change the accumulation outside of that radius, and changes the accumulation inside of that radius only by reducing the total source to the inner radii.

TABLE 4.4.1 STARFIRE Study Parameters

Machine

Major Radius	7.0 m
Minor Radius	1.94 m
Plasma Elongation	1.6
Toroidal Field	5.8 T
Plasma Current	10.1 MAmp
Volume	~830 m

Performance

Average Density	$8 \times 10^{19} / \text{m}^3$
Electron Temperature	22. keV
Ion Temperature	31. keV
Edge Temperature	100. eV
Burn Time	50 sec (nominal)
Fusion Power	3510 MWatt

Beam Used

Energy	200 keV
Beam Mass	2 amu
Power	50. MWatt Co-injected
Current Fractions	E .5
	E/2 .25
	E/3 .25
Injection Angle	90° from perpendicular

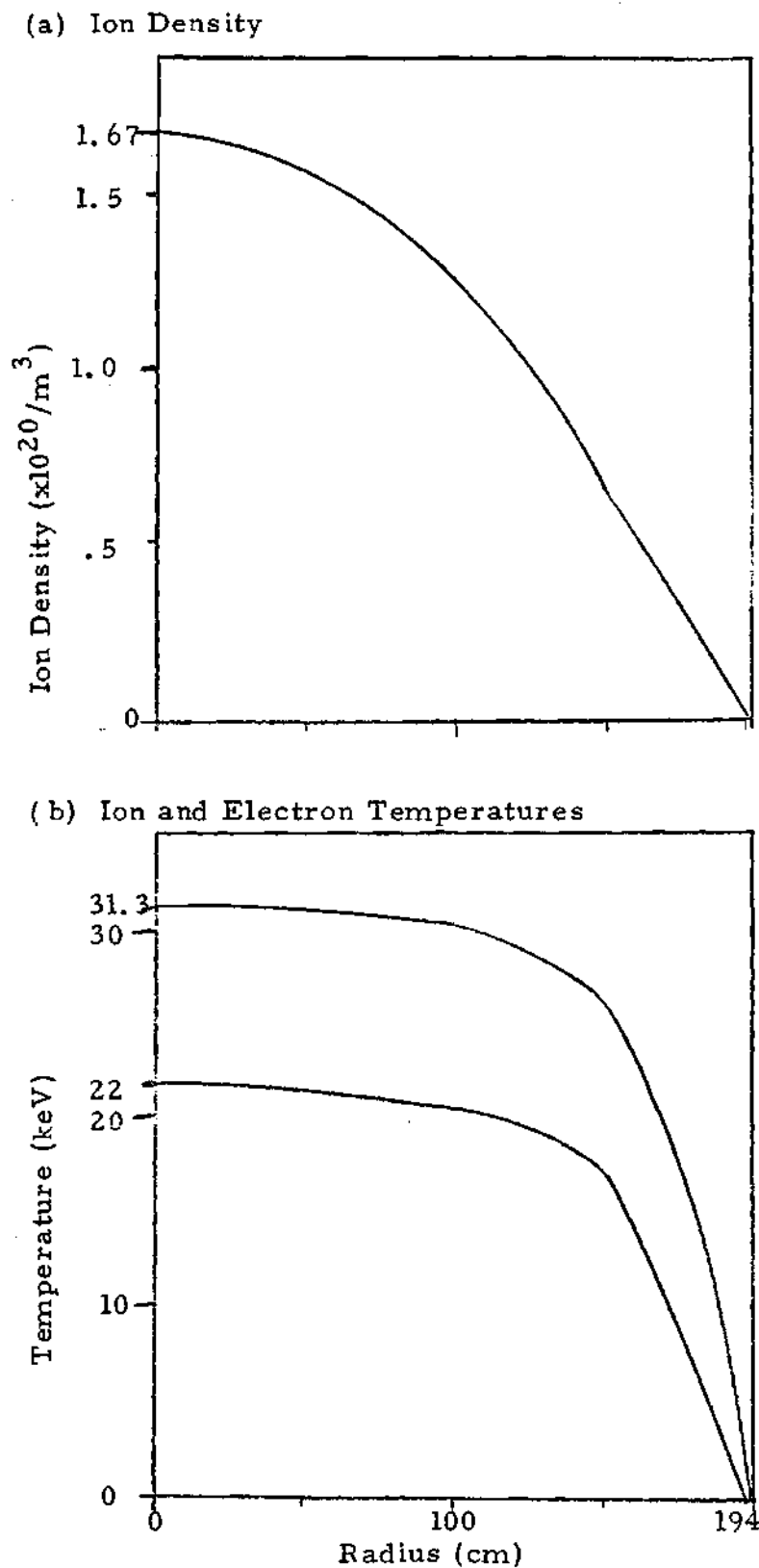
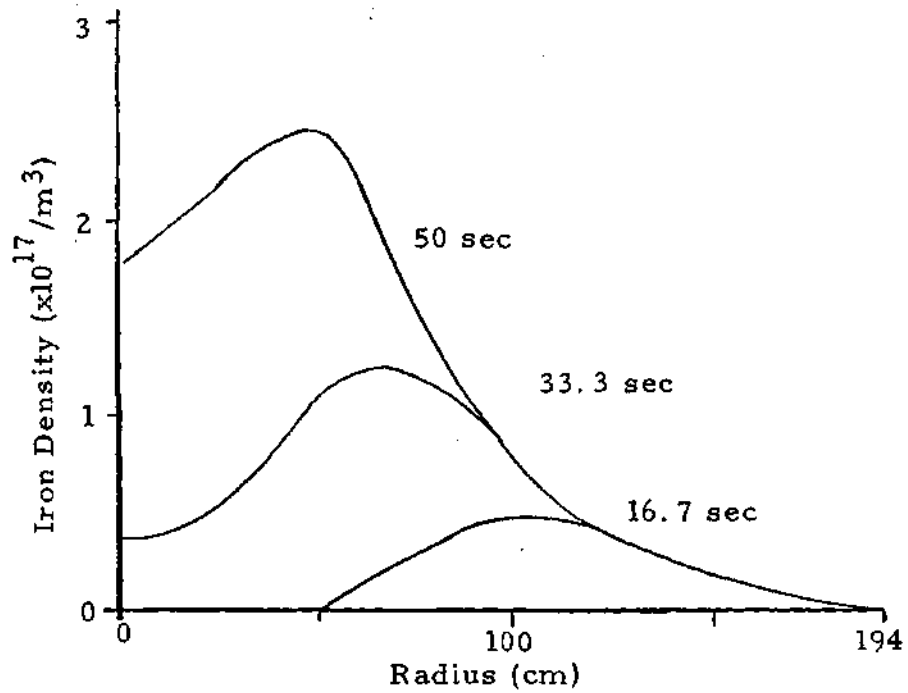
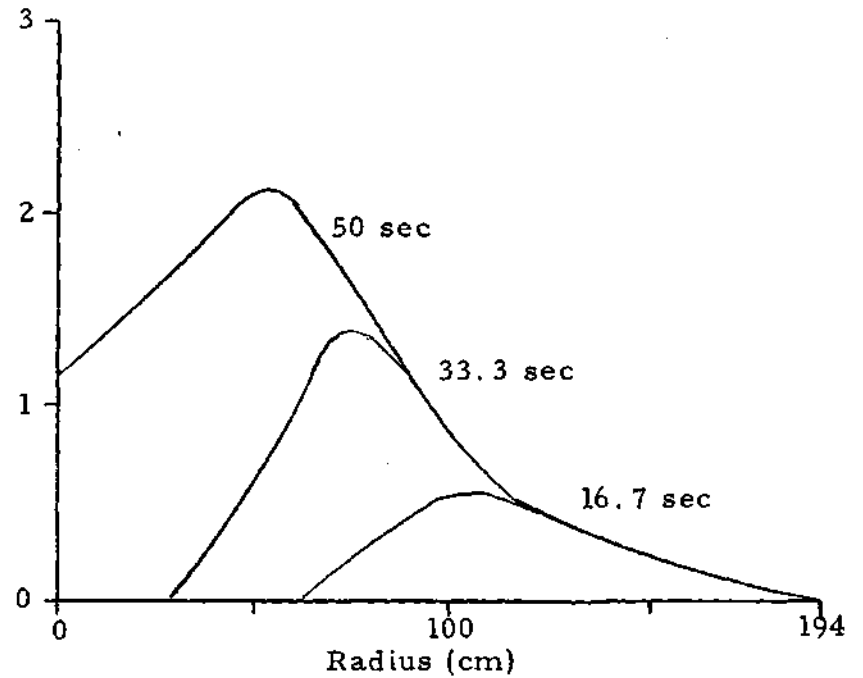


Figure 4.4.1 Density and Temperature Profiles Used in the Analysis of STARFIRE



(a) Balanced Injection



(b) Co-injected Momentum

Figure 4.4.2 Iron Profiles in STARFIRE for the Base Case, $t=50$ sec., $P_b=50$ MWatt, $E_b=200$ keV, Iron Edge Source = $1 \times 10^{15} / \text{m}^2 \text{sec}$, Injection 90° from \perp

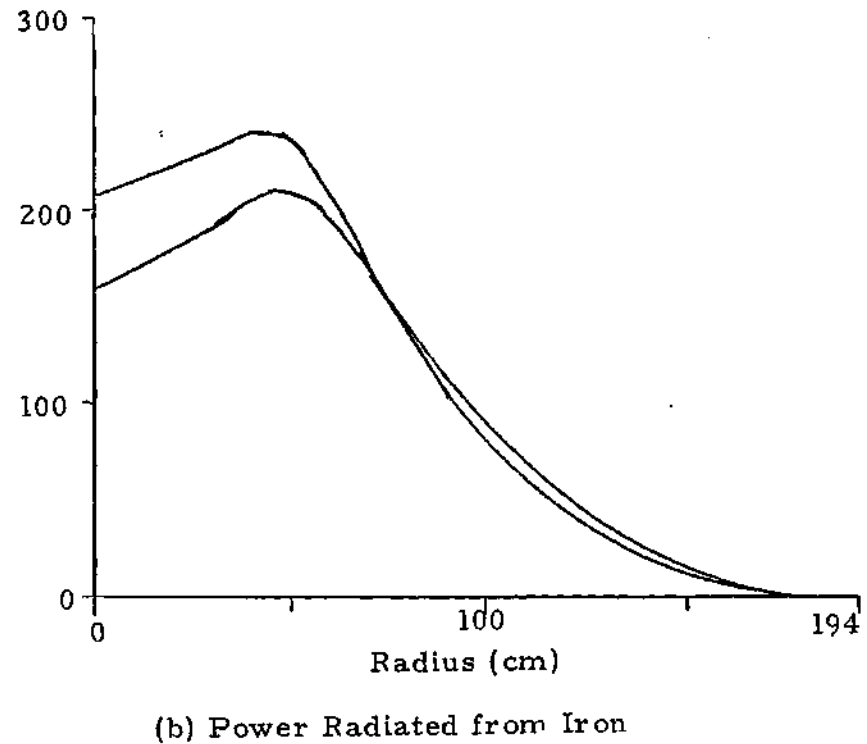
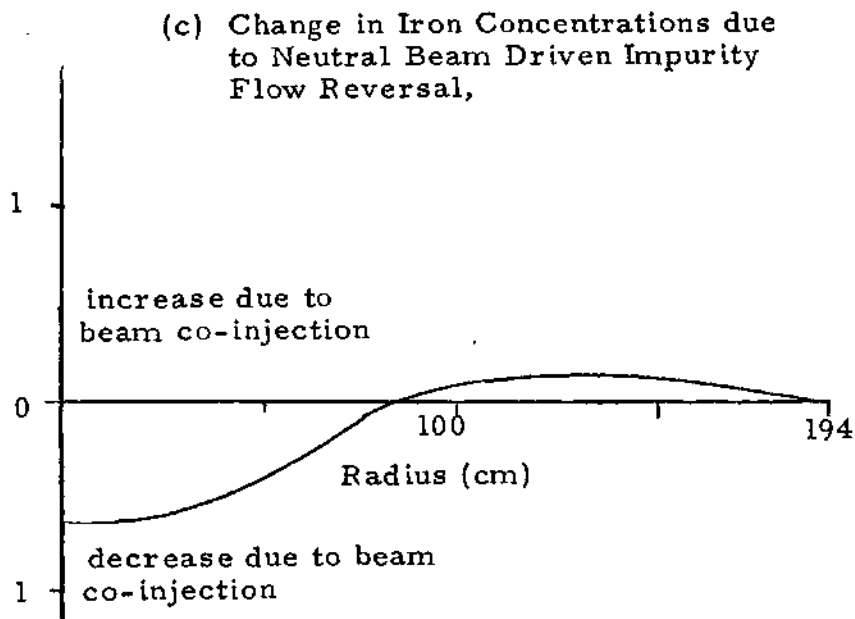


Figure 4.4.2 (continued) Iron Profiles in STARFIRE for the Base Case, $t = 50$ sec, $P_b = 50$ MWatt
 $E_b = 200$ keV, Iron Edge Source = $1 \times 10^{15} / \text{m}^2 \text{sec}$, Injection 90° from \perp

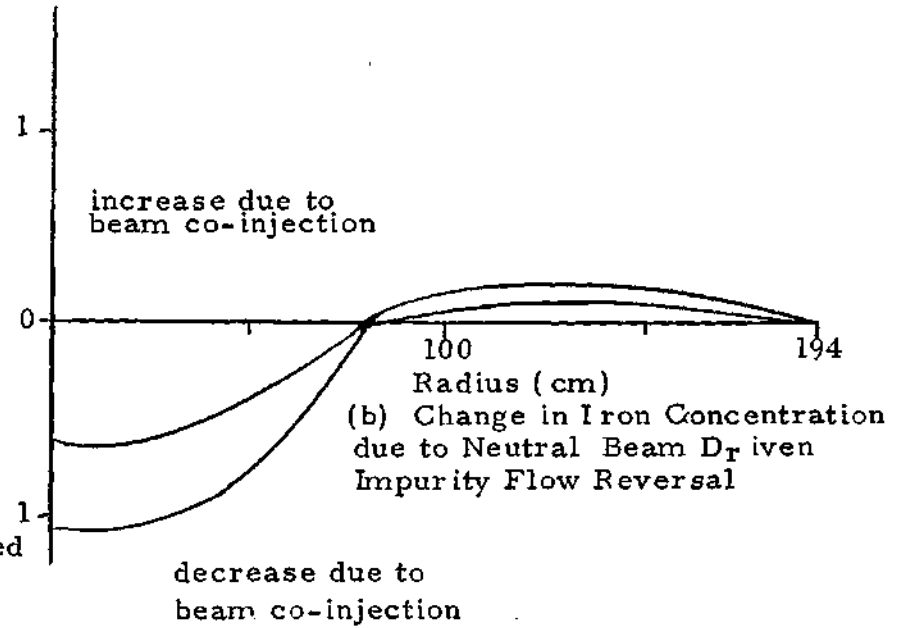
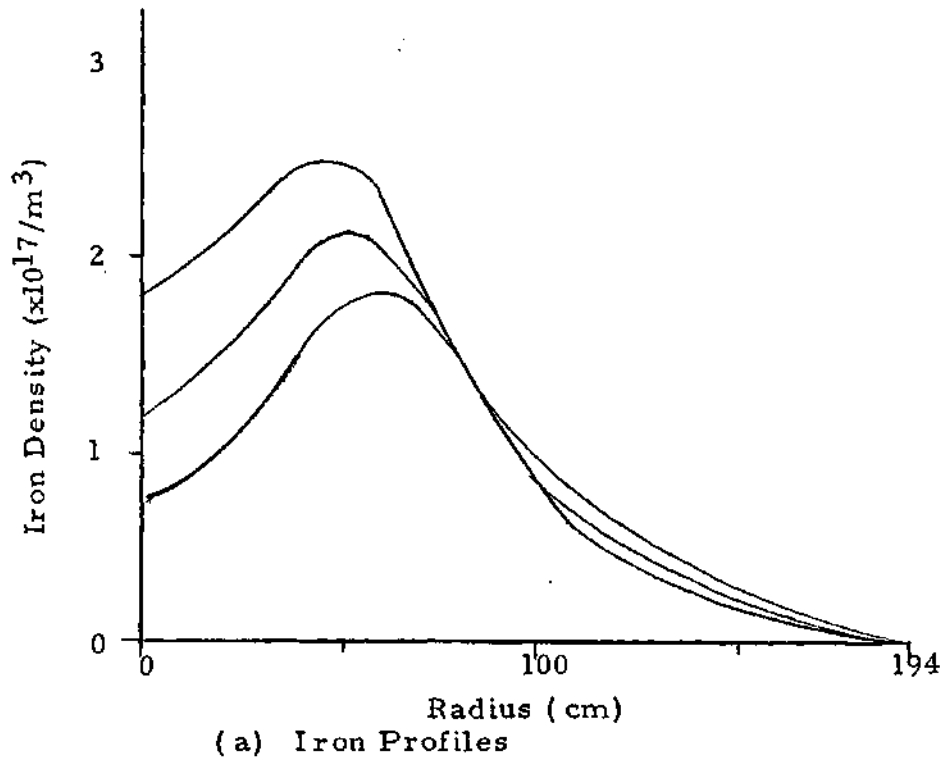


Figure 4.4.3 Iron Profiles in STARFIRE with Balanced Injection and 50 and 100 MWatts of Co-injected Power

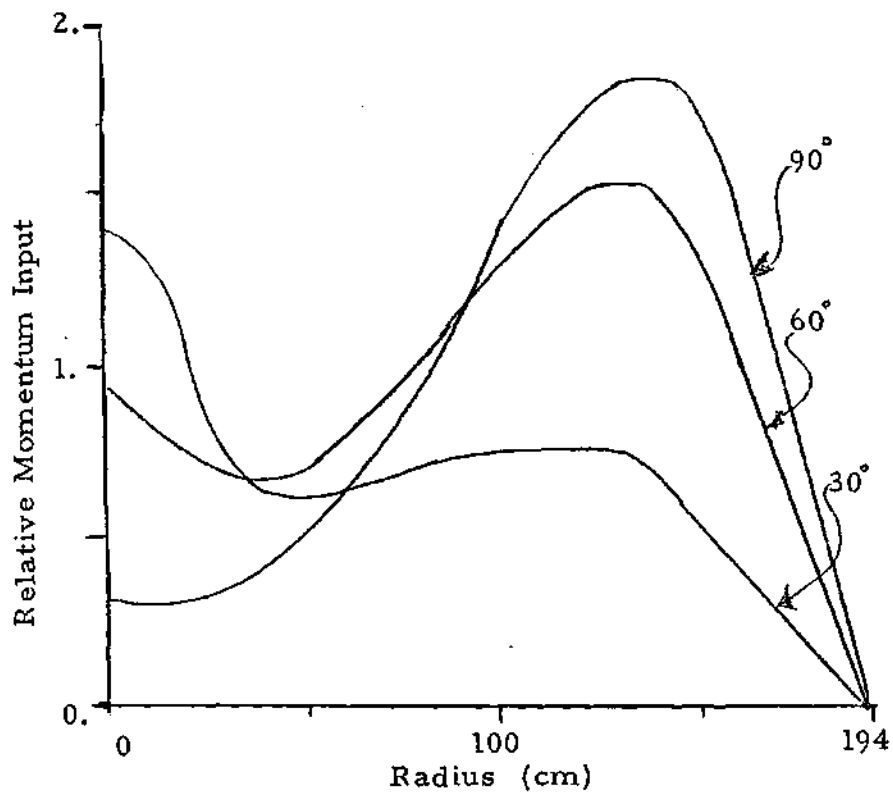


Figure 4.4.4 Relative Toroidal Momentum Input in STARFIRE at 30°, 60°, and 90° Injection Angles

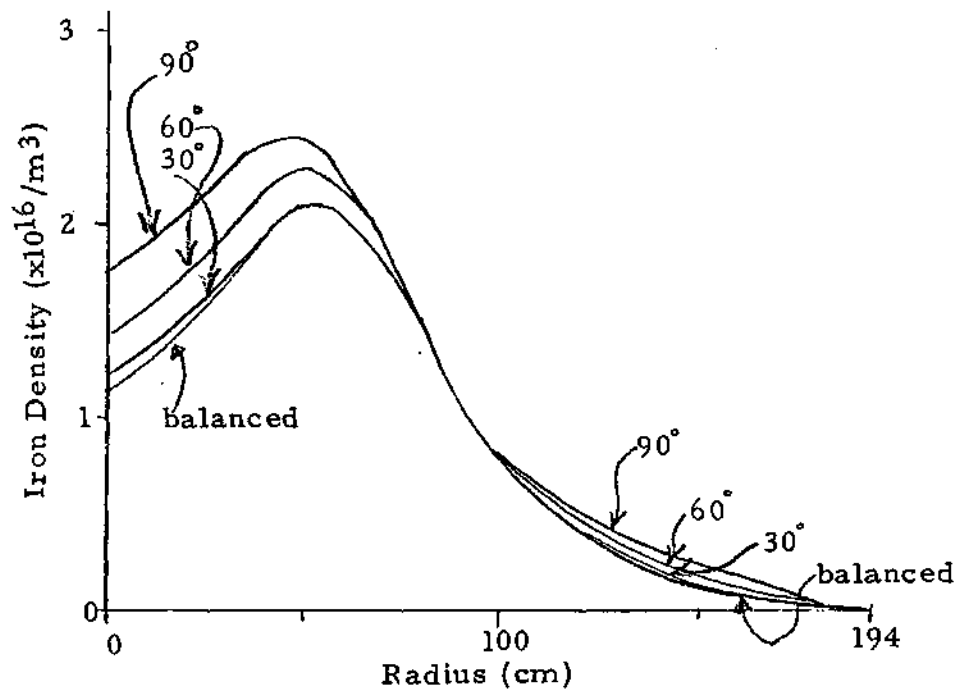


Figure 4.4.5 Iron Profiles in STARFIRE with 30°, 60°, and 90° Injection Angles, $P_b = 50$ MWatt

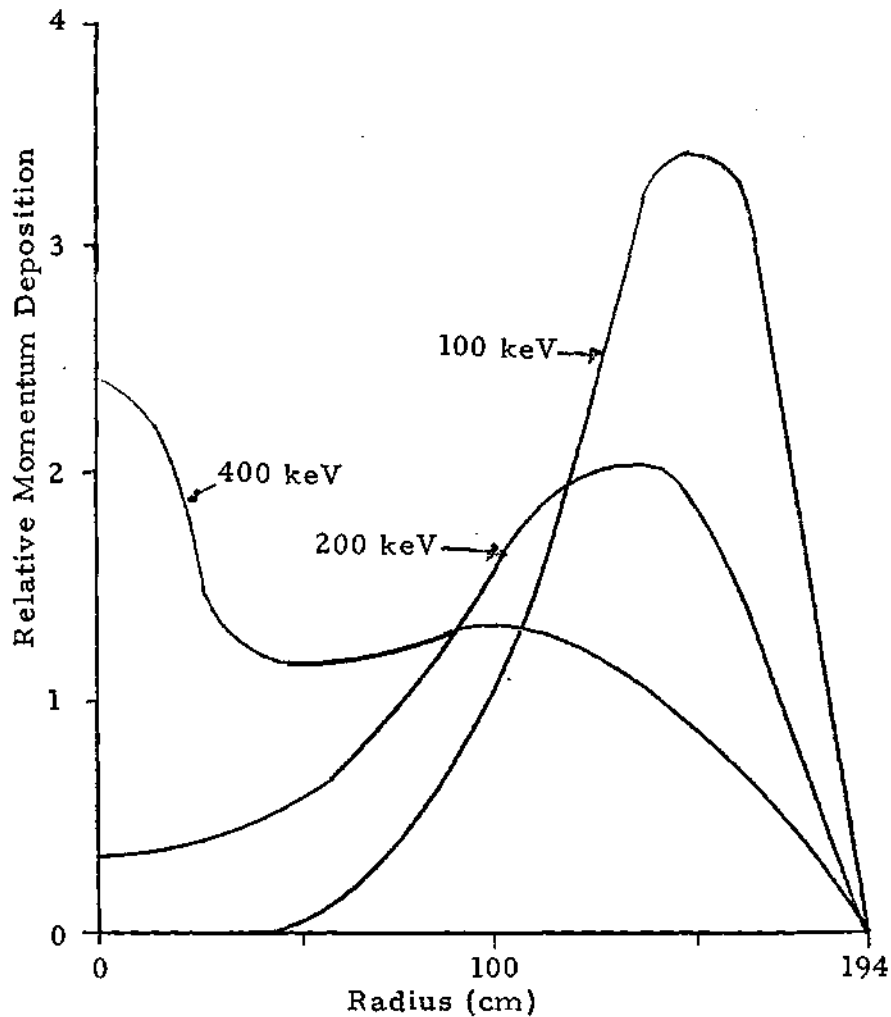


Figure 4.4.6 Relative Momentum Deposition in STARFIRE with 100 keV, 200 keV, and 400 keV Injection Energies

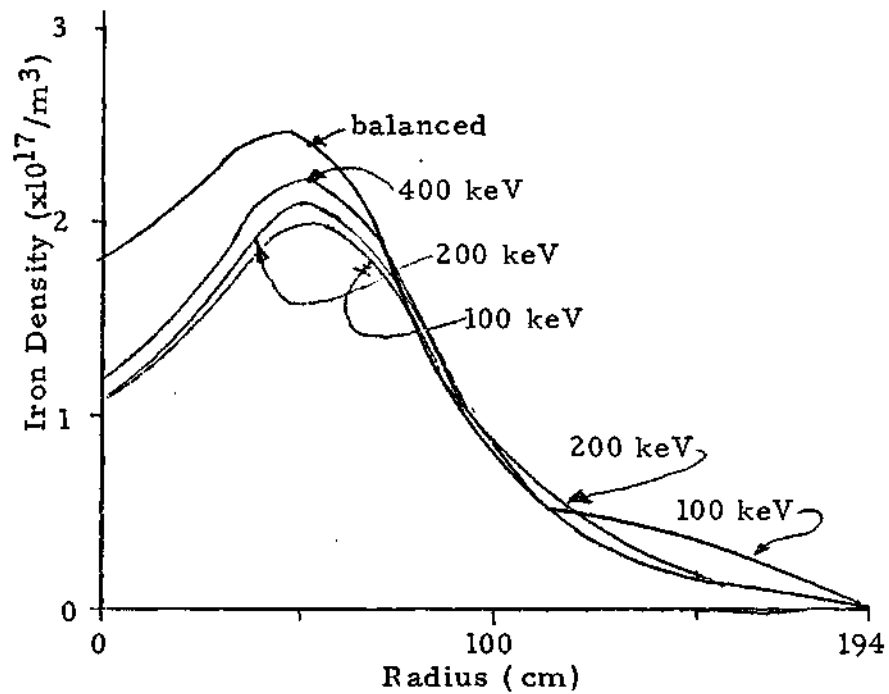


Figure 4.4.7 Iron Concentrations in STARFIRE with Balanced Injection and Co-injection at 100 keV, 200 keV, and 400 keV Beam Energies $P_b = 50$ MWatt, Injection 90° from \perp , Iron Source = $1 \times 10^{15} / m^2 \text{ sec}$

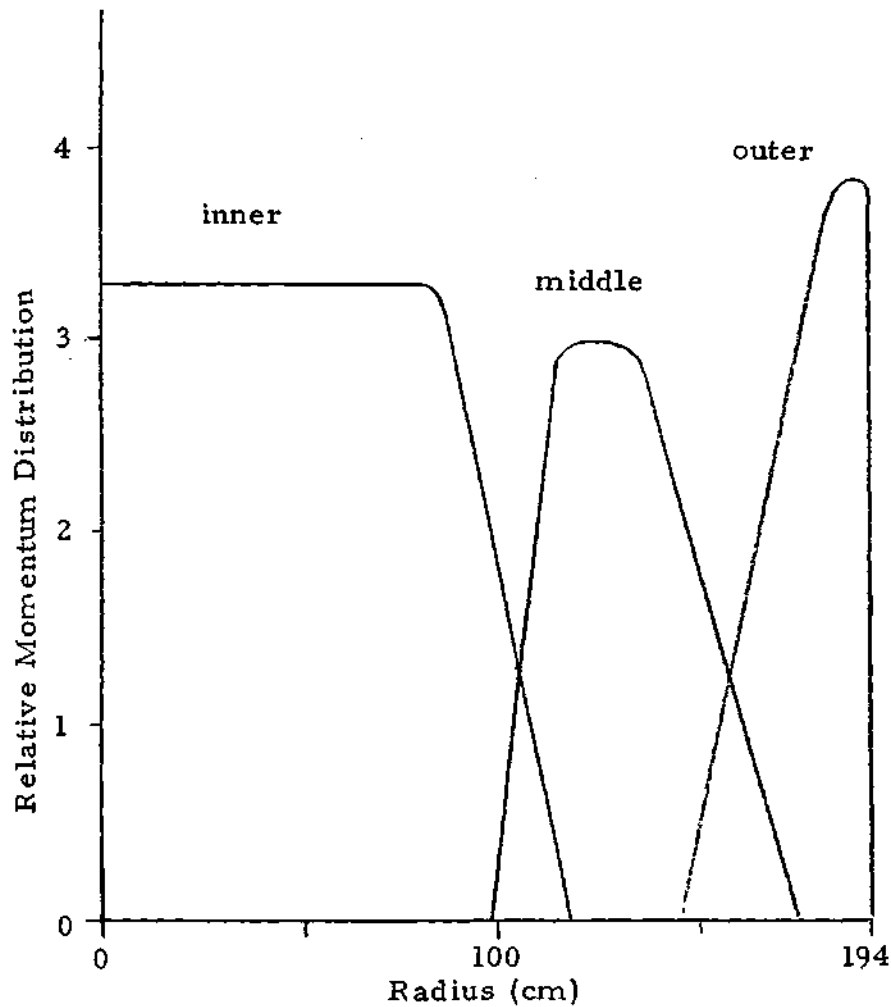


Figure 4.4.8 Relative Momentum Distribution Profiles Used for Regional Momentum Distribution Analysis in STARFIRE

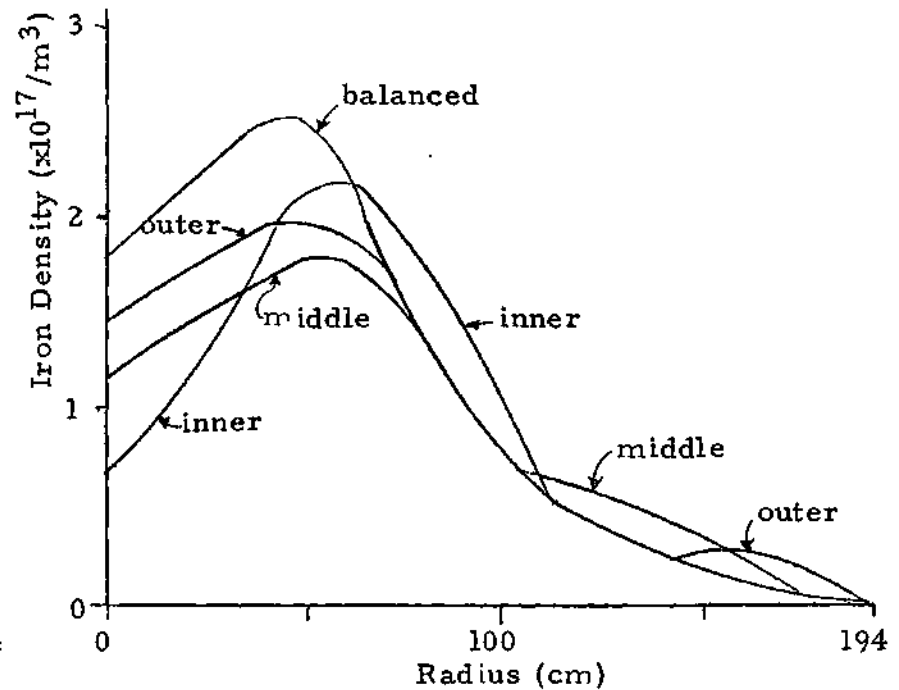


Figure 4.4.9 Iron Concentrations in STARFIRE with Balanced Injection and Regional Deposition of Co-injected Momentum, $P_b=50$ MWatt, $E_b=200$ keV Source Rate= $1 \times 10^{15}/m^2$ sec, Injection 90° from \perp

4.5 Summary of Predictions for Future Machines

The possibility that neutral beam driven impurity flow reversal could be used in future tokamaks to hold impurities to the plasma edge region, thereby radiatively cooling the plasma edge, was considered in this chapter. Three machines were investigated: the Tokamak Fusion Test Reactor, TFTR, which is beginning operation at the Princeton Plasma Physics Laboratory; a machine representative of an engineering test reactor, the Fusion Engineering Device (FED), which is similar in size to the International Tokamak Reactor (INTOR); and a commercial reactor, represented by STARFIRE. The transport model used here, which includes radial impurity fluxes driven by neutral beam injection, was summarized in Section 3.9.

The impurity transport effect of the neutral beam in TFTR was found to be significant at all times in the plasma operating cycle. With a tungsten source at the plasma edge of $1 \times 10^{16} / \text{m}^2 \text{sec}$, co-injection of 16 MWatts of power increases the tungsten accumulation at the plasma edge, and therefore the radiation rate if the electron temperature is constant, by 50% relative to balanced injection. This radiation increase is from 1.6 MWatt to 2.5 MWatt in the outer 25 cm of TFTR's radius. The radiation is a significant fraction of the total external power input, which is predominantly from beam injection. Therefore, the increased radiation due to the flow reversal effect of a co-injected neutral beam in

TFTR should aid in cooling the plasma edge, helping to protect the first wall.

Significant radiative cooling of the plasma edge by iron impurities in FED was found to be possible only with certain plasma edge conditions. FED was analyzed for 50 sec of burn at an edge iron source rate of $1 \times 10^{15} / \text{m}^2 \text{sec}$, which produces an average iron concentration of $\bar{\alpha} = \overline{n_z Z^2} / n_e \sim 0.5$ at the end of the analysis period. Although 30 MWatts of co-injected beam does change the iron accumulation profiles, the very steep main ion gradients at the plasma edge prohibit any significant iron accumulation there. This excludes the iron from electron temperature regions where the iron is incompletely stripped of its electrons, thereby eliminating the enhanced radiation needed to cool the plasma edge. The total power radiated from the plasma is 10 MWatts, about one third of the injected power, but only 5% of the expected fusion power (~ 200 MWatts).

If FED could be operated with a high density plasma edge, in which the main ion density at the plasma edge is essentially equal to the density at the plasma center, radiation from iron at the edge is increased dramatically. The total power radiated with balanced injection is increased from 10 MWatts to 27 MWatts, the additional 17 MWatts being radiated from the outer 25 cm of the plasma. With co-injection, the increased iron accumulation at the edge increases this differential from 17 to 24 MWatts, a 30%

increase. It is noted here that the dominant effect on increased edge cooling is due to the density profile modification, which enables the neutral beam driven impurity flow reversal effect to dominate the transport of impurities.

As in FED, radiation from the iron in STARFIRE can only cool the plasma edge when significant iron concentrations are located in low electron temperature ($< 2\text{keV}$) regions. STARFIRE was analysed with 50 MWatts of beam injection for 50 seconds of the burn, with an iron source rate at the plasma edge of $1 \times 10^{15} / \text{m}^2 \text{sec}$. This source rate produces an average concentration after 50 sec of $\bar{\alpha} \sim .5$. Without enhanced edge radiation, the total power radiated from the electrons due to the presence of iron is 50 MWatts, which is only 1.4 percent of the 3510 MWatts of fusion power produced.

In FED and STARFIRE, the beam injection parameters and plasma profiles were modified to note their effect on iron accumulation. The effectiveness of the beam driven flow reversal in holding the iron nearer the plasma edge was found to increase: when the main ion edge density is high, which reduces the ion density gradients; when the ion temperature at the plasma edge is high, which reduces the ion and temperature gradient driven fluxes, $\Gamma_{e, \text{rad}} \propto 1/\sqrt{T}$; when the impurity charge state is low, often requiring a low electron temperature, which reduces the ion and temperature

gradient driven flux $\Gamma_{\text{grad}} \propto Z$ and increases the beam driven flux, $\Gamma_{\text{beam}} \propto 1/Z$; and when the injection angle is nearly tangent to the magnetic axis and the injection energy is low, both of which increase the momentum deposition at the plasma edge. Of course, larger co-injected beam powers also increase the flow reversal driven by the beam.

CHAPTER V

CONCLUSIONS

1. Inclusion of temperature gradient effects into the neutral beam driven flow reversal theory does not modify the beam driven impurity fluxes when the impurities are collisional. When the impurities are collisionless, the inclusion of temperature gradient effects increases slightly the magnitude but does not change the direction of the beam driven fluxes. The direction of these fluxes is typically radially outward with beam co-injection.
2. Co-injection of momentum enhances the outward flow of heat when the impurities are collisional. When the impurities are collisionless, and the impurity collisionality is comparable to or larger than that of the main ions, co-injection reduces the outward flow of ion heat. In both collisionality cases, for typical plasma conditions and injection powers in the Princeton Large Torus, the effect of the beam on the heat conduction is the same order as ion heat conduction driven by temperature gradients.
3. The impurity flow reversal theory provides a reasonable basis for interpretation of experiments in the Princeton

Large Torus. By employing an ad hoc multiplicative factor of two to the theory, the observed inward impurity fluxes before injection and outward impurity fluxes during neutral beam co-injection are predicted reasonably well. A multiplicative factor of four is required to predict the enhanced inward impurity flux with neutral beam counter-injection. Underpredictions of experiment by neoclassical ion transport calculations by a factor of two to four are common.

4. Use of 16 MWatt of co-injected beam power in the Tokamak Fusion Test Reactor (TFTR) is predicted to significantly reduce the penetration of impurities to the center of the plasma, relative to balanced momentum injection, and to significantly increase the impurity radiation from the outer regions of the plasma. This could lead to a cold, radiating plasma edge and to reduced limiter erosion. Thus, co-injected neutral beams may be an important impurity control mechanism in TFTR.

5. The effect of co-injected neutral beams on impurity transport in larger future tokamaks, such as represented by the Fusion Engineering Device (FED) and STARFIRE designs, is not so dramatic as in TFTR, because for modest beam power input the beam power per unit plasma volume is much less for the former. However, if relatively high edge densities can be achieved in FED and STARFIRE type tokamaks, then a modest amount of neutral beam injection (~ 30 MWatts) could produce

a significant reduction in impurity penetration and possibly produce a cold, radiating edge for impurity control.

6. The ratio of the radial momentum transfer rates for impurity and main ions, which is important in the theory, is not known either experimentally or from first principles. An experimental measurement of both the impurity and the main ion toroidal rotation velocities can resolve this issue, and it is recommended that such fundamental quantities be measured if possible.

APPENDIX A

TWO SPECIES PARALLEL FLOW SOLUTION

The averaged parallel flows of particles and heat are required for a complete specification of the first order flows. As stated in the text, the averaged parallel anisotropic shear must be driven by the averaged parallel friction and external sources. For two species, this balance is expressed by the set of equations

$$\begin{aligned} \langle \vec{B} \cdot \nabla \cdot \vec{\Pi}_i \rangle &= 3 \langle (\hat{n} \cdot \nabla B)^2 \rangle \left(\mu_i \Gamma_{ip} + N_{2i} \frac{q_{ip}}{T_i} \right) \\ &= \langle \vec{B} \cdot \vec{R}_i \rangle + \langle \vec{B} \cdot \vec{S}_i \rangle \end{aligned} \quad \text{A-1a)}$$

and

$$\begin{aligned} \langle \vec{B} \cdot \nabla \cdot \left(\vec{\Theta}_i - \frac{5}{2} \frac{T_i}{m_i} \vec{P}_i \right) \rangle &= 3 \langle (\hat{n} \cdot \nabla B)^2 \rangle \frac{T_i}{m_i} \left(N_{2i} \Gamma_{ip} + N_{2i} \frac{q_{ip}}{T_i} \right) \\ &= \frac{T_i}{m_i} \langle \vec{B} \cdot \vec{R}_i^s \rangle + \langle \vec{B} \cdot \vec{S}_i^s \rangle - \frac{5}{2} \frac{T_i}{m_i} \langle \vec{B} \cdot \vec{S}_i \rangle \end{aligned} \quad \text{A-1b)}$$

for each species. The complete solution of this set of equations for two species, an impurity z and main ion i , is given here.

Specializing to the two species, the averaged parallel friction forces are, from Equations 2.3.5 and 2.3.6,

$$\langle \vec{B} \cdot \vec{R}_i^1 \rangle = -\langle \vec{B} \cdot \vec{R}_z^1 \rangle = -C_1 m_i n_i v_{iz} (\langle B V_{i||} \rangle - \langle B V_{z||} \rangle)$$

, A-2a)

$$+ \frac{z}{s} C_2 m_i n_i v_{iz} \left(\frac{\langle B q_{i||} \rangle}{P_i} - \frac{\langle B q_{z||} \rangle}{P_z} \right)$$

$$\langle \vec{B} \cdot \vec{R}_z^2 \rangle = C_2 m_i n_i v_{iz} (\langle B V_{i||} \rangle - \langle B V_{z||} \rangle)$$

, A-2b)

$$- \frac{z}{s} \left(C_2 + \frac{Y_{iz}}{v_{iz}} \sqrt{2} \right) \frac{\langle B q_{i||} \rangle}{P_i} m_i n_i v_{iz}$$

and

$$\langle \vec{B} \cdot \vec{R}_z^3 \rangle = C_2 m_i n_i v_{iz} (\langle B v_{i||} \rangle - \langle B v_{z||} \rangle)$$

. A-2c)

$$-2/\epsilon (\sqrt{2} \frac{\gamma_{zz}}{\gamma_{zi}}) m_i n_i v_{iz} \frac{\langle B q_{z||} \rangle}{F_z}$$

The asterisks on the C factors are omitted here and below for convenience, as all refer to the forms of Hirshman [35].

The average parallel sources are calculated,

$$\langle \vec{B} \cdot \vec{S}_z^1 \rangle = \langle B K_{i||} \rangle - m_i n_i v_{iz} \beta_i \langle B v_{i||} \rangle$$

A-3a)

and

$$\langle \vec{B} \cdot \vec{S}_z^3 \rangle = \langle B K_{i||}^3 \rangle - m_i n_i v_{iz} \beta_i \frac{\langle B Q_{i||} \rangle}{F_i}$$

. A-3b)

In the above equations, β_i is the ratio of the drag frequency to the collision frequency, $\beta_i \equiv \nu_{di} / \nu_{iz}$. The

equivalent equations for the impurity sources are found by exchanging i and z subscripts.

Utilizing the ion heat shear equation, Equation A-1b, with the appropriate substitutions of the frictions, sources and flows, leads to the expression for species i ,

$$n_i \tilde{\mu}_i \frac{\mu_{zi}}{\mu_{zi}} \left[F \left(\frac{P_i}{n_i e_i} + \Phi' \right) + \frac{\langle \Delta_i^0 \rangle}{n_i} + \langle B V_{i||} \rangle + \frac{z}{s} \frac{N_{zi}}{\mu_{zi}} \left(F \frac{s T_i'}{c e_i} + \frac{\langle \Delta_i^0 \rangle}{P_i} + \frac{\langle B q_{i||} \rangle}{P_i} \right) \right]$$

$$= \frac{m_i}{T_i} \langle B K_{i||}^3 \rangle - \frac{s}{2} \langle B K_{i||}^1 \rangle - \frac{s}{2} m_i n_i v_{iz} \beta_i \frac{\langle B q_{i||} \rangle}{P_i} + \quad \text{A-4)}$$

$$+ C_2 m_i n_i v_{iz} (\langle B V_{i||} \rangle - \langle B^{1/2}_{i||} \rangle) - \frac{2}{s} \left(C_3 + \frac{v_{iz}}{v_{iz} \sqrt{2}} \right) m_i n_i v_{iz} \frac{\langle B q_{i||} \rangle}{P_i}$$

In the above equation the terms

$$\tilde{\mu}_i \equiv 3 \mu_{zi} \langle (\hat{n} \cdot \nabla B)^2 \rangle / n_i \langle B^2 \rangle \quad \text{A-5a)}$$

$$\langle \Delta_i^0 \rangle \equiv \langle B^2 \rangle I_i^0 - \langle B^2 I_i^0 \rangle \quad \text{A-5b)}$$

and

$$\langle \Delta_i^2 \rangle \equiv \langle B^2 \rangle I_i^2 - \langle B^2 I_i^2 \rangle - \frac{5}{2} \frac{T_i}{m_i} \langle \Delta_i^0 \rangle \quad \text{A-5c)}$$

were defined. An similar expression for the z species is obtained from Equation A-1b,

$$\begin{aligned} n_z \tilde{N}_z \frac{\mu_{z2}}{N_{12}} \left[F \left(\frac{P_z'}{n_i c_z} + Q' \right) + \frac{\langle \Delta_z^0 \rangle}{n_z} + \langle B V_{z11} \rangle + \frac{2}{5} \frac{\mu_{z2}}{\mu_{12}} \left(F \frac{5}{2} \frac{T_z'}{c_z} + \frac{\langle \Delta_z^2 \rangle}{P_z} \frac{\langle B q_{z11} \rangle}{P_z} \right) \right] \\ = \frac{m_z}{T_z} \langle B K_{z11}^2 \rangle - \frac{5}{2} \langle B K_{z11}^2 \rangle - \frac{5}{2} m_i n_i \nu_{iz} \beta_z \frac{\langle B q_{z11} \rangle}{P_z} \end{aligned} \quad \text{A-6)}$$

$$- \frac{2}{5} \frac{\nu_{z2} \sqrt{2}}{\nu_{zi}} m_i n_i \nu_{iz} \frac{\langle B q_{z11} \rangle}{P_z} + C_2 m_i n_i \nu_{iz} (\langle B V_{z11} \rangle - \langle B V_{z11} \rangle)$$

These two equations are solved independently for the averaged parallel heat flows, $\langle B q_{z11} \rangle$ and $\langle B q_{z11} \rangle$, with the averaged parallel particle flows undetermined. A larger number of species would be coupled, and could be solved for using matrices. The constant

$$\langle \frac{B q_{z11}}{P_z} \rangle = \frac{5}{2} \left[\frac{Q_i}{m_i n_i \nu_{iz}} - \frac{n_i \tilde{p}_i}{m_i n_i \nu_{iz}} \frac{\mu_{z1}}{\mu_{12}} \langle B V_{z11} \rangle + C_2 (\langle B V_{z11} \rangle - \langle B V_{z11} \rangle) \right] \quad \text{A-7)}$$

is found, where

$$a_i = \frac{5}{2} \beta_i + C_3 + \frac{\sqrt{z} \nu_{ie}}{\nu_{iz}} + \frac{n_i \hat{\rho}_i}{m_i n_i \nu_{iz}} \frac{\mu_{zi}}{\mu_{ii}} \quad \text{A-8a)}$$

The combination of terms,

$$Q_i = \frac{m_i}{T_i} \langle BK_{i||}^3 \rangle - \frac{5}{2} \langle BK_{i||}^1 \rangle - n_i \hat{\rho}_i \left[\frac{\mu_{zi}}{\mu_{ie}} \left(F \left(\frac{\rho_i'}{n_i e_i} + \Phi' \right) + \frac{\langle \Delta_i^2 \rangle}{n_i} \right) + \frac{\mu_{zi}}{\mu_{ze}} \left(F \frac{5}{2} \frac{T_i}{e_i} + \frac{\langle \Delta_i^2 \rangle}{\rho_i} \right) \right] \quad \text{A-8b)}$$

is defined and left in this form due to the complexity involved in it. The form of the solution for the averaged parallel impurity heat flux is the same as Equation A-7 with z exchanged for i , with the exception that the term

$$a_z = \frac{5}{2} \beta_z + \frac{\nu_{z2}}{\nu_{ze}} \sqrt{z} + \frac{n_z \hat{\rho}_z}{m_z n_z \nu_{iz}} \frac{\mu_{z2}}{\mu_{iz}} \quad \text{A-9)}$$

is slightly modified.

Similarly, the parallel particle flows are found by solving the particle friction equation, Equation A-1a. Solving simultaneously with the solution for the averaged parallel heat flux, the parallel averaged particle flow is

found,

$$\langle BV_{i||} \rangle = [(\xi_i + \lambda) N_i + \lambda N_z] / m_i n_i v_{iz} d_{zi} \quad , \quad A-10)$$

where

$$N_i = \langle BK_{i||} \rangle - n_i \tilde{\rho}_i \left[F \left(\frac{\beta_i}{n_i c_i} + \Phi' \right) + \frac{\langle \Delta_i^2 \rangle}{n_i} + \frac{\mu_{zi}}{\mu_{zi}} \left(\frac{F}{c_i} \frac{1}{2} T_i' + \frac{\langle \Delta_i^2 \rangle}{\rho_i} \right) \right] \\ + \frac{1}{2} C_2 \left(\frac{Q_i}{a_i} - \frac{Q_z}{a_z} \right) - \frac{n_i \tilde{\rho}_i}{m_i n_i v_{iz}} \frac{\mu_{zi}}{\mu_{zi}} \frac{1}{2} \frac{Q_i}{a_i} \quad , \quad A-11a)$$

$$\lambda = C_1 - C_2^2 \left(\frac{1}{a_i} + \frac{1}{a_z} \right) + \frac{C_2}{a_i} \frac{n_i \tilde{\rho}_i}{m_i n_i v_{iz}} \frac{\mu_{zi}}{\mu_{zi}} + \frac{C_2}{a_z} \frac{n_z \tilde{\rho}_z}{m_z n_z v_{iz}} \frac{\mu_{z2}}{\mu_{z2}} \quad , \quad A-11b)$$

$$\xi_i = \beta_i + \frac{n_i \tilde{\rho}_i}{m_i n_i v_{iz}} - \left(\frac{n_i \tilde{\rho}_i}{m_i n_i v_{iz}} \frac{\mu_{zi}}{\mu_{zi}} \right)^2 / a_i \\ + C_2 \frac{n_i \tilde{\rho}_i}{m_i n_i v_{iz}} \frac{\mu_{zi}}{\mu_{zi}} / a_i - C_2 \frac{n_z \tilde{\rho}_z}{m_z n_z v_{iz}} \frac{\mu_{z2}}{\mu_{z2}} / a_z \quad , \quad A-11c)$$

and

$$d_{zi} = (\xi_i + \xi_z) \lambda + \xi_i \xi_z \quad . \quad \text{A-11d)}$$

$\langle Bn_z V_{z\parallel} \rangle$ is found by interchanging subscripts, and the first order flows are now known in terms of gradients, sources, and the electrostatic potential gradient.

APPENDIX B

TWO SPECIES ELECTROSTATIC POTENTIAL

To determine the electrostatic potential in the radial direction, it is first necessary to take the sum over all species of the flux surface averaged toroidal component of the momentum balance equation, obtaining to first order,

$$\sum_i m_i n_i \langle R^2 \nabla \phi \cdot \frac{\partial \vec{V}_i}{\partial t} \rangle = \sum_i [n_i e_i \langle R^2 \nabla \phi \cdot \vec{V}_i \times \vec{B} \rangle + \langle R^2 \nabla \phi \cdot \vec{S}_i \rangle] \quad , \quad B-1)$$

where the remaining terms have been removed by axisymmetry, charge neutrality, and conservation of momentum in elastic collisions. Following Stacey and Sigmar [15], by rewriting the first term on the right hand side,

$$\begin{aligned} \sum_i [n_i e_i \langle R^2 \nabla \phi \cdot \vec{V}_i \times \vec{B} \rangle] &= \sum_i n_i e_i \langle R^2 \nabla \phi \cdot (\vec{V}_i \times (\nabla \phi + \nabla \phi \times \nabla \psi)) \rangle \\ &= \sum_i n_i e_i \langle \nabla \psi \cdot \vec{V}_i \rangle \quad , \quad B-2) \\ &= \langle \vec{j} \cdot \nabla \psi \rangle \end{aligned}$$

with \vec{j} being the current, Equation B-1 reaches the following form,

$$\sum_i m_i n_i \langle R^2 \nabla \phi \cdot \frac{\partial \vec{V}_i}{\partial t} \rangle = \sum_i \langle R^2 \nabla \phi \cdot \vec{S}_i' \rangle + \langle \vec{j} \cdot \nabla \psi \rangle \quad . \quad \text{B-3)}$$

The radial component of Amperes Law,

$$\langle \vec{j} \cdot \nabla \psi \rangle + \epsilon_0 \frac{\partial}{\partial t} \langle \vec{E} \cdot \nabla \psi \rangle = 0 \quad , \quad \text{B-4)}$$

requires that, for steady state, $\langle \vec{j} \cdot \nabla \psi \rangle = 0$. This requires that the net momentum source must vanish in the toroidal direction,

$$\sum_i \langle R^2 \nabla \phi \cdot \vec{S}_i' \rangle = 0 \quad . \quad \text{B-5)}$$

Hence, ambipolarity here is dictated by both charge flux balance and momentum conservation.

Specializing to two species, i and z , and substituting in the form for the velocity found in Equation 2.2.24, the solution for Φ' is found,

$$\begin{aligned}
& - \left[\left\langle 1 - \frac{B^2}{\langle B^2 \rangle} \right\rangle + \frac{1}{m_i n_i v_{i2} (\beta_i + \beta_z) d z_i} \left[\gamma_z \frac{[N_i]_{\phi'}}{F \Phi'} + \frac{[N_z]_{\phi'} \gamma_i}{F \Phi'} \right] \right] \Phi' = \\
& - \frac{\langle R^2 \nabla \phi \cdot (\bar{K}_i + \bar{K}_z) \rangle \langle B^2 \rangle}{m_i n_i v_{i2} (\beta_i + \beta_z) F^2} + \left\langle 1 - \frac{B^2}{\langle B^2 \rangle} \right\rangle \left(\frac{\beta_i}{\beta_i + \beta_z} \frac{P_i'}{n_i \epsilon_i} + \frac{\beta_z}{\beta_i + \beta_z} \frac{P_z'}{n_z \epsilon_z} \right) \quad \text{B-6} \\
& + \frac{1}{\beta_i + \beta_z} \left(\beta_i \frac{\langle \Delta_i^0 \rangle}{n_i} + \beta_z \frac{\langle \Delta_z^0 \rangle}{n_z} \right) + \frac{\gamma_i [N_i]_{\phi'} + \gamma_z [N_z]_{\phi'}}{m_i n_i v_{i2} (\beta_i + \beta_z) F d z_i}
\end{aligned}$$

where

$$\gamma_z = \lambda (\beta_i + \beta_z) + \beta_z \zeta_i \quad \text{B-7) }$$

and the $N_{i,z}$ terms are determined from Appendix A. The $[N_i]_{\phi}$ denotes terms including the electrostatic potential and $[N_i]_{\phi'}$ denotes terms that do not.

In order to limit the electrostatic potential to the three collisionality regimes described in the text, the reductions found in the text for each regime are used. In addition, the terms $\gamma_{i,z}$ are, for each collisionality regime: collisional,

$$\gamma_i = \gamma_z = \lambda (\beta_i + \beta_z) + \beta_i \beta_z \quad ; \quad \text{B-8) }$$

mixed,

$$Y_i = \lambda(\beta_i + \beta_z) + \beta_i \left(\beta_z - C_z \frac{n_i \hat{\rho}_i}{m_i n_i v_{iz}} \frac{\mu_{z0}}{\mu_i} / a_i \right) \quad \text{B-9a)}$$

and

$$Y_z = \lambda(\beta_i + \beta_z) + \beta_z \left(\beta_i + \frac{n_i \hat{\rho}_i}{m_i n_i v_{iz}} - \frac{n_i \hat{\rho}_i}{m_i n_i v_{iz}} \frac{\mu_{z0}}{\mu_i} \left(\frac{n_i \hat{\rho}_i}{m_i n_i v_{iz}} \frac{\mu_{z0}}{\mu_i} - C_z \right) / a_i \right) ; \quad \text{B-9b)}$$

and, in the collisionless regime, the terms are unchanged in form and are given in Equation B-7.

Using the low beta, high aspect ratio limit, the electrostatic potential for the collisional regime becomes,

$$\begin{aligned} \Phi' = & -\frac{1}{Z} \frac{K_{\theta i} + K_{\theta z}}{m_i n_i v_{iz} (\beta_i + \beta_z) R_0} - \frac{1}{R_0 B_{p0} (\beta_i + \beta_z)} \left(\frac{\beta_i}{n_i c} \frac{\partial p_i}{\partial r} + \frac{\beta_z}{n_z e_z} \frac{\partial p_z}{\partial r} \right) \\ & + \frac{1}{\beta_i + \beta_z} \frac{1}{2 \epsilon^2} \left[\beta_i \frac{\langle \Delta_i^{\circ 0} \rangle}{n_i} - \frac{\langle \Delta_z^{\circ 0} \rangle}{n_z} \beta_z \right] \end{aligned} \quad \text{B-10)}$$

ignoring ϵ^2 terms. Similarly, the electrostatic potential in the mixed regime is found to be

$$\begin{aligned}
 FD_{\phi m} \Phi' &= -B_0 K_{\phi i} (d_{zi} - Y_i) - B_0 K_{\phi z} (d_{zi} - Y_z) \\
 &- n_i \tilde{\mu}_i Y_i \left(\frac{P_i'}{n_i \epsilon_i} + \frac{N_{zi}}{\mu_i} \frac{1}{2} \frac{T_i'}{\epsilon_i} \right) + \left[C_1 (\beta_i \xi_{iz} - \beta_z \xi_{iz}) - \frac{n_i \tilde{\mu}_i}{m_i n_i v_{iz}} \frac{\mu_{zi}}{\mu_i} \right] \frac{1}{2} Q_i / a_i, \quad \text{B-11)} \\
 &+ C_2 (\beta_z \xi_{iz} - \beta_i \xi_{iz}) \frac{1}{2} Q_z / a_z
 \end{aligned}$$

where

$$D_{\phi m} = n_i \tilde{\mu}_i \left[Y_i + \frac{1}{2} \frac{N_{zi}}{\mu_i} / a_i \left(C_2 (Y_i - Y_z) + \frac{n_i \tilde{\mu}_i}{m_i n_i v_{iz}} \frac{\mu_{zi}}{\mu_i} \right) \right] \quad \text{B-12)}$$

In the collisionless regime, only ϵ^2 or smaller terms are ignored,

$$\begin{aligned}
 FD_{\phi c} \Phi' &= -B_0 K_{\phi i} (d_{zi} - Y_i) - B_0 K_{\phi z} (d_{zi} - Y_z) \\
 &- n_i \tilde{\mu}_i Y_i F \left(\frac{P_i'}{n_i \epsilon_i} + \frac{N_{zi}}{\mu_i} \frac{1}{2} \frac{T_i'}{\epsilon_i} \right) - n_z \tilde{\mu}_z Y_z F \left(\frac{P_z'}{n_z \epsilon_z} + \frac{\mu_{zz}}{\mu_z} \frac{1}{2} \frac{T_z'}{\epsilon_z} \right) \\
 &+ \left(C_2 (\beta_i \xi_{iz} - \beta_z \xi_{iz}) - \frac{n_i \tilde{\mu}_i}{m_i n_i v_{iz}} \frac{\mu_{zi}}{\mu_i} \right) \frac{1}{2} Q_i / a_i \\
 &+ \left(C_2 (\beta_z \xi_{iz} - \beta_i \xi_{iz}) - \frac{n_z \tilde{\mu}_z}{m_i n_i v_{iz}} \frac{\mu_{zz}}{\mu_z} \right) \frac{1}{2} Q_z / a_z
 \end{aligned} \quad \text{B-13)}$$

where

$$D_{\phi c} = - \left[\gamma_1 [N_1]_{\phi'} + \gamma_2 [N_2]_{\phi'} \right] / F \Phi' \quad . \quad \text{B-14)}$$

These results reduce to those of Stacey and Sigmar [16] when the temperature gradients and heat sources are ignored, and when $C_1 = 1$, $C_2 = C_3 = 0$, and when $\mu_2 = \mu_3 = 0$. The electrostatic potential is identical to that found by Stacey and Sigmar [16] in the collisional limit.

APPENDIX C

BEAM DRIVEN FLUXES FOR MULTIPLE SPECIES

This appendix covers an approximate solution for the beam driven fluxes when more than two ion species are present. The method used for two species could of course be extended, but this method would quickly become very complicated. Hence, approximations are used to simplify the solution.

In the text, the beam driven and pressure gradient driven fluxes were found to be independent of each other, so only the beam driven fluxes are calculated here. The pressure and temperature gradient driven transport fluxes for multiple species are presented in a review by Hirshman and Sigmar [38]. Since the inclusion of the calculation of heat fluxes had little effect on the resulting beam driven radial fluxes, these effects are also ignored here. With these limitations, the important equation for the particle flows, the flux surface averaged parallel momentum balance equation, is, from Equations 2.3.1 and 2.3.3,

$$\langle \vec{B} \cdot \nabla \vec{\pi}_j \rangle = \langle B^2 \rangle n_j \tilde{\rho}_j (\Gamma_{jP}/n_j) = \langle \vec{B} \cdot (\vec{R}_j + \vec{S}_j) \rangle \quad \text{C-1)}$$

First, the general equation for the radial particle fluxes is examined to determine to what accuracy the particle flows on the flux surface are needed. Combining Equations C-1 and 2.4.3, the radial particle flux can be written

$$e_j \Gamma_j = -n_j \tilde{\rho}_j \frac{F}{\langle B^2 \rangle} [\langle R V_{j||} \rangle + F \Phi'] - \varepsilon^2 R_0 K_{\phi j} - 2\varepsilon^2 m_j n_j \nu_{dj} \frac{F^2}{\langle B^2 \rangle} \Phi' \quad \text{C-2)}$$

The first term is of collisionless ordering ($\sqrt{\varepsilon}$), and the second term is of collisional ordering (ε^2). If species j is collisionless, $\tilde{\rho}_j \neq 0$, only the first term is required for the order $\sqrt{\varepsilon}$ fluxes. When species j is collisional, $\tilde{\rho}_j = 0$, only the second term contributes to the collisional, order ε^2 , fluxes.

The friction between species is assumed to dominate over the external drags, so that the toroidal velocity difference between two species is small compared to the

toroidal velocity of either species. This was found to be true experimentally, the total drag or momentum diffusion rate being found to be approximately times smaller than the ion collision rate, or about the same magnitude as the parallel viscosity. Thus, the particle flows can be written as a bulk velocity plus a smaller velocity differential for each species,

$$\langle BV_{ij} \rangle = \langle BU_{ij} \rangle + \langle B\tilde{V}_{ij} \rangle \quad \text{C-3}$$

Using this and summing over the parallel momentum balance, Equation C-1, the bulk parallel flow is found to be

$$\langle BU_{ij} \rangle = \frac{\sum \langle BK_{ij} \rangle - F\Phi' \sum n_j \tilde{\rho}_j - \sum (n_j \tilde{\rho}_j + m_j n_j \gamma_{aj}) \langle B\tilde{V}_{ij} \rangle}{\sum (n_j \tilde{\rho}_j + m_j n_j \gamma_{aj})} \quad \text{C-4}$$

where the summation is over all species j .

At this point, two solutions are followed, one for the collisionless flux and one for the collisional flux. When species j is collisional, only the electrostatic potential need be evaluated. By summing over Equation C-2, and by requiring ambipolarity, ($\sum_j e_j \Gamma_j = 0$), the

electrostatic potential is found for this condition,

$$F\Phi' = - \frac{\sum (n_j \tilde{\rho}_j + \varepsilon^2 (m_j n_j v_{d_j} + n_j \tilde{\rho}_j)) \sum \langle BK_{n_j} \rangle}{\sum (n_j \tilde{\rho}_j + 2\varepsilon^2 m_j n_j v_{d_j}) \sum n_j m_j v_{d_j}} \quad \text{C-5)}$$

This reduces to

$$F\Phi' = - \frac{\sum \langle BK_{n_j} \rangle}{\sum n_j n_j v_{d_j}} a \quad \text{C-6)}$$

where $a = 1$ when any $\tilde{\rho}_j$ is non-zero and $a = 1/2$ when all are zero.

With the electrostatic potential determined, the collisional beam driven flux is

$$e_j \Gamma_j = -\varepsilon^2 R_0 \left[K_{\Phi_j} - \frac{2a m_j n_j v_{d_j}}{\sum_{all j} n_j n_j v_{d_j}} \sum_{all j} K_{\Phi_j} \right] \quad \text{C-7)}$$

For two species, this result is approximately the same as the mixed and collisional regime beam driven impurity fluxes

found in the text, Equations 2.6.4 and 2.7.5, the fluxes differing only by a factor of $(1 + O(\sqrt{\epsilon}))$.

The solution for the collisionless beam driven flux is similar. The $O(\epsilon^2)$ terms are ignored, and requiring ambipolarity leads to the condition

$$\langle BU_{||} \rangle + F \Phi' = - \frac{\sum n_j \tilde{p}_j \langle B \tilde{V}_{||j} \rangle}{\sum n_j \tilde{p}_j} \quad \text{C-8)}$$

The flux can now be written,

$$e_j \Pi_j = -n_j \tilde{p}_j \frac{F}{\langle B^2 \rangle} \left[\langle B \tilde{V}_{||j} \rangle - \frac{\sum n_j \tilde{p}_j \langle B \tilde{V}_{||j} \rangle}{\sum n_j \tilde{p}_j} \right] \quad \text{C-9)}$$

The perturbed velocities are unknown, and must be found by solving a series of coupled parallel momentum balance equations in the form of Equation C-1, similar to the solution for two species found in Appendix A, for each species present. An example of the flux of species 1 in a three species plasma (1,2,3) is

$$\begin{aligned}
e_i \Gamma_i = & -R_0 \frac{1}{2} \frac{n_i \tilde{\rho}_i}{\sum_{j=3} n_j \tilde{\rho}_j} \frac{1}{\sum_{l=3} n_l m_l v_{il}} \left\{ \frac{n_i \tilde{\rho}_i + n_2 \tilde{\rho}_2}{C_{23}} [(n_2 m_2 v_{i2} + n_3 m_3 v_{i3}) K_{\phi 1} - n_i m_i v_{il} (K_{\phi 2} + K_{\phi 3})] \right. \\
& - \frac{n_2 \tilde{\rho}_2 - n_3 \tilde{\rho}_3}{C_{13}} [(n_1 m_1 v_{i1} + n_3 m_3 v_{i3}) K_{\phi 2} - n_2 m_2 v_{i2} (K_{\phi 1} + K_{\phi 3})] \\
& \left. - \frac{n_3 \tilde{\rho}_3 - n_2 \tilde{\rho}_2}{C_{12}} [(n_1 m_1 v_{i1} + n_2 m_2 v_{i2}) K_{\phi 3} - n_3 m_3 v_{i3} (K_{\phi 1} + K_{\phi 2})] \right\} \quad \text{C-10) }
\end{aligned}$$

In this example, the form used for the friction was

$$\vec{R}_j = \sum_{k \neq j} C_{jk} (\vec{V}_k - \vec{V}_j) \quad \text{C-11) }$$

APPENDIX D

DEFINITIONS AND EVALUATION OF COEFFICIENTS

Many of the fluid terms found in the text are derived from kinetic theory. The kinetic theory definitions of the fluid properties found in the four moment equations of Section 2.2 are given in this appendix. In addition, the friction and parallel viscosity coefficients are given, and some of the properties of the parallel viscosity are evaluated.

By using the kinetic distribution function, $f=f(x,v,t)$, the following fluid properties are defined [32]: the particle density,

$$n = \int d^3v f \quad ; \quad D-1)$$

the particle flow,

$$n\vec{V} = \int d^3v v f \quad ; \quad D-2)$$

the total momentum stress,

$$\hat{\mathbf{M}} = \int d^3\vec{v} m \vec{v} \vec{v} f \quad , \quad \text{D-3)}$$

to which the pressure tensor,

$$\begin{aligned} \hat{\mathbf{P}} &= \int d^3\vec{v} m (\vec{v} - \vec{V})(\vec{v} - \vec{V}) f \\ &= \hat{\mathbf{M}} - nm \vec{V} \vec{V} \end{aligned} \quad , \quad \text{D-4)}$$

the scalar pressure

$$p \equiv nT = \text{Trace} [\hat{\mathbf{P}}] \quad , \quad \text{D-5)}$$

and the anisotropic shear stress tensor

$$\hat{\mathbf{\Pi}} = (\hat{\mathbf{P}} - p \hat{\mathbf{I}}) \quad , \quad \text{D-6)}$$

are related; the heat flow

$$\vec{Q} = \int d^3\vec{v} (m v^2/2) \vec{v} f \quad , \quad \text{D-7)}$$

to which the energy flux is related,

$$q = \int d^3\vec{v} (m/2) (\vec{v} - \vec{V})^2 (\vec{v} - \vec{V}) f \quad ; \quad \text{D-8)}$$

and the energy weighted stress tensor

$$\vec{H} = \int d^3\vec{v} (m\vec{v}/2) \vec{v} \vec{v} f \quad . \quad \text{D-9)}$$

With the addition of the collision operator, $C(f)$, the particle and heat friction is defined,

$$R' = \int d^3\vec{v} m \vec{v} C(f) \quad \text{D-10)}$$

and

$$R^3 = \int d^3\vec{v} (mv^2/2) C(f) \quad \text{D-11)}$$

From Hirshman and Sigmar [38], the particle and heat friction due to the first order flows are written

$$R_a^1 = \sum_b (l_{11}^{ab} \vec{V}_b - z/s l_{12}^{ab} \frac{\vec{q}_b}{P_b}) \quad \text{D-12)}$$

and

$$R_a^{3'} = (R_a^3 - \frac{T}{m} R_a^1) = \sum_b (-l_{12}^{ab} \vec{V}_b + z/s l_{22}^{ab} \frac{\vec{q}_b}{P_b}) \quad \text{D-13)}$$

where

$$l_{ij}^{ab} = (\sum_k n_a m_a k_k M_{ak}^{i-1, j-1}) \delta_{ab} + m_a n_a v_{ab} N_{ab}^{i-1, j-1} \quad \text{D-14)}$$

and δ_{ab} is the delta function ($\delta_{ab} = 1$ when $a=b$ and $\delta_{ab} = 0$ when $a \neq b$). Symmetry properties of the matrix elements are

$$M_{ab}^{ij} = M_{ab}^{ji} \quad , \quad \text{D-15)}$$

$$(\tau_a V_{tha})^{-1} N_{ab}^{ij} = (\tau_b V_{tmb})^{-1} N_{ba}^{ji} \quad , \quad \text{D-16)}$$

and

$$l_{ij}^{ab} = l_{ji}^{ab} \quad . \quad \text{D-17)}$$

Also, momentum conservation requires that

$$M_{ab}^{j0} + N_{ab}^{j0} = 0 \quad \text{D-18)}$$

for all j .

For a Coulomb collision operator when the ion is in the collisionless regime, the matrix elements are:

$$M_{ab}^{01} = M_{ab}^{10} = -\frac{3}{2} \left(1 + \frac{m_a}{m_b}\right) (1 + x_{ab}^2)^{-5/2} = -N_{ab}^{10} \quad , \quad \text{D-19)}$$

$$M_{ab}^{00} = - \left(1 + \frac{m_a}{m_b}\right) (1 + x_{ab}^2)^{-3/2} = -N_{ab}^{00} \quad , \quad \text{D-20)}$$

$$M_{ab}^{11} = - \left(\frac{13}{4} + 4 x_{ab}^2 + \frac{15}{4} x_{ab}^4\right) (1 + x_{ab}^2)^{-5/2} \quad , \quad \text{D-21)}$$

and

$$N_{ab}^{11} = \frac{27}{4} \frac{T_a}{T_b} x_{ab}^2 (1 + x_{ab}^2)^{-5/2} \quad , \quad \text{D-22)}$$

where $x_{ab} = v_{thb} / v_{tha}$. In the large mass ratio limit used

in the text, ($m_a/m_b \rightarrow 0$, so $x_{ab} \rightarrow 0$), $M_{ab}^{00} = -N_{ab}^{00} = -C_1$,

$M_{ab}^{01} = M_{ab}^{10} = -N_{ab}^{10} = -3/2 = -C_2$, $M_{ab}^{11} = -13/4 = -C_3$, and

$N_{ab}^{11} = 0$.

Also in Reference [38], the parallel viscosity coefficient are defined by

$$\mu_{ai} = f n_a m_a \frac{\langle B^2 \rangle}{3 \langle (\hat{n} \cdot \nabla B)^2 \rangle} \left\{ (\alpha^2 - 5/2)^{i-1} \nu_t^a \right\} \quad \text{D-23)}$$

where ν_t^a is the neoclassical frequency for stress anisotropy relaxation,

$$\nu_t^a = \nu_{coll}^a (1 + \nu_{*a})^{-1} \left(1 + \frac{5\pi}{8} \nu_{th}^a / \omega_{ca} \right)^{-1} \quad \text{D-24)}$$

and the braces denote the velocity integration operator

$$\left\{ A(v) \right\} = \frac{8}{3\sqrt{\pi}} \int dx x^4 \exp(-x^2) A(x) \quad , \quad \text{D-25)}$$

Computer evaluation of the viscosity coefficients lead to the fits,

$$\mu_{ai} = \mu_{a0} K_{ii}(\nu_{*a}, \alpha) \quad , \quad \text{D-26)}$$

$$\mu_{a2} = \mu_{a0} (K_{12} - 5/2 K_{11})$$

, D-27)

and

$$\mu_{a3} = \mu_{a0} (K_{13} - 5 K_{12} + \frac{25}{4} K_{11})$$

, D-28)

where

$$\mu_{a0} = 1.38 \rho (R_g/\alpha) v_t^a$$

. D-29)

The coefficients are fitted over the range $10^{-2} < \alpha v_{ta} < 10^2 \xi^{-3/2}$ to the analytic function

$$K_{mn} = K_{mn}^0 [1 + (A_{mn} v_{ta})^{1/2} + (B_{mn} v_{ta})]^{-1} \times [1 + (C_{mn} v_{ta} \xi^{3/2})^{1/2} + (D_{mn} v_{ta} \xi^{5/2})^{1/2}]^{-1}$$

, D-30)

where the parameters K_{mn}^0 , ect., are given in Table D-1. This fit was found in Reference [10].

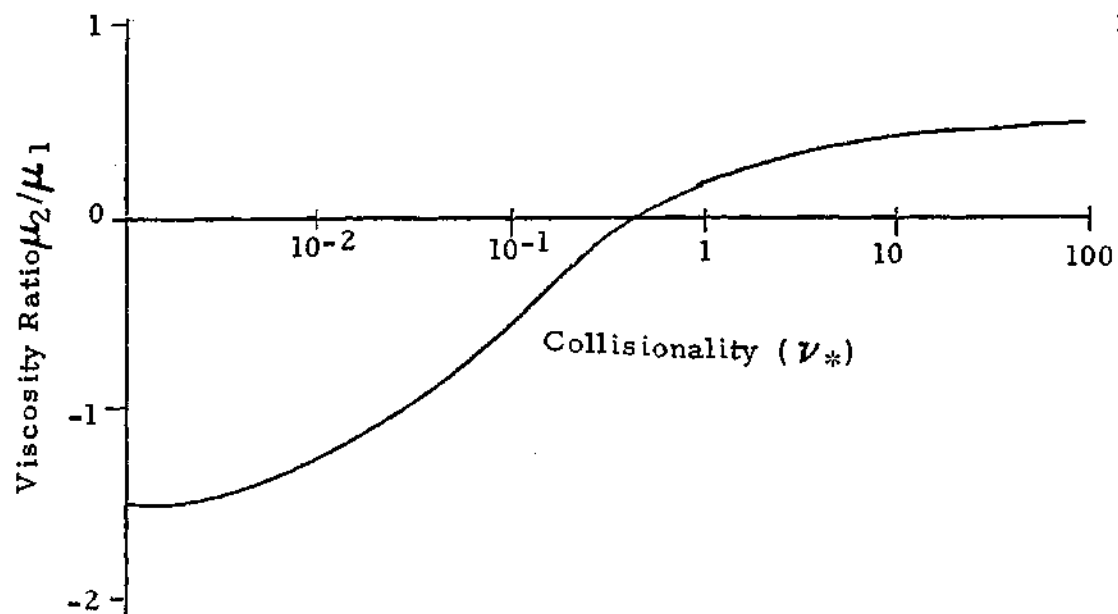


Figure D-1 Variance of Viscosity Ratio μ_2/μ_1 with Collisionality

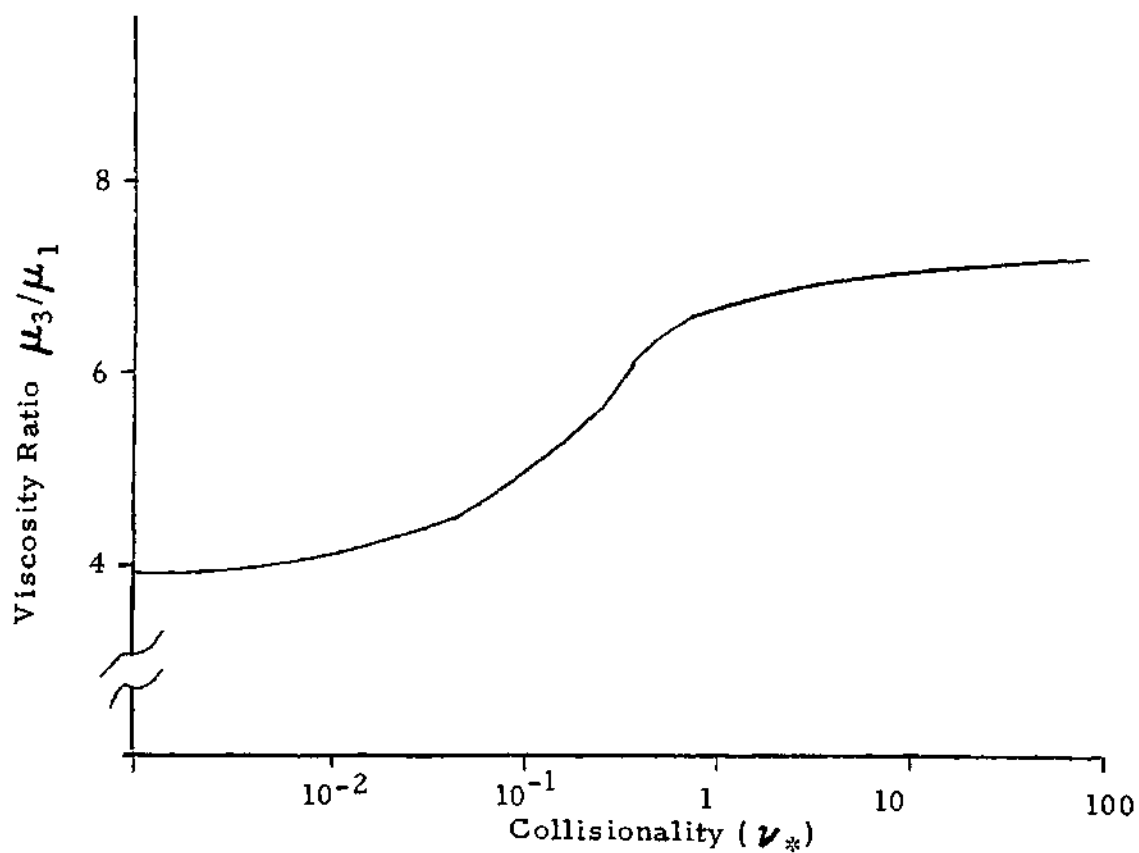


Figure D-2 Variance of Viscosity Ratio μ_3/μ_1 with Collisionality

Graphs of the evaluation of the ratio μ_2/μ_1 and μ_3/μ_1 , which are important in the text, were evaluated here and appear in Figures D-1 and D-2 as a function of γ_{ra} .

TABLE D-1 Summary of least squares fits.

m	$K_{\text{res}}^{(0)}$	A_{res}	B_{res}	C_{res}	D_{res}
11	$0.53 + Z_2^*$	$\frac{0.52 - 0.42Z_2^*}{1 + 1.35Z_2^*} + 3.44Z_2^*$	$0.58 + 0.96Z_2^*$	$\frac{0.14 + 0.55Z_2^*}{1 + 5.0Z_2^*} + 0.25Z_2^*$	$\frac{0.7 + 0.78Z_2^*}{1 + Z_2^*} + 0.51Z_2^*$
12	$0.71 + Z_2^*$	$\frac{0.10 + 0.08Z_2^*}{1 + 1.3Z_2^*} + 0.31Z_2^*$	$0.26 + 0.35Z_2^*$	$\frac{0.072 + 0.15Z_2^*}{1 + 3.0Z_2^*} + 0.081Z_2^*$	$\frac{0.42 + 0.62Z_2^*}{1 + 1.42Z_2^*} + 0.29Z_2^*$
13	$1 + \frac{(0.53 + Z_2^*)}{Z_2^*(1 + 1.35Z_2^*)}$	$0.52 + Z_2^* \left[0.13 + \frac{1.53}{(1 + 2.1Z_2^*)^2} \right]$	$0.56 + 0.25Z_2^*$	$0.25 + 0.051Z_2^*$ $\frac{0.11 + 0.74Z_2^*}{1 + 2.29Z_2^* + 0.85(Z_2^*)^2}$	$\frac{0.70 + 2.99Z_2^*}{1 + 5Z_2^*} + 0.22Z_2^*$
23	$2.5 + \frac{0.72 - 0.127Z_2^*}{Z_2^*(1 + 0.26Z_2^*)}$	$0.12 + 0.041Z_2^*$	$0.26 + 0.141Z_2^*$	$0.21 + 0.022Z_2^*$ $\frac{0.14 + 0.84Z_2^*}{1 + 3.28Z_2^* + 1.22(Z_2^*)^2}$	$\frac{0.43 + 1.95Z_2^*}{1 + 5Z_2^*} + 0.15Z_2^*$

BIBLIOGRAPHY

1. L. A. Artsimovich, Nucl. Fusion 2, 215 (1972); also H. P. Furth, Nucl. Fusion 15, 487 (1975).
2. C. L. Longmire and M. N. Rosenbluth, Phys. Rev. 103, 507 (1956).
3. S. I. Braginskii, in Reviews of Plasma Physics, edited by M. A. Leontovich (Consultants Bureau, New York, 1965) Vol. 1, 205.
4. D. Pfirsich and A. Schlueter, Max-Planck-Institute for Physics and Astrophysics, München, Report MPI/PA/62.
5. P. H. Rutherford, Phys. Fluids 17, 1782 (1974).
6. C. D. Boley, E. M. Gelbard, and W. M. Stacey, Jr., Phys. Fluids 19, 2051 (1976).
7. J. W. Connor, Plasma Phys. 15, 767 (1973).
8. F. L. Hinton, and T. B. Moore, Nucl. Fusion 14, 639 (1974).
9. S. P. Hirshman, Phys. Fluids 19, 155 (1976).
10. S. P. Hirshman, Phys. Fluids 21, 224 (1978).
11. R. D. Hazeltine and A. A. Ware, Nucl. Fusion 16, 538 (1976).
12. A. Samain, Centre d'Etudes Nucleaires, Commissariat a l'Energie Atomique, Report No. Euratom CEA-FC-745 (1974); also A. Samain, F. Werkoff, Nucl. Fusion 17, 53 (1977).
13. T. Ohkawa, General Atomic Report GA-12926 (1974).
14. Z. El Derini and G. A. Emmert, Nucl. Fusion 16, 342 (1976).
15. W. M. Stacey, Jr. and D. J. Sigmar, Phys, Fluids 22, 2000 (1979).
16. W. M. Stacey, Jr. and D. J. Sigmar, Nucl. Fusion 19, 1665 (1979).

17. T. Ohkawa, Kakuyago-Kenkyu 32, 61 (1974).
18. K. H. Burrell, Phys. Fluids 19, 401 (1976).
19. S. K. Wong, Phys. Fluids 21, 299 (1978).
20. M. S. Chu and J. M. Rawls, Phys. Fluids 20, 1787 (1977).
21. W. M. Stacey, Jr., Phys. Fluids 21, 1404 (1978).
22. W. M. Stacey, Jr., Phys. Fluids 23, 2332 (1980).
23. K. H. Burrell, Alteration of Pfirsch-Schlueter Transport in Tokamaks by All Four External Sources, GA-A15419 (1979).
24. P. B. Parks, K. M. Burrell, and S. K. Wong, Nucl. Fusion 20, 27 (1980).
25. K. H. Burrell, T. Ohkawa, and S. K. Wong, Phys. Rev. Lett., 47, 511 (1981); also GA-A16082 (1980).
26. S. K. Wong and K. H. Burrell, Phys. Fluids 25, 1863 (1982).
27. W. M. Stacey, Jr., D. J. Sigmar, The Effects of Neutral Beam Injection on Impurity Transport in Tokamaks, Georgia Tech Report GTR-43 (1983), Submitted to Phys. Fluids.
28. M. Murakami, et al, Proc. Seventh Inter. Conf. on Plasma Physics and Controlled Nuclear Fusion, Innsbruck 1978, IAEA (Vienna, 1979) 1, 26.
29. D. Eames, Ultra-soft X-Ray Emission from the Princeton Large Torus Tokamak, Ph.D. Thesis, Princeton (1981).
30. A. R. Bragdasarov, et al, Proc. Seventh Inter. Conf. on Plasma Physics and Controlled Nuclear Fusion, Innsbruck 1978, IAEA (Vienna, 1979) 1, 35.
31. R. C. Isler, et al, Nucl. Fusion 23, 1017 (1983); also R. C. Isler and L. E. Murray, in Fusion Energy Division Annual Progress Report, ORNL-5843, p. 47 (1981).
32. F. L. Hinton and R. D. Hazeltine, Rev. Mod. Phys. 48, 239 (1976).
33. W. M. Stacey, Jr., Fusion Plasma Analysis, (Wiley, New York), 1981.
34. S. P. Hirshman and D. J. Sigmar, Phys. Fluids 20, 589 (1977).

35. S. P. Hirshman, *Phys. Fluids* 20, 418 (1977).
36. S. P. Hirshman, *Phys. Fluids* 21, 1295 (1978).
37. S. Suckewer, et al, *Nucl. Fusion* 21, 1301 (1981); also PPPL-1792 (1981).
38. S. P. Hirshman and D. J. Sigmar, *Nucl. Fusion* 21, 1079 (1981).
39. S. Suckewer, et al, *Phys. Rev. Lett.* 43, 207 (1979); also PPPL-1542 (1979).
40. L. A. Berry, et al, Proc. Fifth Inter. Conf. on Plasma Physics and Controlled Nuclear Fusion, Tokyo 1974, IAEA (Vienna, 1975) 1, 113.
41. R. V. Neidigh and J. F. Lyon, *Bull. Am. Phys. Soc.* 23, 711 (1978).
42. D. J. Sigmar, J. F. Clarke, R. V. Neidigh, and K. L. Vander Sluis, *Phys. Rev. Lett.* 33, 1376 (1974).
43. M. N. Rosenbluth, P. H. Rutherford, J. B. Taylor, E. A. Frieman, and L. M. Kovrizhnilch, Proc. Fourth Inter. Conf. on Plasma Physics and Controlled Nuclear Fusion, Madison 1971 IAEA (Vienna, 1972) p. 495.
44. K. T. Tsang and E. A. Frieman, *Phys. Fluids* 19, 747 (1976).
45. M. N. Rosenbluth, R. D. Hazeltine, and F. L. Hinton, *Phys. Fluids* 15, 116 (1972).
46. B. B. Kadomtsev and O. P. Pogutse, in Reviews of Plasma Physics, Edited by M. A. Leontovich (Consultants Bureau, New York, 1970), Vol. 5.
47. R. Z. Sagdeev and A. A. Galeev, Nonlinear Plasma Theory, (Benjamin, New York, 1969).
48. W. Horton, *Phys. Rev. Lett.* 37, 1269 (1976).
49. P. Graff and D. Pfirsch, *Z. Naturforsch* 37a, 795 (1982).
50. S. D. Scott, Ph. D. Thesis, Massachusetts Institute of Technology, March 1982.
51. F. L. Hinton and M. N. Rosenbluth, *Phys. Fluids* 16, 836 (1973).

52. N. A. Krall and A. W. Trivelpiece, Principles of Plasma Physics, (McGraw-Hill, New York, 1973).
53. D. J. Sigmar, H. Howe, Sherwood Theory Meeting (1981); also in USDOE Report DOE/TIC-11600, Vol. IV pp. 4-43 to 4-50 (1981).
54. R. C. Isler, et al, Phys. Rev. Lett. 47, 649 (1981).
55. P. C. Efthimion, et al, "Electron Energy Balance during Neutral Beam Injection", paper 7 in Status of Neutral Beam Heating in PLT, Vol. II, Princeton, NJ, (May, 1978).
56. H. Eubank, et al, Proc. Seventh Inter. Conf. on Plasma Physics and Controlled Nuclear Fusion, Innsbruck 1978, IAEA (Vienna, 1979) 1, 26; also PPPL-1491 (1978)
57. D. Grove, et al, Proc. Sixth Inter. Conf. on Plasma Physic and Controlled Nuclear Fusion, Berchtesgaden 1976, IAEA (Vienna 1977), 1, 26; also PPPL-1302 (1976).
58. H. Howe, the PROCTR transport code, private communication (1980).
59. TFTR Final Conceptual Design Report, C. Yakimo, ed., Princeton Report PPPL-1275; also PH-R-001.
60. FED Group, The Fusion Engineering Device, USDOE Report DOE/TID-11600 (1981).
61. W. M. Stacey, Jr., et al, U. S. FED-INTOR Activity and U. S. Contribution to the International Tokamak Reactor Phase 2A Workshop-1982, Critical Issues, Georgia Institute of Technology, Atlanta, GA (1982).
62. STARFIRE, A Commercial Tokamak Fusion Power Plant Study, Argonne Report ANL/FPP-80-1 (1980).
63. S. S. Medley, R. J. Goldston, H. H. Towner, Performance Study of the TFTR Neutral Beam for Active Charge Exchange Measurements, Princeton report PPPL-1673 (1980).
64. J. L. Cecchi, published in 4th International Conference on Plasma Surface Interaction in Controlled Fusion Devices, Garmisch-Partenkirchen, West Germany, April 1980, as a 'suppliment to the Journal of Nuclear Materials; also PPPL-1668.
65. J. A. Schmidt, private communication (1984)

66. D. E. Post, et al, "Steady State Radiative Cooling Rates for Low Density, High Temperature Plasmas", PPPL-1352 (1977).
67. J. A. Rome, J. D. Callen, J. F. Clarke, Nucl. Fusion 14, 141 (1974); also R. J. Colchin and J. Wooten, ORMAK Technical Memo 163 (1974).
68. J. M. Rawls, Editor, Status of Tokamak Research, U. S. DOE/ER-0034, (October, 1979).